Engineering Materials and Processes

Hua-Xin Peng
Faxiang Qin
Manh-Huong Phan

Ferromagnetic Microwire Composites

From Sensors to Microwave Applications

Springer

Engineering Materials and Processes

Series editor

Brian Derby, Manchester, UK

More information about this series at http://www.springer.com/series/4604

Hua-Xin Peng · Faxiang Qin
Manh-Huong Phan

Ferromagnetic Microwire Composites

From Sensors to Microwave Applications

Springer

Hua-Xin Peng
Institute for Composites Science Innovation (InCSI), School of Materials Science and Engineering
Zhejiang University
Hangzhou, Zhejiang
China

Faxiang Qin
Institute for Composites Science Innovation (InCSI), School of Materials Science and Engineering
Zhejiang University
Hangzhou, Zhejiang
China

Manh-Huong Phan
Department of Physics
University of South Florida
Tampa, FL
USA

ISSN 1619-0181 ISSN 2365-0761 (electronic)
Engineering Materials and Processes
ISBN 978-3-319-29274-8 ISBN 978-3-319-29276-2 (eBook)
DOI 10.1007/978-3-319-29276-2

Library of Congress Control Number: 2016930266

Printed on acid-free paper

This Springer imprint is published by SpringerNature
The registered company is Springer International Publishing AG Switzerland

Foreword

Research on magnetic microwires is largely extended in the recent years as a consequence of their outstanding magnetic properties, and profiting of the particular geometry, with a reduced micrometric diameter but continuous length of up to kilometres. As an important member of the microwire family, amorphous magnetic microwires coated with glassy cover are currently employed in a number of technological applications especially as sensing elements in a variety of sensor devices for high-frequency applications. They derive from the giant magnetoimpedance and microwave phenomena, among the most outstanding and technologically profitable effects observed in ultrasoft amorphous microwires. Built upon solid work in this area, the authors have elucidated these aspects in the first part of the book with chapters dealing with the correlation between magnetic domain structure and magnetic properties after a general introduction. Its content then focuses on the giant magnetoimpedance effect with an overview on the influence of various processing and measuring conditions. Subsequent chapters analyse the criteria for innovative sensors based on magnetoimpedance and the current technological perspectives. In the second part of the book, its core actually, chapters discuss on the multifunctional microwires composites and, more innovatively, the so-called metacomposites. Ferromagnetic microwires and their arrangements are introduced together with their design and fabrication, followed by an overview of mechanical and magnetic properties. Their high-frequency behaviour is analysed in detail, referring particularly to tunable absorption and metamaterial properties at microwave frequencies.

This book represents an innovative and rigorous effort from the authors who have made such a significant progress in amorphous microwires and the microwave properties of their composites, which opens up a new territory in multifunctional composites. In particular, I want to highlight their recent work on metamaterial characteristics of composites with engineered microwire arrangements that has led to the concept of metacomposites from an engineering perspective. I am therefore confident that the content of this book will attract much attention from scientists and engineers with interests in magnetic microwires and their arrangements, in

magnetoimpedance and metamaterial composites, and of course in their microwave technological applications.

The team of authors, led by Prof. Hua-Xin Peng at Zhejiang University, is internationally well acknowledged for their pioneering contributions to the field of multifunctional composite through the developing of ferromagnetic microwire composites. This line of research was firstly activated at Bristol University by Dr. Manh-Huong Phan, presently a research professor at South Florida University, and followed by Dr. Faxiang Qin, currently a research professor at Zhejiang University, both under the guidance of Prof. Peng. All these have put them in a unique position to bring such a topic of significant scientific and technical importance to the academia. I would like to congratulate them for the publication of this book and wish them every success in their future research.

Manuel Vazquez
Institute of Materials Science of Madrid, CSIC

Preface

The idea of writing a book about ferromagnetic microwires and their multifunctional composites initiated after the Ph.D. work of Dr. Manh-Huong Phan on novel magnetic materials in 2006 and that of Dr. Faxiang Qin on composites containing ferromagnetic microwires in 2010. With three more years' continued exploration along this line of work, we felt ready to commit ourselves to such a task and the book proposal to Springer was accepted in 2013. It took us two furthermore years, with a lot of ups and downs, to put a full stop on the writing.

The subject of magnetic microwires and their composites is essentially of interdisciplinary nature, and it touches on multiple fields ranging from materials science and engineering, electrical, and mechanical engineering to physics and chemistry science. We structured the book in two major parts: microwires and their composites, and spared no effort in elaborating the fundamental structure–property relationship through detailed discussions of all types of factors influencing their magnetic and microwave properties. We then described the application potentials from an engineering perspective.

Owning to their exceptional giant magnetoimpedance (GMI) property, ferromagnetic microwires find themselves of great usefulness in high-performance sensor applications where the ultrahigh sensitivity is a distinct advantage over conventional sensors. Driven by such advantages, researchers have spent decades to investigate the fundamental GMI mechanisms and related phenomena in order to advance the design, fabrication, and modulation techniques. The advent of ferromagnetic microwire composites is a direct result of the pursuit of multifunctionality of a composite. Starting from combining electromagnetic characteristics to potentially monitoring the structural health of aerospace composite components, we have presented in the second half of the book, relevant field-tunable microwave behaviour of the composites together with associated fundamental and technical analyses. Subsequently, the readers will find a spectrum of intriguing microwave performance of microwire-based composites in microwave absorption and EMI shielding. Last but not least, we highlighted the most recent work on the so-called *metacomposites*, an emerging topic that we have intensively studied during the

course of writing the book, which is aimed at bridging conventional metamaterials with engineering composites.

The main purpose of the book is to provide a comprehensive knowledge about functional soft ferromagnetic microwires and their composites. The philosophy behind the selection of functional element and the architectural design of composite is expected to be useful for those endeavoured to develop special functional filler for particular composite with various targeted applications, such as medical diagnosis of different types of virus and microwave absorbers operating on different frequency bands. It is pitched at the level of postgraduate students and researchers who are working or having an interest in this exciting research field.

It has been a long, challenging but also fulfilling journey to write such a book, as it involves a wide range of subjects in which our knowledge and expertise are not fully reached. Despite of our enormous efforts in connecting the dots and making sense of each sentence, the book cannot be free from unclear parts. Constructive comments from the interested readers are most welcome to enable us to further improve the book in future editions.

We are indebted to our collaborators worldwide, including Prof. Larissa Panina, Prof. Christian Brosseau, Prof. Arcady Zhukov, Prof. Julia Gaonzalez, Prof. Hari Srikanth, Dr. Dimitry Makhnovskiy, Dr. Mihai Ipatov, Prof. Victorino Franco, Dr. Nikolay Pankratove, Dr. Slava Popov, Prof. Jie Tang, Prof. Lu-Chang Qin, Prof. Walther Schwarzacher, Dr. Geoff Hilton, Mr. Yang Luo, Dr. Huan Wang, Dr. Jingshun Liu, Prof. Jianfei Sun, and all those who have offered us their kind help without which the completion of this book would not be possible. Finally, we extend our great appreciation to Prof. Manual Vazquez who has kindly agreed to write the Foreword with much generosity.

Hangzhou, Zhejiang, China
November 2015

Hua-Xin Peng
Faxiang Qin
Manh-Huong Phan

Contents

About the Authors

Prof. Hua-Xin Peng joined Zhejiang University as a distinguished professor of Aerospace Materials in 2014 under the Global Talent Recruitment Plan from the University of Bristol, UK, where he was a full professor in the Advanced Composites Centre for Innovation and Science (ACCIS) in the Department of Aerospace Engineering. He gained his Ph.D. (1996) and M.Sc. (1993) in composite materials in Harbin Institute of Technology and BEng (1990) in Zhejiang University. He was the founding deputy director of the Bristol Centre for Nanoscience and Quantum Information and worked as a research fellow in the Materials Department at Oxford University (2001–2002) and Brunel University (1998–2000). His research activities focus on nanomaterial through engineering to applications and innovative design of composite microstructures for multifunctionalities. The latter involves the development of ferromagnetic microwire (meta-)composites for a range of ingenious engineering applications such as structural health monitoring and microwave absorption. Prof. Peng is the founding director of the Institute for Composites Science Innovation (InCSI) at Zhejiang University and one of the founding editors of the Elsevier journal *Composites Communications* (*COCO*).

Dr. Faxiang Qin is currently a research professor in the School of Materials Science and Engineering at Zhejiang University, China. He also serves as the associate director of the Institute for Composites Science Innovation there. He was a JSPS fellow at National Institute for Materials Science, Japan, from 2013 to 2015. Prior to that, he was a postdoctoral researcher in Advanced Composite Centre for Innovation and Science at the University of Bristol and Lab-STICC at Université de Bretagne Occidentale from 2010 to 2013. He received the MSc in nanomaterials from the South China University of Technology in 2007 and Ph.D. in multifunctional composites from the University of Bristol in 2010. He was a recipient of the Overseas Research Students Awards Scheme (ORSAS) and the University of Bristol Postgraduate Student Scholarship. He was nominated for the Exceptional Thesis Prize and selected as one of the two candidates at Bristol for UK Royal Academy Engineering Fellowship. He was also an awardee of Youth Thousand

Talents Senior Fellowship in China, Discovery Early Career Researcher Award in Australia, Finistère Postdoctoral Fellowship in France, and Japan Society for the Promotion of Science (JSPS) Fellowship. His research interest lies in magnetic materials, nanomaterials, multifunctional composites, and applied physics. His work has been documented in more than 60 international refereed journal papers published in prestigious journals in materials and physics.

Dr. Manh-Huong Phan is an associate professor of Physics at the University of South Florida, USA. He received B.S., M.S., and Ph.D. degrees in Physics from Vietnam National University in 2000, Chungbuk National University in 2003, and Bristol University in 2006, respectively. Dr. Phan's research interests lie in the physics and applications of magnetic materials. He is a leading expert in the area of functional magnetic materials and nanostructures with magnetocaloric and magnetoimpedance effects for energy-efficient magnetic refrigeration and smart sensor technologies. He has co-authored more than 200 peer-reviewed journal papers (h-index: 30), 4 review papers, and 5 book chapters. He serves as an associate editor of the Journal of Electronic Materials (ISI journal, Impact factor: 1.8) and is an active reviewer for more than 90 major international journals, with "Outstanding Referee" awards from the Journal of Magnetism and Magnetic Materials in 2013 and 2015. He has delivered plenary and invited talks at professional meetings on Magnetism and Magnetic Materials (2007–present) and involved in organising international conferences on Nanomaterials, Energy, and Nanotechnology (2011–present).

Chapter 1
Introduction

Soft ferromagnetic microwires have attracted strong research interest in the past two decades in the physics and materials community, in that they can be conveniently fabricated into microsized continuous wires with uniform and singular mechanical and magnetic properties, including their outstanding giant magnetoimpedance (GMI) properties. Massive research efforts have been devoted to two directions: (i) the microwires' (magnetic) structure optimisation in the context of various sensor applications in megahertz and (ii) innovative design of mesostructure constituted by arrays of wires in composites for microwave (gigahertz) applications such as structural health self-monitoring and absorption/shielding. This comprehensive book that bridges the knowledge of the microwires themselves and their multifunctional polymer composite materials is aimed at maximising the value of previous studies on either microwires or their composites and inspiring further efforts on this line of work with target applications extended herein.

1.1 Giant Magnetoimpedance Sensors Using Magnetic Microwires

Magnetic sensors play an essential role in modern technology. They are widely used in nearly all engineering and industrial sectors, such as high-density magnetic recording, navigation, military and security, target detection and tracking, antitheft systems, non-destructive testing, magnetic marking and labelling, geomagnetic measurements, space research, measurements of magnetic fields onboard spacecraft, and biomagnetic measurements in the human body [1–3].

A wide range of magnetic sensors, such as induction sensors, fluxgate sensors, Hall-effect magnetic sensors, magneto-optical sensors, giant magnetoresistive (GMR) sensors, resonance magnetometers, and superconducting quantum interference device (SQUID) gradiometers, are now available [3]. A magnetic sensor directly converts the magnetic field into a voltage or resistance with, at most, a dc current supply, and the field sensitivity of a magnetic sensor plays a key role in determining its operating regime and potential applications. For instance, SQUID gradiometers

H.-X. Peng et al., *Ferromagnetic Microwire Composites*,
Engineering Materials and Processes, DOI 10.1007/978-3-319-29276-2_1

with a high sensitivity of 10^{-10}–10^{-4} Oe have been used for measuring field gradients or differences due to permanent dipole magnets in major applications of brain function mapping and magnetic anomaly detection. Induction, fluxgate, and GMR sensors with a medium sensitivity of 10^{-6}–10^{2} Oe have been used for measuring perturbations in the magnitudes and/or direction of the Earth's field due to induced or permanent dipoles in major applications of magnetic compasses, munitions fuzzing, and mineral prospecting. Hall-effect sensors with a low sensitivity of 1–10^{6} Oe have been used for applications of non-contact switching, magnetic memory read-out, and current measurements. In addition to the sensitivity requirement, other factors affecting the practical uses of magnetic sensors include the processing cost and power consumption. As compared to existing magnetic sensors, the GMR sensor shows the lowest cost and power consumption. However, the field sensitivity of the GMR sensor is rather low ($\sim$1 %/Oe).

Recently, the development of high-performance magnetic sensors has benefited from the discovery of a new magnetic phenomenon, **giant magnetoimpedance** (GMI) (i.e. a large change in the ac impedance of a soft ferromagnetic conductor subject to an applied dc magnetic field), in metal-based amorphous alloys [4, 5]. It has been demonstrated that magnetic sensors based on the GMI effect offer several advantages over conventional magnetic sensors. The decisive factor is the ultrahigh sensitivity of GMI sensors. When compared with a GMR sensor that has a sensitivity of $\sim$1 %/Oe, the field sensitivity of a typical GMI sensor can reach a value as high as 500 %/Oe [3]. Different classes of novel GMI field sensors using Co-rich amorphous wires have been developed and are being widely used in smartphones and automobile devices [6, 7]. The GMI sensors with a 10^{-8} Oe resolution, the so-called *Super* GMI field sensors, have proved their usefulness for biomagnetic measurements without any magnetic shielding at room temperature [8–10]. The biomagnetic field in living cell tissues has been successfully detected using these sensors.

Historically, GMI has attracted particular interest in the scientific community only since Panina and Mohri in Japan and Beach and Berkowitz in the USA announced their independent discoveries of the so-called GMI effect in Co-based amorphous wires in 1994 [4]. In actual ferromagnetic materials, the maximum value of the GMI effect experimentally obtained to date is much smaller than the theoretically predicted value [3]. Research in this field has thus been focused mainly on special thermal treatments and/or on the development of new materials for improved GMI responses [11, 12]. In order to design and produce novel GMI sensors, a thorough understanding of the GMI phenomena and the properties of GMI materials with an emphasis on how a magnetic sensor utilising the GMI effect can be best designed for technological applications is essential.

GMI materials range from microwires, ribbons, films, and so forth. Microwires, among other materials, have been the focus of the GMI materials research and offer plenty of dimensions to carry out fundamental and technical studies, especially in terms of sensor commercialisation as in Aichi Company and their multifunctional applications as functional fillers. In this context, we organise the first half of the book to present a systematic and comprehensive analysis of the fundamental

aspects of GMI and its potential applications. Chapter 2 introduces the major fabrication techniques in terms of the pros and cons of each method. Chapter 3 discusses the properties and domain structures of microwires, and a correlation between the domain structures and magnetic properties is established therein. The basic concept, theory, and related GMI phenomena are examined in Chap. 4. The effects of measuring and processing parameters on GMI are examined in Chaps. 5 and 6. The wire selection criteria for the design of novel GMI sensors are discussed in Chap. 7. Chapter 8, the last chapter prior to the composite part, describes at length GMI sensors and their current and perspective applications.

1.2 Multifunctional Microwire-Based Composites

Composite materials are attractive because they can combine the superior properties and functionalities of each of their constituents. Much research currently focuses on developing multifunctional composites, which combine good mechanical (structural) attributes along with the functional properties such as thermal, electrical, or magnetic characteristics. A particularly interesting example of such a composite is ferromagnetic microwires embedded in a polymer matrix. These composites can exploit phenomena occurring in the wires such as the giant magnetoimpedance effect and can also offer emergent properties that arise from the mesoscale arrangement of the microwires (so-called metacomposites). Possible applications include remote monitoring of structural integrity, electromagnetic shielding, and cloaking at microwave wavelengths.

Materials today can be conveniently divided into two categories: structural materials and functional materials. Structural materials, for which the most important qualities are their mechanical properties, have undergone development for centuries, due to the lasting need for all kinds of structures, such as buildings, bridges, and vehicles. The pursuit of new materials or new techniques for tailoring materials to obtain better mechanical properties remains one of the major goals of materials research. More recently, the unprecedented development of functional materials (e.g. semiconductors) and devices exploiting them has to some extent stolen the thunder of structural materials. Inert stone could meet the basic needs of ancient humans as it could be built into a robust shelter, but it cannot remotely meet the needs of modern mankind because it cannot take the place of transistors to build a mobile phone or a computer.

It might seem we have nothing to worry about since we have both stone and transistors. But very often, we need both good mechanical and functional properties. Composite materials can fulfil this need for materials that combine multiple desirable properties. A composite, simply put, is composed of two or more kinds of materials or phases, which are referred to as constituents. A composite is attractive in that it can exhibit properties (structural and functional) of each of its constituents. The development of composites is thus driven by the desire for combinations of superior properties and functionalities that a monolithic material cannot offer.

The aeronautical industry, for example, is making greater use of lightweight carbon fibre composites to replace metals, but it must also address the issue of invisible damage occurring inside the composite, for which only viable structural health monitoring can ensure the safety of passengers. Other issues include lightning strike protection, de-icing, and electromagnetic shielding, for which the composite parts must have good electrical or thermal conductivity.

The current trend in research and development is therefore to bring in additional functionalities (e.g. thermal, electrical, or magnetic functions) to a structural composite, giving rise to what are known as multifunctional composites. The ideal approach is to develop multifunctional composites with indiscriminate properties (i.e. with a good all-round combination of properties rather than a single exceptional quality) that can meet all these structural and functional demands in a most economical way. Of particular interest are multifunctional metacomposites, which can offer "new emerging" properties that may not exist in a single constituent. Metacomposites are similar to metamaterials. A traditional metamaterial is constructed with a precise regular arrangement of mesoscale structures, such as conducting rods and rings, which can result in extraordinary electromagnetic properties at wavelengths longer than this scale. Metacomposites, by contrast, can have a somewhat disordered structure, so they are more amenable to industrial-scale fabrication techniques instead of necessarily requiring delicate nano- or microfabrication.

A particularly interesting approach to realising multifunctional metacomposites is by incorporating soft ferromagnetic microwires into a polymer matrix. The polymer matrix largely supplies the structural properties we seek, and the microwires provide the functional (electromagnetic) properties. The science and philosophy behind this specific line of work apply more generally to the development of functional composites using a single kind of fine-sized functional filler, as well as the broader application-driven efforts to develop advanced multifunctional metacomposites, which is exciting and inspiring for the future.

One of the most prominent works on ferromagnetic microwire composites was contributed by Larissa Panina of the University of Plymouth, UK. As the co-discoverer of the giant magnetoimpedance (GMI) effect in microwires [4], she was the first to propose developing GMI microwire-based tunable composite media [13]. The basic idea for exploiting the GMI effect in a composite is to arrange cobalt–iron (CoFe)-based microwires in a certain geometry in order to tune the wire media's response to an incident electromagnetic wave. Depending on the set-up, this response can be modulated by a stimulus such as magnetic field, mechanical stress, or temperature. The dependence of the GMI effect on the external magnetic field helps define the material's electromagnetic response, thus making the composite potentially useful for reconfigurable microwave devices. After establishing the theoretical framework, Panina's group later proposed a new class of microwire-based metamaterials that could display negative permittivity.

From Panina's work, it follows that the microwires are the magic key to some specific electromagnetic functionalities. Regarding the researches in GMI microwires and their sensor applications, the world's leading experts include Manuel

Vázquez at the Institute of Materials Science of Madrid (ICMM) and Arkady Zhukov at the University of the Basque Country (UPV/EHU), both in Spain, and Horia Chiriac of the National Institute of Research and Development for Technical Physics, Romania. These metallic microwires are often coated with a glass layer, and the GMI effect in them is dependent on a number of factors such as geometry, the metal-to-total-diameter ratio, measuring parameters (e.g. temperature and frequency), and tailoring techniques such as field annealing or stress annealing (i.e. annealing of the wires in the presence of an external magnetic field or under mechanical stress) [14, 15]. The knowledge gained in Zhukov, Vázquez, and Chiriac's pioneering works on tailoring the magnetic structure of microwires and optimising their GMI performance is essential in the design and fabrication of novel microwire-based composites, as well as understanding their outstanding combined properties and performance.

The group in the Institute for Composites Science Innovation (InCSI) at Zhejiang University, China, is performing exploratory work on microwire-based composite materials. But the inspiring works (jointly conducted by Faxiang Qin, Hua-Xin Peng, and Manh-Huong Phan) started off at Bristol University, UK, back in 2006, as we have demonstrated that by embedding a number of microwires in a polymer matrix, the soft magnetic properties and GMI effect can be significantly enhanced as compared to a single embedded wire [16]. This study really paves the way for the development of structural microwire-based composites that are of great engineering interest. In the past few years, the group has been working extensively on the multiple functionalities of microwire composites [17].

One significant aspect of multifunctionality is to capitalise on the magnetic field dependence of tunable microwave properties for structural health self-monitoring applications. We need fine elements in the composite to serve as sensor arrays that interrogate the material's structural integrity. This sensor-embedding technique is not new. Researchers have been attempting to embed all kinds of sensors (e.g. fibre optics) into composite structures, but this approach typically degrades the composite's mechanical performance a great deal because of the diameter mismatch between the structural reinforcing fibres and the embedded sensors. In the case of microwire composites, the microwires' fine diameter (e.g. 20 μm) proves to have no detrimental effect and the microwires can potentially fulfil the task of in-flight self-monitoring [18, 19].

Microwire composites can also provide electromagnetic shielding. A number of research groups (e.g. Pilar Marín of Complutense University of Madrid and co-workers [20]) have reported that the wires, being both electrically and magnetically conductive, are excellent candidate materials for shielding or absorption. In either low or high concentrations, the microwire composites can show useful levels (more than 10 dB) of absorption or shielding effectiveness (SE). Notably, as compared to other shielding fillers, the microwires enable a relatively thin composite with low filler concentration to have a very large SE [21]. Furthermore, absorption characteristics such as the absorption frequency, which we need to adjust for different applications, can be easily formulated by changing the wire geometry and patterns. Such microwire composites could be used for wind turbines, which

simultaneously need good impact resistance and electromagnetic shielding to ensure that the rotating turbines do not create interference with Doppler radar systems. From another approach, Phan's group at the University of South Florida has developed a new class of microwave energy sensors using the fibre Bragg grating (FBG) technology and a soft ferromagnetic glass-coated amorphous microwire as a microwave absorber [22, 23]. The ferromagnetic microwire absorbs microwave energy and heats up, thus raising the temperature of the FBG. As compared to a similar sensor that uses gold to absorb electromagnetic radiation, this newly developed sensor shows a greater sensitivity relative to the perturbation of the microwave field. Since the sensor is physically small and only minimally perturbs the field being measured, it can be deployed as a distributed sensor.

The most exciting property of ferromagnetic microwire composites, which we have only recently tapped into, is that of metacomposite behaviour. Some initial contributions in this field have been made by Lie Liu of the National University of Singapore [24], Serghei Baranov of the Institute of Applied Physics in Chisinau, Moldova [25], Konstantin Rozanov of the Institute for Theoretical and Applied Electromagnetics in Moscow, Russia [26], and Jorge Carbonell of the Polytechnic University of Valencia in Spain [27], and their co-workers. As mentioned earlier, metamaterials' unique properties originate from the precise mesostructure of their constituents. The complicated structure of a metamaterial can manipulate electromagnetic waves to achieve feats such as Harry Potter-like invisible cloaking, but metamaterials are generally not suitable for mass production. Wire metacomposites, with a simpler structure that is susceptible to control and production at engineering scale, can realise a transmission window (i.e. a range of wavelengths) in which the material's magnetic and dielectric responses are both negative. Such a metacomposite might be used to make a cloaked craft that would be invisible in the microwave range.

All the above-mentioned works pertaining to multifunctional microwire composites and metacomposites are discussed in the second half of the book. After a detailed presentation of the concept, design, and fabrication of composites in Chap. 9, we then explore the static mechanical and magnetic properties of the composites in Chap. 10. Central to the book, Chaps. 11–13 elucidate the microwave tunable, absorption, and metacomposite properties of the composites, respectively.

References

1. Lenz JE (1990) A review of magnetic sensors. Proc IEEE 78:973–989
2. Meydan T (1995) Application of amorphous materials to sensors. J Magn Magn Mater 133:525–532
3. Ripka P (2001) Magnetic sensors and magnetometers. Artech House Publishers
4. Panina LV, Mohri K (1994) Magneto-impedance effect in amorphous wires. Appl Phys Lett 65:1189–1191

5. Panina LV, Mohri K, Uchiyama T, Noda M (1995) Giant magneto-impedance in co-rich amorphous wires and films. IEEE Trans Magnet 31:1249–1260
6. Honkura Y (2002) Development of amorphous wire type MI sensors for automobile use. J Magn Magn Mater 249:375–377
7. Uchiyama T, Mohri K, Honkura Y, Panina LV (2012) Recent advances of pico-tesla resolution magneto-impedance sensor based on amorphous wire CMOS IC MI sensor. IEEE Trans Magn 48:3833
8. Uchiyama T, Nakayama S, Mohri K, Bushida K (2009) Biomagnetic field detection using very high sensitivity magneto-impedance sensors for medical applications. Phys Status Solidi A 206(4):639–643
9. Uchiyama T, Mohri K, Nakayama S (2011) Measurement of spontaneous oscillatory magnetic field of guinea-pig smooth muscle preparation using pico-tesla resolution amorphous wire magneto-impedance sensor. IEEE Trans Magn 47(10):3070–3073
10. Mohri K, Nakamura Y, Uchiyama T, Mohri Y, Mohri Yu, Inden Y (2010) Sensing of human micro-vibration transmitted along solid using pico-tesla magneto-impedance sensor (pT-MI sensor). Piers Online 6(2):161–164
11. Chiriac H, Ovari TA (1996) Amorphous glass-covered magnetic wires:p, properties, applications. Prog Mater Sci 40:333–407
12. Tannous C, Gieraltowski J (2004) Giant magneto-impedance and its applications. J Mater Sci: Mater Electro 15:125–133
13. Makhnovskiy DP, Panina LV, Garcia C, Zhukov AP, Gonzalez J (2006) Phys. Rev. B 74:064205
14. Zhukov A, Zhukova V (2009) Magnetic properties and applications of ferromagnetic microwires with amorphous and nanocrystalline structure. Nova Science Publishers, Inc., New York
15. Vázquez M (2007) Advanced magnetic microwires. In: Handbook of magnetism and advanced magnetic materials. Wiley, New York, p 2193
16. Phan MH, Peng HX, Yu SC, Wisnom MR (2007) Large enhancement of GMI effect in polymer composites containing co-based ferromagnetic microwires. J Magn Magn Mater 316: e253–e256
17. Qin F, Peng H-X (2013) Ferromagnetic microwires enabled multifunctional composite materials. Prog Mater Sci 58:183–259
18. Qin FX, Pankratov N, Peng HX, Phan MH, Panina LV, Ipatov M, Zhukova V, Zhukov A, Gonzalez J (2010) Novel magnetic microwires-embedded composites for structural health monitoring applications. J Appl Phys 107:09A314
19. Qin F, Peng H-X, Tang J, Qin L-C (2010) Ferromagnetic microwires enabled polymer composites for sensing applications. Compos A Appl Sci Manuf 41:1823–1828
20. Marín P, Cortina D, Hernando A (2005) High-frequency behavior of amorphous microwires and its applications. J Magn Magn Mater 290–291:1597–1600
21. Qin FX, Peng HX, Pankratov N, Phan MH, Panina LV, Ipatov M, Zhukova V, Zhukov A, Gonzalez J (2010) Exceptional EMI shielding properties of ferromagnetic microwires enabled polymer composites. J Appl Phys 108:044510
22. Colosimo P, Chen A, Devkota J, Srikanth H, Phan MH (2014) Sensing RF and microwave energy with fiber Bragg grating heating via soft ferromagnetic glass-coated microwires. Sens Actuators A 210:25
23. Devkota J, Colosimo P, Chen A, Larin VS, Srikanth H, Phan MH (2014) Tailoring magnetic and microwave absorption properties of glass-coated soft ferromagnetic amorphous microwires for microwave energy sensing. J Appl Phys 115:17A525
24. Liu L, Kong LB, Lin GQ, Matitsine S, Deng CR (2008) Microwave permeability of ferromagnetic microwires composites/metamaterials and potential applications. IEEE Trans Magn 44:3119–3122

25. Baranov SA (2009) Radioabsorption properties of amorphous microwires. Moldavian J Phys Sci 8:332–336
26. Starostenko SN, Rozanov KN (2009) Microwave screen with magnetically controlled attenuation. Prog Electromagn Res 99:405–426
27. Carbonell J, García-Miquel H, Sánchez-Dehesa J (2010) Double negative metamaterials based on ferromagnetic microwires. Phys Rev B 81:024401

Chapter 2
Fabrication of Ferromagnetic Wires

This chapter describes the fabrication methods of amorphous wires and microwires. The advantages and disadvantages of each method are examined and discussed. The existing techniques of glass removal for amorphous glass-covered wires (AGCW) are also discussed in this chapter.

2.1 Melt Spinning

Amorphous metallic alloys can be produced by a variety of rapid solidification processing techniques, including splat quenching, melt spinning, gas atomisation, and condensation from the gas phase. Among the existing techniques, the melt spinning technique has been most widely used to produce amorphous metallic alloys at cooling rates of 10^4–10^6 K/s [1]. Metallic amorphous wires are also prepared by the melt spinning method, which has been used to yield amorphous ribbons [2, 3]. The diameters of the produced wires range from 1 to 300 μm [3, 4]. The central element of this process is the pressure ejection of the melt stream through an outlet into a cooling fluid, followed by rapid solidification of this stream before it breaks into droplets. It has been highlighted that the following important conditions need to be satisfied to allow the production of metallic wires directly by the rapid solidification from the melt: (i) solidification of the metallic melt stream at high cooling rates and within the "stability" distance from the ejection point, (ii) use of a cooling fluid with low viscosity and surface tension, and (iii) stable and non-turbulent flow of the cooling liquid at high velocities. In reality, because of the difficulty of simultaneously maintaining the high supercooling capacity of the metallic melt stream without the precipitation of crystalline phases in a temperature range between the melting temperature and glass transition temperature, the melt spinning method is limited to producing metallic alloy wires with a high glass-forming ability. To overcome this problem, Ohnaka et al. [5] developed this method into the so-called in-rotating water spinning method.

H.-X. Peng et al., *Ferromagnetic Microwire Composites*,
Engineering Materials and Processes, DOI 10.1007/978-3-319-29276-2_2

2.2 In-rotating Water Spinning

This technique is modified from the melt spinning technique in that, instead of allowing the melt stream to impinge on the interior of a rotating drum, the melt stream is directly ejected into rotating water [5–7]. A cross-sectional view of an in-rotating water spinning device for producing magnetic wires is illustrated in Fig. 2.1.

It has been shown that during the in-rotating water spinning process, a jet of molten metal is ejected through a quartz nozzle of 80–200 mm diameter into a liquid cooling layer formed by a centrifugal force on the inner surface of a rotating drum of about 400–600 mm diameter. The speeds of the rotating coolant and the melt jet can be controlled by the rotation of the drum and the ejection gas pressure, respectively [6]. Depending upon the alloy being cast, it is necessary to adjust the distance between the nozzle tip and the coolant surface, the ejection angle, the depth of the coolant layer, and the coolant temperature. The in-rotating water spinning technique allows production of continuous wires of round cross section. In these wires, a dendritic structure forms along the wire direction, whereas for melt-spun ribbons, this structure tends to grow transverse to the casting direction. The cooling

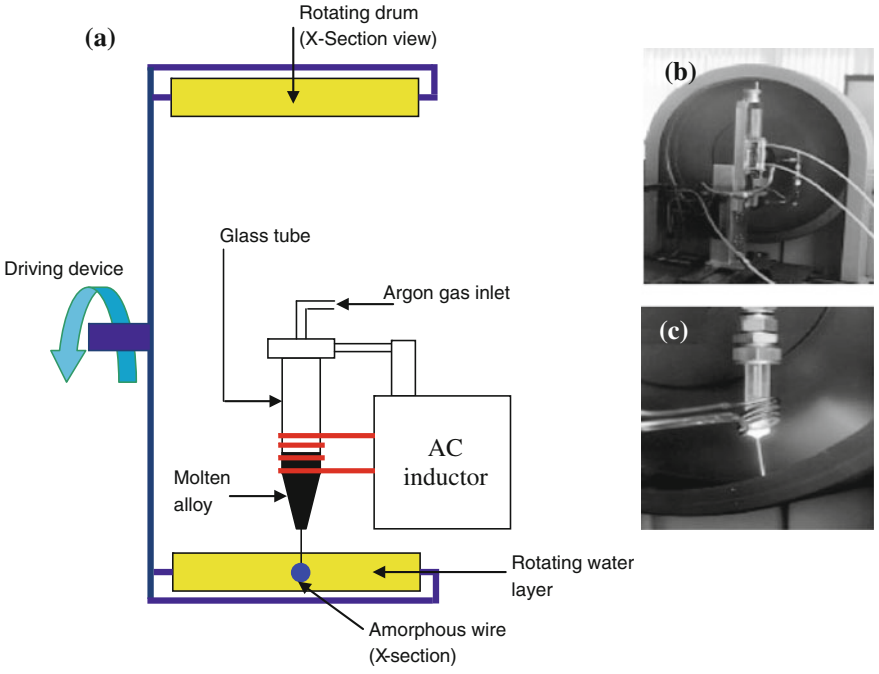

Fig. 2.1 (**a**) Cross-sectional view of the in-rotating water spinning device for producing magnetic wires with a general view (**b**) and during the melting process (**c**) (reproduced with permission from John Wiley & Sons [7])

rate is often around 10^5 K/s. A wide variety of ferrous and non-ferrous alloys have been cast into amorphous or microcrystalline wires. Amorphous metallic wires with diameters ranging from 80 to 160 μm were obtained by the in-rotating water spinning method [5]. Wires with thicker diameters of up to ~300 μm [8], or with thinner diameters down to 30 μm [9], have also been reported. One of the main advantages of the in-rotating water spinning method is that it can be used to produce wires with alloy compositions that are difficult to obtain using the conventional methods.

2.3 Taylor-Wire Process

In 1924, Taylor [10, 11] first introduced a technique that allows the production of fine wires of uniform cross section. A schematic illustration of the Taylor-wire process can be found in [10]. In this process, a metallic charge is put in a glass tube and this material is melted by induction heating. As a result, the glass tube is softened due to its contact with the molten metal and it can then be drawn. While acting as a continuous mould crucible during solidification of the metal, it ensures a regular surface and uniform diameter of the wire. The final product consists of a metallic wire in a glass sheath and is collected on a rotating drum at speeds of around 5 m/s. The cooling rate of this process might vary in the range of 10^4–10^6 K/s for producing wires of 50 μm down to 2 μm diameter [11, 12]. A wide range of metallic wires has been produced by the Taylor method, including steels, coppers, and noble metals as well as low-melting point metals [12]. One of the main challenges of this technique is to find sheath materials that possess a sufficient chemical inertness towards the molten metal used, as well as having a softening temperature consistent with the melting temperature of the metal. However, one problem arising in this technique is the contamination of the material by the glass sheath. To avoid this problem, it is necessary to choose a glass that is compatible with the material in terms of its chemical properties, viscosity, and melting temperature. A number of recent works have evaluated the microstructure, as well as the mechanical, electrical, and magnetic properties of several microcrystalline and amorphous alloys [13].

2.4 Glass-Coated Melt Spinning

This is a modification of the Taylor-wire technique, which allows alloy systems with low wire-forming capacity to be easily produced. The ability of a metallic melt stream to break into droplets before solidification is drastically reduced by the presence of the glass covering, which prevents direct contact between the molten metal and the cooling liquid [14–19]. The glass covering ensures a smooth cylindrical shape for the melt stream. Compared with the in-rotating water spinning method, the

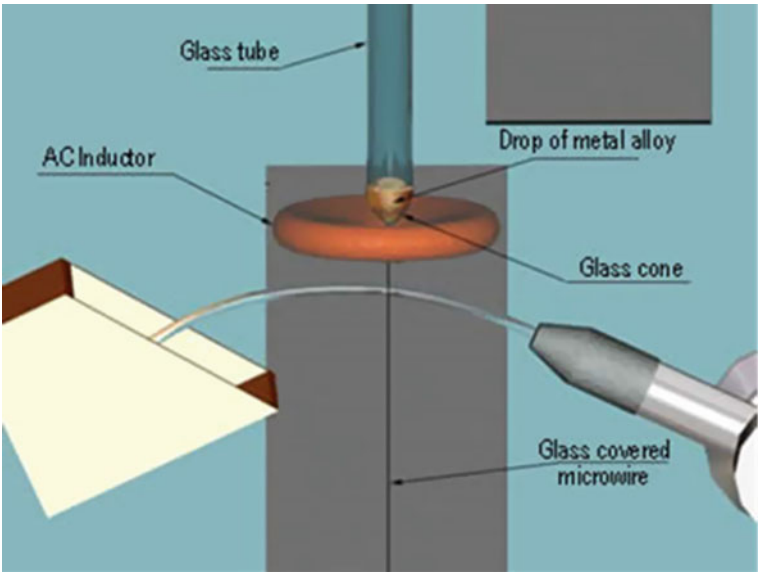

Fig. 2.2 Schematic illustration of amorphous wires/microwires fabrication process by the glass-coated melt spinning method (reproduced with permission from Elsevier [18])

glass-coated melt spinning method ensures higher cooling rates, thus producing amorphous wires more easily, even in the presence of the glass covering [18, 19].

This technique was originally proposed by Wiesner and Schneider [14] and later developed by Ulitovskiy [15, 16]. A schematic illustration of the glass-coated melt spinning method is presented in Fig. 2.2 [18]. In this process, the molten metal is captured as soon as the rapid drawing of a softened glass capillary takes place. The capillary is drawn from the end of a glass tube containing the molten metal. Alloy pieces are first put into the glass tube and then melted by a high-frequency furnace using an inductive coil. There is a softened glass covering around the molten metal drop and this allows the drawing of the capillary to take place.

To avoid any occurrence of metal oxidation, it is usual to apply a low level of vacuum of about 50–200 Pa, or an inert gas atmosphere (e.g. argon) within the glass tube. In order for the drawing process to be continuous, Chiriac et al. [17] proposed that the glass tube be displaced with a uniform speed of 0.5–7 mm/min. The as-formed wire is cooled by a water jet at approximately 1 cm under the high-frequency induction heating. Depending upon the drawing velocity, it is likely that the cooling rate varies from 10^4 to 10^7 K/s. Detailed analyses on external parameters affecting the preparation routes of wires can be found in [17–19]. Using this method, Chiriac et al. [17] produced metallic AGCW with metallic core diameters of 3–25 μm and glass thicknesses of 2–15 μm. In the case of microwires, the metallic core diameter is typically between 0.8 and 30 μm, while the thickness of the coating is in the range of 2–15 μm [18, 19]. For example, a scanning electron

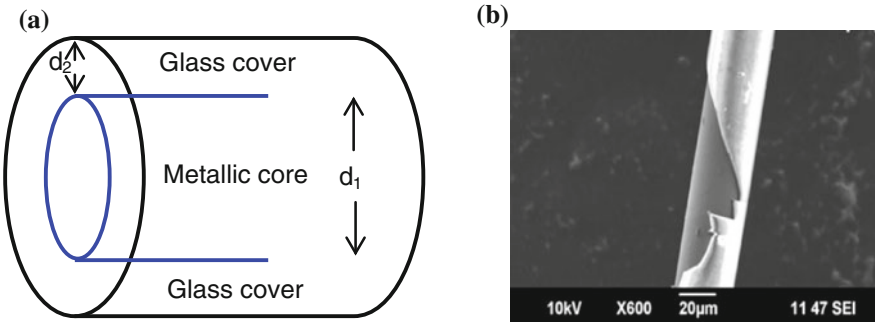

Fig. 2.3 **a** Schematic illustration of an amorphous glass-covered metallic wire. **b** Fracture surface of an amorphous $Co_{68}B_{15}Si_{10}Mn_7$ glass-covered wire

microscopy (SEM) image of a Co-rich glass-coated amorphous microwire is displayed in Fig. 2.3. Final wire dimensions such as the metallic core diameter and glass covering thickness can be accurately determined with the help of a high-resolution optical microscope engaged with a video camera and both controlled by a computer [17–19].

The glass-coated melt spinning method of wire/microwire fabrication provides several advantages over the other methods, such as (i) repeatability of wire properties at mass production and (ii) a wide range of variation in parameters (geometrical and physical), possible fabrication of continuous long wires up to 10 km and possible control and adjustment of geometrical parameters during the preparation process. Therefore, amorphous wires/microwires (Co-based and Fe-based alloys) have usually been produced by this method.

2.5 Electrodeposition

Electrodeposition is a method that has been used recently to produce uniform wires consisting of non-magnetic conducting inner core (e.g. Cu, BeCu, and W), and magnetic outer shell layers (e.g. FeNi, FeNi–Al_2O_3, and CoP) [20–36]. This method is used for coating a metallic wire with a similar or dissimilar metallic plating layer having the desired uniform thickness and a compact metallic structure by passing the wire through electrolytic baths and through surface smoothing stations. In this process, the wire is passed through an electrolytic bath to coat the wire with a plating layer and then pressed against the peripheral surfaces of rotating rollers to smooth the surface of the plating layer over the entire periphery. Finally, the wire is coated with a secondary electrolytic plating layer. The non-magnetic conducting inner cores are often wires with diameters of around 20 μm [21–24]. The magnetic layer is often thin, ranging between 2 and 7 μm. In the electrodeposition process, the thin magnetic layer is formed over the inner wire using a

constant electrolytic current density. By keeping the current density constant, the layer thickness can be controlled by the deposition time. The main difficulty of this method is controlling the desired composition ratio [21–26]. This problem can be overcome by applying a longitudinal magnetic field during the deposition process, which is currently known as the magnetically controlled electroplating method [27, 28]. In addition, the application of a longitudinal magnetic field during electrodeposition results in an improvement of the uniform surface properties of the wires, which is beneficial for sensor applications [28]. In general, the electrodeposition method has the following advantages: (i) a wide range of materials (metals, alloys, and composites) that can be processed by electrodeposition is available; (ii) both continuous and batch processing are possible; (iii) materials with different grain sizes and shapes can be produced; (iv) materials with full density (i.e. negligible porosity) can be produced; and (v) the final product can be in the form of a coating or bulk material.

By combining the melt spinning and electroplating techniques, Torrejon et al. [37, 38] produced a new type of biphase magnetic microwire composed of a ferromagnetic nucleus, an intermediate glass layer, and a ferromagnetic outer shell (Fig. 2.4a). The glass-covered amorphous magnetic wires and microwires can be

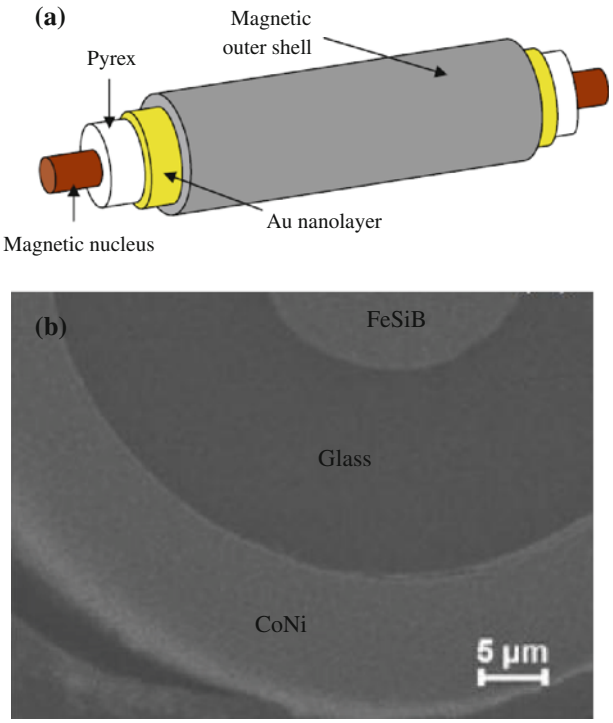

Fig. 2.4 **a** Scheme of a multilayer microwire. **b** Cross-sectional SEM image of the FeSiB/glass/Au/CoNi multilayer microwire (reproduced with permission from Elsevier [37])

obtained by the quenching and drawing method, as described above. The diameter of the nucleus and thickness of the glass covering typically range between 1 and 20 μm, respectively. Figure 2.4b displays a cross-sectional SEM image of a FeSiB/glass/Au/CoNi multilayer microwire.

A large number of different magnetic configurations such as soft/hard CoFeSiB/CoNi and FeSiB/CoNi, soft/soft CoFeSiB/FeNi, and hard/soft FePtSi/FeNi have been developed [37, 38]. It has been reported that the magnetic properties of these biphasic structures are mainly determined by the magnetic interactions between both magnetic phases, which provide the possibility of tailoring the magnetisation reversal of the soft phase through the tuning of the magnetic coupling between the two phases desirable for a number of technological applications, including multifunctional sensor devices.

2.6 Melt Extraction

Melt extraction was first applied to prepare metallic fibres as long as four decades ago [39]. It was further developed to find wide use in the fabrication of amorphous wires, ceramic fibres such as calcium aluminate [40] and high-resistivity alloy wires such as MgZnCa [41]. Recently, it has been increasingly used in the fabrication of magnetic microwires [42–46]. The basic principle of MET is to apply a high-speed wheel with a sharp edge to contact the molten alloy surface and then to rapidly extract and cool a molten layer to be wires, as schematically shown in Fig. 2.5.

There are three main advantages of this technique: (i) MET gives a higher solidification rate of 10^5–10^6 K/s than any other method, which is in favour of the form of amorphous phase. (ii) The wires produced by this method possess

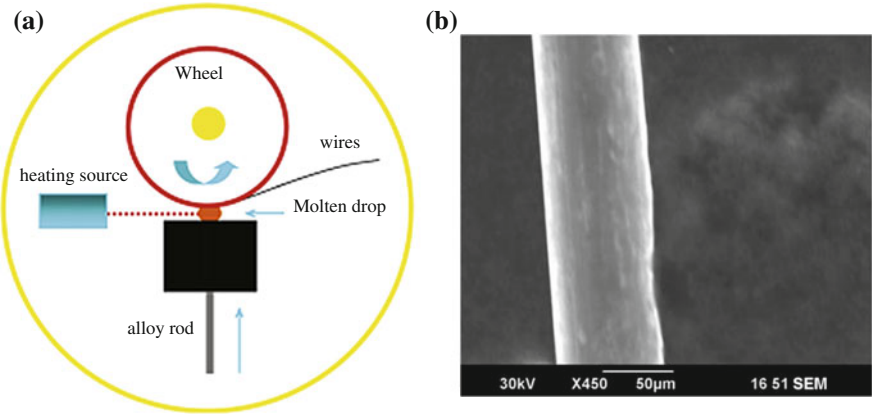

Fig. 2.5 **a** Schematic of melt extraction facility. **b** SEM image of a melt-extracted $Co_{68.2}Fe_{4.3}B_{15}Si_{12.5}$ microwire

extraordinary mechanical properties due to the high quality faultless surface and circular geometry [40, 47]. (iii) The soft magnetic properties of the materials are significantly improved by fabricating into microwires via MET; this is believed to be attributable to the considerable quenched-in stress [44]. The main drawback of this method is that it has lost control of the diameter of the produced wires. The typical diameter range for the magnetic wires is about 30–60 μm [42–44, 48] depending on the processing parameters. Apparently, it is not suitable for preparing ultrathin magnetic microwires.

2.7 Comparison of the Fabrication Technologies

In order to compare the dimensions of the wire samples produced by the above-mentioned techniques, Table 2.1 summarises the fabrication technologies and their product parameters. It is worth noting from Table 2.1 that such knowledge of the cooling rates could help us in the first instance to evaluate the relative efficiencies of the different quenching techniques. The first two methods (melt spinning and in-rotating water spinning) allow the production of metallic amorphous wires without a glass covering and are preferred for conventional amorphous wires (CAW), while the glass-coated melt spinning method (or Taylor-wire method) produces thin amorphous glass-covered wires (AGCW). From an engineering point of view, AGCW is more promising for technological applications when compared with CAW. In particular, amorphous microwires are ideal for sensing applications in microsystems [7]. The magnetic wires with glass covering are particularly useful for electrical applications in industry. Electrodeposited wires are also of interest here because of their uniform magnetic properties. However, it is quite difficult to produce such long wires using the electrodeposition technique. The synthesis of nanocrystalline wires through crystallising their amorphous precursors has been a popular method for improving the soft magnetic properties of the materials, while retaining the same dimensions of the sample. A variety of

Table 2.1 Fabrication technologies and their product parameters

Technique	Product type	Typical dimensions (μm)	Typical cooling rate (K/s)
Melt spinning	Circular section wire	1–300 diameter	10^4–10^6
In-rotating water spinning	Circular section wire	30–300 diameter	10^5–10^6
Taylor-wire process	Circular section wire	2–100 diameter	10^3–10^6
Glass-coated melt spinning	Wire/microwire with glass covering	3–50 diameter	10^4–10^7
Electrodeposition	Wire with magnetic layer	20–1000 diameter	–
Melt extraction	Amorphous wires	30–60 diameter	10^5–10^6

annealing methods (e.g. current annealing, field annealing, stress annealing, and laser annealing) have been proposed and used to produce such nanocrystalline materials. To this end, it is worth mentioning that, in the case of glass-covered wires, the removal of the glass covering may be of interest in developing specific sensing devices. The technique of glass removal is described in Sect. 2.8.

2.8 Techniques of Glass-Covering Removal

Magnetic AGCW and microwires are ideal for several applications, particularly in electrical industries, owing to the presence of the insulating glass-covered layer. In some cases, however, removal of the glass-covered layer of AGCW may be of significant interest in fundamental research as well as in practical uses, because this process can cause considerable variation in the mechanical and magnetic properties of the wire [7].

In practice, removal of the glass can be conducted either by the conventional mechanical method or by chemical etching with a hydrofluoric acid (HFA) solution. The former usually leads to a degradation of the material properties (e.g. mechanical, electrical, and magnetic) and is therefore not recommended. The latter has been shown to be a useful tool for the glass removal of AGCW, and to result in less damage. However, when the chemical etching method is used, the following features should be considered: firstly, the concentration of the HFA solution must be gradually diminished in order to avoid the etching of the metal; secondly, the last glass pieces are washed with water for the same reason. This entire process can be monitored by permanent optic control.

2.9 Concluding Remarks

The glass-coated melt spinning and single-roller melt spinning methods have been effective for preparing amorphous magnetic wires. Novel nanocrystalline wires can be obtained by annealing their corresponding amorphous alloys under optimal treatment conditions (i.e. the optimal annealing temperature and time), which have been determined based on systematic analyses by means of X-ray diffraction (XRD), differential scanning calorimetry (DSC), scanning electron microscopy (SEM), and transmission electron microscopy (TEM). The chemical method, i.e. chemical etching with a suitable HFA solution, should be employed to remove glass coating layers of magnetic wires, in order to avoid a degradation of the material properties.

References

1. Davies HA, Lewis BG, Donald IW (1978) In: R. Mehrabian R, Kear BH, Cohen M (eds) Rapid solidification processing: principles and technologies. Claitor's Pub. Div., Baton Rouge, 78–83
2. Luborsky FE, Walter JL, Liebermann HH (1979) Engineering magnetic properties of Fe–Ni–B amorphous alloys. IEEE Trans Magn 15:909–911
3. Goto T (1980) Fe–B and Fe–Si–B system alloy filaments produced by glass-coated melt spinning. Trans Jan Inst Met 21:219–225
4. Squire PT, Atkinson D, Gibbs MRJ, Atalay SJ (1994) Amorphous wires and their applications. J Magn Magn Mater 132:10–21
5. Ohnaka I, Fukusako T, Matui T (1981) Preparation of amorphous wires. Journal of Japan Institute of Metals 45:751–762
6. Matsumoto T, Ohnaka I, Inoue A, Hagiwara M (1981) Scr Metal 15:293–306
7. Vazquez M (2007) Handbook of magnetism and advanced magnetic materials (chap. Advanced magnetic microwires). In: Novel materials, vol 4. John Wiley & Sons Ltd, NJ, pp 1–29
8. Nderu JN, Shinokawa Y, Yamasaki J, Humphrey FB, Ogasawara I (1996) Dependence of magnetic properties of $(Fe_{50}Co_{50})_{78}Si_7B_{15}$ amorphous wire on the diameter. IEEE Trans Magn 32:4878–4880
9. Ogasawara I, Mohri K (1990) Tension annealing cold-drawn amorphous CoFeSiB wires. IEEE Trans Magn 26:1795–1797
10. Taylor GF (1924) A method of drawing metallic filaments and a discussion of their properties and uses. Phys Rev 23:655–660
11. Taylor GF (1931) Process and apparatus for making filaments, Patented 24 Feb 1931, United States Patent Office, 1, 793, 529
12. Donald IW (1987) Production, properties and applications of microwire and related products. J Mater Sci 22:2261–2279
13. Goto T, Nagano M, Tanaka K (1977) Tensile strength of copper and iron filaments produced by method of glass-coated melt spinning. Transactions of the Japan Institute of Metals 18:209–213
14. Wiesner H, Schneider J (1974) Magnetic properties of amorphous FeP alloys containing Ga, Ge, and As. Phys Stat Soli A 26:71–75
15. Ulitovsky A V (1951) In: Micro-technology in design of electric devices, vol 7, Leningrad, p 6
16. Ulitovsky AV, Maianski IM, Avramenco AI (1960) Method of continuous casting of glass coated microwire. Patent No. 128427 (USSR), 15 May 1960, Bulletin. No. 10, p 14
17. Chiriac H (2001) Preparation and characterization of glass covered magnetic wire. Mater Sci Eng A 304–306:166–171
18. Larin VS, Torcunov AV, Zhukov A, Gonzalez J, Vazquez M, Panina L (2002) Preparation and properties of glass-coated microwires. J Magn Magn Mater 249:39–45
19. Zhukov A, Gonzalez J, Vazquez M, Larin V, Torcunov A (2004) Nanocrystalline and amorphous magnetic microwires. In: Nalwa HS (ed.) Encyclopedia of nanoscience and nanotechnology, vol X, pp 1–22
20. Beach RS, Smith N, Platt CL, Jeffers F, Berkowitz AE (1996) Magneto-impedance effect in NiFe plated wire. Appl Phys Lett 68:2753–2755
21. Sinnecker JP, Garcia JM, Asenjo A, Vazquez M, Garcia-Arribas A (2000) Giant magnetoimpedance in CoP electrodeposited microtubes. J Mater Res 15:751–755
22. Yu RH, Landry G, Li YF, Basu S, Xiao JQ (2000) Magneto-impedance effect in soft magnetic tubes. J Appl Phys 87:4807–4809
23. Sinnecker JP, Knobel M, Pirota KR, Garcia JM, Asenjo A, Vazquez M (2000) Frequency dependence of the magnetoimpedance in amorphous CoP electrodeposited layers. J Appl Phys 87:4825–4827

24. Garcia JM, Sinnecker JP, Asenjo A, Vazquez M (2001) Enhanced magnetoimpedance in CoP electrodeposited microtubes. J Magn Magn Mater 226–230:704–706
25. Garcia JM, Asenjo A, Vazquez M, Yakunin AM, Antonov AS, Sinnecker JP (2001) Determination of closure domain penetration in electrodeposited microtubes by combined magnetic force microscopy and giant magneto-impedance techniques. J Appl Phys 89:3888–3891
26. Jantaratana P, Sirisathitkul C (2006) Effects of thickness and heat treatments on giant magnetoimpedance of electrodeposited cobalt on silver wires. IEEE Trans Magn 42:358–362
27. Li XP, Zhao ZJ, Seet HL, Heng WM, Oh TB, Lee JY (2003) Effect of magnetic field on the magnetic properties of electroplated NiFe/Cu composite wires. J Appl Phys 94:6655–6658
28. Li XP, Zhao ZJ, Chua C, Seet HL, Lu L (2003) Enhancement of giant magnetoimpedance effect of electroplated NiFe/Cu composite wires by dc Joule annealing. J Appl Phys 94:7626–7630
29. Hu J, Qin H, Zhang L, Chen J (2004) Giant magnetoimpedance effect in Ag/NiFe plate wire. Mater Sci Eng, B 106:202–206
30. Atalay FE, Kaya H, Atalay S (2006) Unusual grain growth in electrodeposited CoNiFe/Cu wires and their magnetoimpedance properties. Mater Sci Eng, B 131:242–247
31. Atalay FE, Kaya H, Atalay S (2006) Giant magnetoimpedance effect in electrodeposited CoNiFe/Cu wires with varying Ni, Fe and Co content. J All Comp 420:9–14
32. Atalay FE, Kaya H, Atalay S (2006) Magnetoimpedance effect in electroplated NiFeRu/Cu wire. J Phys D Appl Phys 39:431–436
33. Velleuer J, Munoz AG, Yakabchuk H, Schiefer C, Hackl A, Kisker E Giant magnetoimpedance in electroplated NiFeMo/Cu microwires. J Magn Magn Mater (in press)
34. Zhang Z, Wu Q, Zhong K, Yang S, Lin X, Huang Z (2006) The size and space arrangement roles on coercivity of electrodeposited $Co_{1-x}Cu_x$ nanowires. J Magn Magn Mater 303:e304–e307
35. Wang XZ, Yuan WZ, Zhao Z, Li XD, Ruan JZ, Yang XL (2005) Giant magnetoimpedance effect in CuBe/NiFeB and CuBe/Insulator/NiFeB electroless-deposited composite wires. IEEE Trans Magn 41:113–115
36. Wang XZ, Yuan WZ, Zhao Z, Li XD, Ruan JZ, Zhao ZJ, Yang JX, Yang XL, Sun Z (2007) Enhancement of giant magnetoimpedance in composite wire with insulator layer. J Magn Magn Mater 308:269–272
37. Torrejón J, Badini G, Pirota K, Vázquez M (2007) Acta Mater. 55:4271
38. Torrejón J, Infante G, Badini-Confalonieri G, Pirota KR, Vázquez M (2013) Electroplated bimagnetic microwires: from processing to magnetic properties and sensor devices. JOM 65:890
39. Maringer RE, Mobley CE (1974) Casting of metallic filament and fiber. J Vac Sci Technol 11:1067–1071
40. Allahverdi M, Drew R, Rudkowska P, Rudkowski G, Strom-Olsen J (1996) Amorphous $CaOAl_2O_3$ fibers by melt extraction. Mater Sci Eng, A 207:12–21
41. Zberg B, Arata ER, Uggowitzer PJ, Lofler JF (2009) Tensile properties of glassy MgZnCa wires and reliability analysis using Weibull statistics. Acta Mater 57:3223–3231
42. Wang H, Xing D, Wang X, Sun J (2011) Fabrication and characterization of melt-extracted co-based amorphous wires. Metall Mater Trans A 42:1103–1108
43. Man-Gui H, Yu O, Di-Fei L, Long-Jiang D (2009) Annealing effects on the microwave permittivity and permeability properties of $Fe_{79}Si_{16}B_5$ microwires and their microwave absorption performances. Chin Phys B 18:1261
44. Zhukova V, Zhukov A, García KL, Kraposhin V, Prokoshin A, Gonzalez J et al. (2003) Magnetic properties and GMI of soft melt-extracted magnetic amorphous fibers. Sens Act A: Phys 106:225–229
45. Wang H, Xing D, Peng HX, Qin FX, Cao F, Wang G et al (2012) Nanocrystallization enabled tensile ductility of co-based amorphous microwires. Scripta Mater 66:1041–1044
46. Wang H, Qin FX, Xing D, Peng HX, Cao F, Wang X et al. (2012) Enhanced mechanical and GMI properties due to deformationinduced residual stress and microstructural changes in

Co–Fe–Si–B amorphous microwires. Acta Mater. http://dx.doi.org/10.1016/j.actamat.2012.06.047

47. Strom-Olsen J (1994) Fine fibres by melt extraction. Mater Sci Eng A 178:239–243 (NATO-Advanced research workshop on undercooled metallic melts: properties, solidification and metastable phases)
48. Di Y, Jiang J, Du G, Tian B, Bie S, He H (2007) Magnetic and microwave properties of glass-coated amorphous ferromagnetic microwires. Trans Nonferr Metal Soc China 17:1352–1357

Chapter 3
Domain Structure and Properties of GMI Materials

The domain structure of a rapidly quenched material is often determined by coupling between magnetostriction and internal stresses frozen in during the fabrication process. Such knowledge of the domain structure of an actual material is extremely important in controlling and tailoring the magnetic properties of the material. This chapter is devoted to describing the formation of the domain structures of wires in tandem with their magnetisation processes and their magnetic characteristics.

3.1 Domain Structure

In a rapidly quenched wire, a complex radial distribution of internal stress with axial, radial and circular components is often generated due to different quenching rates between the surface layer and the central region of the wire [1–5]. Here, the sign and magnitude of the magnetostriction constant (λ) determines the type of domain structure in the wires.

For amorphous wires with positive magnetostriction (e.g. Fe-based wires), the quenched-in stress distribution may result in a longitudinal easy axis in the cylindrical core and radial easy axes in the tubular shell. The inner core usually occupies about 70–90 % of the total volume of the wire [2]. A schematic illustration of the simplified domain configuration of this commonly used wire is presented in Fig. 3.1. There is an inner cylindrical domain with longitudinal magnetisation and a basic radial domain with complicated closure domains. Such a domain structure is responsible for an axial large Barkhausen effect (LBE) in the wire, which is desirable for several technical applications [1, 2]. The closure domain structure has been realised by domain pattern observation and by magnetisation and

H.-X. Peng et al., *Ferromagnetic Microwire Composites*,
Engineering Materials and Processes, DOI 10.1007/978-3-319-29276-2_3

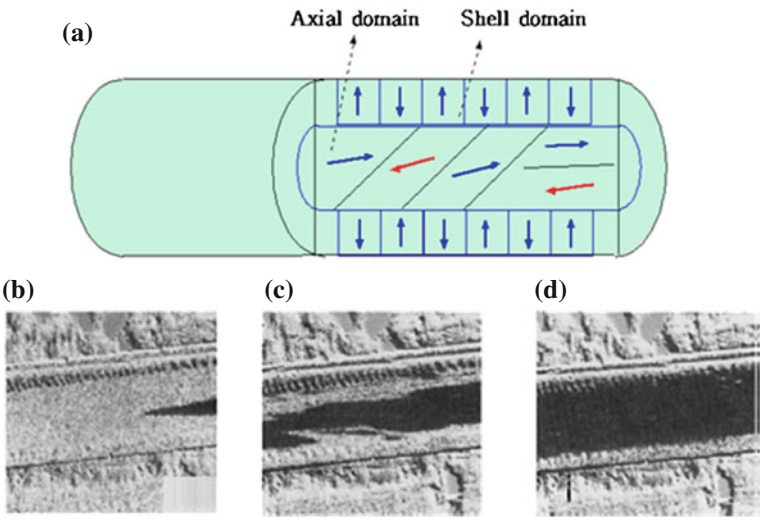

Fig. 3.1 (**a**) Simplified domain configuration of a typical conventional amorphous wire (CAW) with positive magnetostriction. Magnetic domain images taken at different fields $H = 0$ A/m (**b**), $H = 3$ A/m (**c**) and $H = 8$ A/m (**d**) for an $Fe_{75}Si_{15}B_{10}$ in-water-quenched microwire (reproduced with permission from John Wiley & Sons [6])

susceptibility profiles [3, 5, 6]. For a low magnetostrictive wire with a normal length ($\sim$4 mm), the core of the wire actually has a multidomain structure [7].

For amorphous wires with negative magnetostriction (e.g. Co–Si–B wires), the quenched-in stresses may cause the surface anisotropy to be circular and the inner anisotropy to be perpendicular to the wire axis, thereby leading to the formation of a specific domain structure, which consists of outer shell circular domains and inner core axial domains, as illustrated in Fig. 3.2. It is the coupling between the compressive stress and the negative magnetostriction that leads to an alignment of the magnetic moments in a circumferential direction. The minimal demagnetising energy favours the circumferential orientation, as was observed experimentally [2, 5, 6]. It can be seen that the inner core domain structure of negative magnetostrictive CAWs (Fig. 3.2) is the same as that of positive magnetostrictive CAWs (Fig. 3.1), and this results in the negative magnetostrictive CAWs also exhibiting an axial LBE. It should be noted, however, that there the inner core domain structures of negative magnetostrictive CAW and amorphous glass-covered wire (AGCW) are actually different. The easy axis of the inner core domains of CAW is axial while it is radial for AGCW. The reason for this is that the presence of the glass-covered layer in AGCW leads to a specific distribution of internal stresses in the inner core of the wire. In the case of amorphous glass-covered microwires with large and

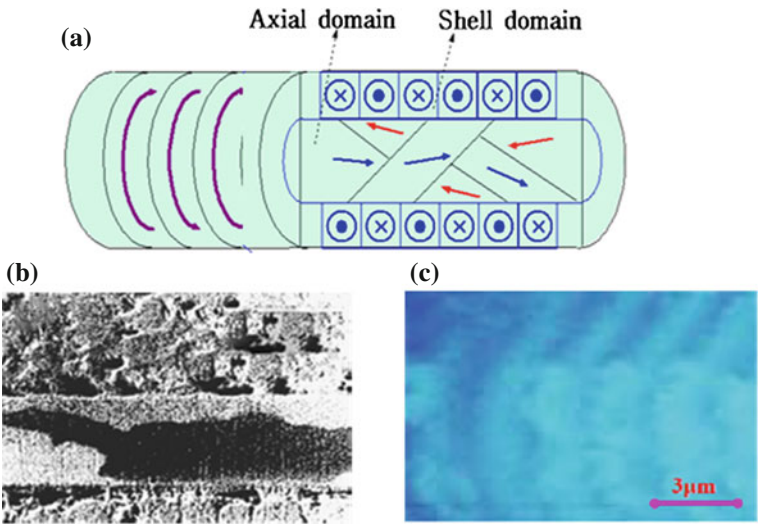

Fig. 3.2 (**a**) Simplified domain configuration of a typical conventional amorphous wire (CAW) with negative magnetostriction, with magnetic domain images of a Co-rich amorphous microwire taken by (**b**) the Kerr magneto-optical and (**c**) MFM techniques (reproduced with permission from John Wiley & Sons [6])

negative magnetostriction, the shell with circular domains occupies practically the entire volume of the wire as a consequence of the strong circular magneto-elastic anisotropy.

The main difference in the domain structure between typical positive and negative magnetostrictive amorphous wires is that the easy magnetisation direction in the shell is radial in the case of positive magnetostriction (Fe-based) wires, whereas for negative magnetostriction (Co-based) wires it becomes circular. This is understood to be the main reason for the difference in the magnetic behaviours of the Fe-based and Co-based wires.

For amorphous wires with negative and nearly zero magnetostriction (or vanishing magnetostrictive wires, Co–Fe–Si–B, for example), other kinds of anisotropies may overcome the stress anisotropy, and consequently, the domain structure is not well defined. In practice, the domain structure of these wires is often considered to be similar to that of the negative magnetostrictive amorphous wires [8, 9]. It is noted that thermal and mechanical treatments may significantly modify the domain structures of these rapidly quenched wires. A typical example of the domain structure modification caused by changes of internal stresses is the case of removing the glass-covering layer from a typical AGCW, as illustrated in Figs. 3.3

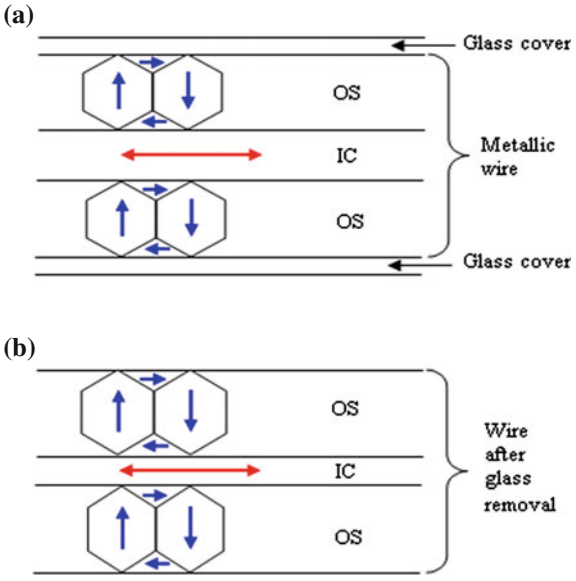

Fig. 3.3 Schematic illustration of the domain structure in a typical positive magnetostrictive amorphous glass-covered wire (AGCW): (**a**) as-cast glass-covered wire and (**b**) wire after glass removal. *OS* outer shell; *IC* inner core (reproduced with permission from Elsevier [2])

and 3.4. It can be seen that for the case of the positive magnetostrictive AGCWs, the glass removal leads to an increase in the outer shell domains' volume, but a decrease in the inner core domains' volume. As a result, the domain configuration remains unchanged for the positive magnetostrictive AGCWs after glass removal (see Fig. 3.3a, b). It is estimated that the maximum value of the axial tensile stress for glass-removed wires is approximately 50 % smaller than for glass-covered ones [2, 6]. This may result in a further improvement in the magnetic softness as well as the GMI effect of such positive magnetostrictive AGCWs after glass removal.

For negative magnetostrictive AGCWs, the glass removal causes a change in the easy axis of the inner core domains from radial to axial (see Fig. 3.4a, b), but does not change the outer shell domain configuration, except for an increase in the domain volume. The domain structure of the negative magnetostrictive AGCWs after glass removal (see Fig. 3.4b) is similar to that of the negative magnetostrictive CAWs (Fig. 3.2). However, the application of a tensile stress ($\sim$50 MPa) on the glass-removed wire may cause the return of the original inner core domain structure (see Fig. 3.4a, c).

The influences of annealing and external stresses on the domain structure and properties of the amorphous wires have been extensively studied [2, 5, 6]. In these studies, annealing under mechanical stress or magnetic field has been shown to induce magnetic anisotropy with the corresponding modification of the domain structure. A direct observation of the more well-defined circumferential anisotropy

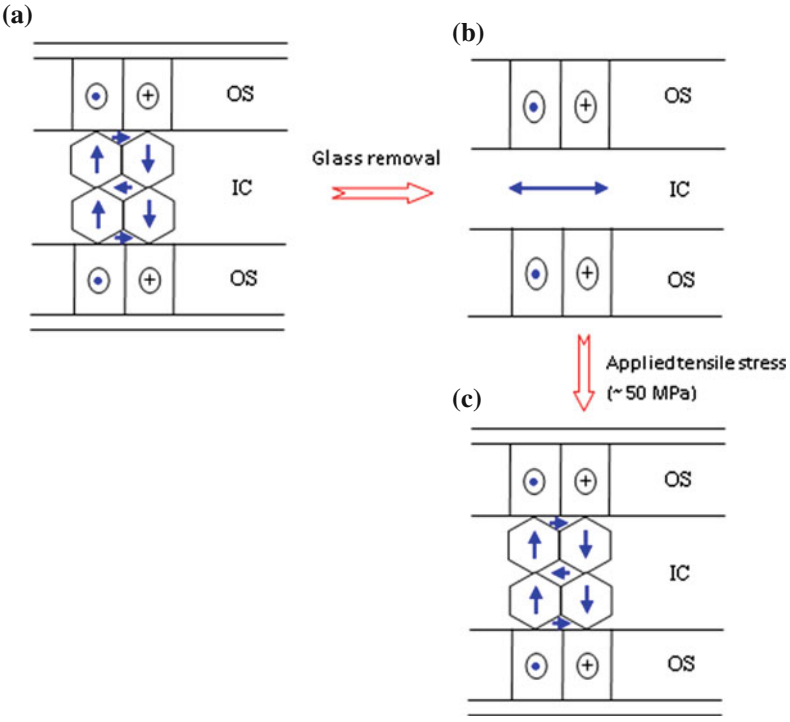

Fig. 3.4 Schematic illustration of the domain structure in a typical negative magnetostrictive amorphous glass-covered wire (AGCW): (**a**) as-cast glass-covered wire; (**b**) wire after glass removal; (**c**) the sample without glass is subjected to an external tensile stress. *OS* outer shell; *IC* inner core (reproduced with permission from Elsevier [2])

has been presented by Chen et al. [10], who compared the domain structure of Co-rich amorphous wires Joule-annealed under different currents. As shown in Fig. 3.5, the increasing annealing current reduces the burrs for the as-cast wire and transforms the unevenly distributed domains to regular well-defined circular domains. Such a domain structure regulation yields an improved GMI ratio. Similar results have also been reported in [9]. MFM has established itself in these studies as a very effective tool to perform ex situ detailed observations of the domain structures. In addition to the static domain observation, the in situ observation of domain wall dynamics and the domain structure transformation has been intensively studied by Chizhik et al. [11, 12]. By virtue of MOKE, either domain nucleation regulated by the applied current or the surface domain structure by the axial magnetic field can be well recorded. As exemplified in Fig. 3.6, with magnetic field varying from

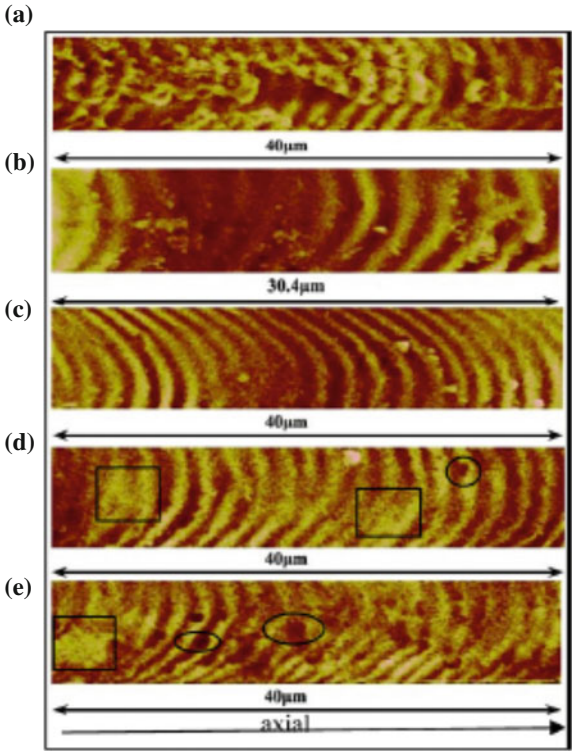

Fig. 3.5 Magnetic domain structures of melt-extracted $Co_{68.15}Fe_{4.35}Si_{12.25}B_{13.75}Nb_1Cu_{0.5}$ amorphous wires with different Joule annealing: (**a**) as-cast state, (**b**) 30 mA, (**c**) 80 mA, (**d**) 100 mA, and (**e**) 200 mA; domain-merger phenomenon in *rectangular box* (**d**); domain wall pinning marked with *oval* (**e**) (reproduced with permission from Wiley [10])

−10 to 10 Oe, one can observe domain rotation to the circular direction, domain wall motion, and finally domain rotation to the axial direction. Its ability to capture these dynamic features makes MOKE a very useful tool to study the domain wall dynamics, which is of vital importance for designing magnetic memory and switching sensor devices.

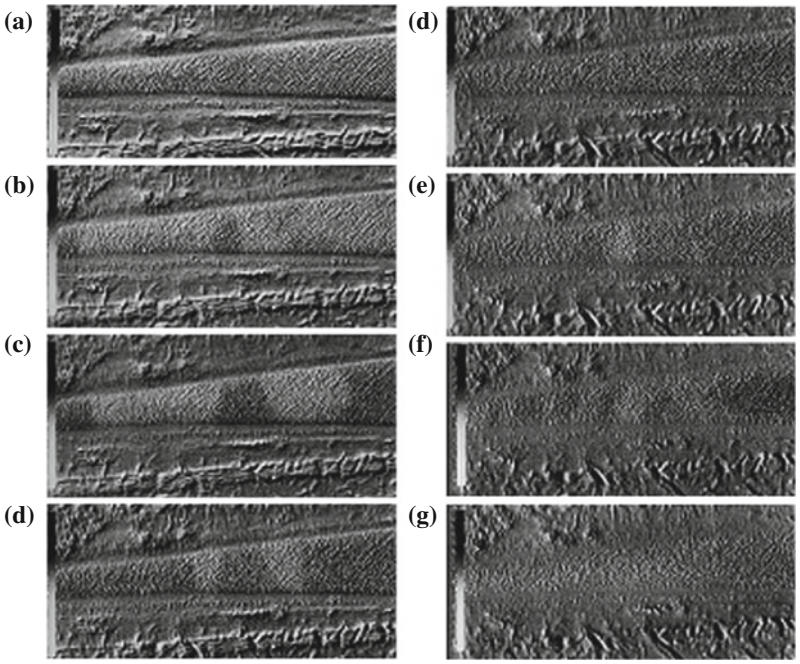

Fig. 3.6 Images of the surface domain structure for the position 1 in the wedge: (**a**)−10 Oe, (**b**)−2 Oe, (**c**)−0.3 Oe, (**d**) 0.03 Oe, (**e**) 0.3 Oe, (**f**) 1.3 Oe, (**g**) 2 **Oe**, and (**h**) 10 Oe (reproduced with permission from Elsevier [11])

3.2 Magnetic Properties

3.2.1 Hysteresis Loops

Hysteresis loops are one of the key magnetic properties and provide useful information on the magnetic properties of materials. As a result of the different coupling between the internal stress and magnetostriction, different hysteresis behaviours have been observed in materials (e.g. wires, ribbons, and thin films) with positive, negative, and nearly zero but negative magnetostriction.

The magnetic hysteresis behaviour of wires can be investigated by measuring either longitudinal or circular hysteresis loops with the application of a longitudinal magnetic field or a circular magnetic field, respectively. However, the change in the interior circumferential magnetisation for wire-shaped samples cannot be measured by conventional magnetometry. It can be observed, however, by filtering out and integrating an inductive voltage signal which appears across the wire due to its magnetisation by a low frequency current [13]. Due to a simplified experimental set-up, the longitudinal hysteresis loop measurement has mainly been employed [2, 5, 6, 14]. Figure 3.7 displays the typical hysteresis loops of amorphous

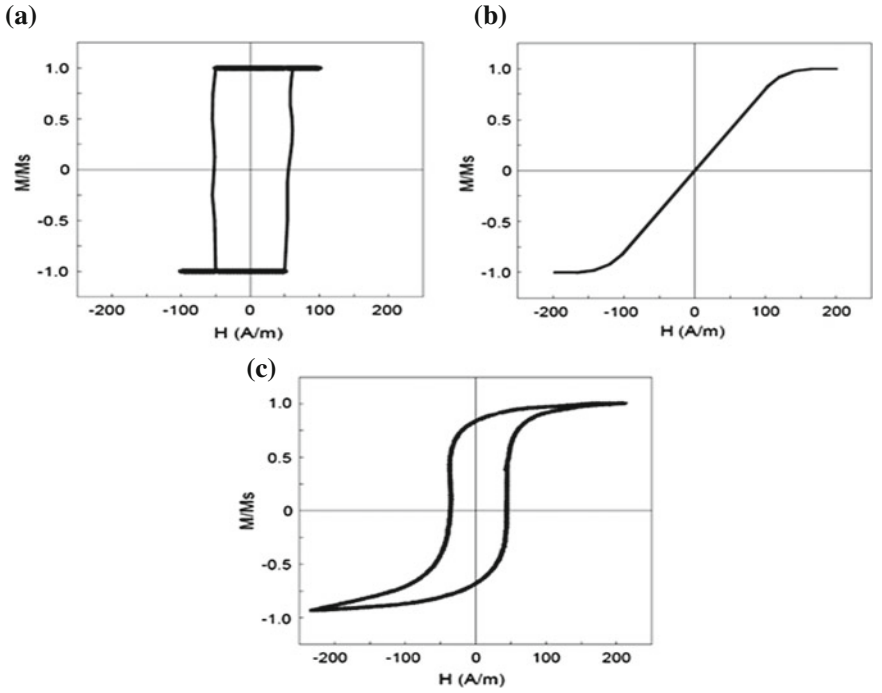

Fig. 3.7 Typical hysteresis loops of Co–Mn–Si–B amorphous microwires with (**a**) positive, (**b**) negative, and (**c**) negative and nearly zero magnetostriction (reproduced with permission from Elsevier [15])

glass-covered microwires with (a) positive, (b) negative, and (c) nearly zero but negative magnetostriction [15].

For the positive magnetostrictive AGCWs (e.g. Fe-based wires), the magnetoelastic anisotropies result in axial easy axes, which enhance the shape anisotropy. Consequently, the rectangular hysteresis loop—which exhibits a large axial LBE due to the presence of the inner core axial domain structure in the wire (see Fig. 3.3a)—is observed (Fig. 3.7a). When the glass covering is removed, this rectangular hysteresis loop becomes smaller, reducing the LBE effect due to the decrease of the inner core axial domain volume of the wire (see Fig. 3.3b). This has been experimentally verified [2, 5, 6]. Such an LBE effect may be observed even in positive magnetostrictive AGCWs with a very short length of about 1–2 mm, due to the reduced demagnetising factor resulting from the very small wire diameter to length ratio. This is useful for the development of miniature sensing devices [1, 6]. It was also found that, when a Fe-based AGCW became nanocrystalline under heat treatments, the shape of the hysteresis loop could change from rectangular to flat, with the LBE effect disappearing. In these findings, the coercivity decreased drastically due to the presence of the nanosized α-Fe(Si) grains [16].

For the negative magnetostrictive AGCWs (e.g. Co–Si–B wires), the mechanical stress gives rise to an easy axis direction perpendicular to the wire axis, therefore leading to an alignment of the magnetic moments in the direction which is perpendicular (circumferential) to the wire axis. As a result, only small hysteresis is observed when an axial magnetic field is applied (see Fig. 3.7b). It has been shown that these wires do not show LBE, due to the absence of the inner core axial domain structure (see Fig. 3.4a). It appears that, in the case of the negative magnetostrictive AGCWs, the glass removal resulted in the LBE [2, 6]. This was a direct consequence of the appearance of the inner core axial domain structure due to the increased axial anisotropy (see Fig. 3.4b). Applying an external tensile stress ($\sim$50 MPa) onto the glass-removed amorphous wire could also lead to the suppression of the LBE [6], because of the reappearance of the inner core radial domain structure, as in the case of the glass-covered amorphous wire without an applied tensile stress (see Fig. 3.4c). However, the difference in the magnitude of the internal stresses between AGCWs and CAWs with negative magnetostriction ($\lambda < 0$), which is reflected by the existence of the different inner core domain structures (radial versus axial), can help interpret the different magnetic hysteresis behaviours of these wires.

For the nearly zero and negative magnetostrictive AGCWs (e.g. Co–Fe–Si–B wires), there is a compensation of induced anisotropies resulting from the balance between the magnetoelastic and magnetostatic energies. Consequently, the hysteresis loop exhibits a normal shape with no observed LBE effect (see Fig. 3.7c). It was found that glass removal could result in the appearance of the LBE—which was again suppressed by applying an external tensile stress ($\sim$30 MPa), as was the case for the negative magnetostrictive AGCWs [2, 6, 16]. The tensile stress needed to suppress the LBE for the nearly zero and negative magnetostrictive AGCW ($\sim$30 MPa) is obviously smaller than that for the negative magnetostrictive AGCW ($\sim$50 MPa) [2]. This is attributed to the smaller value of the magnetostriction constant of the nearly zero and negative magnetostrictive AGCW compared to the negative magnetostrictive AGCW.

3.2.2 Permeability

Magnetic permeability is a key parameter for evaluating the magnetic softness and therefore potential applications of soft ferromagnetic materials. A high value of permeability is required and is related to the specific domain structure of the configuration. In particular, the permeability depends on the sample geometry, stress distribution in the material as well as the internal configuration of magnetisation, which might be frequency-dependent. It is therefore necessary to evaluate the magnitude of the magnetic permeability and its changes upon the application of an external field such as a magnetic field and a mechanical stress.

It has been shown that the relative magnetic permeability of a typical vanishing magnetostrictive amorphous wire (e.g. CoFeSiB amorphous wire) is the largest

among the amorphous wires investigated [2, 6]. This wire, together with its peculiar domain structure, is ideal for sensor applications based on the GMI effect. Meanwhile, both large negative and positive magnetostrictive amorphous wires have relatively small permeability. It has generally been found that the glass removal of AGCWs leads to a drastic increase of the relative permeability due to the relief of internal stress. Applying an appropriate tensile stress onto a glass-removed amorphous wire leads to an improvement of the relative permeability [2]. The application of high external stresses usually causes a drastic reduction of the relative permeability. Proper annealing of amorphous wires (e.g. Fe-based alloys) also results in a strong increase of the relative permeability due to the appearance of the nanosized α-Fe(Si) grains [2, 5, 6, 14].

Applying a magnetic field perpendicular to the wire axis (or in the circular direction) may improve the relative permeability of the wire, because of the increase of the circular component of the permeability due to increased domain wall displacement or the magnetisation rotation process in the circular direction. In contrast to this, applying a magnetic field along the wire axis (or in the longitudinal direction) may slightly increase the relative permeability when the magnetic field is below the switching field (or the anisotropy field), but it strongly reduces the relative permeability at higher fields. Therefore, the maximum value of permeability is often obtained near the switching field or the anisotropy field [2, 6]. Utilising the magnetic field dependence of the permeability, a number of technical applications have been proposed [5, 6].

We now extend the static permeability to the frequency-dependent dynamic one, which often serves as an essential index for evaluating magnetic materials in the context of high-frequency applications. A number of studies have been directed towards this direction. Liu and co-workers showed that the magnetic permeability can be tuned sensitively by applying a biasing field [17]. Han and co-workers reported that the permeability spectra of Fe–Si–B microwires follow Kittel's law and the LLG equation [18]. Note that the permeability varies with frequency; generally, with increasing frequency, the wires have less time to respond to external field, so the permeability will decrease. At gigahertz range, the permeability of the wire media is very close to 1, as only the parallel wires respond weakly to the magnetic field at such a high-frequency range. Details of these phenomena will be discussed later in the chapters dealing with microwire composites [19, 20].

3.2.3 Magnetisation Processes

The magnetisation process of a magnetic material occurs in relation to its specific domain structure. Owing to the specific domain structure of each material (wire or ribbon), either a circular magnetisation process or an axial magnetisation process, or both, can be considered. Understanding the underlying mechanisms of these magnetisation processes helps us to tailor the material properties for particular engineering applications.

For a negative (e.g. Co–Si–B) or vanishing magnetostrictive (e.g. Co–Fe–Si–B) amorphous wire, a magnetic field applied perpendicular to the wire axis is an easy axis field with respect to the circumferential anisotropy. Depending upon its magnitude, applying such a field precedes domain wall displacement and magnetisation rotation processes, thus changing the circular component of the magnetisation [21, 22]. In contrast, the application of a magnetic field along the wire axis suppresses the circular magnetisation via the domain wall displacement, because this magnetic field is a hard axis field with respect to the circumferential anisotropy. The longitudinal magnetic field leads to a gradual transition from an almost square-shaped hysteresis loop to a linear one as the remagnetisation grows [23]. A domain model was proposed by Landau and Lifshitz [24] to interpret this feature. In the case of magnetic wires, the change in the circular component of the magnetisation is related to that of the impedance. Consequently, the GMI effect is observed because the application of an external magnetic field changes the magnetisation component [2, 5].

Unlike the negative and nearly zero magnetostrictive amorphous wires with an outer shell circular domain structure, the positive magnetostrictive (Fe-based) amorphous wires usually exhibit a small GMI effect because of the presence of the outer shell radial domain structure. Such a domain structure is not favourable for domain wall displacements in the circular/transverse direction. It has been observed that, when a magnetic field is applied along the wire axis, the pre-existing closure domain structures at both ends will enlarge towards the centre of the wire [5]. At the switching field, the domain wall from one of the two closure structures de-pins and irreversibly moves towards the other end, giving rise to a sharp change in magnetisation (Fig. 3.6). This is related to the well-known wall propagation mode, in which the wall-propagating velocity depends on external factors such as magnetic fields or applied mechanical stresses. This is useful for some technical applications [25–27].

3.3 Mechanical Properties

The mechanical properties of the amorphous metals are generally superior to their crystalline counterparts. For instance, the Al-based amorphous alloys have been found to be twice as strong as their commercial crystalline versions [28]. Some Fe-based amorphous alloys display a fracture strength of about 3.5 GPa, which is greater than that obtained in some special steels [29].

Recently, the mechanical properties of several CAWs and AGCWs have been investigated [30–33]. It has been found that these wires have good mechanical properties, and the tensile strength of the AGCWs after glass removal becomes comparable to the CAWs [2, 31–33]. The influence of wire diameter on tensile strength has also been studied [34]. The size effect was observed in AGCWs with respect to the difference in the thermal expansion coefficients of the metal and the glass; that is, the tensile strength increased with decreasing wire diameter when the

thermal expansion coefficient of the metal was considerably different from that of the glass covering [34].

Annealing treatment of amorphous metallic alloys may lead to considerable change in the mechanical properties [30–34]. It has been found that Fe-based amorphous ribbons show a ductile–brittle transition temperature and the phenomenon of thermal embrittlement. The latter is marked by an increase in the ductile–brittle transition temperature when annealing below the crystallisation temperature [35]. The mechanism of thermal embrittlement is related to the removal of excess free volume and/or to the separation of the homogeneous amorphous phase in the sample upon annealing. For instance, when studying the fracture behaviour of Fe-based amorphous glass-covered microwires upon annealing, Zhukova et al. [33] observed a strong drop in tensile yield strength at annealing temperatures near the onset crystallisation temperature (see Fig. 3.8). The magnitude of the tensile yield strength of the nanocrystalline sample annealed at 600 °C is the largest among all the samples annealed, even though it is smaller than that of the as-cast amorphous sample. This indicates that the presence of the nanosized α-Fe (Si) grains and their uniform distribution in the nanocrystalline sample led to a slight improvement of the tensile yield strength. In contrast to this, annealing over 600 °C made the sample extremely brittle, which was attributed to the

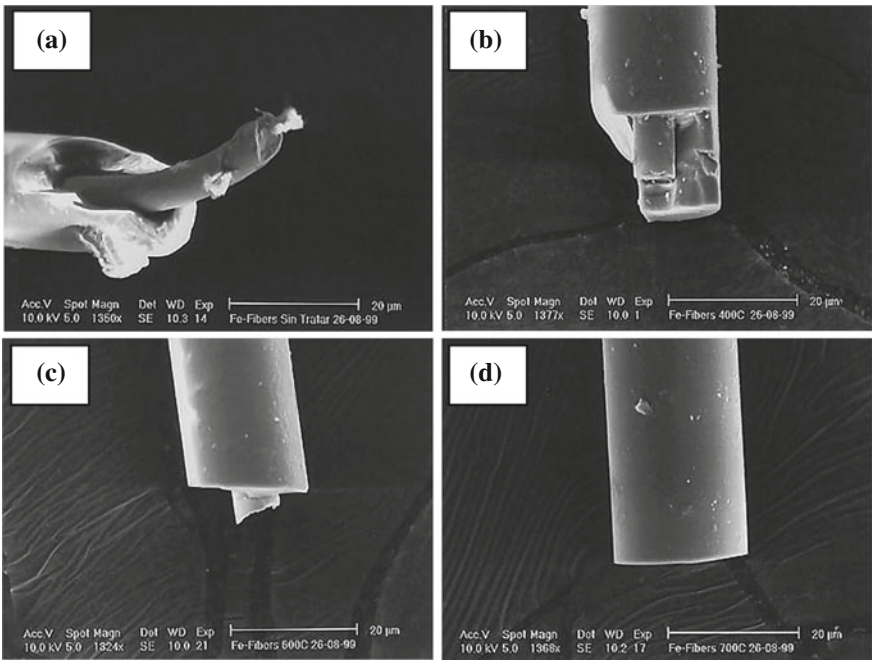

Fig. 3.8 Micrographs of the fractured Fe–Si–B–Cu–Nb glass-coated microwire samples in (**a**) as-prepared amorphous state and annealed at (**b**) 400 °C, (**c**) 600 °C, and (**d**) 700 °C (reproduced with permission from Elsevier [33])

microstructural change in the sample, where a completely crystallised structure was observed [33]. This is consistent with the change in morphology of a fractured Fe–Si–B–Cu–Nb glass-coated microwire in as-prepared and annealed states (see Fig. 3.8). The effects of different annealing processes (furnace, current, and pulse annealing) on the mechanical properties of the Fe-based amorphous wire were also investigated [32].

Another effective and facile tailoring technique is cold-drawing. Wang et al. [36] reported that with appropriate cold-drawing, both tensile strength and plasticity can be significantly improved. They claimed that the tensile stress can induce the generation of nanocrystallites, which can dissipate the elastic strain energy, stabilise the shear bands, and arrest its rapid propagation, leading to enhanced global plasticity. This method can also effectively improve the GMI effect by modifying the domain structure with the influence of stress and microstructural evolution [37].

In practice, owing to their good mechanical properties, amorphous wires are useful for applications such as reinforcement in composites and cutting utensils. For example, a reasonable reinforcing effect was observed in polymer matrix composites containing amorphous wires [38]. Such wires can also be used as reinforcement for motor tyres [39]. It is believed that Fe-based amorphous wires with a suitable coating (e.g. AGCWs) are the most promising candidates to fulfil the requirements of tyre reinforcement, where high tensile strength, good adhesion to rubber, and excellent resistance to fatigue and corrosion are required.

When considering nanocrystalline wires, although excellent magnetic properties can be achieved, embrittlement of these materials may to some extent limit their use in applications such as sensors. To avoid this problem, the annealing time for an amorphous sample should be as short as possible. Alternatively, it is recommended that the annealed amorphous sample should be as near net shape as possible in actual devices.

3.4 Electrical Properties

In general, the electrical resistivities of the amorphous alloys (wires and ribbons) are higher than those of their crystalline counterparts with the same composition. For example, the resistivity of the Fe–Si–B AGCW was found to be about 20 % higher than that of the corresponding crystalline alloy [2]. This is useful for high-frequency applications, due to the greatly reduced eddy current losses [40]. However, for developing GMI-based sensors, the reduction of resistivity of the amorphous materials is necessary to improve the GMI effect. It is important to note that nanocrystalline materials—which have been synthesised by annealing their amorphous precursors—usually exhibit much lower resistivity relative to their amorphous counterparts. Figure 3.9 shows the dependence of the resistivity of the Fe-based ribbon and wire on the annealing temperature. It can be seen that the resistivity decreases with the annealing temperature up to 540 °C and then tends to increase at higher annealing temperatures. This is related to the increase of magnetic

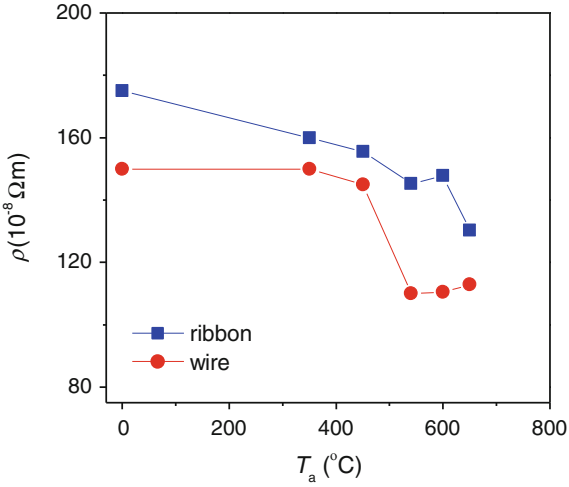

Fig. 3.9 The resistivity changes with the annealing temperature for Fe–Si–B–Cu–Nb ribbon and wire samples

softness at annealing temperatures below 550 °C and to the microstructural change upon higher temperature annealing, i.e. the appearance of the nanosized α-Fe(Si) crystalline grains after annealing below 540 °C [5]. In this context, the emphasis is on the measured temperature dependence of the resistivity of the amorphous sample, the structural relaxation, and crystallisation processes occurring in these materials, which can be monitored and controlled. Furthermore, the resistivity of amorphous ribbons and wires strongly depends on the alloys' composition and external factors such as magnetic field, mechanical stress, and pressure. Therefore, the magnitude of the alloy's resistivity can be modified either by the addition of chemical elements or by the application of magnetic fields, tensile stress, and pressure. In the case of AGCWs, glass removal can lead to a considerable decrease of the wires' resistivity, which is useful for GMI sensor applications.

3.5 Chemical Properties

Among the chemical properties often investigated, several works have paid much attention to the wet corrosion resistance of amorphous metallic materials [41–44]. In particular, research has been focused on Fe-based amorphous materials containing metalloid addition in various acids and sodium chloride solutions. Due to the absence of grain boundaries in amorphous metals, the corrosion resistance of these materials is higher than that of conventional crystalline materials, including stainless steels. It has been shown that the addition of elements such as Cr and Mo or both into Fe-based amorphous ribbons [41–43], thin films [44], and wires [2] leads to an improvement in corrosion resistance. Pardo et al. [43] have shown that the addition of Cr to Fe–Cr–Si–Cu–Nb–B ribbons, in both the amorphous and

nanocrystalline states, significantly improves the corrosion resistance of these materials in humid environments with a high SO_2 concentration, while retaining their excellent soft magnetic properties.

The superior corrosion resistance of Fe-based amorphous and nanocrystalline materials is useful for their application in chemical environments, where they can be used for protection of other materials [43]. For example, Fe–Cr–P–C amorphous ribbons are used as the active element in electromagnetic filters to remove rust from water, their high corrosion resistance ensuring a long life of the filter elements [42]. Further information on the corrosion resistance properties of typical amorphous metals as well as their applications can be found in Refs. [41–43].

References

1. Vazquez M, Hernando A (1996) A soft magnetic wire for sensor applications. J Phys D Appl Phys 29:939–949
2. Chiriac H, Ovari TA (1996) Amorphous glass-covered magnetic wires: Preparation, properties, applications. Prog Mater Sci 40:333–407
3. Velazquez J, Vazquez M, Hernando A, Savage HT, Wun-Fogle M (1992) Magnetoelastic anisotropy in amorphous wires due to quenching. J App Phys 70:6525–6527
4. Reininger T, Kronmuller H, Gomez-Polo C, Vazquez M (1993) Magnetic domain observation in amorphous wires. J Appl Phys 73:5357–5359
5. Phan MH, Peng HX (2008) Giant magnetoimpedance materials: fundamentals and applications. Prog Mater Sci 53:323–420
6. Vazquez M (2007) Handbook of magnetism and advanced magnetic materials (Chap. Advanced magnetic microwires). In: Novel materials, vol 4. John Wiley & Sons Ltd., NJ, pp 1–29
7. Usov NA (2002) Stress distribution and domain structure in amorphous ferromagnetic wires. J Magn Magn Mater 249:3–8
8. Devkota J, Trang L, Liu J, Qin F, Sun J, Mukherjee P, Srikanth H, Phan MH (2014) A soft ferromagnetic multiwire-based inductance coil sensor for sensing applications. J Appl Phys 116:234504
9. Liu JS, Qin FX, Chen DM, Wang H, Shen HX, Xing D, Phan MH, Sun JF (2014) Combined current-modulation annealing induced enhancement of GMI effect of Co-rich amorphous microwires. J Appl Phys 115:17A326
10. Chen DM, Xing DW, Qin FX, Liu JS, Wang H, Wang XD, Sun JF (2013) Correlation of magnetic domains, microstructure and GMI effect of Joule-annealed melt-extracted Co68.15Fe4.35Si12.25B13.754 Nb1Cu0.5 microwires for double function sensors. Phys Status Solidi A 210:2515–2520
11. Chizhik A, Gonzalez J, Zhukov A, Blanco J (2007) Transformation of surface domain structure in Co-rich amorphous wires. Sens Actuators B 126:235
12. Chizhik A, Zablotskii V, Stupakiewicz A, Dejneka A, Polyakova T et al (2013) Circular domains nucleation in magnetic microwires. Appl Phys Lett 102:202406
13. Hernando A, Barandiaran JM (1978) Circular magnetisation measurement in ferromagnetic wires. J Phys D Appl Phys 11:1539–1541
14. Chiriac H, Ovari TA, Vazquez M, Hernando A (1998) Magnetic hysteresis in glass-covered and water-quenched amorphous wires. J Magn Magn Mater 177–181:205–206
15. Larin VS, Torcunov AV, Zhukov A, Gonzalez J, Vazquez M, Panina L (2002) Preparation and properties of glass-coated microwires. J Magn Magn Mater 249:39–45

16. Zhukov A, Gonzalez J, Vazquez M, Larin V, Torcunov A (2004) Nanocrystalline and amorphous magnetic microwires. In: Nalwa HS (ed) Encyclopedia of nanoscience and nanotechnology, vol X, pp 1–22
17. Liu L, Matitsine SM, Tang CB, Rozanov KN (2009) Measurement of tunable permeability and permittivity of microwires composites at microwave frequency. PIERS Proceeding, Moscow, Russia, pp 1662–1666
18. Han M, Liang D, Deng LJ (2011) Appl Phys Lett 99:082503
19. Makhnovskiy DP, Panina LV, Garcia C, Zhukov AP, Gonzalez J (2006) Phys Rev B: Condens Matter 74(6):064205
20. Starostenko SN, Rozanov KN (2009) Prog Electromagnet Res 99:405
21. Dominguez L, Blanco JM, Aragoneses P, Gonzalez J, Valenzuela R, Vazquez M, Hernando A (1996) Circumferential magnetization processes in CoFeBSi wires. J Appl Phys 79:6539–6541
22. Zhukova V, Zhukov AP, Usov NA, Blanco JM, Gonzalez J (2004) Magnetization reversal process at low applied magnetic field in a Co-rich amorphous wire. Phys B 343:369–373
23. Radkovskaia AA, Sandacci SI, Panina LV, Mapps DJ (2004) Valve-like behavior of the magnetoimpedance in the GHz range. J Magn Magn Mater 272–276:1855–1857
24. Landau LD, Lifshitz EM (1975) Electrodynamics of continuous media. Pergamon Press, Oxford
25. Zhukov A (2001) Domain wall propagation in a Fe-rich glass-coated amorphous microwire. Appl Phys Lett 78:3106–3108
26. Puerta S, Cortina D, Garcia-Miquel H, Chen DX, Vazquez M (2001) Propagation of domain walls in bistable amorphous wires and microwires. J Non-Cryst Sol 287:370–373
27. Chiriac H, Hristoforou E, Neagu M, Darie I (2001) On the domain wall propagation in glass covered amorphous wires. Mater Sci Eng A 304–306:1011–1013
28. Bechet D, Regazzoni G, Dubois JM (1989) Pour la Science 139:30
29. Li JCM (1993) In: Liebermann HH (ed) Rapidly solidified alloys: processes, structures, properties, applications. Marcel Dekker Inc., New York, p. 379 (Chap. 13)
30. Chen HS, Sherwood RC, Jin S, Chi GC, Inoue A, Masumoto T, Hagiwara M (1984) Mechanical properties and magnetic behavior of deformed metal glass wires. J Appl Phys 55:1796–1798
31. Goto T, Toyama T (1985) The preparation of ductile high-strength Fe-based filaments using the methods of glass-coated melt spinning. J Mater Sci 20:1883–1888
32. Atalay S, Adiguzel HI, Kamer O (2001) Effect of different heat treatments on magnetoelastic properties of Fe-based amorphous wire. Mater Sci Eng A 304–306:495–498
33. Zhukova V, Cobeno AF, Zhukov A, de Arellano Lopez AR, Lopez-Pombero S, Blanco JM, Larin V, Gonzalez J (2002) Correlation between magnetic and mechanical properties of devitrified glass-coated $Fe_{71.8}Cu_1Nb_{3.1}Si_{15}B_{9.1}$ microwires. J Magn Magn Mater 249:79–84
34. Goto T, Nagano M, Tanaka K (1977) Tensile strength of copper and iron filaments produced by method of glass-coated melt spinning. Transactions of the Japan Institute of Metals 18:209–213
35. Spaepen F, Tsao SS, Wu TW (1985) In: Haasen P, Jafee RI (eds) Amorphous metals and semiconductors. Oxford, Pergamon, pp 365–378
36. Wang Huan, Xing Dawei, Peng Huaxin, Qin Faxiang, Cao Fuyang, Wang Guoqiang, Sun Jianfei (2012) Scripta Mater 66:1041
37. Wang H, Qin FX, Xing D, Cao F, Wang XD, Peng H, Sun J (2012) Acta Mater 60:5425
38. Fels A, Friedrich K, Hornbogen E (1984) Reinforcement of brittle epoxy resin by metallic glass ribbons. J Mater Sci Lett 3:569–574
39. Ohnaka I (1985) Melt spinning into a liquid cooling medium. Int J Rapid Solidification 1:219–236
40. Marin P, Hernando A (2000) Applications of amorphous and nanocrystalline magnetic materials. J Magn Magn Mater 215–216:729–734
41. Hashimoto K (1985) In: Steeb S, Warlimont H (eds) Proceedings of 5th international conference on rapidly quenched metals Amsterdam, North-Holland, pp 1449–1456

42. Kawashima A, Asami K, Sato T, Hashimoto K (1985) In: Steeb S, Warlimont H (eds) Proceedings of 5th international conference on rapidly quenched metals Amsterdam, North-Holland, pp 1671–1674
43. Pardo A, Otero E, Merino MC, Lopez MD, Vazquez M, Agudo P (2001) The Influence of Cr Addition on the Corrosion Resistance of $Fe_{73.5}Si_{13.5}Nb_3Cu_1$ Metallic Glass in SO_2 Contaminated Environments. Corros Sci 43:689–705
44. Choi HW, Kim HK, Kim J, Han SH, Kim HJ (2001) The effect of Cr addition on structure and corrosion resistance in FeTiN nanocrystalline soft magnetic thin films. IEEE Trans Magn 37:1773–1775

Chapter 4
Giant Magnetoimpedance: Concept, Theoretical Models, and Related Phenomena

In this chapter, the fundamental aspects of giant magnetoimpedance (GMI) and related phenomena are discussed. Prior to defining the GMI, the concepts of eddy current and the skin effect associated with GMI are comprehensively introduced. The existing models developed on the frequency dependence of GMI have been systematically examined in order to check the validity of each model in relation to the operating frequency range. It is concluded that the development of theoretical models that can rigorously predict the GMI effect in a wide frequency range from kHz to GHz is a challenging task.

4.1 Eddy Currents and Skin Effect

Since eddy currents and the skin effect are related to the GMI phenomenon, it is essential to understand these concepts. Let us recall the following phenomenon: when a rod-shaped magnetic material is wound with a conductive wire carrying a dc current i_w (Fig. 4.1), this i_w will induce a dc magnetic field H_a directed along the rod axis and uniform throughout the rod cross section [1]. H_a magnetises the rod, and the magnetic induction B increases from its original value of zero. According to Faraday's law, an emf e will be induced in the rod, which is proportional to dB/dt. As i_w is increased, the direction of e tends to establish a current, the so-called eddy current i_{ec}, in a circular path (Fig. 4.1). The direction of i_{ec} is antiparallel to that of i_w in accordance with Lenz's law.

At the same time, i_{ec} will induce a magnetic field H_{ec}, which opposes H_a. A simple relationship between the emf e and dB/dt is expressed as

$$e = -10^{-8}\frac{d\phi}{dt} = -10^{-8}A\frac{dB}{dt}, \tag{4.1}$$

H.-X. Peng et al., *Ferromagnetic Microwire Composites*,
Engineering Materials and Processes, DOI 10.1007/978-3-319-29276-2_4

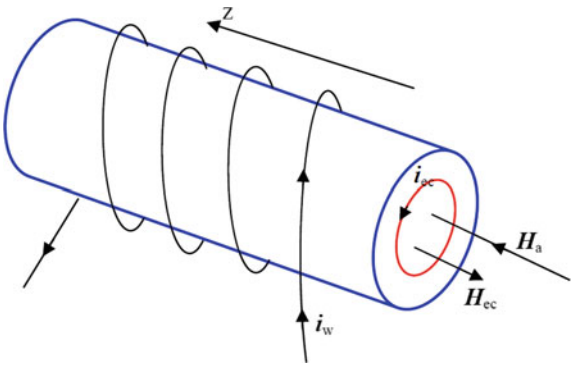

Fig. 4.1 A schematic illustration of the appearance of eddy currents in a *rod-shaped* magnetic material (reproduced with permission from Addision-Wesley [1])

where $A = \pi r^2$ is the cross-sectional area of the rod, ϕ is the flux, and t is the time. Accordingly, it is inferred that e can be induced in both magnetic and non-magnetic materials. In a magnetic material, the higher the magnetic permeability of a material, the larger the induced e. Therefore, the eddy current effect is much stronger in magnetic materials than in non-magnetic materials. This explains why GMI effects can be observed in magnetic materials, but not in non-magnetic materials. It is also noted that for a given dB/dt, the lower the electrical resistivity of a magnetic material, the larger the eddy current obtained. No eddy current effect appears in insulating materials such as ferromagnets. For some practical applications, it is essential to raise the resistivity of a material to minimise undesirable eddy current effects. For example, in transformer cores, eddy current heating is a source of power loss, and therefore, current efforts are focused on reducing the effect by increasing the resistivity of the core material [1, 2].

It is worth noting that the eddy current field is strongest at the centre of the rod as a direct consequence of the contributions of all the current rings and becomes weaker towards the edge of the rod. As a result, the actual field H acting in the material is the vector sum of H_a and H_{ec}, and this field decreases below the surface of the rod and is a minimum at the centre of the rod (Fig. 4.2a). This effect can be alternatively illustrated in Fig. 4.2b, showing how H changes with time at various points along the radius of the rod. When the switch is closed at time t_1, H is immediately established at its full value at the rod surface. But the field at mid-radius takes some time to reach this value and the field at the centre takes longer still, becoming equal to the surface field at time t_4. The field profile in the rod interior is sketched in Fig. 4.2c for various times. The time required (t_4 s) for the eddy current effect to disappear, i.e. for the magnetic induction (B) to reach a stationary value at the centre of the rod, depends on the magnetic permeability (μ), the electrical resistivity (ρ), and the rod diameter. For example, a stationary state is reached within a fraction of a second in an annealed iron rod of about 1/4 in. diameter, but in thick pieces of high-μ and low-ρ material, eddy current effects may persist for several seconds.

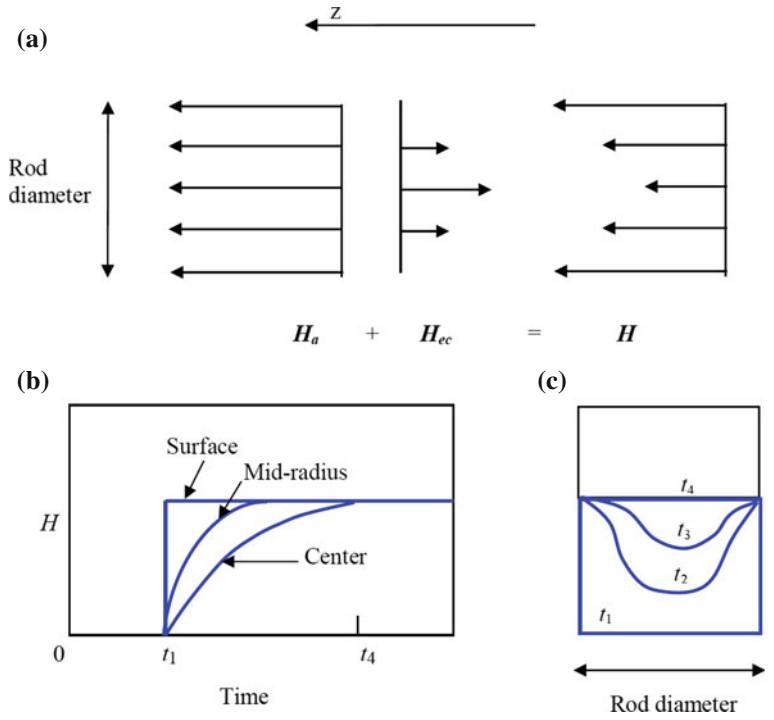

Fig. 4.2 A schematic illustration of magnetic fields in a *rod-shaped* magnetic material (reproduced with permission from Addision-Wesley [1])

Skin effect: If a magnetic field applied to a magnetic rod is alternating (i_w is an ac current, as illustrated in Fig. 4.1) at a fixed frequency, H_a goes through a maximum and begins to decrease before B at the centre of the rod can attain the same maximum value that was reached by B at the surface. The maximum value of B will then be less at the centre than at the surface of the rod. This phenomenon is known as a skin effect. In this case, the exponential decay of current density from the surface into the interior is described by the skin depth,

$$\delta = \sqrt{2\rho/\omega\mu}, \tag{4.2}$$

which depends on the circular frequency of the ac current ω, the electrical resistivity ρ, and the magnetic permeability μ. In non-ferromagnetic materials, the permeability is independent of the frequency and applied magnetic field, whereas in ferromagnetic materials, μ depends on the frequency, the amplitude of the ac magnetic field induced by i_w, and other external parameters such as the applied dc magnetic field, mechanical strain, and temperature. Owing to the dc magnetic field dependence of the skin depth and hence the ac impedance of ferromagnetic materials, the so-called GMI effects are observed in these materials.

4.2 Giant Magnetoimpedance (GMI) Effect

The giant magnetoimpedance (GMI) effect is a large change in the ac complex impedance (Z) of a ferromagnetic conductor subject to a dc applied magnetic field [3, 4]. Since $Z = R + jX$ (R and X are the ac resistance and reactance, respectively), it is essential to consider the relative contributions of R and X to Z over a measured frequency range [5, 6]. The relative changes in R, X, and Z with the applied field (H) at a given frequency of the driving current (defined as the MR, MX, and MI ratios, respectively) are often calculated by using the following equations:

$$\frac{\Delta R}{R} = \frac{R(H) - R(H_{\max})}{R(H_{\max})} \times 100\,\%; \tag{4.3}$$

$$\frac{\Delta X}{X} = \frac{X(H) - X(H_{\max})}{X(H_{\max})} \times 100\,\%; \tag{4.4}$$

$$\frac{\Delta Z}{Z} = \frac{Z(H) - Z(H_{\max})}{Z(H_{\max})} \times 100\,\%, \tag{4.5}$$

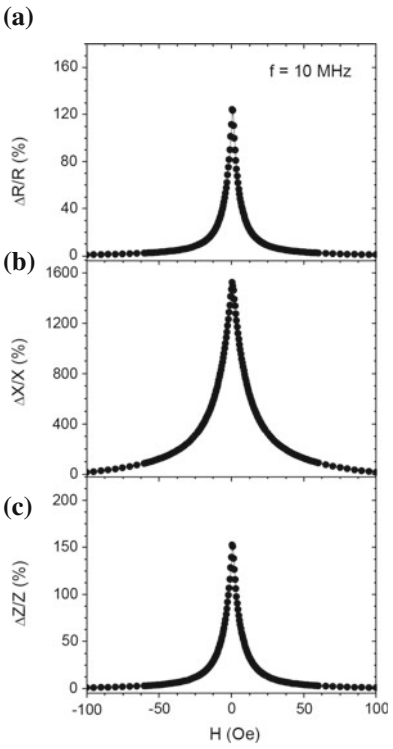

Fig. 4.3 Magnetic field dependence of the (**a**) magnetoresistance ($\Delta R/R$), (**b**) magnetoreactance ($\Delta X/X$), and (**c**) magnetoimpedance ($\Delta Z/Z$) ratios for a soft ferromagnetic amorphous glass-coated $Co_{68}B_{15}Si_{10}Mn_7$ microwire at 10 MHz

where H_{max} is usually the external magnetic field sufficient to saturate the impedance. In practice, the value of H_{max} is available for the given experimental equipment. While some researchers use $H_{max} = 0$, this definition may not be appropriate, because the value of $Z(0)$ depends on the remanent magnetic state of the material. If the MI ratio ($\Delta Z/Z$) is greater than 20 %, it is often considered a GMI effect. A typical example of the field dependence of the MR, MX, and MI effects of a soft ferromagnetic microwire is displayed in Fig. 4.3.

4.3 Impedance of a Magnetic Conductor

According to the definition, the complex impedance, Z, of a magnetic conductor is given by the ratio V_{ac}/I_{ac}, where I_{ac} is the amplitude of a sinusoidal current $I = I_{ac}\exp(-j\omega t)$ passing through the conductor and V_{ac} is the voltage measured between the ends of the conductor. Figure 4.4 shows a schematic illustration of the impedance definition.

Note that this definition is valid only for a uniform magnetic conductor. Nonetheless, for a metallic ferromagnet having the length l and the cross-sectional area q, its impedance can still be, in linear approximation, expressed as follows [5–7]:

$$Z = \frac{V_{ac}}{I_{ac}} = \frac{LE_z(S)}{q\langle j_z\rangle_q} = R_{dc}\frac{j_z(S)}{\langle j_z\rangle_q}, \tag{4.6}$$

where E_z and j_z are the longitudinal components of an electric field and current density, respectively, and R_{dc} is the dc electrical resistance. S denotes the value at the surface, and $\langle\rangle_q$ is the average value over the cross-sectional area q. Alternatively, the expression of Z can be given in terms of the surface impedance tensor $\hat{\xi}$:

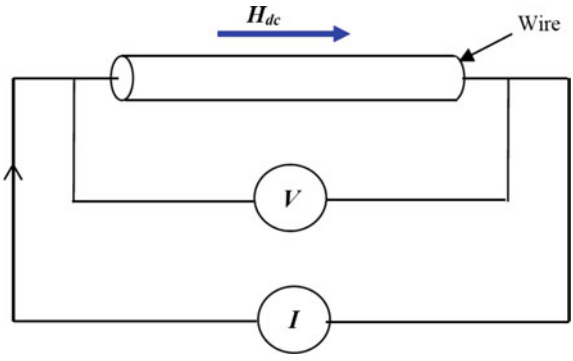

Fig. 4.4 The definition of impedance

$$Z = R_{\mathrm{dc}} \frac{q}{\rho l} \left(\xi_{zz} - \xi_{z\phi} \frac{H_z(S)}{H_\phi(S)} \right), \tag{4.7}$$

where ρ is the resistivity, l the length of the conductor, and H_z and H_ϕ are the axial and circumferential components of the ac magnetic field, respectively.

The current density $j(r)$ in Eq. (4.6) or the magnetic field H in Eq. (4.7) of the conductor can generally be obtained within the framework of classical electrodynamics of continuous media, by solving simultaneously the reduced Maxwell equation

$$\nabla^2 \boldsymbol{H} - \frac{\mu_0}{\rho} \dot{\boldsymbol{H}} = \frac{\mu}{\rho} \dot{\boldsymbol{M}} - \mathrm{grad}\,\mathrm{div}\,\boldsymbol{M}, \tag{4.8}$$

and the Landau–Lifshitz equation for the motion of the magnetisation vector

$$\boldsymbol{M} = \gamma \boldsymbol{M} \times \boldsymbol{H}_{\mathrm{eff}} - \frac{\alpha}{M_s} \boldsymbol{M} \times \dot{\boldsymbol{M}} - \frac{1}{\tau} (\boldsymbol{M} - \boldsymbol{M}_0), \tag{4.9}$$

where γ is the gyromagnetic ratio, M_s the saturation magnetisation, M_0 the static magnetisation, H_{eff} the effective magnetic field, and α the damping parameter [7–9]. In this context, the effective field can be calculated from the free energy density of the system, which depends on the particular magnetic domain structure of the sample. According to this method, the current density depends on the material parameters and the conductor geometry, as well as the actual magnetic state of the sample [8, 9]. It is therefore difficult to obtain the exact solution of the problem. However, a number of theoretical models have been proposed, using the simplified assumptions, to approach the solution of Eqs. (4.8) and (4.9) with appropriate boundary conditions [8–14].

In order to avoid such complicated calculations, it is often assumed that the material relationship between the induction and magnetic field is linear ($B = \mu H$ and μ is constant). Using this relationship, only the Maxwell equation must be solved while ignoring the Landau–Lifshitz equation of motion Eq. (4.9). For example, as the classical skin effect solution of Eq. (4.8) is obtained [3, 4], the calculated impedance Z of a cylindrical magnetic conductor is

$$Z = R_{\mathrm{dc}} kr J_0(kr) / 2 J_1(kr), \tag{4.10}$$

where J_0 and J_1 are the Bessel functions of the first kind, r is the radius of the wire, R_{dc} is the electrical resistance for a dc, $k = (1 + j)/\delta_{\mathrm{m}}$ with imaginary unit j; δ_{m} is the penetration depth in a magnetic medium, with the circumferential permeability (μ_ϕ) for the case of the wire [3],

$$\delta_{\mathrm{m}} = \frac{c}{\sqrt{4\pi^2 f \sigma \mu_\phi}}, \tag{4.11}$$

where c is the speed of light, σ is the electrical conductivity, and $f = \omega/2\pi$ is the frequency of the ac (I_{ac}) flowing along the sample.

According to Eqs. (4.10) and (4.11), GMI can be understood as a consequence of the increase of the skin depth until it becomes equal to the radius of the wire (r) through the decrease of the circumferential permeability in Eq. (4.11) under an applied dc magnetic field. In order to maximise GMI values, it is necessary to reduce the skin depth by choosing magnetic materials that have large μ_ϕ and small δ_m and R_{dc}. It is clear that the large permeability reduces the skin depth, which is later increased by the applied field as shown in Fig. 4.5. In fact, the real and imaginary components of Z change with the dc applied field, H_{dc}. In first-order approximation, the in-plane component of resistance, R, can be expressed as [7, 15]:

$$R = (\rho l)/2\pi(r - \delta_m)\delta_m. \tag{4.12}$$

The dependence of Z on skin depth is then clear from Eqs. (4.10) and (4.12). Experimentally, the skin depth can be evaluated as a function of H_{dc} through the measurement of R. The reactance X can be expressed as

$$X = 0.175\mu_0 lf\langle\mu_r\rangle, \tag{4.13}$$

where μ_0 and $\langle\mu_r\rangle$ are the vacuum permeability and the average relative circumferential permeability, respectively. The reactance will thus also depend on H_{dc}, which affects the permeability term $\langle\mu_r\rangle$. Consequently, field-induced changes in both R and X contribute to those in Z and therefore to GMI [16].

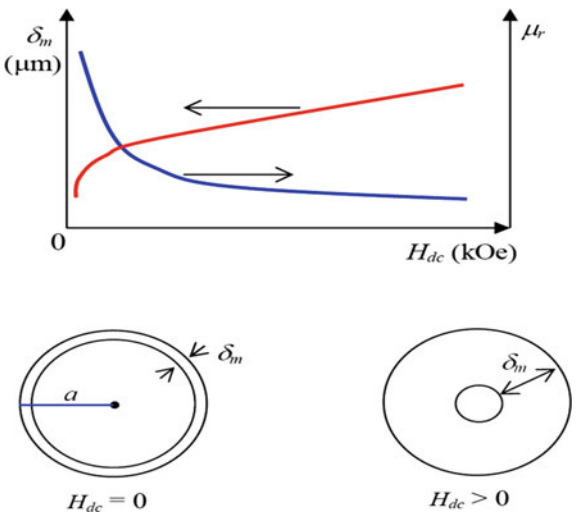

Fig. 4.5 *Upper panel* dc applied magnetic field (H_{dc}) dependences of skin depth (δ_m) and reversible permeability (μ_r). *Lower panel* a schematic view of the change of δ_m with H_{dc} for a magnetic wire

4.4 Theoretical Models

Based on the frequency (f) of the driving ac current, the GMI can be roughly separated into the following frequency regimes:

(i) *Low-frequency regime* ($f \leq 1$ MHz): changes in the voltage at the sample's ends are mainly due to the so-called magnetoinductive effect [17]. The skin effect is very weak in this case. The change in the impedance of the sample upon application of the magnetic field (H_{dc}) results mainly from the contribution of inductance (L), which is proportional to the circumferential permeability (μ_ϕ) for a cylindrical magnetic conductor [4].

(ii) *Intermediate-frequency regime* (1 MHz $\leq f <$ 1 GHz): GMI originates mainly from the variation of the skin depth due to strong changes of the effective magnetic permeability caused by the applied dc magnetic field. It is noted here that, depending on the sample geometry, the GMI profile can reach its peak in the frequency range of 1–10 MHz, as a consequence of the contribution of the permeability from both domain wall motion and magnetisation rotation to GMI [18]. Reduction in GMI at higher frequencies is related to the domain walls becoming strongly damped by eddy currents, and only magnetisation rotation contributes to GMI.

(iii) *High-frequency regime* (1 GHz $\leq f$): the origin of GMI is believed to be related to the gyromagnetic effect and the ferromagnetic relaxation. The maxima in GMI profiles are shifted towards higher fields, where the samples are already saturated magnetically [19]. Strong change in the skin depth is caused by the same mechanism as in the ferromagnetic resonance (FMR) [20].

The theoretical models of GMI representing each of the above-mentioned frequency ranges are examined and discussed below.

4.4.1 Quasi-Static Model

The quasi-static model has been proposed based on an assumption that the measuring frequency is small enough for an equilibrium state of the system to be reached at every moment [11, 12, 19]. Using this hypothesis, it is possible to use Eqs. (4.10) and (4.11) with the effective magnetic permeability or susceptibility calculated from Eq. (4.9), where $f = 0$. It has been theoretically shown that when the easy direction is perpendicular to the sample axis, the contribution of the circumferential/transverse permeability to GMI is mainly due to domain wall displacements if the domain walls are easy movable [19]. Otherwise, the contribution of the circumferential/transverse permeability to GMI results mainly from magnetisation rotation when the easy direction is parallel to the conductor axis. In general, the quasi-static model can describe basic features of GMI at relatively low

frequencies, but cannot interpret the frequency dependence of GMI in the intermediate and high frequency ranges. This actually lies in the original assumption of the models.

4.4.2 Eddy Current Model

The quasi-static model is valid only where the skin effect is very weak. However, at higher frequencies, one must take into account the contribution of the circumferential/transverse permeability to GMI in addition to the dominant role played by the skin effect [2, 5, 16]. In this context, Panina and Mohri [3] have proposed the eddy current model, which calculates the circumferential permeability for a periodic bamboo-like domain structure in cylindrical wires. It is worth mentioning that these authors extended, in an effective medium approximation, the validity of Eq. (4.10) to the case of an inhomogeneous magnetisation arising from the domain wall structure. Herein, the microscopic eddy currents created by moving walls are averaged on the domain wall scale, thereby resulting in the frequency dependence of complex permeability in Eq. (4.11), which describes damped domain wall motion as characterised by a relaxation frequency, ω_{dw}. In fact, the magnetisation processes can occur due to not only domain wall motion but also spin rotation. Meanwhile, losses accompanying spin rotation arise, and these are therefore described by another relaxation parameter ω_{rot}. In general, the relaxation from rotational magnetisation is much faster than that from domain wall motion, and consequently $\omega_{rot} \gg \omega_{dw}$. At relatively low frequencies $\omega < \omega_{dw}$, the decrease of the permeability with frequency is related to damped domain wall motion due to eddy currents. It has been shown that, at low frequencies, the external magnetic field dependence of the impedance is associated with the internal part of the inductance L, which is proportional to the static circumferential permeability, μ_ϕ. It has also been highlighted that the eddy current loss is much less in a wire-shaped sample with a circular domain structure than one with a stripe domain structure [3, 6]. This explains why the permeability retains its value at higher frequencies. In the high-frequency case ($a \gg \delta_m$ and $\omega_{dw} < \omega \leq \omega_{rot}$), both R and L depend on μ_ϕ and thereby contribute to the GMI behaviour. The skin effect is dominant in this case, and the impedance is proportional to the square root of frequency and circular permeability, $Z \propto (\omega.\mu_\phi)^{1/2}$. As the frequency is further increased ($\omega > \omega_{rot}$), the resistive term becomes greater and contributes to the total impedance Z. In this instance, the impedance is independent of the external magnetic field, because the permeability is magnetic field independent [6]. Figure 4.6 compares the experimental results with those calculated using the eddy current model for a ferromagnetic FeCoSiB wire. It is shown in Fig. 4.6a that the eddy current model finds a good agreement with the experiment at low frequency ($f = 1$ MHz), but a significant deviation between the experimental and calculated results is seen in at higher frequencies ($f = 3$ and 10 MHz). Nonetheless, the model has successfully explained

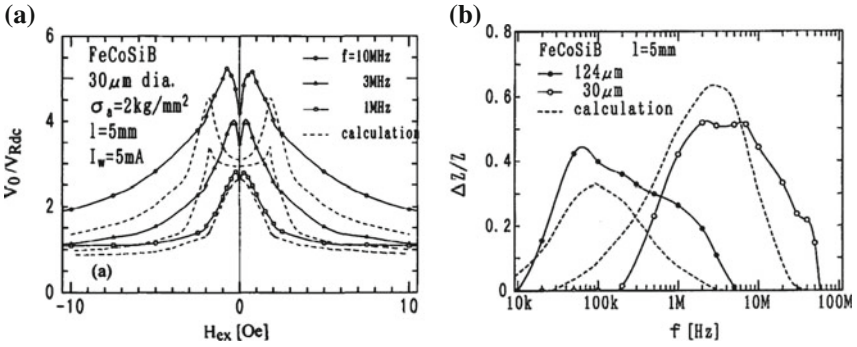

Fig. 4.6 **a** Magnetic field dependence of voltage amplitude of a ferromagnetic FeCoSiB wire with a diameter of 30 μm for different frequencies (reprinted with permission from IEEE [6]). **b** Frequency dependence of the maximum MI ratio of a ferromagnetic FeCoSiB wire with diameters of 30 and 124 μm (reprinted with permission from AIP [3])

the occurrence of a single peak in the GMI profile at low frequency and its transformation into a double peak at high frequency, as well as a trend that the maximum MI ratio varies with frequency in the frequency range up to 100 MHz.

In general, the eddy current model can describe the basic GMI features and most experimental results in the frequency range of 100–100 MHz. The significant deviation in GMI magnitude between the experiment and theory arises from the simplifying assumption of circular domain structures that are rather more complicated in actual ferromagnetic wires. Since the circular domain structure could be greatly modified as the diameter of a wire is varied, a deviation in GMI magnitude between the experiment and theory has been observed (Fig. 4.6b). In addition, other important effects, such as the exchange-conductivity effect as discussed below, have not been taken into account in the eddy current model.

4.4.3 Domain Model

The domain model provides a more rigorous treatment for the GMI problem of a metallic soft magnetic wire with periodic circular domains than the eddy current model. It was initially proposed by Chen and Munoz [13, 21] and has allowed one to interpret qualitatively single- and double-peak GMI curves and several experimental results observed in the GMI of amorphous wires. Although theoretical calculations for Z were quite consistent with experimental data, a poor agreement between the theoretical and experimental results of the circumferential permeability was found. This has recently been resolved by Betancourt et al. [14] by modifying the proposed domain models [13], in which only complex inductance formalism (L) was used to calculate the circumferential permeability, instead of using Z equations. The correlation between the inductance and permeability was established, allowing the

evaluation of the circumferential permeability as a function of frequency and resolving its dispersion law. However, the domain models could not explain satisfactorily the underlying mechanism of relaxation dispersions of permeability spectra in amorphous magnetic materials [22–26]. In this context, Kim et al. [22, 23] have proposed a phenomenological model that allows us to separate the reversible domain wall motion and magnetisation rotation components in permeability (or susceptibility) spectra of amorphous magnetic wires. These studies have provided a basic physical understanding of the realistic contribution of the domain wall motion and rotational magnetisation processes to GMI for a small driving field.

In general, the eddy current and domain models have explained successfully several basic features of GMI at frequencies below 100 MHz. However, when a high frequency leads to a skin depth comparable with the exchange length, both models fail [18]. This is because ferromagnetic resonance (FMR) occurs at high frequencies $f \sim 1$ GHz and becomes the main effect responsible for GMI behaviour [20]. In this context, the high-frequency models, including the electromagnetic and exchange-conductivity models, should be considered.

4.4.4 *Electromagnetic Model: Relationship Between GMI and FMR*

It is generally known that both GMI and FMR experiments involve similar static and driving magnetic field configurations. A typical FMR experiment is performed at a microwave frequency ($\sim$GHz) in dc magnetic fields as high as kOe, while GMI can be easily achieved at much lower frequencies in the MHz range and in dc fields of a few oersteds. A fundamental question thus emerges: *How are the GMI and FMR related to each other*? Experimentally, a sample is placed in a cavity in an FMR set-up, so that the power absorption is proportional to the surface impedance of the sample, Z_s [27–29]. In a GMI experiment, the skin effect is strong enough to confine the ac current to a sheath close to the surface of the conductor. As a result, GMI is a surface-related phenomenon [30, 31]. Depending upon a measured frequency, the electrical impedance (Z) of a magnetic conductor will approach the value of its surface impedance (Z_s). A simple relation between Z and Z_s has been established for the case of a wire of uniform cross section [29]:

$$Z = (l/p)Z_s, \tag{4.14}$$

where l is the length of the wire and p is its perimeter.

The relationship between GMI and FMR has been reported by Yelon et al. [11, 20] for magnetically saturated samples. Accordingly, an electromagnetic model has been proposed which has approached the solution of Eqs. (4.8) and (4.9) using the theoretical procedures of FMR, without considering the exchange interactions in the effective field [19, 29]. The absorption of energy is understood as an increase of impedance to the electromagnetic radiation that occurs at the resonance frequency,

$$\omega_r = \gamma\mu[(H + M_s)(H + 2K/\mu M_s)]^{1/2}, \tag{4.15}$$

where γ and K are the gyromagnetic ratio and the anisotropy constant, respectively. Here, the circumferential/transverse permeability shows a typically resonant behaviour with the maximum of the imaginary part and the change of sign of the real part at the resonance field determined by the FMR resonance condition [30]. At the resonance field, the effective permeability increases drastically and the skin depth is very small. At a given frequency, an increase of H_{dc} leads to a shift of the resonance frequency, thereby reducing the permeability and resulting in a remarkable GMI effect. The theoretical skin depth reaches its minimum value ($\sim$0.1 μm)

$$\delta_{min} = \sqrt{\frac{\alpha\rho}{\gamma\mu M_s}}, \tag{4.16}$$

and the GMI reaches its maximum value. The maximum GMI value calculated using the results of Eq. (4.16) is independent of frequency, and its magnitude (of the order of $\sim 10^3$) is much larger than the experimentally obtained value [27, 29]. This arises from the fact that GMI measurements are usually conducted at frequencies less than 100 MHz, where the FMR condition cannot be easily satisfied [29]. Furthermore, the magnitude of GMI calculated by the electromagnetic models can be obtained only in uniaxial magnetic materials with easy direction of the anisotropy exactly perpendicular to the sample axis and the dc applied magnetic field. However, in real materials, there always exists a deviation of the easy axis from the perpendicular direction of the anisotropy [29]. It is for this reason that a substantial difference between the experimentally observed and theoretically calculated GMI values has been found [27]. It is worth mentioning that in the GHz region, the experimentally observed GMI data are in good agreement with the theoretical prediction, since the FMR condition can be satisfied in this frequency regime [27, 30].

In general, the electromagnetic model can interpret qualitatively the basic features of GMI and most of the experimental data in the high-frequency regime. However, some aspects of GMI cannot be completely resolved using this model, because the role of the exchange interactions in the effective field is neglected [28].

4.4.5 Exchange-Conductivity Effect and Related Model

The exchange-conductivity effect is the damping arising from the competition between the magnetic exchange and conductivity that occurs in a magnetic wire under a GMI experiment [28, 29]. While the magnetic exchange tends to keep the ac magnetisation in adjacent layers aligned, the conductivity tends to reduce the alignment as it modifies the amplitude and the phase of the magnetic field to which

it is coupled. In actuality, the exchange-conductivity effect is caused by the interplay between the skin effect and exchange interaction. Due to the skin effect, the ac component of magnetisation induced by an ac current flowing along the conductor axis decreases in its magnitude from the surface to the centre. Consequently, the magnetisation is inhomogeneous, and exchange energy arises accordingly. Such an increase of the exchange energy (or exchange interaction) weakens the skin effect, and the skin depth is consequently increased. It is the inhomogeneous ac magnetic field that excites spin waves with wavelengths of the order of skin depth, which enhances the energy dissipated by eddy currents. This can be understood as an apparent increase of resistivity in ferromagnetic materials [29].

In addition to the role played by the exchange interactions in the electromagnetic model, the exchange-conductivity model has taken into account the factor of the exchange stiffness [28]. As a result, when the exchange term is incorporated into the effective magnetic field H_{eff}, Eqs. (4.8) and (4.9) must be solved simultaneously. Using the simplified solution to Eqs. (4.10) and (4.11), the exchange-conductivity models have shown that, when the damping is neglected ($\alpha = 0$), the skin depth reaches its minimum value [19, 28]

$$\delta_{\min} = \left(\frac{A\rho}{\omega\mu^2 M_s^2}\right)^{1/4}, \tag{4.17}$$

when ω is less than the characteristic frequency

$$\omega_c = \frac{4\alpha^2\gamma^2 A M_s}{\rho}, \tag{4.18}$$

where A is the exchange stiffness constant. ω_c is evaluated to be about 100 MHz for soft magnetic amorphous materials. At low and intermediate frequencies ($\omega < \omega_c$), the calculated maximum GMI scales as $\omega^{1/4}$. Above the characteristic frequency ($\omega \geq \omega_c$), the GMI is calculated using Eq. (4.17). While the exchange-conductivity effect was generally considered to be important only at high frequencies, with the related model valid in the corresponding high frequency range, Ménard et al. [28] have shown that this effect is actually most important at low frequencies. It has been argued that the exchange-conductivity effect puts a fundamental limit on the maximum impedance of a magnetic conductor, particularly at low frequency. This can be clearly shown in Fig. 4.7, in which the exchange-conductivity model describes the magnetic field dependence of R/R_{dc} well at a high frequency of 5 GHz but failed to reproduce the experimental results precisely at lower frequencies (<10 MHz). In all these cases, a significant deviation between the experiment and theory has been found in low magnetic field ranges.

In general, the exchange-conductivity model allows the qualitative interpretation of the frequency and magnetic field dependences of GMI in a wider range of frequencies than the electromagnetic models. However, none of these approaches deals satisfactorily with the problem of GMI as a whole, arising from the complex

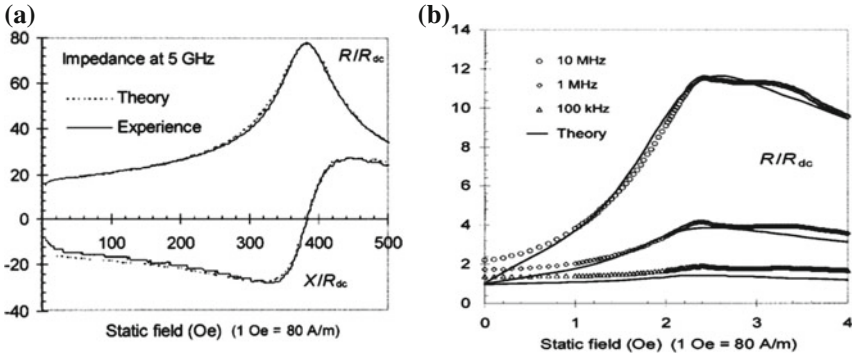

Fig. 4.7 **a** A comparison of the theoretical and experimental real (R/R_{dc}) and imaginary (X/R_{dc}) parts of the impedance of an ideal anisotropic magnetic wire at $f = 5$ GHz. **b** A comparison of the theoretical and experimental R/R_{dc} of the same wire at different frequencies $f = 100$ kHz, 1 and 10 MHz (reprinted with permission from AIP [28])

domain structures of actual magnetic materials [18] given the underlying approximating assumptions [27, 28]. The theoretical limits of GMI have been pointed out by Kraus [32], revealing the complex nature of the GMI phenomena.

4.4.6 Other Models

In addition to the models discussed above, other theoretical models have also been proposed to address various issues [33–38], such as the energy conservation of the GMI effect [39], the validity of the relationship between GMI and FMR at low frequency range [29, 40], and the unusual GMI features observed in composite wires which are composed of a non-magnetic conductive wire coated with a ferromagnetic layer [18, 36]. However, a good agreement between the experiment and theory has been obtained either in a narrow frequency range or in high dc field ranges, and for the specific cases of the studied ferromagnetic materials [33–38]. For the case of amorphous magnetic wires subject to current/field annealing and applied stress, the domain structures of the wires are strongly modified, and these models fail to reproduce the experimentally obtained results [35, 37, 38]. Most recently, Kaya has proposed that it is possible to predict the GMI effect in glass-coated amorphous microwires using the so-called artificial neural network [41]. While the authors claimed that this model had a $\sim$99 % correlation with experimental data, it remains unclear how the experimental parameters were incorporated into the model, and how the model could even reproduce variations in the experimental data points in the GMI profiles. Further study is needed to clarify this.

4.5 Concluding Remarks

In terms of the above analyses, it is concluded that the quasi-static model is most appropriate for explaining GMI features in the low frequency range ($f \leq 1$ MHz). Meanwhile, the skin effect and domain models have been most commonly used to explain the GMI features in the intermediate frequency range (1 MHz $\leq f <$ 1 GHz). In the high frequency range (1 GHz $\leq f$), the GMI features have been well understood within the framework of the electromagnetic and exchange-conductivity models.

The theory of GMI may be understood to a reasonable degree; however, more research is needed to fully understand the theory. The finding of a new model that can explain all GMI features in the whole frequency range is still challenging. It is believed that, to assess the underlying mechanism of GMI for a variety of materials, further theoretical models must be developed on the basis of the identified domain structures of the materials. It should be noted that the formation of characteristic domain structures of GMI materials is mainly related to the preparation process.

References

1. Cullity BD (1972) Introduction to magnetic materials. Addision-Wesley, Reading
2. Jiles D (1998) Introduction to magnetism and magnetic materials, 2nd edn. Chapman and Hall, London
3. Panina LV, Mohri K (1994) Magneto-impedance effect in amorphous wires. Appl Phys Lett 65:1189–1191
4. Beach RS, Berkowitz AE (1994) Giant magnetic field dependent impedance of amorphous FeCoSiB wire. Appl Phys Lett 64:3652–3654
5. Beach RS, Berkowitz AE (1994) Sensitive field- and frequency-dependent impedance spectra of amorphous FeCoSiB wire and ribbon. J Appl Phys 76:6209–6213
6. Panina LV, Mohri K, Uchiyama T, Noda M (1995) Giant magneto-impedance in Co-rich amorphous wires and films. IEEE Trans Magn 31:1249–1260
7. Landau LD, Lifshitz EM (1975) Electrodynamics of continuous media. Pergamon Press, Oxford
8. Menard D, Britel M, Ciureanu P, Yelon A (1998) Giant magnetoimpedance in a cylindrical magnetic conductor. J Appl Phys 84:2805–2814
9. Kraus L (1999) Theory of giant magneto-impedance in the planar conductor with uniaxial magnetic anisotropy. J Magn Magn Mater 195:764–778
10. Machado FLA, Rezende SM (1996) A theoretical model for the giant magnetoimpedance in ribbons of amorphous soft-ferromagnetic alloys. J Appl Phys 79:6558–6560
11. Yelon A, Menard D, Brittel M, Ciureanu P (1996) Calculations of giant magnetoimpedance and of ferromagnetic resonance response are rigorously equivalent. Appl Phys Lett 69: 3084–3085
12. Atkinson D, Squire PT (1998) Phenonemological model for magnetoimpedance in soft ferromagnet. J Appl Phys 83:6569–6571
13. Chen DX, Munoz JL, Hernando A, Vazquez M (1998) Magnetoimpedance of metallic ferromagnetic wires. Phys Rev B 57:10699–10704
14. Betancourt I, Valenzuela R, Vazquez M (2003) Domain model for the magnetoimpedance of metallic ferromagnetic wires. J Appl Phys 93:8110–8112

15. Knobel M, Sanchez ML, Gomez-Polo C, Marin P, Vazquez M, Hernando A (1996) Giant magneto-impedance effect in nanostructured magnetic wires. J Appl Phys 79:1646–1648
16. Devkota J, Ruiz A, Mukherjee P, Srikanth H, Phan MH (2013) Magneto-resistance, magneto-reactance, magneto-impedance effects in single and multi-wire systems. J Alloy Compd 549:295
17. Mohri K, Kohsawa T, Kawashima K, Yoshida H, Panina LV (1992) Magneto-inductive effect (MI effect) in amorphous wires. IEEE Trans Magn 28:3150–3152
18. Phan MH, Peng HX (2008) Giant magnetoimpedance materials: fundamentals and applications. Prog Mater Sci 53:323–420
19. Kraus L (2003) GMI modeling and material optimization. Sens Actuators Phys A 106:187–194
20. Brittel MR, Menard D, Melo LGC, Ciureanu P, Yelon A, Cochrane CW, Rouabhi M, Cornut B (2000) Magnetoimpedance measurements of ferromagnetic resonance and antiresonance. Appl Phys Lett 77:2737–2739
21. Chen DX, Munoz JL (1999) AC impedance and circular permeability of slab and cylinder. IEEE Trans Magn 35:1906–1923
22. Kim CG, Yoon SS, Yu SC (2000) Decomposition of susceptibility spectra in a torsion-stressed Fe-based amorphous wire. Appl Phys Lett 76:3463–3465
23. Yoon SS, Kim CG (2001) Separation of reversible domain-wall motion and magnetization rotation components in susceptibility spectra of amorphous magnetic materials. Appl Phys Lett 78:3280–3282
24. Carara M, Baibich MN, Sommer RL (2000) Magnetization dynamics as derived from magneto impedance measurements. J Appl Phys 88:331–335
25. Buttino G, Cecchetti A, Poppi M (2004) Domain wall relaxation frequency and magnetocrystalline anisotropy in Co- and Fe-based nanostructured alloys. J Magn Magn Mater 269:70–77
26. Knobel M, Vazquez M, Kraus L (2003) Giant magnetoimpedance (Chap 5). In: Buschow KH (ed.) Handbook of magnetic materials, vol 15. Elsevier Science B.V., Amsterdam, pp 1–69
27. Ménard D, Yelon A (2000) Theory of longitudinal magnetoimpedance in wires. J Appl Phys 88:379–393
28. Ménard D, Melo LGC, Brittel MR, Ciureanu P, Yelon A, Rouabhi M, Cochrane CW (2000) Modeling the magnetoimpedance in anisotropic wires. J Appl Phys 87:4801–4803
29. Ciureanu P, Melo LGC, Seddaoui D, Ménard D, Yelon A (2007) Physical models of magnetoimpedance. J Appl Phys 102:073908
30. Machado FLA, de Araujo AEP, Puca AA, Rodrigues A, Rezende SM (1999) Surface magnetoimpedance measurements in soft-ferromagnetic materials. Phys Status Solidi A 173:135–144
31. Patton CE (1976) Classical theory of spin-wave dispersion for ferromagnetic metals. Czech J Phys 26:925–935
32. Kraus L (1999) The theoretical limits of giant magnetoimpedance. J Magn Magn Mater 196–197:354–356
33. Tatara G (2001) Theory of electron scattering by domain wall in nano-wires. J Magn Magn Mater 226–230:1873–1874
34. Gomez-Polo C, Knobel M, Pirota KR, Vazquez M (2001) Giant magnetoimpedance modelling using Fourier analysis in soft magnetic amorphous wires. Phys B 299:322–328
35. Usov NA, Gudoshnikov SA (2013) Giant magneto-impedance effect in amorphous ferromagnetic wire with a weak helical anisotropy: theory and experiment. J Appl Phys 113:243902
36. Betzholz R, Gao H, Zhao Z, Hartmann U (2013) Phenomenological theory of the giant magnetoimpedance of composite wires. EPL 101:17005
37. Buznikov NA, Yoon SS, Kim CG, Kim CO (2006) A model for exchange-biased asymmetric giant magneto-impedance in amorphous wires. J Phys D Appl Phys 39:3525

38. Buznikov NA, Antonov AS, Rakhmanov AA (2011) A model for torsion-stress effect on nonlinear magnetoimpedance in amorphous wires with negative magnetostriction. J Magn Magn Mater 323:190
39. Dong C, Chen S, Hsu TY (2002) A simple model of giant magneto-impedance effect in amorphous thin films. J Magn Magn Mater 250:288–294
40. Lofland SE, Baghat SM, Dominguez M, Garciabeneytez JM, Guerrero F, Vazquez M (1999) Low-field microwave magnetoimpedance in amorphous microwires. J Appl Phys 85: 4442–4444
41. Ayten Kaya A (2013) Prediction of giant magnetoimpedance effect in amorphous glass-coated micro-wires using artificial neural network. J Inequalities Appl 2013:216

Chapter 5
Influence of Measurement Parameters on Giant Magnetoimpedance

In this chapter, the influences of the measurement parameters (e.g. alternating current, dc magnetic field, frequency, and temperature) on giant magnetoimpedance (GMI) have been systematically analysed and clarified. This ensures the selection of optimal conditions for designing high-performance GMI-based sensors.

5.1 Alternating Current Amplitude

When a magnetic wire is subjected to a GMI experiment (Fig. 4.4), a circular magnetisation process takes place in it due to the ac circular magnetic field created by an alternating current (I_{ac}). Any change in I_{ac} will result in a change in the circular permeability (μ_ϕ) and hence the ac impedance, Z. This points to a dependence of the impedance on the current; the higher the current amplitude, the larger the expected value of the impedance. It has been theoretically predicted that for a double-peak (DP) profile of GMI in ferromagnetic amorphous wires, the magnetic field (H_K) at which the value of Z reaches a maximum should decrease as the amplitude of the ac current is increased [1]. This hypothesis has been experimentally confirmed (see Fig. 5.1, for example, for a Co-based amorphous wire), where GMI curves are found to exhibit a DP behaviour for low-amplitude currents where only reversible wall motion takes place, but only a single peak (SP) is observed at high amplitudes corresponding to circular coercivity [2].

Through investigating the dependence of GMI on ac in different materials (e.g. amorphous microwires/wires, nanocrystalline ribbons), Aragoneses et al. [3] found the variation of the GMI effect with current amplitude to be material-dependent. For an amorphous $Co_{68.5}Mn_{6.5}Si_{10}B_{15}$ microwire, when I_{ac} was increased the GMI effect increased until $I_{ac} = 2.8$ mA and then decreased at higher values of I_{ac}. This is consistent with the behaviour of an $(Fe_6Co_{94})_{72.5}Si_{12.5}B_{15}$ amorphous wire, where the maximum GMI effect was achieved for $I_{ac} = 4$ mA, as I_{ac} was varied from 2 to 7 mA [4]. With increasing I_{ac}, however, the GMI effect decreased gradually for an

H.-X. Peng et al., *Ferromagnetic Microwire Composites*,
Engineering Materials and Processes, DOI 10.1007/978-3-319-29276-2_5

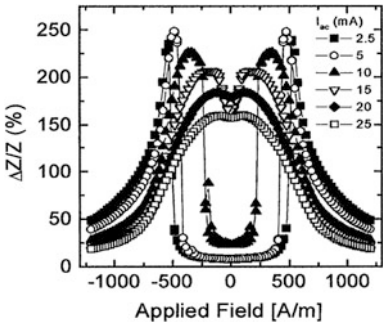

Fig. 5.1 Magnetic field dependence of the GMI ratio ($\Delta Z/Z$) at different alternating current amplitudes (I_{ac}) for a Co-based amorphous wire with an induced circular anisotropy. An evolution from the DP to SP feature with increasing amplitude has been observed (reproduced with permission from Elsevier [2])

$(Fe_{0.94}Co_{0.06})_{72.5}B_{15}Si_{12.5}$ amorphous wire, while it sharply increased for a $Fe_{73.5}Si_{13.5}B_9Nb_3Cu_1$ nanocrystalline ribbon [3]. In these examples, the observed effect of driving current could be explained by consideration of the tensor character of the magnetic permeability and was ascribed to the components of that tensor which are responsible for the transverse magnetic anisotropy [5]. The different dependences of GMI on driving alternating current can also be caused by the difference in the domain structures of the investigated samples. It is worth noting that there is an inhomogeneous distribution of local critical magnetic fields at low-amplitude currents, causing the "spike" feature in GMI profiles or the instability of the GMI signal. Increasing the amplitude has been shown to greatly improve the stability of the GMI signal [6]. It is therefore important to select an appropriate range of current amplitudes for the design and operation of actual GMI sensor devices.

5.2 Magnetic Field

In a typical GMI experiment, the dc magnetic field is usually applied so as to be collinear with the alternating current along the longitudinal direction of the wire (Fig. 4.4). This configuration yields the longitudinal GMI effect. As discussed previously in Chap. 4, at a given frequency, the application of a dc magnetic field (H_{dc}) changes the circular permeability (μ_ϕ) and hence the magnetic penetration depth (δ_m), which in turn alters the impedance Z until the value of δ_m reaches the radius of the wire (t). In a magnetic amorphous wire with a circular domain structure, H_{dc} may compensate the circular magnetic anisotropy field (H_k) as its magnitude becomes similar [2, 7]. For $H_{dc} \cong H_k$, the quasi-free magnetisation responds quickly to the external oscillating magnetic field, giving rise to the maximum circular permeability. When the applied dc magnetic field exceeds the

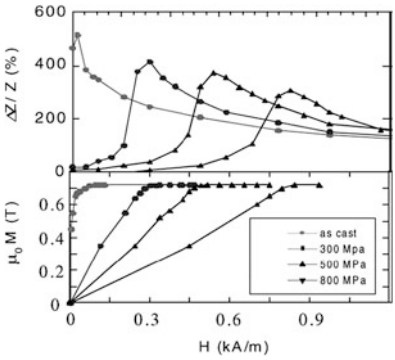

Fig. 5.2 Magnetic field dependence of the GMI ratio and axial magnetisation curves for a stress-annealed Co-based wire (different tensile stresses were applied during annealing). This shows a correlation between the maximum GMI values and circular anisotropy fields (reproduced with permission from Elsevier [2])

circular magnetic anisotropy field ($H_{dc} > H_k$), the circular permeability is decreased due to the unidirectional magnetostatic anisotropy caused by H_{dc}. In this case, the skin depth increases, which corresponds to the decrease of the impedance of the wire as the dc magnetic field is increased. Since the value of the anisotropy field is actually very small in magnetic wires in which the magnetostriction constant is near zero, the maximum value of GMI is observed at nearly zero field for low frequencies [8]. As a result, the GMI profile shows an SP behaviour centred around zero field. At higher frequencies, however, GMI profiles will show a DP feature. Such SP and DP features of GMI are often determined by the relative contribution from domain wall motion and magnetisation rotation processes to the circular permeability [9–11]. Complex domain structures and distribution of local anisotropies in actual materials can also influence the dependence of GMI on the dc magnetic field [12].

When studying the effects of tensile stress on the dc magnetisation and GMI of a Co-based wire, Vazquez has demonstrated the existence of a correlation between the circular magnetic anisotropy field and the GMI peak [2]. As can be clearly seen in Fig. 5.2, the GMI magnitude and the circular anisotropy field decrease as the applied stress is increased. The magnetic field at which the GMI peak is observed consistently corresponds to the circular magnetic anisotropy field determined from the magnetisation data and this field increases with an increase in the applied stress.

5.3 Measurement Frequency

According to the theory (Chap. 4), GMI and its behaviour depend strongly on the measurement frequency. Indeed, the frequency-dependent GMI features have been experimentally studied in a wide range of frequencies up to GHz in different

materials [12]. It has been shown that, with increasing frequency, the magnetisation process via domain wall displacement relaxes at relatively low frequencies ranging between 0.1 and 1 MHz in amorphous wires [13]. For amorphous glass-covered microwires, the permeability spectra showed dispersion laws at higher frequencies [14]. It is generally accepted that at low frequencies $f \ll f_o$—a characteristic frequency or the frequency at which the maximum GMI value is obtained ($a < \delta_m$), the maximum value of GMI, $[\Delta Z/Z(\%)]_{\max}$, is found to be relatively low due to the contribution of the induced magnetoinductive voltage to magnetoimpedance [15]. In this case, GMI features can be well interpreted on the basis of the quasi-static models, as discussed in Chap. 4. As $f \sim f_o$ ($a \approx \delta_m$), the skin effect is dominant, and a higher $[\Delta Z/Z(\%)]_{\max}$ is found. Beyond $f \geq f_o$, $[\Delta Z/Z(\%)]_{\max}$ decreases with increasing frequency. It is believed that, in this frequency region, the domain wall displacement is strongly damped by eddy currents, thus contributing less to the circular permeability, i.e. a small $[\Delta Z/Z(\%)]_{\max}$. A typical example of this dependence is shown in Fig. 4.6b. We should note here that the magnetoimpedance is increasing as the frequency increases because the impedance is proportional to $(\omega\mu_\phi)^{1/2}$ even in the case of decreasing circular permeability at high frequencies. Despite this, f_o depends strongly on the dimensions of the samples. It has been found that, for amorphous microwires, GMI usually reaches its maximum value at higher frequencies than those for amorphous wires [16]. The eddy current and domain models are valid for interpreting basic GMI features in the frequency range of 0.1–100 MHz, as discussed in Chap. 4. At higher frequencies, where ferromagnetic resonance can occur, such GMI features were successfully explained by the electromagnetic and exchange-conductivity models [17]. Furthermore, with increasing frequency, the low-frequency SP behaviour may become DP-like as a consequence of the frequency dependence of circular permeability [2].

From a fundamental research viewpoint, it is essential to understand the frequency dependences of the real and imaginary parts of impedance and their contributions to the GMI effect. Figure 5.3 shows, for example, the frequency dependences of the maximum MR, MX, and MI ratios for a glass-coated amorphous microwire. It is generally thought that the MX contribution to the MI ratio is dominant at the low-frequency range, while the main contribution to the MI in the high-frequency range can be attributed to the MR. As one can see in Fig. 5.3, however, the frequency dependence of MI follows that of MR, suggesting the dominant contribution of MR to the MI for the case of this microwire throughout the investigated frequency range.

From an experimental point of view, we should note that most GMI measurements are performed at measuring frequencies up to 10 MHz only, due to the fact that, in this frequency range, standard voltage–current measurement techniques can be easily employed to directly probe the transport properties of the sample. At higher frequencies, both voltage and current are not always well defined quantitatively and the classic measurement technique fails. To overcome this problem, another technique based on the S-parameter measurement of a transmission line section by means of an automatic vectorial network analyser has been exploited to measure the GMI effect in the microwave region in soft amorphous ferromagnetic samples [18].

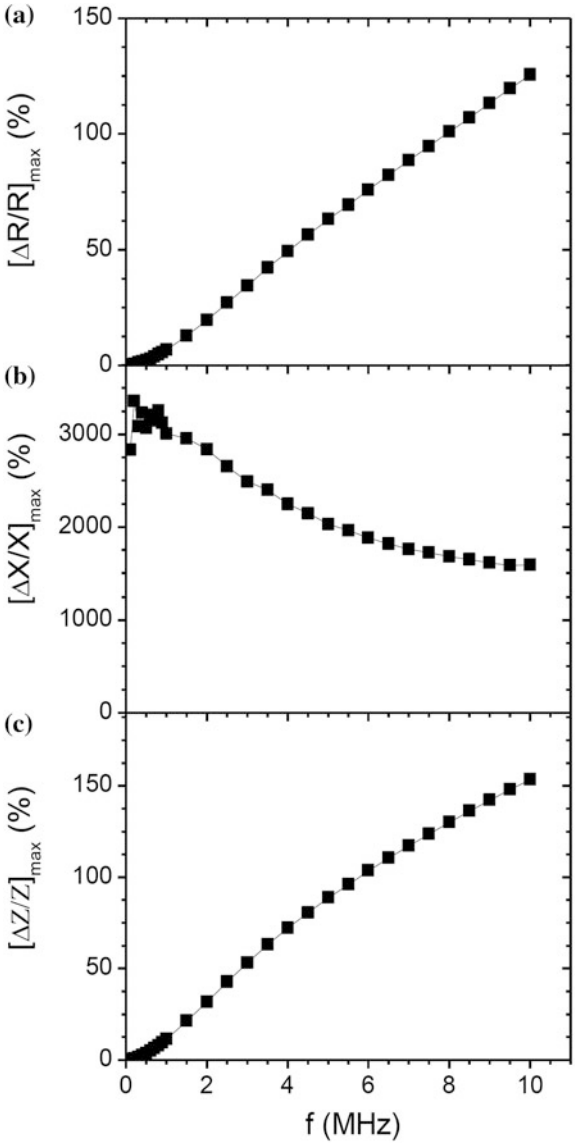

Fig. 5.3 Frequency dependence of the maximum magnetoresistance (*MR*), magnetoreactance (*MX*), and magnetoimpedance (*MI*) ratios of soft ferromagnetic amorphous glass-coated $Co_{68}B_{15}Si_{10}Mn_7$ microwire

5.4 Measurement Temperature

A thorough knowledge of the measurement temperature dependence of GMI is important and necessary from both the fundamental and practical points of view. A number of works have investigated the influence of the measurement temperature on GMI in magnetic amorphous wires [19–23]. It is now accepted that the GMI

effect increases with temperature and reaches a maximum value near the Curie temperature of the material, and then decreases at higher temperatures [19, 21, 23]. The initial increase of GMI with temperature is attributed to the rise in circular permeability resulting from the enhanced circular motion of magnetic moments which are frozen at low temperature. It is believed that the magnetic coupling between magnetic moments at a low temperature is larger than that at a high temperature. The maximum of GMI is achieved close to the Curie temperature because the largest value of circular permeability is achieved at this temperature. It has been reported that the magnitude of GMI of an amorphous $Co_{68.15}Fe_{4.35}Si_{12.5}B_{15}$ wire measured at 300 K ($\sim T_C$) was about two times larger than that measured at 100 K [19]. At temperatures above the Curie point, the observed decrease of GMI is ascribed to the collapse of the magnetic coupling in the material [21].

Figure 5.4 shows the results of a study of the effects of three consecutive sweeps in temperature from 80 to 400 K for an amorphous $Co_{68.15}Fe_{4.35}Si_{12.5}B_{15}$ wire with a diameter of 130 μm, which was prepared using the in-rotating water quenching technique [19]. It is worth noting that there is a significant reduction in the GMI magnitude as well as a displacement of the GMI maximum in temperature. It has been suggested that in the first sweep a slight increase of the temperature determines a reversible relaxation of internal stresses induced during rapid solidification, which results in a slight reduction of the circular anisotropy and hence an improvement of the magnetic softness of the wire without alternating its specific circular magnetic structure [19]. Once the first temperature sweep is completed, stress annealing and atomic diffusion are believed to manifest in the wire when passing the Curie temperature. These processes last until thermal equilibrium is re-established in the wire at room temperature. This sets in a new temperature for the GMI maximum and a new temperature maximum of the circular permeability, which are observed in the subsequent temperature sweep. Magnetic hysteresis measurements were conducted around the Curie temperature after each sweep to determine whether the effects of temperature processes on the static magnetic properties are significant. As one can see in Fig. 5.4b, changes in the M–H loops are not very large, unlike the

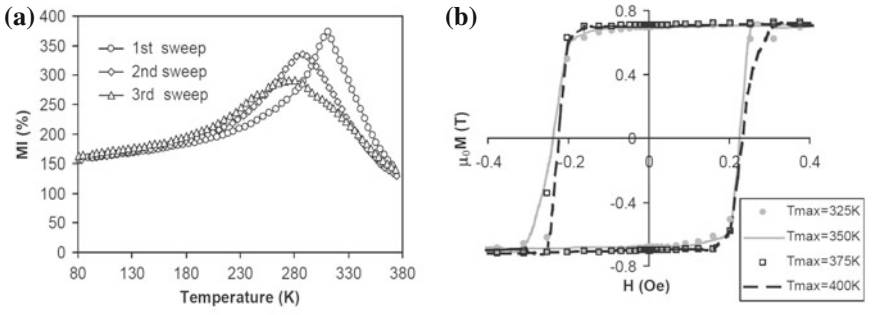

Fig. 5.4 **a** Temperature dependence of the MI ratio of an amorphous $Co_{68.15}Fe_{4.35}Si_{12.5}B_{15}$ wire for three consecutive temperature sweeps. **b** Hysteresis loops after temperature processing (reproduced with permission from Elsevier [19])

GMI data obtained at the corresponding temperatures. However, we should note that the data obtained from a VSM reflect the bulk magnetic property of the wire, while the GMI profile provides near-surface magnetic information.

5.5 Concluding Remarks

Because the measurement parameters (alternating current, dc magnetic field, and frequency) directly affect the measured value of GMI, the selection of appropriate parameters becomes extremely important in designing practical GMI sensors. Depending upon the different kinds of GMI materials, the amplitude of an applied alternating current should be large or small. Similarly, the maximum dc magnetic field applied to saturate the magnetoimpedance varies among GMI materials. However, for practical uses, the amplitude of the applied current and the maximum dc magnetic field should be as small as possible. Furthermore, because of the magnitude of GMI and the way in which its sensitivity varies strongly with measurement frequency, it is necessary to select the working frequency range for a certain material. At relatively low frequencies such as these, it should be noted that the SP behaviour of GMI is often observed and this is usually useful for practical applications. In contrast, the DP behaviour of GMI observed in the high-frequency range is not desirable. However, such a symmetrical feature in low-field GMI profiles can be tailored for developing a new class of linear field sensors. Finally, it is worth noting that a sensor based on the GMI effect has an increasing sensitivity at room temperature because the Curie temperatures of GMI materials are well above 300 K, whereas the field sensitivity of a magnetic sensor based on the giant magnetoresistance (GMR) effect in thin films and in perovskite-like structured materials is drastically reduced at room temperature. Therefore, for practical use, GMI-based sensors are more promising than the GMR sensors.

References

1. Chen DX, Munoz JL, Hernando A, Vazquez M (1998) Magnetoimpedance of metallic ferromagnetic wires. Phys Rev B 57:10699–10704
2. Vazquez M (2001) Giant magnetoimpedance in soft magnetic “wires”. J Magn Magn Mater 226–230:693–699
3. Aragoneses P, Zhukov A, Gonzalez J, Blanco JM, Dominguez L (2000) Effect of AC driving current on magneto-impedance effect. Sen Act A 81:86–90
4. Pal SK, Manik NB, Mitra A (2006) Dependence of frequency and amplitude of the ac current on the GMI properties of Co based amorphous wires. Mater Sci Eng A 415:195–201
5. Chen AP, Britel MR, Zhukova V, Zhukov A, Dominguez L, Chizhik AB, Blanco JM, González J (2004) Influence of AC magnetic field amplitude on the surface magnetoimpedance tensor in amorphous wire with helical magnetic anisotropy. IEEE Trans Magn 40:3368–3377

6. Sun J-F, Liu J-S, Xing D-W, Xue X (2011) Experimental study on the effect of alternating-current amplitude on GMI output stability of Co-based amorphous wires. Phys Status Solidi A 208(4):910–914
7. Mandal K, Pan Mandal S, Vazquez M, Puerta S, Hernando A (2002) Giant magnetoimpedance effect in a positive magnetostrictive glass-coated amorphous microwire. Phys Rev B 65:064402, 1–6
8. Devkota J, Ruiz A, Mukherjee P, Srikanth H, Phan MH (2013) Magneto-resistance, magneto-reactance, magneto-impedance effects in single and multi-wire systems. J Alloy Compd 549:295
9. Usov NA, Gudoshnikov SA (2013) Giant magneto-impedance effect in amorphous ferromagnetic wire with a weak helical anisotropy: theory and experiment. J Appl Phys 113:243902
10. Lachowicz HK, Garcia KL, Kuzminski M, Zhukov A, Vazquez M (2005) Skin-effect and circumferential permeability in micro-wires utilized in GMI-sensors. Sens Act A 119:384–389
11. Pirota KR, Kraus L, Chiriac H, Knobel M (2000) Magnetic properties and giant magnetoimpedance in a CoFeSiB glass-covered microwire. J Magn Magn Mater 221: L243–L247
12. Phan MH, Peng HX (2008) Giant magnetoimpedance materials: fundamentals and applications. Prog Mater Sci 53:323–420
13. Kim CG, Yoon SS, Yu SC (2000) Decomposition of susceptibility spectra in a torsion-stressed Fe-based amorphous wire. Appl Phys Lett 76:3463–3465
14. Zhukov A, González J, Vázquez M, Larin V, Torcunov A (2004) Nanocrystalline and amorphous magnetic microwires. In: Nalwa HS (ed) Encyclopedia of nanoscience and nanotechnology, vol 23, Chap. 62. American Scientific Publishers, pp 1–22
15. Mohri K, Kohsawa T, Kawashima K, Yoshida H, Panina LV (1992) Magneto-inductive effect (MI effect) in amorphous wires. IEEE Trans Magn 28:3150–3152
16. Chiriac H, Ovari TA (1996) Amorphous glass-covered magnetic wires: preparation, properties, applications. Prog Mater Sci 40:333–407
17. Ciureanu P, Melo LGC, Seddaoui D, Ménard D, Yelon A (2007) Physical models of magnetoimpedance. J Appl Phys 102:073908
18. Zhukov A, Zhukova V, Blanco JM, Gonzalez J (2005) Recent research on magnetic properties of glass-coated microwires. J Magn Magn Mater 294(2):182–192
19. Chiriac H, Marinescu CS, Ovari TA (1999) Temperature dependence of the magneto-impedance effect. J Magn Magn Mater 196–197:162–163
20. Rakhmanov AA, Perov N, Sheverdyaeva P, Granovsky A, Antonov AS (2003) The temperature dependence of the magneto-impedance effect in the Co-based amorphous wires. Sens Actuators A 106:240–242
21. Hernando B, Olivera J, Sánchez ML, Prida VM, Varga R (2008) Temperature dependence of magnetoimpedance and anisotropy in nanocrystalline finemet wire. IEEE Trans Magn 44:3965
22. Wang XD, Liu JS, Xing DW, Chen DM, Wang H, Sun JF (2013) Thermal stability of giant magneto-impedance effect in glass-covered amorphous wires. Phys Procedia 48:152–159
23. Liu J-S, Sun J-F, Xing D-W, Xue X (2012) Twin-detector sensor of Co-rich amorphous microwires to overcome GMI fluctuation induced by ambient temperature. IEEE Trans Magn 48:2449

Chapter 6
Influence of Processing Parameters on GMI

The influences of the processing parameters, e.g. glass coating, sample geometry, heat treatment, stresses, neutron irradiation, hydrogen charging, magnetostriction, and after-effect, on giant magnetoimpedance are reviewed and discussed in this chapter.

6.1 Effect of Glass Coating on GMI

The influence of a glass coating on the domain structure and magnetic properties of amorphous wires has been discussed in [1–5]. This section will focus on describing the influence of the glass coating on the GMI profile in amorphous and nanocrystalline wires. The effects of removing the glass coating on the GMI profile are also discussed.

6.1.1 Amorphous Wires

Figure 6.1 shows the magnetic field dependence of the GMI profile measured at different frequencies, for nearly zero magnetostrictive Co-based amorphous microwires (a) before and (b) after glass removal.

As is shown in Fig. 6.1, over the entire measured frequency range, the GMI effect decreased considerably for the microwire after glass removal. This is likely to be a consequence of the glass removal causing a reduction of circumferential permeability in the microwire and hence a reduction of the GMI effect [6–8]. At low frequencies ($f = 0.1$–1 MHz), the GMI effect is obtained in the glass-covered sample (see Fig. 6.1a), but not in the glass-removed sample (see Fig. 6.1b). This is somewhat different to what is reported in [2], where no GMI effect was observed in either

H.-X. Peng et al., *Ferromagnetic Microwire Composites*,
Engineering Materials and Processes, DOI 10.1007/978-3-319-29276-2_6

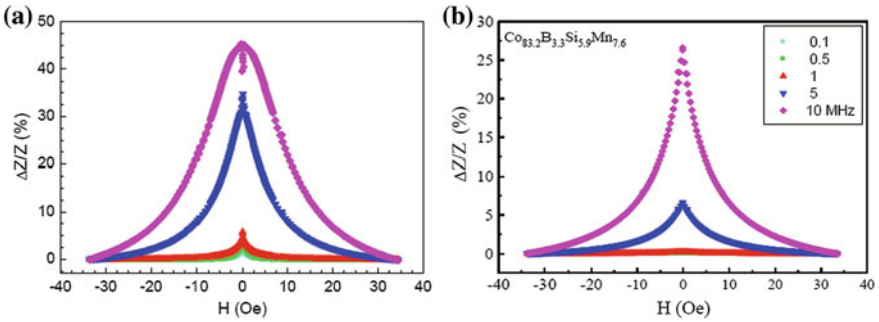

Fig. 6.1 Magnetic field dependence of GMI profile measured at different frequencies for the Co–B–Si–Mn amorphous microwire: (**a**) before and (**b**) after glass removal

glass-covered or glass-removed Co-based wires. This probably arises from the fact that, in the frequency range ($f < 1$ MHz), the circumferential permeability is relatively large and the skin effect is noticeable in the glass-covered microwire [1, 2, 5].

At higher frequencies (1 MHz < f), the GMI effect is obtained in the wire both before and after glass removal, and it increases with increasing frequency up to 10 MHz. Here, the skin effect is dominant and the magnetoimpedance is proportional to the square root of the circumferential permeability and frequency. More noticeably, at the highest frequency of 10 MHz, a DP behaviour is observed in the glass-covered microwire, while an SP behaviour remains for the glass-removed microwire. This can be understood by accounting for the less sensitive circumferential permeability of the microwire after glass removal. Concerning the different GMI features of Co-based, conventional, and glass-covered/glass-removed wires with the same composition, a detailed analysis can be found in [2]. It was shown that the largest GMI effect was obtained for the conventional wire at relatively low frequencies, but for the glass-removed wire, it was found at high frequencies due to the high value of magnetic permeability retained. The largest GMI effect was achieved in the glass-covered wire only in a relatively narrow and intermediate frequency range (f = 4–6 MHz) [2]. Furthermore, it has been shown that the thicker the glass coating, the larger the stress and the higher the level of induced circumferential anisotropy. Therefore, the magnetic field at which the GMI peak is observed reduces with the thickness of glass coating applied [6–8]. In fact, the coating not only changes the anisotropy distribution, but also reduces the magnitude of the magnetic permeability. Consequently, the GMI effect is smaller for a wire with a thicker glass coating.

In the case of positive magnetostrictive glass-covered amorphous wires/microwires (e.g. Fe-based amorphous glass-covered alloys), a relatively small MI effect was observed [2, 5, 9, 10]. For instance, a small MI effect ($\sim$1 %) was obtained in the Fe-based glass-covered amorphous wire, which was attributed to the high positive magnetostriction of the sample ($\lambda \sim 25 \times 10^{-6}$) that led to a domain structure with an axially magnetised inner core and radically magnetised outer shell through magnetomechanical coupling with internal stresses. After the glass

covering was removed, a higher MI effect (∼5 %) was achieved [10]. This was attributed to the stress relief caused by the glass removal [2, 5]. Such different behaviours of GMI observed in Co-based and Fe-based amorphous wires can be understood through the difference in their domain structure determined by the sign of magnetostriction of the sample.

6.1.2 Nanocrystalline Wires

Many previous investigations have reported on the influence of the glass coating on the GMI profile in nanostructured wires/microwires [9–12]. Such nanostructured wires (or nanocrystalline magnetic wires) were usually obtained by proper annealing of their precursor as-cast amorphous wires. Both Co-based negative and Fe-based positive magnetostrictive nanostructured wires were investigated [10, 12], with much attention being paid to an Fe-based nanostructured wire, where a much improved GMI effect was obtained after glass removal [9]. For example, the GMI ratio of the FeSiBCuNb nanostructured wire reached a value of about 28 % after glass removal [10], which is much larger than that of the glass-covered sample (∼5 %). Because the Fe-based nanostructured wires without a glass cover are magnetically softer than the glass-covered ones, a much more sensitive GMI response was observed in these samples [9, 10]. Furthermore, it was found that the GMI ratio of the FeSiBCuNb nanocrystalline wire without glass covering was even larger than that of CoFeSiB amorphous wires after glass removal (∼20 %), because of the fact that the Fe-based nanocrystalline wire without glass covering was magnetically softer due to its vanishing magnetostriction [10]. Another feature to be noted is that the frequency at which the maximum GMI value was obtained was often lower in Fe-based nanocrystalline wires without glass covering than in both Fe-based nanocrystalline wires with glass covering and Co-based amorphous wires without glass covering [5, 10]. This probably results from the lowest value of resistivity observed in the Fe-based nanocrystalline wire without a glass covering [9]. These results indicate that the Fe-based nanocrystalline wires with glass covering removed can be competitive candidate materials for high-performance sensor applications.

6.2 Effect of Sample Geometry on GMI

6.2.1 Sample Length

The influence of the sample length on the magnetisation processes and GMI effect has been investigated [13–17]. It was found that the spontaneous magnetic bistability observed in a Co-based amorphous wire was lost when the sample length became less than a critical length [14, 15]. The critical length was smaller for Co-based amorphous wires than for Fe-based amorphous wires [14]. The loss of magnetic

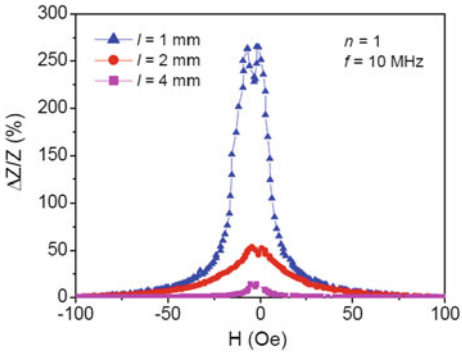

Fig. 6.2 GMI profiles measured at $f = 10$ MHz for a single microwire with varying length ($l = 1, 2, 4$ mm)

bistability can be attributed to the influence of shape anisotropy, where for short wires the demagnetising field becomes large enough to destroy the original domain structure of the sample. In a recent work, Vazquez et al. [15] analysed in detail the influence of sample length on the magnetic properties (e.g. coercivity, susceptibility) and GMI of an Fe-based nanocrystalline wire. It was found that, with decreasing wire length, the coercivity increased, the susceptibility decreased, and the GMI effect consequently reduced [15]. This phenomenon has been attributed to the formation of closure domain structures near the ends of the wire due to the demagnetising field [13–17]. It was the significant modification in the domain structure near the ends of the sample that led to different GMI features with respect to the change of sample length [15, 16]. It was also found that the field sensitivity of GMI was reduced in samples where such a "border effect" was large enough [15]. However, Phan et al. [17] recently observed that the decrease of length (l) of a Co-based microwire (e.g. AGCW) resulted in a strong increase of the GMI ratio, as shown in Fig. 6.2.

It can be seen that at the highest measured frequency of 10 MHz, the GMI ratio increased from 15.5 to 268 % as the microwire length decreased from 4 to 1 mm, respectively. This can be attributed to the decrease of electrical resistance from 19.7 to 3.1 Ωm with decreasing length from 4 to 1 mm, respectively. This finding is of practical importance because it shows that the ferromagnetic microwires or composites containing these microwires are ideally suited to designing miniaturised magnetic sensing devices which are compatible with biological systems for health monitoring purposes. This difference is likely to be a result of the "border effect" being larger in the normal wire [15] than in the microwire [17]. These results suggest that such geometrical effects should be considered carefully whenever GMI results are analysed and reported.

6.2.2 *Sample Thickness*

Efforts have been made to investigate the influence of sample thickness on the GMI effect in different materials, including amorphous wires [18–20], layered and

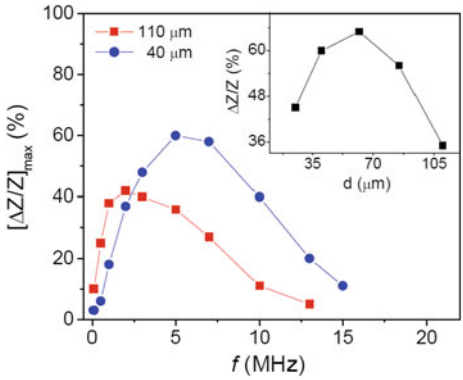

Fig. 6.3 Frequency dependence of the maximum GMI effect $[\Delta Z/Z]_{max}$ for CoFeSiB wires with different diameters. The inset shows the change of the GMI effect ($\Delta Z/Z$) with the wire diameter, measured at $f = 5$ MHz

multilayered films [21–24], amorphous ribbons [25–27], and layered composite wires [28–31]. A typical example of the wire diameter dependence of the GMI effect is displayed in Fig. 6.3. It can be seen that the largest GMI value was obtained in samples with an optimal diameter [18–20]. Due to the skin effect, the maximum value of GMI shifted to a lower frequency for the thicker wire [18]. It is the transformation of the longitudinal domain structure in the inner core of hard-drawn wires to a circular domain structure that results in the increase of the GMI effect in hard-drawn wires [19]. Both circumferential and longitudinal axial anisotropies depend on the radial distance of the wire [18, 20], and this in turn causes the wire diameter-dependent GMI features [28, 31].

Similar behaviours were also observed in layered and multilayered films [21, 22, 24] and amorphous ribbons [25–27]. The GMI ratio increased with increasing the thickness of the conducting spacer layer (Cu or Ag) [21, 22]. When the film width was less than a critical value, which depends on the transverse permeability and the layer thickness, the flux leakage through the conductive layer resulted in a considerable drop in the GMI ratio [22]. With increasing film thickness, a variation from an SP feature to a DP one occurred [5]. This was attributed to the different anisotropy axes induced by the strain in the multilayers [22].

6.2.3 *Sample Surface*

It has been shown that, in the case of a large skin effect, the surface roughness becomes important [1, 2, 5]. This is not only because the skin depth may become smaller than the surface irregularities, but also due to stray fields, which appear on

the rough surface and cause a considerable reduction in the GMI magnitude. Indeed, the GMI effect was significantly improved in chemically thinned and polished magnetic amorphous ribbons [25], because the polishing resulted in a smoother ribbon surface, thereby reducing the effective anisotropy as well as making the sample magnetically softer.

This has been experimentally verified by Le et al. [32] when studying the GMI effect and surface morphological developments in the nanocrystalline $Fe_{73.5-x}Cr_xSi_{13.5}B_9Nb_3Au_1$ (x = 1–5) ribbons. Herein, the surface morphology of these samples was studied by atomic force microscopy (AFM). It was found that the GMI ratio reached a maximum in the sample with the smallest surface roughness (see Fig. 6.3). The GMI ratio strongly decreased in samples with large surface roughness. Recently, Chaturvedi et al. [33] have established the correlation between magnetic softness, sample surface, and GMI in $Co_{69}Fe_{4.5}X_{1.5}Si_{10}B_{15}$ (X = Ni, Al, Cr) amorphous ribbons in the frequency (f) range of 0.1–10 MHz. The authors have found that at $f < 5$ MHz, the GMI effect and Z reach the largest values for the Al-containing sample and the smallest values for the Ni-containing sample, while an opposite trend is observed at $f > 5$ MHz. Magnetisation and atomic force microscopy (AFM) experiments reveal that the largest values of the low-frequency GMI effect and Z for the Al-containing sample result from the largest value of magnetic permeability, while the largest values of the high-frequency GMI effect and Z for the Ni-containing sample are attributed to the smallest surface roughness of this sample. These results point to the importance of the sample surface in determining high-frequency GMI behaviour. Therefore, it is recommended that for rapidly quenched magnetic ribbons and wires, the sample surfaces should be polished before they are used for making sensors. Regarding the effect of the sample surface, electrodeposited wires and films usually have higher quality surfaces than rapidly quenched wires and ribbons, and a higher GMI response is consequently achieved [5].

6.2.4 Sample Axes

The influence of the sample's axis direction on the GMI effect of Co-based amorphous ribbons and films has been studied [34, 35]. Kurlyandskaya et al. [35] investigated the angular dependence of the GMI profile for the angles $0 \leq \alpha \leq 90^0$, where α is the angle between the long side of the ribbon and the external magnetic field. The results indicated that the GMI behaviour remained stable for angles up to 30°, revealing that the field sensitivity of GMI-based magnetic sensors is not critically limited by the orientation of the applied magnetic field. However, the orientation of the applied magnetic field at larger angles ($\alpha \geq 30°$) resulted in a significant reduction in the field sensitivity of GMI and hence in the sensitivity of the GMI sensor. This warrants careful examination in the design of GMI sensors when using magnetic wires or ribbons as sensing elements.

6.3 Effect of Annealing on GMI

The GMI effect can be improved when an amorphous ferromagnetic material is subjected to proper heat treatments such as an annealing treatment. The effects of different annealing procedures on the GMI effect in amorphous magnetic wires/microwires and ribbons are discussed below.

6.3.1 Conventional Annealing

Conventional annealing is a process where samples are simply heated in an air/vacuum furnace for a given time. It has been shown that conventional annealing causes a considerable reduction in the GMI effect for Co-based amorphous wires/microwires [36] and ribbons [37] due to the fluctuation of the circumferential/transverse anisotropy in the circumferential/transverse direction of the wire/ribbon. However, it causes a drastic improvement in the GMI effect for Fe-based amorphous wires [9, 10] and ribbons [38–45], resulting from the improved magnetic softness of the samples after annealing. Conventional annealing of amorphous ribbons can relieve the quench-in strains, reduce the transverse magnetic anisotropy, and therefore reduce the GMI effect, even though the magnetic permeability is increased. Therefore, Sommer et al. [37] claimed that a high permeability did not necessarily lead to a large MI effect. However, this statement is not entirely true, since the MI effect was only studied at relatively low frequencies ($\sim$100 kHz) [37]. The situation would be different if MI measurements were carried out at higher frequencies (1–10 MHz), where higher permeability is needed for a larger MI effect [5]. Indeed, Phan et al. [46, 47] recently revealed that a suitable conventional annealing treatment (i.e. relatively low annealing temperature $\sim$300 °C and short annealing time $\sim$25 min) of Co-based amorphous ribbons resulted in a significantly improved GMI effect from $\sim$50 to $\sim$70 % in the frequency range of 1–10 MHz. Suitable annealing treatment is also believed to lead to the relief of internal stress while retaining the orientation of the magnetic moments in the transverse direction of the ribbon [47]. Furthermore, it was found that the magnetic softness (e.g. magnetic permeability, saturation magnetisation) increased and the resistivity decreased in an Fe-based amorphous wire/ribbon when subjected to proper conventional annealing [9, 10]. It is the increase in magnetic softness and the decrease in resistivity that results in the much improved GMI effect [9, 10, 42–45]. In this context, the magnetic softness may be used as a second criterion in selecting an appropriate material for GMI-based sensor applications [10]. The correlation between the microstructure and magnetic properties, including the GMI effect, in Fe-based nanocrystalline ribbons has been clarified [38]. It has been shown that the magnitude of GMI for the Fe-based nanocrystalline materials (both wires and ribbons) is comparable with that for the Co-based amorphous ones [5]. This makes them useful for practical sensor applications.

6.3.2 Field Annealing

The presence of a dc magnetic field along the sample axis during annealing (the so-called field annealing method) led to a further improvement in the GMI effect when compared to conventional annealing [37, 48–50]. For Co-based amorphous ribbons, the GMI effect was found to be significantly improved in samples subjected to transverse field annealing, while it was almost suppressed upon longitudinal field annealing [37]. A large hysteresis in the GMI curves with respect to increasing and decreasing dc magnetic fields was observed in the case of transverse field annealing. This hysteresis occurred at magnetic fields smaller than the anisotropy field and is probably related to the irreversible magnetisation process due to domain wall displacement. It is worth mentioning that the field annealing not only led to an increase of the GMI ratio, but also improved the magnetic response of the GMI [50]. This is beneficial for GMI-based sensor applications.

To improve the efficiency of field annealing, it can adopt differing angles and be combined with isothermal annealing to yield a new annealing method, i.e. multi-angle combined magnetic field annealing (MCMFA). Liu et al. [51] have shown that such a method is capable of releasing the stress adequately and bettering the circumferential anisotropy with a two-step annealing. Relative to their as-cast wires, the GMI enhancement reported for the annealed wires is impressive at more than 200 %.

6.3.3 Current Annealing

6.3.3.1 Joule Heating

Joule heating is a method that allows a sample to be heated directly by the action of a dc current flowing along the sample axis for a certain time [52]. Low current densities have been exploited to perform annealing at temperatures well below the crystallisation temperature and the Curie temperature of the investigated sample. During Joule heating, the dc magnetic field generated by the dc current allows a thermal treatment under the self-generated external circular magnetic field. Therefore, this method is useful for inducing additional circular/transverse magnetic anisotropy in amorphous ferromagnetic wires/microwires [52–58] and consequently providing an improved GMI effect. For a Co-based amorphous microwire, Joule heating without applied stress can produce a short-range order relaxation and hence improve the soft magnetic properties [52]. Consequently, the GMI effect can be optimised when the applied annealing current density is properly adjusted [55–58]. With increasing annealing current density, the GMI ratio first increased due to the relief of internal stress caused by heating [52], while the decrease of the GMI ratio after completion of the annealing process was attributed to the microstructural change in the sample [54]. More interestingly, the GMI ratio measured at a

frequency of 15 MHz reached a maximum value of about 600 % and the magnetic response of 320 %/Oe under specific current annealing (i.e. 10-min annealing with an applied dc current of 70 mA) [52]. This value of GMI is about 10 times larger than the maximum value reported so far for glass-coated microwires and is ideal for high-performance magnetic sensor applications. When investigating high-frequency GMI features in Joule-heated Co-based amorphous ribbons and wires, Brunetti et al. [58] showed that the GMI variation was more pronounced in the as-cast wire than in the as-cast ribbon. This is likely to be due to the higher value of circular permeability compared to that for transverse permeability [52]. The difference in the magnitude of the GMI effect between as-cast ribbon and wire observed at low frequencies ($\sim$500 MHz) tends to vanish at higher frequencies ($\sim$2600 MHz) [58]. Most recently, Liu et al. developed twin-zone Joule annealing consisting of two stages: the first annealing stage with duration of 15 min at a current intensity of 80 mA (3.37×10^5 A/μm^2) followed by the second annealing stage with duration of 5 min at a current intensity of 110 mA (4.63×10^5 A/μm^2) [59]. The former stage could release internal stress adequately, while the latter stage can generate a toroidal magnetic field by dc current to induce structural relaxation with circumferential magnetic moments in the wires. Such a compound annealing method helps generate regularly arranged atomic microregions (RAAMs) with a suitable size and volume fraction that benefit the soft magnetic properties of microwires (cf. Fig. 6.3), as against the formation of medium-range order regions (MRORs) and hard magnetic nanophases in conventionally annealed wire that severely degrade the GMI performance.

6.3.3.2 Alternating Current Annealing

Alternating current (ac) annealing is considered as the conventional annealing process with the presence of an ac flowing along the sample axis during the annealing process. It was found that the GMI ratio of an ac annealed Co-based ribbon was much larger than that of a sample annealed without the presence of an ac [60, 61]. The increase in the GMI effect of ac annealed ribbon samples can be attributed to the increased transverse permeability and the increased transverse magnetic anisotropy due to the ac-induced magnetic field, which is similar to the Joule heating method [61]. In general, both the Joule heating and ac current annealing techniques allow the improvement of the GMI effect in amorphous ferromagnetic materials. These methods are efficient in homogenising the GMI response, irrespective of the sample shape. Figure 6.4

6.3.4 Conventional Stress Annealing

The conventional annealing method with the presence of an applied stress during the annealing process is known as the conventional stress annealing method [63].

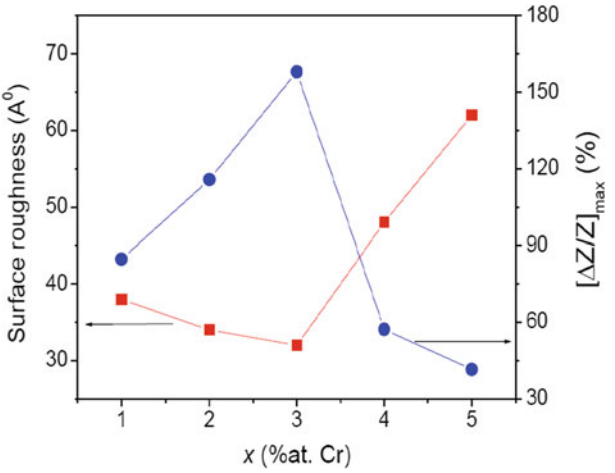

Fig. 6.4 The dependence of the maximum GMI measured at 2 MHz and the surface roughness on Cr-doped content for nanocrystalline $Fe_{73.5-x}Cr_xSi_{13.5}B_9Nb_3Au_1$ (x = 1–5) ribbons (courtesy of A.T. Le)

The influence of applied stress during annealing on the magnetic properties and GMI effect of several amorphous ferromagnetic materials, including ribbons [62–65] and wires [66], have been investigated. It was shown that, in the case of Co-based amorphous ribbons, the transverse magnetic anisotropy was induced by stress annealing [62–64]. Samples with similar anisotropy strengths were found to show very different GMI responses [62]. When a Co-based amorphous ribbon was annealed under an applied tensile stress of 500 MPa, the field sensitivity of GMI measured at a frequency of 3 MHz was found to reach up to 83 %/Oe [64]. In contrast, for stress-annealed Fe-based amorphous ribbons [65], the GMI effect was found to decrease gradually with increasing annealing stress. This is because the application of a tensile stress introduces a different transverse anisotropy that, in turn, significantly reduces the transverse magnetic permeability [60]. The different dependences of GMI on applied stress between the stress-annealed Co-based and Fe-based amorphous ribbons can be attributed to the difference in their domain structures that are determined by the samples' signal of magnetostriction [62, 63].

6.3.5 Simultaneous Stress and Magnetic Field Annealing

The simultaneous presence of an applied tensile stress and a longitudinal dc magnetic field during the annealing process was found to have a strong influence on magnetic anisotropy and hence field-dependent GMI features of Co-based amorphous ribbon samples [67]. Asymmetry in the GMI profile was also observed in this case, and it was believed to originate from a ferromagnetic exchange coupling of

the soft magnetic amorphous phase with a magnetically harder crystalline surface layer. Such asymmetry may be of interest in developing auto-biased linear GMI field sensors [1].

6.3.6 Simultaneous Stress and Current Annealing

This is a modified Joule heating technique with the addition of an applied stress during the heat treatment [52, 60, 66–68]. For stress–Joule-heated Fe-based amorphous wires, the GMI ratio increased with increasing annealing stress up to 275 MPa [66]. The GMI behaviour of the wire was interpreted by considering a simple effective field model, where the anisotropy of the material is altered by annealing and applied stress [69]. Mandal et al. [67] found that the stress–Joule heating of positive magnetostrictive glass-coated amorphous microwires caused a considerable reduction in the GMI ratio compared to the Joule heating method [52]. With respect to these findings, it is worth mentioning that field-dependent GMI features at magnetic fields lower than the anisotropy field varied strongly upon the application of stress during the annealing process. Remarkably, a reduction in hysteresis in the GMI profile with respect to increasing and decreasing fields was observed in such stress–Joule-heated samples, which is useful for non-hysteretic GMI-based sensor applications.

Interestingly, a giant stress impedance (SI) effect was observed in stress–Joule-heated Fe-based amorphous ribbons. With increasing annealing current density up to 42 A/mm^2, a maximum SI ratio of 350 % was achieved in samples annealed by Joule heating at a current density of 33 A/mm^2 in the presence of a longitudinal applied tensile stress of 100 MPa [61]. This is consistent with what was reported for Joule-heated nearly zero magnetostrictive amorphous wires and microwires [68, 70]. In these examples, the torsion stress dependence of the GMI effect may be useful for stress-sensing applications [70].

6.3.7 Laser Annealing

The influence of laser annealing energy on the GMI effect in Co-based amorphous ribbons and microwires was first investigated by Ahn et al. [71, 72]. These samples were annealed by a pulsed Nd:YAG laser at various annealing energies between 65 and 230 mJ/pulse in air. For laser-annealed Co-based amorphous ribbons, with increasing laser annealing energy, the GMI ratio first increased until reaching a maximum ($\Delta Z/Z$ = 30 %) at 136 mJ and then decreased at higher energies [71]. It was also found that when the laser annealing energy increased up to 100 mJ, the anisotropy field in as-quenched samples decreased from 1.9 Oe to ~0.5 Oe because of the increase of magnetic softness caused by the laser annealing effect. The decrease of the GMI effect and the increase of the anisotropy field were probably

due to the microstructural change caused by laser annealing [72]. For a Co-based amorphous microwire after glass removal by chemical etching, the GMI effect was found to be enhanced by illuminating the Nd:YAG laser at high frequency. This is a consequence of internal stress relief, resulting from laser energy absorption [72]. The increase in the high-frequency GMI effect reflects the fact that the contribution to the circumferential magnetisation from magnetic moment rotation in core domains increased due to magnetic softening.

The application of a small field (~3 Oe) along the microwire during laser annealing led to a considerable increase in the GMI effect in both low- and high-frequency ranges [72]. Recently, Roozmeh et al. [73] studied the effect of laser annealing on the GMI of Co-based amorphous ribbons with and without the presence of a transverse magnetic field. It was shown that laser annealing without an applied magnetic field had little influence on the GMI effect, while laser annealing with the presence of a transverse magnetic field strongly improved the GMI effect of as-quenched amorphous ribbons. It was also found that upon laser annealing, the GMI effect first increased with increasing annealing time, reached a maximum for the sample laser-annealed for 1 min, and then decreased for longer annealing times. The combination of magnetic field and laser annealing caused a local structural change and hence induced an excess anisotropy, as seen from the GMI curves [73].

In general, laser annealing is regarded as a superior method for improving the soft magnetic properties and the GMI effect of amorphous ferromagnetic materials compared to furnace annealing (conventional annealing) because it is non-contact, is quick to perform (a few microseconds), and can be performed in open air.

6.4 Effect of Applied Stress on GMI

The influence of applied stress on the GMI effect has been investigated in several amorphous ferromagnetic materials including amorphous microwires/wires [67, 68, 74]. For a positive magnetostrictive glass-coated amorphous microwire (e.g. $Co_{83.2}Mn_{7.6}Si_{5.8}B_{3.3}$), the application of a tensile stress led to a considerable reduction in the magnitude of the GMI effect at frequencies below 8 MHz, but at higher frequencies, the magnitude of the GMI effect is equal to that without an applied tensile stress [67]. It should be noted that the magnetic field at which the GMI peak occurred decreased in the stressed samples. In contrast, an improvement of the GMI effect (~130 %) measured at a frequency of 10 MHz was achieved in a nearly zero and negative magnetostrictive amorphous microwire [e.g. $Co_{68.5}Mn_{6.5}Si_{10}B_{15}$] under an applied tensile stress of 66 MPa [68]. Based on the stress dependence of the GMI effect in these amorphous microwires, a magnetoelastic sensor has been developed [70]. Torsion stress-dependent GMI features were also observed in Co-based amorphous and Fe-based nanocrystalline wires with vanishing or transverse anisotropy [68, 72]. Such variation in the shape of the GMI curve as well as its magnitude can be explained by considering the competition

between the magnetoelastic anisotropy induced by the processing and the helical anisotropy induced by the torsion [72]. A more complicated case is that both tensile and torsional stresses are present. There is competition between these two kinds of stresses on the critical field via the interactions with the intrinsic anisotropy. The tensile (torsional) stress dependency of the critical field under the constant torsional (tensile) stress that can help optimise the sensitivity can be exploited for the stress-sensing application. Qin and co-workers reasoned that the physical origin of the magnetic hysteresis induced by the stress can be understood from the core–shell model built upon the influence of stress on the magnetisation process of studied wires [75].

6.5 Effect of Neutron Irradiation on GMI

The effect of neutron irradiation on the permeability spectra and GMI of Fe-based amorphous and nanocrystalline materials was first investigated by Phan et al. [76–78]. The results indicated that neutron irradiation increased the permeability of the amorphous alloy but decreased the permeability of the nanocrystalline alloy in a high-frequency region ($f \geq 1$ MHz), while the opposite was found in a low-frequency region ($f < 1$ MHz). The magnetic relaxations in the low- and high-frequency regions were attributed to the irreversible domain wall motion and reversible rotational magnetisation, respectively. It was the increase in permeability of the neutron-irradiated amorphous alloy, resulting from reversible magnetisation rotation that caused an improvement in the GMI effect. In contrast, the decrease in permeability of the neutron-irradiated nanocrystalline alloy caused by reversible magnetisation rotation produced a reduction in the GMI effect relative to the nanocrystalline alloys. These results have important implications for the application of these materials as sensing elements in a nuclear environment, when the magnetoimpedance effect is used. This is because, compared with annealed amorphous alloy, amorphous materials are less brittle and easier to handle, which provides the necessary manufacturing flexibility, and more importantly, their magnetoimpedance properties can be enhanced by subsequent neutron irradiation. This offers an opportunity to explore the high magnetic sensing application of neutron-irradiated amorphous ferromagnetic materials, including amorphous microwires/wires.

Recently, Cayssol et al. [79] also investigated the influence of low-energy He ion irradiation on the dynamics of a single Bloch domain wall in magnetic wires based on Pt/Co/Pt trilayers with perpendicular anisotropy. The results showed that uniform ion irradiation caused a significant reduction in the pinning centre's density and the pinning force, resulting in improved domain wall motion. This reveals that the GMI effect can be further enhanced in amorphous magnetic wires when submitted to appropriate ion irradiation, because the enhancement of GMI is related to improved domain wall motion. This is of practical importance for future magnetic devices.

6.6 Effect of Hydrogen Charging on GMI

The influence of hydrogen charging on the magnetic softness and the GMI effect have been studied in amorphous Fe–Si–B and Co–Fe–Si–B wires [80]. The hydrogen charging was carried out at 25 °C and in a stirred solution by applying a constant current density of 20 mA/cm^2 for 1 h. It was found that hydrogen charging caused a drastic reduction in the GMI effect from 24.4 to 7.1 % in the Fe–Si–B amorphous wire, while no significant variation in the GMI effect was observed in the Co–Fe–Si–B amorphous wire after hydrogenation. This indicates that such Co–Fe–Si–B amorphous wires with vanishing magnetostriction are more promising for sensor applications. In fact, the change of the GMI effect has been correlated with that of the magnetic softness (i.e. the magnetisation and coercivity) [80]. In this case, it was believed that hydrogen charging modified the domain structure and hence the magnetic properties of the samples. After 2700-min degassing, the GMI effect was found to be larger in the hydrogen-charged Fe–Si–B amorphous wire than in the as-received Fe–Si–B amorphous wire. It is believed that this is due to stress relief on the surface layer of the wire.

6.7 Effect of pH Value on GMI

The influences of pH value on the GMI of electrodeposited CoNiFe/Cu wires have been systematically studied by Atalay et al. [81]. The results show that the composition, surface quality, and magnetic and magnetoimpedance properties were strongly affected by the pH value of the electrochemical bath. Under the same processing, with increasing pH, the wire diameter gradually increased, while the coercivity first decreased and then increased [81]. In particular, the GMI effect first increased with increasing pH, reached a maximum at pH = 2.4, and then decreased for higher pH. This suggests that the selection of a solution with an appropriate pH is important for optimising the GMI effect of electrodeposited wires.

6.8 Effect of Magnetostriction on GMI

The influence of magnetostriction on the GMI effect has been studied in several amorphous wires [55, 82]. Barandianran and Hernando [83] have simulated the influence of magnetostriction on the GMI effect, revealing that magnetostriction is a key parameter in determining the magnitude of GMI. In order to assess the influence of magnetostriction on GMI, Table 6.1 shows the relationship between the GMI effect and magnetostriction in both amorphous and annealed $(Co_{1-x}Fe_x)_{70}Si_{12}B_{18}$ ribbons [84]. It can be seen that the largest GMI effect is obtained in samples with vanishing magnetostriction. The magnitude and sign of the magnetostriction constant

Table 6.1 Saturation magnetostriction (λ_s) and GMI ratio $[\Delta Z/Z]_{max}(\%)$ measured at $f = 100$ kHz and $i = 5$ mA for $(Co_{1-x}Fe_x)_{70}Si_{12}B_{18}$ ribbons before (as-quenched) and after annealing

Composition (x)	As-quenched λ_s ($\times 10^{-6}$)	As-quenched $[\Delta Z/Z]_{max}(\%)$	Annealed λ_s ($\times 10^{-6}$)	Annealed $[\Delta Z/Z]_{max}(\%)$
0.04	−0.48	3	−0.26	9
0.045	−0.35	4	−0.14	3
0.047	−0.30	13	−0.083	12
0.048	−0.28	2.5	−0.09	8
0.049	−0.20	11	−0.013	13
0.05	−0.16	14	0.065	7
0.053	−0.10	18	0.14	11
0.057	0	21	0.25	7.5

of a sample can be changed either by modifying the alloy's composition or by annealing (see Table 6.1). However, it should be noted from Table 6.1 that the ribbons with similar values of λ_s do not have the same level of GMI effect. This means that the magnetostriction constant is not the only factor affecting the GMI magnitude. It was also found that for the same ribbon, the change in GMI effect due to annealing tended to follow the change in magnetostriction constant. This shows that annealing under an applied magnetic field, and/or tensile stress, and/or torsion may induce specific anisotropies, which can be either beneficial or detrimental to the GMI effect, depending on the annealing temperature and time [83]. Annealing at low temperatures and/or in a short time should be recommended for Co-based samples, because this will relieve the quenched-in stresses and result in an increase of magnetic permeability, hence increasing the GMI effect. As for Fe-based samples, annealing at temperatures close to the onset crystallisation temperature of the alloy has proved useful in producing nearly zero magnetostrictive nanocrystalline materials with a much improved GMI effect [38].

6.9 After-Effect of GMI

The so-called magnetoimpedance after-effect is known as the change in GMI effect with time and has been observed in amorphous wires and ribbons [85–91]. The origin of the magnetoimpedance after-effect can be related to the permeability after-effect of the diffusive type, and it has been experimentally shown that the occurrence of magnetoimpedance relaxation is a direct consequence of the diffusion permeability after-effect. Therefore, the permeability after-effect is the main mechanism behind the magnetoimpedance after-effect [85]. Furthermore, Raposo et al. [90, 91] studied the temperature dependence of the magnetic after-effect in Co-based amorphous wires in the range of 80–400 K and found the highest after-effect of GMI at temperatures around 350 K. Accordingly, they proposed that

the existence of long-range diffusion processes governed the dynamics of this system. Nonetheless, this phenomenon is not thoroughly understood and it warrants further investigation.

From an engineering perspective, the magnetoimpedance after-effect is undesirable for GMI sensor applications and it should be reduced as much as possible. Fortunately, a proper annealing treatment has been shown to be effective not only for improving the GMI effect, but also for considerably reducing the GMI after-effect. A very small GMI after-effect was obtained in samples with vanishing magnetostriction. This once again indicates that such zero magnetostrictive samples are the most promising candidates for GMI sensor applications.

6.10 Effect of LC Resonance Circuit on GMI

The influences of the LC resonance circuit on GMI in amorphous microwires have been investigated [92–97]. Lee et al. [92] produced a new LC resonator using a glass-coated magnetic microwire, in which the LC resonator was directly constructed on the microwire by forming two capacitive terminal electrodes at the ends of the microwire without direct contact to its ferromagnetic core. The electrodes act as capacitors in the LC resonance circuit. Because the change of impedance in the LC resonator results from both the change in permeability of the microwire and the LC resonance of the circuit, the GMI response can be greatly improved by adjusting the frequency of the ac flowing through the sample. The GMI effect reached an extremely large value of 450,000 % by precisely tuning the frequency at a value of around 551.9075 MHz [92].

With increasing frequency, GMI profiles showed either a single-peak (SP) or double-peak (DP) feature [94–96]. Remarkably, a multiple peak GMI behaviour appeared to occur in the frequency range of 100–1000 MHz, as displayed in Fig. 6.5. This is different from that observed for Co-based microwires [3] in the intermediate frequency range of 1–100 MHz, in which GMI curves often show an SP feature at low frequencies and a DP feature at higher frequencies, with only a maximum of GMI ratio obtained over this frequency range. This also differs from what was observed in GMI curves with respect to ferromagnetic resonance in the frequency range of 1–10 GHz, for a typical Co-based microwire [3]. It is believed that the circumferential permeability can be increased by applying an ac current with a frequency sufficiently high to excite resonance of the wire sample through LC circuit matching [92, 93]. The occurrence of resonance has been evidenced by a sudden change in phase angle by as much as 180° at a given external dc magnetic field. Accordingly, the GMI features can be explained in terms of the LC resonance effect [92] and the formation of standing waves in the sample [93]. However, in a high-frequency range where ferromagnetic resonance occurs, an additional contribution to the GMI effect from this resonance must also be included.

To further assess the origin of GMI, Tuan et al. [96] have recently studied the influences of annealing and sample geometry on the GMI effect in a glass-coated

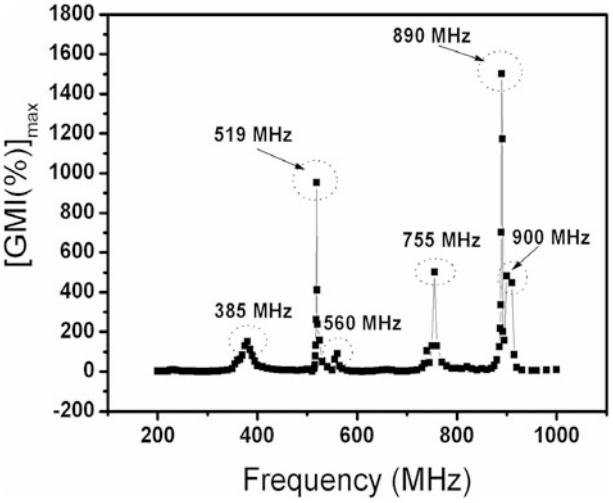

Fig. 6.5 The frequency dependence of the maximum GMI ratio, $[GMI(\%)]_{max}$, for a glass-covered microwire *LC* resonator (courtesy of A.T. Le)

microwire *LC* resonator. The results indicated that annealing magnetic microwires significantly changed the permeability and hence the GMI ratio, whereas the magnetoimpedance response was sensitive to varying sample geometry. Accordingly, the authors attributed the observed GMI features to the soft magnetic characteristics, the LC resonance circuit, and the formation of standing magnetic waves within the sample [96]. Nonetheless, the underlying mechanism of GMI in a glass-coated microwire LC resonator still remains a subject of debate and thus warrants further study. In general, the features of an LC resonance circuit can be exploited to increase the sensitivity of GMI-based magnetic sensors while selecting the working frequency. A new class of micromachined magnetic resonator for high-frequency magnetic sensor applications has been proposed [97]. In particular, Kim et al. [96] have recently demonstrated the superior features of LC filter-type magnetoimpedance sensors. The LC filter circuit showed the output-changing ratio per 1 Oe of 5 % at a high frequency of 50 MHz. This value was 2.5 times larger than that expected in a conventional bridge circuit with constant current excitation. This indicates that LC filter-type MI sensors can be used for a wide range of technological applications [98–100].

References

1. Vazquez M, Hernando A (1996) A soft magnetic wire for sensor applications. J Phys D Appl Phys 29:939–949
2. Chiriac H, Ovari TA (1996) Amorphous glass-covered magnetic wires: preparation, properties, applications. Prog Mater Sci 40:333–407

3. Knobel M, Vazquez M, Kraus L (2003) Giant magnetoimpedance. In: Buschow KH (ed) Handbook of magnetic materials, vol 15. Elsevier Science B.V., Amsterdam, pp 1–69 (Chap. 5)
4. Vazquez M (2007) Handbook of magnetism and advanced magnetic materials. In: Novel materials, vol 4. Wiley, pp 1–29 [chap. Advanced magnetic microwires]
5. Phan MH, Peng HX (2008) Giant magnetoimpedance materials: fundamentals and applications. Prog Mater Sci 53:323–420
6. Chiriac H, Ovari TA, Marinescu CS (1997) Comparative study of the giant magneto-impedance effect in CoFeSiB glass-covered and cold-drawn amorphous wires. IEEE Trans Magn 33:3352–3354
7. Nie HB, Zhang XX, Pakhomov AB, Xie Z, Yan X, Zhukov A, Vazquez M (1999) Giant magnetoimpedance of glass-covered amorphous microwires of Co–Mn–Si–B and Co–Si–B. J Appl Phys 85:4445–4447
8. Zhukova V, Larin VS, Zhukov A (2003) Stress induced magnetic anisotropy and giant magnetoimpedance in Fe-rich glass-coated magnetic microwires. J Appl Phys 94:1115–1118
9. Knobel M, Sanchez ML, Gomez-Polo C, Marin P, Vazquez M, Hernando A (1996) Giant magneto-impedance effect in nanostructured magnetic wires. J Appl Phys 79:1646–1648
10. Chiriac H, Ovari TA, Marinescu CS (1998) Giant magneto-impedance effect in nanocrystalline glass-covered wires. J Appl Phys 83:6584–6586
11. Antonenco A, Manov V, Shepelev L, Sorkine E, Tarakanov J (2001) Annealing induced evolution of structure and high frequency magnetic properties in nanocrystalline glass-coated microwires. Mater Sci Eng A 304–306:975–978
12. Vazquez M, Garcia-Beneytez JM, Garcia JM, Sinnecker JP, Zhukov AP (2000) Giant magneto-impedance in heterogeneous microwires. J Appl Phys 88:6501–6505
13. Zhukova V, Usov NA, Zhukov A, Gonzalez J (2002) Length effect in a Co-rich amorphous wire. Phys Rev B 65:134407, 1–7
14. Vazquez V, Zhukov AP, Garcia KL, Pirota KR, Ruiz A, Martinez JL, Knobel M (2004) Temperature dependence of magnetization reversal in magnetostrictive glass-coated amorphous microwires. Mater Sci Eng A 375–377:1145–1148
15. Vazquez V, Li YF, Chen DX (2002) Influence of the sample length and profile of the magnetoimpedance effect in FeCrSiBCuNb ultrasoft magnetic wires. J Appl Phys 91: 6539–6544
16. Ruiz J, Atienza JM, Elices M (2003) Residual stresses in wires: influence of wire length. J Mater Eng Perform 12:480–489
17. Phan MH, Peng HX, Yu, SC, Wisnom MR (2007) Large enhancement of GMI effect in polymer composites containing Co-based ferromagnetic microwires. J Magn Magn Mater 316:e253–e256
18. Panina LV, Mohri K, Bushida K, Noda M (1994) Giant magneto-impedance and magneto-inductive effects in amorphous alloys. J Appl Phys 76:6198–6203
19. Hu J, Qin H, Zhang F, Zheng RK (2002) Diameter dependence of the giant magnetoimpedance in hard-drawn CoFeSiB amorphous wires. J Appl Phys 91:7418–7420
20. Jantaratana P, Sirisathitkul C (2006) Effects of thickness and heat treatments on giant magnetoimpedance of electrodeposited cobalt on silver wires. IEEE Trans Magn 42:358–362
21. Xiao SQ, Liu YH, Dai YY, Zhang L, Zhou SX, Liu GD (1999) Giant magnetoimpedance effect in sandwiched films. J Appl Phys 85:4127–4130
22. Makhnovskiy DP, Panina LV (2000) Size effect on magneto-impedance in layered films. Sen Act A 81:91–94
23. Panina LV, Mohri K (2000) Magneto-impedance in multilayer films. Sen Act A 81:71–77
24. Zhou Y, Yu JQ, Zhao XL, Cai BC (2001) Giant magnetoimpedance in layered FeSiB/Cu/FeSiB films. J Appl Phys 89:1816–1819
25. Amalou F, Gijs MAM (2001) Giant magnetoimpedance of chemically thinned and polished magnetic amorphous ribbons. J Appl Phys 90:3466–3470
26. Amalou F, Gijs MAM (2002) Giant magnetoimpedance in trilayer structures of patterned magnetic amorphous ribbons. Appl Phys Lett 81:1654–1656

27. Amalou F, Gijs MAM (2004) Giant magnetoimpedance of amorphous ribbon/Cu/amorphous ribbon trilayer microstructures. J Appl Phys 95:1364–1371
28. Sinnecker JP, Garcia JM, Asenjo A, Vazquez M, Garcia-Arribas A (2000) Giant magnetoimpedance in CoP electrodeposited microtubes. J Mater Res 15:751–755
29. Sinnecker JP, Knobel M, Pirota KR, Garcia JM, Asenjo A, Vazquez M (2000) Frequency dependence of the magnetoimpedance in amorphous CoP electrodeposited layers. J Appl Phys 87:4825–4827
30. Jantaratana P, Sirisathitkul C (2006) Effects of thickness and heat treatments on giant magnetoimpedance of electrodeposited cobalt on silver wires. IEEE Trans Magn 42:358–362
31. Li XP, Zhao ZJ, Seet HL, Heng WM, Oh TB, Lee JY (2003) Effect of magnetic field on the magnetic properties of electroplated NiFe/Cu composite wires. J Appl Phys 94:6655–6658
32. Le AT, Kim CO, Chau N, Cuong ND, Tho ND, Hoa NQ, Lee HB (2006) Soft magnetic properties and giant magneto-impedance effect of $Fe_{73.5-x}Cr_xSi_{13.5}B_9Nb_3Au_1$ (x = 1-5) alloys. J Magn Magn Mater 307:178–185
33. Chaturvedi A, Dhakal T, Le A-T, Phan MH, Srikanth H (2010) Correlation between magnetic softness, sample surface and magneto-impedance in Co69Fe4.5X1.5Si10B15 (X = Ni, Al, Cr) amorphous ribbons. Physica B 405:2836–2839
34. Pirota KR, Kraus L, Knobel M, Pagliuso PG, Rettori C (1999) Angular dependence of giant magnetoimpedance in an amorphous Co-Fe-Si-B ribbon. Phys Rev B 60:6685–6691
35. Kurlyandskaya GV, Barandianran JM, Vazquez M, Garcia D, Dmitrieva NV (2000) Influence of geometrical parameters on the giant magnetoimpedance response in amorphous ribbons. J Magn Magn Mater 215–216:740–742
36. Vazquez M, Garcia-Beneytez JM, Garcia JM, Sinnecker JP, Zhukov AP (2000) Giant magneto-impedance in heterogeneous microwires. J Appl Phys 88:6501–6505
37. Sommer RL, Chien CL (1995) Role of magnetic anisotropy in the magnetoimpedance effect in amorphous alloys. Appl Phys Lett 67:857–859
38. Phan MH, Peng HX, Wisnom MR, Yu SC, Chau N (2006) Effect of annealing on the microstructure and magnetic properties of Fe-based nanocomposite materials. Compos A 37:191–196
39. Atalay S, Adiguzel HI, Kamer O (2001) Effect of different heat treatments on magnetoelastic properties of Fe-based amorphous wire. Mater Sci Eng A 304–306:495–498
40. Chen C, Luan KZ, Liu YH, Mei LM, Guo HQ, Shen BG, Zhao JG (1996) Giant magnetoimpedance effects in the soft ferromagnet $Fe_{73.5}CuNb_3Si_{13.5}B_9$. Phys Rev B 54:6092–6094
41. Knobel M, Chiriac H, Sinecker JP, Marinescu S, Ovari TA, Inoue A (1997) Comparative study of the giant magneto-impedance effect in Fe-based nanocrystalline ribbons. Sen Act A 59:256–260
42. Lee HB, Kim YK, Kim TK, Song YH, Yu SC (1999) Magnetoimpedance effect in nanocrystalline $Fe_{90-x}B_xZr_7Cu_1Al_2$ (x = 2,4,6,8) alloys. J Appl Phys 85:5429–5431
43. Lee HB, Kim KJ, Kim TK, Kim CO, Yu SC (2000) Magnetoimpedance effect in the nanocrystalline Fe–Zr–Cu–B–Al alloy system. J Appl Phys 87:5269–5291
44. He J, Guo HQ, Shen BG, He KY, Zhang HW (2001) Influence of annealing on the magnetic properties and magneto-impedance response in $Fe_{84}Zr_7B_8Cu_1$ ribbons. Mater Sci Eng A 304–306:988–991
45. Lee HB, Kim KJ, Kim YK, Kim KS, Yu SC (2001) Ultra-soft magnetic properties in nanocrystalline $Fe_{81}B_{11}Nb_7Cu_1$ alloy. J All Comp 326:313–316
46. Phan MH, Kim YS, Chien NX, Yu SC, Lee HB, Chau N (2003) Giant magnetoimpedance effect in amorphous $Co_{70}Fe_5Si_{15}B_{10}$ and $Co_{70}Fe_5Si_{15}Nb_{2.2}Cu_{0.8}B_7$ ribbons. Jpn J Appl Phys 42:5571–5574
47. Phan MH, Peng HX, Wisnom MR, Yu SC, Chau N (2004) Enhanced GMI effect in a $Co_{70}Fe_5Si_{15}B_{10}$ ribbon due to Cu and Nb substitution for B. Phys Stat Sol A 201:1558–1562
48. Rao KV, Humphrey FB, Costa-Kramer JL (1994) Very large magneto-impedance in amorphous soft ferromagnetic wires. J Appl Phys 76:6204–6208

49. Machado LA, da Silva BL, Rezende SM, Martins CS (1994) Giant ac magnetoresistance in the soft ferromagnet $Co_{70.4}Fe_{4.6}Si_{15}B_{10}$. J Appl Phys 75:6563–6565
50. Ku W, Ge F, Zhu J (1997) Effect of magnetic field annealing on the giant magnetoimpedance in FeCuMoSiB ribbons. J Appl Phys 82:5050–5053
51. Liu JS, Zhang DY, Cao FY, Xing DW, Chen DM, Xue X, Sun JF (2012) Multiangle combined magnetic-field annealing of Co-based amorphous microwires for sensor applications. Phys Status Solidi A 209(5):984–989. doi:10.1002/pssa.201127538
52. Pirota KR, Kraus L, Chiriac H, Knobel M (2000) Magnetic properties and giant magnetoimpedance in a CoFeSiB glass-covered microwire. J Magn Magn Mater 221: L243–L247
53. Raposo V, Garcia D, Zazo M, Flores AG, Iniguez JI (2004) Frequency dependence of the giant magnetoimpedance in current annealed amorphous wires. J Magn Magn Mater 272–276:1463–1465
54. Jantaratana P, Sirisathitkul C (2006) Effects of thickness and heat treatments on giant magnetoimpedance of electrodeposited cobalt on silver wires. IEEE Trans Magn 42:358–362
55. Kraus L, Knobel M, Kane SN, Chiriac H (1999) Influence of Joule heating on magnetostriction and giant magnetoimpedance effect in a glass covered CoFeSiB microwire. J Appl Phys 85:5435–5437
56. Kraus L, Chiriac H, Ovari TA (2000) Magnetic properties of stress-Joule-heated amorphous FeCrBSi microwire. J Magn Magn Mater 215–216:343–345
57. Pirota KR, Kraus L, Chiriac H, Knobel M (2001) Magnetostriction and GMI in Joule-heated CoFeSiB glass-covered microwires. J Magn Magn Mater 226–230:730–732
58. Brunetti L, Tiberto P, Vinai F, Chiriac H (2001) High-frequency giant magnetoimpedance in Joule-heated Co-based amorphous ribbons and wires. Mater Sci Eng A 304–306:961–964
59. Liu JS et al (2012) Enhancing GMI properties of melt-extracted Co-based amorphous wires by twin-zone Joule annealing. J Alloy Compd 541:215–221
60. Li DR, Lu ZC, Zhou SX (2004) Magnetic anisotropy and stress-impedance effect in Joule heated $Fe_{73.5}Cu_1Nb_3Si_{13.5}B_9$ ribbons. J Appl Phys 95:204–207
61. Lee HB, Kim YK, Kim KJ, Kim TK (2000) A novel annealing technique for the magneto-impedance effect in amorphous $Co_{66}Fe_4Ni_1B_{14}Si_{15}$ alloy. J Magn Magn Mater 215–216:310–312
62. Hernando B, Sanchez ML, Prida VM, Tejedor M, Vazquez M (2001) Magnetoimpedance effect in amorphous and nanocrystalline ribbons. J Appl Phys 90:4783–4790
63. Kurlyandskaya GV, Vazquez M, Munoz JL, Garcia D, McCord J (1999) Effect of induced magnetic anisotropy and domain structure features on magneto-impedance in stress annealed Co-rich amorphous ribbons. J Magn Magn Mater 196–197:259–261
64. Tejedor M, Hernando B, Sanchez ML, Prida VM, Vazquez M (1999) Stress and magnetic field dependence of magneto-impedance in amorphous $Co_{66.3}Fe_{3.7}Si_{12}B_{18}$ ribbons. J Magn Magn Mater 196–197:330–332
65. Wang ZC, Gong FF, Yang XL, Zeng L, Chen G, Yang JX, Quian SM, Yang DP (2000) Longitudinally driven giant magnetoimpedance effect in stress-annealed Fe-based nanocrystalline ribbons. J Appl Phys 87:4819–4821
66. Li YF, Vazquez M, Chen DX (2002) Giant magnetoimpedance effect and magnetoelastic properties in stress-annealed FeCuNbSiB nanocrystalline wire. IEEE Trans Magn 38: 3096–3098
67. Mandal K, Pan Mandal S, Vazquez M, Puerta S, Hernando A (2002) Giant magnetoimpedance effect in a positive magnetostrictive glass-coated amorphous microwire. Phys Rev B 65:064402, 1–6
68. Gonzalez J, Chen AP, Blanco JM, Zhukov A (2002) Effect of applied mechanical stresses on the impedance response in amorphous microwires with vanishing magnetostriction. Phys Stat Sol A 189:599–608
69. Kraus L (2003) GMI modeling and material optimization. Sen Act A 106:187–194
70. Cobeno AF, Zhukov A, Blanco JM, Larin V, Gonzalez J (2001) Magnetoelastic sensor based on GMI of amorphous microwire. Sen Act A 91:95–98

71. Ahn SJ, Kim CG, Park CG, Yu SC (2001) Laser annealing effect of giant magneto-impedance in amorphous $Co_{66}Fe_4Nib_{14}Si_{15}$ ribbon. Mater Sci Eng A 304–306:1026–1029
72. Ahn SJ, Lee BS, Kim CG, Rheem YW, Yoon SS, Kim CO (2003) Giant magnetoimpedance in Co-based microwire annealed by pulsed Nd:YAG laser. Sen Act A 106:221–224
73. Roozmeh SE, Tehranchi MM, Ghanatshoar M, Mohseni SM, Parhizkari M, Ghomi H, Latifi H (2006) Magnetoimpedance effect in laser annealed $Co_{68.25}Fe_{4.5}Si_{12.25}B_{15}$ amorphous ribbons. J Magn Magn Mater 304:e633–e635
74. Ohnuma M, Hono K, Yanai T, Nakano M, Fukunaga H, Yoshizawa Y (2005) Origin of the magnetic anisotropy induced by stress annealing in Fe-based nanocrystalline alloy. Appl Phys Lett 86:152513
75. Popov VV et al (2013) Stress-induced magnetic hysteresis in amorphous microwires probed by microwave giant magnetoimpedance measurements. J Appl Phys 113(17):17A326
76. Phan MH, Peng HX, Wisnom MR, Yu SC, Kim CG, Vazquez M (2005) Neutron irradiation effect on permeability and magnetoimpedance of amorphous and nanocrystalline magnetic materials. Phys Rev B 71:134423, 1–5
77. Kim YS, Phan MH, Yu SC, Kim KS, Lee HB, Kim BG, Kang YH (2003) Annealing and neutron irradiation effects on the permeability in $Fe_{86}Zr_7B_6Cu_1$ alloy. Phys B 327:311–314
78. Le AT, Hoa NQ, Tam PD, Park DG, Phan MH, Srikanth H, Yu SC (2010) Enhancement of the giant magnetoimpedance effect and its magnetic response in ion-irradiated magnetic amorphous ribbons. Mater Sci Eng B 166:89–93
79. Cayssol F, Menendez JL, Ravelosona D, Chappert C, Jamet JP, Ferre J, Bernas H (2005) Enhancing domain wall motion in magnetic wires by ion irradiation. Appl Phys Lett 86:022503, 1–3
80. Atalay F, Atalay S (2005) Giant magnetoimpedance effect in NiFe/Cu plated wire with various plating thicknesses. J All Comp 392:322–328
81. Atalay F, Kaya H, Atalay S (2006) Effect pf pH on the magnetoimpedance properties of electrodeposited CoNiFe microtubes. Phys B 371:327–331
82. Costa-Kramer JL, Rao KV (1995) Influence of magnetostriction on magneto-impedance in amorphous soft ferromagnetic wires. IEEE Trans Magn 31:1261–1265
83. Barandianran JM, Hernando A (2004) Magnetostriction influence on the giant magnetoimpedance effect: a key parameter. J Magn Magn Mater 268:309–314
84. Garcia D, Raposo V, Montero O, Iniguez JI (2006) Influence of magnetostriction constant on magnetoimpedance-frequency dependence. Sen Act A 129:227–230
85. Pirota KR, Sartorelli ML, Knobel M, Gutierrez J, Brandiaran JM (1999) Influence of induced anisotropy and magnetostriction on the giant magnetoimpedance effect and its aftereffect in soft magnetic amorphous ribbon. J Magn Magn Mater 202:431–444
86. Makhotkin VE, Shurukhin BP, Lopatin VA, Marchukov PY, Levin YK (1991) Magnetic field sensors based on amorphous ribbons. Sen Act A 25–27:759–762
87. Sartorelli ML, Knobel M, Schoenmaker J, Gutierrez J, Barandiarán JM (1997) Giant magneto-impedance and its relaxation in Co–Fe–Si–B amorphous ribbons. Appl Phys Lett 71:2208–2210
88. Knobel M, Sartorelli ML, Schoenmaker J (1997) Magnetoimpedance aftereffect in a soft magnetic amorphous wire. Phys Rev B 55:3362–3365
89. Sartorelli ML, Knobel M, Sinnecker JP (1998) Magneto-impedance relaxation in amorphous wires and ribbons. J Magn Magn Mater 177–181:121–122
90. Raposo V, Flores AG, Zazo M, Iniguez JI (2003) Magnetic aftereffect of giant magnetoimpedance in amorphous wires. J Magn Magn Mater 254–255:204–206
91. Raposo V, Montero O, Flores AG, Zazo M, Iniguez JI (2004) Magnetic aftereffect of the giant magnetoimpedance in Cobalt-based amorphous wires. J Magn Magn Mater 272–276:1844–1845
92. Lee HB, Kim YS, Yu SC (2002) Supergiant magnetoimpedance effect of a LC-resonator using a glass-coated amorphous microwire. J Magn 7:160–164
93. Paposo V, Vazquez M, Flores AG, Zazo M, Iniguez JI (2003) Giant magnetoimpedance effect enhancement by circuit matching. Sen Act A 106:329–332

94. Le AT, Phan MH (2012) Advanced magnetic microwires as sensing elements for LC-resonant-type magnetoimpedance sensors: a comprehensive review. J Supercond Nov Magn 25:181–195
95. Kim YS, Yu SC, Le AT, Kim CO, Rhee JR, Vazquez M, Hwang MJ, Lee HB (2006) Supergiant magnetoimpedance effect in a glass-coated microwire LC resonator. J Appl Phys 99:08C510, 1–3
96. Le AT, Kim CO, Phan MH, Lee HB, Yu SC (2007) Very large magnetoimpedance in a glass-coated microwire LC-resonator. Physica B: Condens Matter 395:88–92
97. Le A-T, Phan M-H, Kim C-O, Vázquez M, Lee H, Hoa NQ, Yu S-C (2007) Influences of annealing and sample geometry on the giant magnetoimpedance effect in a glass-coated microwire LC-resonator. J Phys D: Appl Phys 40:4582
98. Kim YS, Yu SC, Lu H, Lee JB, Lee HB (2006) A class of micromachined magnetic resonator for high-frequency magnetic sensor applications. J Appl Phys 99:08B309, 1–3
99. Kim YS, Yu SC, Lee JB, Lee HB (2006) A new class of LC-resonator for micro-magnetic sensor application. J Magn Magn Mater 304:117–121
100. Kim SD, Shin KH, Kim JW, Hak Y, Lim SH, Gong GS (2006) Magnetic field sensitivity of LC filter-type magnetoimpedance sensors. J Magn Magn Mater 304:e391–e393

Chapter 7
Selection of GMI Wires for Sensor Applications

7.1 Criteria for Selecting GMI Materials

To search for a GMI material for GMI sensor applications, two main requirements should be satisfied, namely a high GMI ratio (or a large GMI effect) and a high sensitivity to the applied field (or a high magnetic response). In view of the theoretical analyses and experimental results, it is concluded that a large GMI effect should exist in magnetic materials with the following desirable properties:

- low resistivity, ρ;
- high magnetic permeability, μ;
- high saturation magnetisation, M_s; and
- small ferromagnetic relaxation parameter (or low damping parameter), α.

In this context, crystalline ferromagnetic materials have the advantage of lower resistivity (ρ), but amorphous ones have better soft magnetic behaviour (e.g. higher magnetic permeability, μ, and saturation magnetisation, M_s) because they lack magnetocrystalline anisotropy. In particular, non-magnetostrictive materials can be expected to show the best GMI performance because the magnetoelastic contribution to magnetic anisotropy substantially weakens the soft magnetic behaviour. Improvement in the magnetic softness of an actual amorphous material by appropriate thermal treatment and/or the application of external parameters (mechanical stress, magnetic field, etc.) can lead to a simultaneous improvement in the GMI effect and its field sensitivity. The damping parameter (α) is often considered in the high frequency range where ferromagnetic resonance takes place, while it can be neglected in the intermediate frequency range (i.e. f = 0.1–10 MHz), where most GMI-based sensing applications have been identified (see Chap. 8). In addition, for practical sensor applications, the mass manufacturability and cost of materials are also important factors.

H.-X. Peng et al., *Ferromagnetic Microwire Composites*,
Engineering Materials and Processes, DOI 10.1007/978-3-319-29276-2_7

7.2 Evaluation of GMI Wires

In ferromagnetic materials, the highest value of the GMI effect experimentally observed is much smaller than the theoretically predicted value. Research in the field has been focused on special thermal treatments and on the development of new materials with properties appropriate for practical GMI sensor applications. In this section, all existing GMI wires will be reviewed and evaluated.

7.2.1 Co-Based Wires

Both conventional and glass-covered Co-based amorphous wires exhibit a GMI effect, owing to their high circular permeability. This is mainly due to the presence of circumferential anisotropy and an outer shell circular domain structure that results from coupling between negative magnetostriction and quenching compressive stress [1–5]. Among the Co-based amorphous alloys investigated, an alloy system with the nominal composition of Co–Fe–Si–B exhibits nearly zero and negative magnetostriction of $\lambda_s = -0.4 \times 10^{-7}$. This alloy is often obtained by alloying Fe–Si–B that has a positive λ_s of 25×10^{-6} with Co–Si–B that has a negative λ_s of -3×10^{-6} [5, 6]. As a result, a record value of GMI ratio (1200 % at 14.2 MHz) has been achieved in the conventional amorphous $Co_{68}Fe_{4.35}Si_{12.5}B_{15}$ wire [7]. This value is much larger than that reported earlier (600 %) with the same composition [2, 5]. This larger value of GMI ratio is a result of minimising contact resistance and cancelling parasitic impedance [7]. However, a high field sensitivity of GMI ($\sim$500 %/Oe) was reported by Vazquez [2], while no information was found in the work by Garcia et al. [7].

In an attempt to develop magnetic wires for high-frequency sensor applications, Nie et al. [8] reported that a Co–Mn–Si–B amorphous glass-covered wire with nearly zero magnetostriction exhibited a GMI effect at high frequencies. For the amorphous $Co_{68.2}Mn_7Si_{10}B_{15}$ microwire, the GMI ratio and magnetic response reached the values of 153 and 65 %/Oe, respectively, at a frequency of 30 MHz. Vinai et al. [9] recently revealed that these microwires also exhibited a GMI effect at frequencies up to GHz. In the frequency range of 100 MHz–6 GHz, the GMI ratio reached a maximum value of $\sim$100 % at a frequency of 2 GHz. As shown earlier in Chap. 6, for Co-based amorphous wires, the GMI effect can be further improved by appropriate field annealing [10], Joule current annealing [11–15], or the application of a tensile stress [16, 17].

In summary, the Co-based amorphous wires with nearly zero and negative magnetostriction are good candidates for GMI sensor applications. It should be noted that while the Co-based conventional and glass-covered amorphous wires are suitable for sensor applications in the low and intermediate frequency range (up to several MHz), the glass-covered amorphous microwires can be used for electrotechnical devices operating at much higher frequencies (up to several GHz). Due

to their relatively high resistivity, the microwires retain their large GMI value at higher frequencies, when compared to ribbons and wires. In practice, depending upon the specific requirements of a sensor device (e.g. the operating-frequency range), either wires or microwires should be chosen accordingly.

7.2.2 *Fe-Based Wires*

Fe-based amorphous wires have relatively small or even no MI effects, owing to their relatively small effective permeability, which is due to the presence of an outer shell radial domain configuration that results from the coupling between the highly positive magnetostriction and the quenching compressive stress [4, 10, 18, 19]. A primary alloy of Fe–Si–B having a positive λ_s of 25×10^{-6} was found to show poor magnetic softness and hence a small MI effect ($\sim$3 %), while a larger MI effect ($\sim$36 %) was obtained in the annealed wires [10, 19, 20]. It was the precipitation of an FeSi nanocrystalline phase that significantly decreased the bulk positive magnetostriction and hence gave rise to the MI effect of the annealed Fe–Si–B wires [20]. The crystallisation of Fe–Si–B-based amorphous alloys containing Nb and Cu causes the formation of a nanoscale bcc structure, and the bcc alloys exhibit excellent ultrasoft magnetic properties (i.e. high effective permeability and small coercivity) [6, 10]. In these alloys, the roles that Cu and Nb play are to maximise the density of crystal nuclei and to retard grain growth, respectively, leading to an ultrafine grain structure. Among these alloys, the nanocrystalline alloys with a nominal composition of $Fe_{73.5}Si_{13.5}B_9Nb_3Cu_1$ were found to show the best magnetic softness. These materials are therefore expected to show large MI effects. Indeed, Knobel et al. [10] reported that conventional $Fe_{73.5}Si_{13.5}B_9Nb_3Cu_1$ nanocrystalline wires (e.g. the amorphous wire samples annealed at 550–600 °C) exhibited a GMI effect. The largest value of GMI ratio was about 200 % at a frequency of 500 kHz for the wire sample annealed at 600 °C for 1 h. In another study, Li et al. [21] partially substituted Fe by Cr in $Fe_{73.5}Si_{13.5}B_9Nb_3Cu_1$ nanocrystalline wires with the expectation of further reducing the magnetostriction of the primary alloy. They found that, although the GMI ratio and magnetic response were slightly smaller in Cr-doped samples, the addition of Cr improved the GMI response and significantly reduced the undesirable hysteretic effect in GMI curves with increasing and decreasing applied magnetic fields [21]. In addition, the presence of Cr significantly improved the corrosion resistance properties, which is desirable for sensing applications in a corrosive environment. The GMI effect was also observed in Fe-based nanocrystalline glass-coated wires and microwires [4, 18]. Interestingly, the $Fe_{89}B_1Si_3C_3Mn_4$ nanocrystalline glass-covered microwires were found to show the GMI effect in the GHz frequency range [9]. At a frequency of 4 GHz, the GMI ratio reached a value as high as 70 % for the sample annealed at 350 °C. For this typical microwire, conventional furnace annealing proved more effective in improving the GMI effect compared with current annealing. Furthermore, it should be recalled that for both Fe-based amorphous

and nanocrystalline glass-covered wires, the removal of the glass layer can significantly improve the GMI effect and magnetic response. However, the GMI ratios of Fe-based nanocrystalline wires are often smaller than those of Co-based amorphous wires [5].

7.2.3 *Electrodeposited Wires*

Besides rapidly quenched wires, electrodeposited wires, which comprise a highly conductive non-magnetic metal core (e.g. Cu, CuBe, and Ag) and a thin layer of soft magnetic metal (e.g. NiFe, NiFeRu, NiFeMo, CoP, and CoNiFe), have been found to show excellent GMI behaviours [22–42]. For electrodeposited wires, the magnetic layer has either a circular or a radial domain configuration, depending strongly upon the alloy composition and the sample processing conditions [40]. Wires having a circular domain structure are often expected to show a larger MI effect [38, 42].

In a pioneering work, Usov et al. [38] predicted that the GMI effect could be further improved in a composite amorphous wire when the electrical conductivity of the inner core is much higher than that of the shell region. Since this work, experimental efforts have been devoted to investigating the GMI effect in electrodeposited wires, such as CoP/Cu [22–26, 39], NiFe/Cu [28–30, 41], CoNiFe/Cu [31, 32, 40], NiFeRu/Cu [33], and NiFeMo/Cu [34]. Sinnecker et al. [22] reported that an electrodeposited CoP/Cu wire exhibited radial magnetic anisotropy (i.e. the radial domain structure) and the size of the closure domains increased with the magnetic layer thickness (CoP). It is interesting to note that, although magnetic wires with a radial magnetic anisotropy are not expected to show any GMI effect, a significant increase in GMI ratio with the magnetic layer thickness of the CoP/Cu composite wire was attained [22]. This indicated that the observed GMI effect was associated with the current distribution along the sample radius, with two well-defined regions having different transport and magnetic properties [23–26]. Recently, Phan et al. [39] optimised the processing conditions in order to achieve the largest GMI effect in a typical CoP/Cu electrodeposited wire. The largest GMI ratio was achieved with a deposition time of 6 min and an electrolytic current density of 639 mA/cm^2. At the measured frequency of 10.7 MHz, the GMI ratio and magnetic response reached the highest values of 534 and 21 %/Oe, respectively. It was proposed that the changes of deposition time and electrolytic current density caused variations in the domain structure of the CoP magnetic layer and hence the GMI behaviour [39]. More interestingly, Kurlyandskaya et al. [40] found that the GMI ratio reached a value as high as 1200 % at a frequency of 4 MHz for FeNiCo/CuBe electroplated wire. This is the highest value reported until now, among existing electrodeposited wires. However, no information on the magnetic response of GMI was given [40]. In a comprehensive study investigating the influences of processing parameters (e.g. electrodeposition current density, duty cycle, electrolyte solution, pH value, applied magnetic field, magnetic layers, and

post-annealing) on the GMI of electrodeposited NiFe/Cu wires, Li et al. [41] reported that the GMI ratio and magnetic response reached maximum values of 1110 and 218 %/Oe, respectively, at a frequency of 4 MHz for a dc Joule-annealed wire sample.

Recently, it has been revealed that the GMI effect can be further improved in electrodeposited wires by the inclusion of an insulating interlayer between the core and the magnetic shell (e.g. CuBe/insulator/NiFeB wires) [36, 37]. For instance, the GMI ratio reached a value of 250 % at f = 500kH–1 MHz for an electrodeposited CuBe/insulator/NiFeB wire, which is much larger than that of ~23 % at f = 1 MHz for the electrodeposited CuBe/NiFeB wire without the insulator layer [36]. This can arise from the differences in current distribution under the external magnetic field and from the electromagnetic interaction between the conductive core and the ferromagnetic layer of the composite wires with and without an insulator layer [36, 37]. In this context, Buznikov et al. [42] have recently developed a model for predicting the GMI effect in these typical wires. The model reveals that the field dependence of magnetic shell permeability significantly affects the eddy current distribution and therefore leads to the observed GMI effect. The inclusion of a thin insulator layer can lead to a further improvement in the GMI effect at sufficiently high frequencies, because it actually increases both the diagonal and off-diagonal impedance [42].

In general, electrodeposited composite wires are good candidate materials for producing high-performance magnetic sensors and sensing devices operating at low and intermediate frequencies (up to several MHz). Within this operating regime, electrodeposited composite wires may be even more promising than rapidly quenched wires and ribbons.

7.2.4 Multilayer Wires

Multilayer wire is a new family of magnetic microwires with multilayer bimagnetic characteristics [43, 44]. A typical biphase magnetic microwire consists of a ferromagnetic nucleus, an intermediate glass layer, and a ferromagnetic outer shell, as exemplified in Fig. 7.1. They were prepared by several complementary techniques including quenching and drawing for precursor glass-coated magnetic/metallic core microwire, sputtering for Au metallic intermediate nanolayer, and electroplating for magnetic external microtube. This combination of techniques enables the manipulation of different soft/hard magnetic characteristics at different layers and hence permits one to tune the properties of the biphase microwires. The peculiarity of the multilayer wires lie in the coupling between various layers. The presence of an external magnetic shell around a glass-coated microwire induces a longitudinal anisotropy in the nucleus of the latter, drastically modifying its magnetoinductive behaviour, making it very sensitive to the presence of an applied external stress and temperature [45, 46].

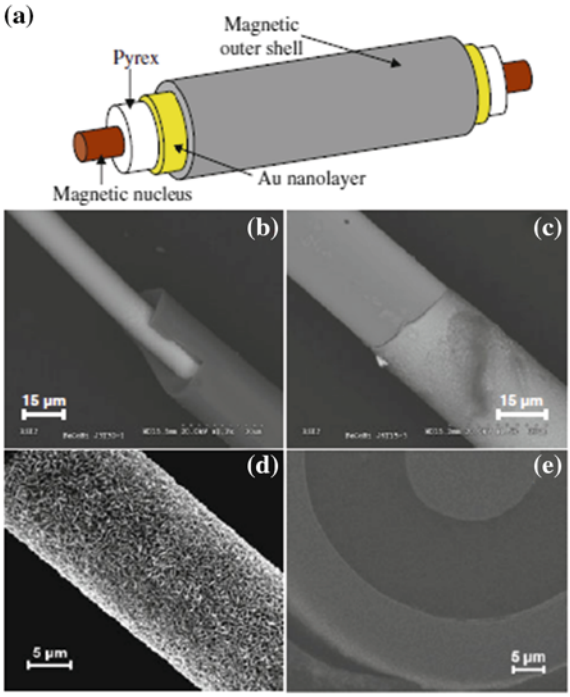

Fig. 7.1 **a** Scheme of multilayer microwire. SEM images of FeSiB/CoNi multilayer microwires: **b** FeSiB nucleus and glass cover, **c** glass layer and CoNi outer shell, **d** CoNi outer shell, and **e** cross-sectional view of the multilayer microstructure (reprinted with the permission of Springer [48])

The most notable magnetic characteristic is the step-like magnetisation process arising from the different magnetic phases and couplings [47]. These can be optimised by specific thermal treatment processing to grow a new structural phase with a hard magnetic character at the magnetic core via conventional thermal annealing, or by inducing suitable helical anisotropy at the magnetic shell via helical magnetic field annealing or torsion annealing. Different magnetic configurations have been explored thus far: soft (nucleus)/hard (outer shell), hard/soft, and soft/soft [48]. One can invariably make use of the magnetic interactions to manipulate the soft magnetic core behaviour. For instance, it can be modulated through the hard phase stray fields, or magnetic bistability can be modified through the magnetoelastic anisotropy induced by the external phase. In addition to the soft/hard magnetic nature of each magnetic phase, an effective tuning of average behaviour can be achieved by adapting the thickness of each layer.

These multilayer wires are of practical significance as sensing core elements in sensor devices. Subject to a delicate control in terms of the reversal magnetisation of the soft phase, this type of microwire has come to be an ideal candidate in a variety of sensor technologies from temperature/tensile stress and torsion/position sensors to coil-less orthogonal fluxgates. The versatility of their properties and the high degree of freedom for tailoring give these wires an outstanding edge in the competitive sensing technology field.

7.3 Nominated GMI Materials for Sensor Applications

A wide variety of GMI materials are currently available for practical GMI sensor applications. Table 7.1 summarises several materials that possess a high GMI ratio and magnetic response and are promising for making high-performance GMI sensors. Appropriate selection is dependent upon specific requirements, such as their field sensitivity, working frequency range, size, and thermal stability. The ultrahigh sensitivity of GMI to external dc magnetic field (down to 10^{-8} Oe) can be used for magnetic field sensors and other sensors based on the change of a local magnetic field. It should be emphasised that not only the GMI ratio (η) and the magnetic response (ζ), but also the particular shape of the $\eta(H)$ curve are important

Table 7.1 Candidate materials for GMI sensors

Materials	Comment	H_{max} (Oe)	η (%)	ξ (%/Oe)	Frequency (MHz)	References
$Co_{68}Fe_{4.35}Si_{12.5}B_{15}$	Conventional amorphous wire	180	1200	–	14.2	[7]
$(Co_{94}Fe_6)_{75}Si_{10}B_{15}$	Amorphous homogeneous microwire	10	125	50	3.22	[49]
$Co_{68.25}Fe_{4.5}Si_{12.25}B_{15}$	Amorphous microwire under Joule annealing	125	600	320	15	[50]
$Co_{83.2}B_{3.3}Si_{5.9}Mn_{7.6}$	Amorphous microwire under dc current	1	7.8	15.6	1	[51]
$Co_{68.2}Mn_7Si_{10}B_{15}$	Amorphous microwire	50	153	65	30	[8]
$Fe_{73.5}Si_{13.5}B_9Cu_1Nb_3$	Conventional wire annealed at 600 °C for 1 h	100	200	–	0.5	[10]
$Fe_{73.5}Si_{13.5}B_9Cu_1Nb_3$	Glass-covered microwire under conventional annealing	25	25.5	8.9	2	[19]
$Fe_{89}B_1Si_3C_3Mn_4$	Annealed at 350 °C for 1 h	300	70	–	4000	[9]
CoP/Cu/CoP electrodeposited layers	Electrodeposited technique	30	190	26	1	[24]
CoP/Cu composite wire	Electrodeposited technique	100	534	21	10.7	[39]
NiFe/Cu composite wire	Electroplated in magnetic field	45	370	47.5	1	[28]
NiFe/Cu composite wire	Joule annealing	45	1100	218	4	[41]
FeNiCo/CuBe composite wire	Electroplated technique	50	1200	–	4	[40]

(continued)

Table 7.1 (continued)

Materials	Comment	H_{max} (Oe)	η (%)	ξ (%/Oe)	Frequency (MHz)	References
$Co_{70}Fe_5Si_{15}Nb_{2.2}Cu_{0.8}B_7$	Ribbon under field annealing in air	2	50	125	0.1	[52]
$Co_{70}Fe_5Si_{15}Nb_{2.2}Cu_{0.8}B_7$	Ribbon under field annealing in air	2	106	35	1	[52]
$Co_{70}Fe_5Si_{15}Nb_{2.2}Cu_{0.8}B_7$	Amorphous ribbon annealed at 300 °C for 25 min	50	513	144	4	[53]
$Fe_{73.5}Si_{13.5}B_9Cu_1Nb_3$	Amorphous ribbon annealed at 550 °C for 3 h	150	400	37	4.5	[54]
$Fe_{71}Al_2Si_{14}B_{8.5}Cu_1Nb_{3.5}$	Amorphous ribbon annealed at 540 °C for 45 min	100	640	40	5	[53]
$Fe_{84}Zr_7B_8Cu_1$	Amorphous ribbon annealed at 550 °C for 1 h	75	1100	40	4.6	[55]
$Fe_{73.5}Si_{13.5}B_9Cu_1Nb_3$	Nanocrystalline sputtered film	50	80	–	500	[56]
NiFe/Au/NiFe multilayered film	RF-sputtered	65	150	30	300	[57]
NiFe/Ag multilayered film	RF-sputtered	150	250	12	18,000	[58]
FeSiBCuNb/Cu/FeSiBCuNb sandwiched film	RF-sputtered	70	1733	87	0.1	[59]
FeNiCrSiB/Cu/FeNiCrSiB sandwiched film	RF-sputtered	70	77	7.2	13	[60]
CoSiB/Cu/CoSiB sandwiched film	RF-sputtered	9	440	49	10	[61]
CoSiB/SiO_2/Cu/SiO_2/CoSiB sandwiched film	RF-sputtered in magnetic field	11	700	304	20	[62]
FeSiBCuNb/SiO_2/Cu /SiO_2/ FeSiBCuNb sandwiched film	RF-sputtered	60	32	4	5.45	[63]
MuMetal alloy	Annealed at 580 °C for 40 min	115.5	310	20	0.6	[64]
Co-based amorphous ribbon/Cu/Co-based amorphous ribbon	Trilayer microstructure	20	830	–	0.28	[65]
$Co_{70.3}Cr_3Fe_{3.7}B_{10}Si_{13}$/ polymer composites	Magnetic microwires embedded in parallel in a polymer matrix	50	470	43	10	[66]

for high-performance sensor applications. In this context, the longitudinal weak-field-annealed amorphous ribbons [64, 67–74] and amorphous wires subjected to dc bias current [75–84] are promising candidate materials for producing auto-biased linear field sensors.

References

1. Chiriac H, Ovari TA (1996) Amorphous glass-covered magnetic wires: preparation, properties, applications. Prog Mater Sci 40:333–407
2. Vazquez M (2001) Giant magnetoimpedance in soft magnetic "wires". J Magn Magn Mater 226–230:693–699
3. Knobel M, Pirota KR (2002) Giant magnetoimpedance: concepts and recent progress. J Magn Magn Mater 242–245:33–40
4. Knobel M, Vazquez M, Kraus L (2003) Giant magnetoimpedance (Chap 5). In: Buschow KH (ed) Handbook of magnetic materials, vol 15. Elsevier Science B.V., Amsterdam, pp 1–69
5. Vazquez M, Knobel M, Sanchez ML, Valenzuela R, Zhukov AP (1997) Giant magneto-impedance effect in soft magnetic wires for sensor applications. Sen Act A 59:20–29
6. McHenry ME, Willard MA, Laughlin DE (1999) Amorphous and nanocrystalline materials for applications as soft magnets. Prog Mater Sci 44:291–433
7. Garcia D, Raposo V, Montero O, Iniguez JI (2006) Influence of magnetostriction constant on magnetoimpedance-frequency dependence. Sen Act A 129:227–230
8. Nie HB, Zhang XX, Pakhomov AB, Xie Z, Yan X, Zhukov A, Vazquez M (1999) Giant magnetoimpedance of glass-covered amorphous microwires of Co–Mn–Si–B and Co–Si–B. J Appl Phys 85:4445–4447
9. Vinai F, Coisson M, Tiberto P (2006) High-frequency magneto-impedance in metastable metallic materials: an overview. J Magn Magn Mater 300:e82–e87
10. Knobel M, Sanchez ML, Gomez-Polo C, Marin P, Vazquez M, Hernando A (1996) Giant magneto-impedance effect in nanostructured magnetic wires. J Appl Phys 79:1646–1648
11. Kraus L, Knobel M, Kane SN, Chiriac H (1999) Influence of Joule heating on magnetostriction and giant magnetoimpedance effect in a glass covered CoFeSiB microwire. J Appl Phys 85:5435–5437
12. Kraus L, Chiriac H, Ovari TA (2000) Magnetic properties of stress-Joule-heated amorphous FeCrBSi microwire. J Magn Magn Mater 215–216:343–345
13. Pirota KR, Kraus L, Chiriac H, Knobel M (2001) Magnetostriction and GMI in Joule-heated CoFeSiB glass-covered microwires. J Magn Magn Mater 226–230:730–732
14. Brunetti L, Tiberto P, Vinai F, Chiriac H (2001) High-frequency giant magnetoimpedance in joule-heated Co-based amorphous ribbons and wires. Mater Sci Eng, A 304–306:961–964
15. Li DR, Lu ZC, Zhou SX (2004) Magnetic anisotropy and stress-impedance effect in Joule heated Fe73.5Cu1Nb3Si13.5B9 ribbons. J Appl Phys 95:204–207
16. Kurlyandskaya GV, Vazquez M, Munoz JL, Garcia D, McCord J (1999) Effect of induced magnetic anisotropy and domain structure features on magneto-impedance in stress annealed Co-rich amorphous ribbons. J Magn Magn Mater 196–197:259–261
17. Tejedor M, Hernando B, Sanchez ML, Prida VM, Vazquez M (1999) Stress and magnetic field dependence of magneto-impedance in amorphous Co66.3Fe3.7Si12B18 ribbons. J Magn Magn Mater 196–197:330–332
18. Vazquez M, Hernando A (1996) A soft magnetic wire for sensor applications. J Phys D Appl Phys 29:939–949
19. Moron C, Garcia A (2005) Giant magneto-impedance in nanocrystalline glass-covered microwires. J Magn Magn Mater 290–291:1085–1088
20. Takemura Y, Tokuda H (1996) IEEE Trans Magn 32:4947–4949

21. Li YF, Vaquez M, Chen DX (2000) GMI effect of Fe73.5−xCrxCu1Nb3Si13.5B9 amorphous and nanocrystalline soft wires. J Magn Magn Mater 249:342–345
22. Sinnecker JP, Garcia JM, Asenjo A, Vazquez M, Garcia-Arribas A (2000) Giant magnetoimpedance in CoP electrodeposited microtubes. J Mater Res 15:751–755
23. Yu RH, Landry G, Li YF, Basu S, Xiao JQ (2000) Magneto-impedance effect in soft magnetic tubes. J Appl Phys 87:4807–4809
24. Sinnecker JP, Knobel M, Pirota KR, Garcia JM, Asenjo A, Vazquez M (2000) Frequency dependence of the magnetoimpedance in amorphous CoP electrodeposited layers. J Appl Phys 87:4825–4827
25. Garcia JM, Sinnecker JP, Asenjo A, Vazquez M (2001) Enhanced magnetoimpedance in CoP electrodeposited microtubes. J Magn Magn Mater 226–230:704–706
26. Garcia JM, Asenjo A, Vazquez M, Yakunin AM, Antonov AS, Sinnecker JP (2001) Determination of closure domain penetration in electrodeposited microtubes by combined magnetic force microscopy and giant magneto-impedance techniques. J Appl Phys 89: 3888–3891
27. Jantaratana P, Sirisathitkul C (2006) Effects of thickness and heat treatments on giant magnetoimpedance of electrodeposited cobalt on silver wires. IEEE Trans Magn 42:358–362
28. Li XP, Zhao ZJ, Seet HL, Heng WM, Oh TB, Lee JY (2003) Effect of magnetic field on the magnetic properties of electroplated NiFe/Cu composite wires. J Appl Phys 94:6655–6658
29. Li XP, Zhao ZJ, Chua C, Seet HL, Lu L (2003) Enhancement of giant magnetoimpedance effect of electroplated NiFe/Cu composite wires by dc Joule annealing. J Appl Phys 94: 7626–7630
30. Hu J, Qin H, Zhang L, Chen J (2004) Giant magnetoimpedance effect in Ag/NiFe plate wire. Mater Sci Eng, B 106:202–206
31. Atalay FE, Kaya H, Atalay S (2006) Unusual grain growth in electrodeposited CoNiFe/Cu wires and their magnetoimpedance properties. Mater Sci Eng, B 131:242–247
32. Atalay FE, Kaya H, Atalay S (2006) Giant magnetoimpedance effect in electrodeposited CoNiFe/Cu wires with varying Ni, Fe and Co content. J Alloys Compd 420:9–14
33. Atalay FE, Kaya H, Atalay S (2006) Magnetoimpedance effect in electroplated NiFeRu/Cu wire. J Phys D Appl Phys 39:431–436
34. Velleuer J, Munoz AG, Yakabchuk H, Schiefer C, Hackl A, Kisker E (2007) Giant magnetoimpedance in electroplated NiFeMo/Cu microwires. J Magn Magn Mater 2:651–657
35. Zhang Z, Wu Q, Zhong K, Yang S, Lin X, Huang Z (2006) The size and space arrangement roles on coercivity of electrodeposited $Co_{1-x}Cu_x$ nanowires. J Magn Magn Mater 303: e304–e307
36. Wang XZ, Yuan WZ, Zhao Z, Li XD, Ruan JZ, Yang XL (2005) Giant magnetoimpedance effect in CuBe/NiFeB and CuBe/insulator/NiFeB electroless-deposited composite wires. IEEE Trans Magn 41:113–115
37. Wang XZ, Yuan WZ, Zhao Z, Li XD, Ruan JZ, Zhao ZJ, Yang JX, Yang XL, Sun Z (2007) Enhancement of giant magnetoimpedance in composite wire with insulator layer. J Magn Magn Mater 308:269–272
38. Usov N, Antonov A, Granovsky A (1997) Theory of giant magntoimpedance effect in composite amorphous wire. J Magn Magn Mater 171:64–68
39. Phan MH, Peng HX, Wisnom MR, Tung MT, Dung NV, Nghi NH (2007) Optimized GMI effect in electrodeposited CoP/Cu composite wires. J Magn Magn Mater 2:244–247
40. Kurlyandskays GV, Garcia-Arribas A, Barandiaran JM (2003) Advantages of nonlinear giant magnetoimpedance for sensor applications. Sens Actuators A 106:234–239
41. Li XP, Seet HL, Fran J, Yi JB (2006) Electrodeposition and characteristics of $Ni_{80}Fe_{20}$/Cu composite wires. J Magn Magn Mater 304:111–116
42. Buznikov NA, Antonov AS, Granovsky AB, Kim CG, Kim CO, Li XP, Yoon SS (2006) Giant magnetoimpedance in composite wires with insulator layer between non-magnetic core and soft magnetic shell. J Magn Magn Mater 300:e63–e66

43. Pirota K, Hernandez-Velez M, Navas D, Zhukov A, Vázquez M (2004) Multilayer microwires: tailoring magnetic behavior by sputtering and electroplating. Adv Funct Mat 14:266–268
44. Pirota K, Provencio M, García K, Hernandez-Velez M, Vázquez MJ (2005) Magn Magn Mat 290–291:68
45. Vázquez M, Pirota K, Torrejon J, Badini G, Torcunov AJ (2006) Magn Magn Mater 304: 197–202
46. Torrejón J, Badini G, Pirota K, Vázquez M (2007) Acta Mater 55:4271–4276
47. Vazquez M (2007) Advanced magnetic microwires. In: Kronmüller H, Parkin S (ed) Handbook of magnetism and advanced magnetic materials. Wiley&Sons, NJ
48. Torrejón J, Infante G, Badini-Confalonieri G et al (2013) J Miner Met Mater Soc 65(7): 890–900
49. Vazquez M, Garcia-Beneytez JM, Garcia JM, Sinnecker JP, Zhukov AP (2000) Giant magneto-impedance in heterogeneous microwires. J Appl Phys 88:6501–6505
50. Pirota KR, Kraus L, Chiriac H, Knobel M (2000) Magnetic properties and giant magnetoimpedance in a CoFeSiB glass-covered microwire. J Magn Magn Mater 221: L243–L247
51. Phan MH, Yu SC, Kim CG, Vazquez M (2003) Origin of asymmetrical magnetoimpedance in a Co-based amorphous microwire due to dc bias current. Appl Phys Lett 83:2871–2873
52. Phan MH, Peng HX, Yu SC, Chau N (2005) Valve behavior of giant magnetoimpedance in field-annealed $Co_{70}Fe_5Si_{15}Nb_{2.2}Cu_{0.8}B_7$ amorphous ribbon. J Appl Phys 97:10M108, 1–3
53. Phan MH, Peng HX, Yu SC, Vazquez M (2006) Optimized giant magnetoimpedance effect in amorphous and nanocrystalline materials. J Appl Phys 99:08C505, 1–3
54. Guo HQ, Kronmuller H, Dragon T, Cheng ZH, Shen BG (2001) Influence of nanocrystallization on the evolution of domain patterns and the magnetoimpedance effect in amorphous Fe73.5Cu1Nb3Si13.5B9 ribbons. J Appl Phys 89:514–516
55. Lee HB, Kim KJ, Kim TK, Kim CO, Yu SC (2000) Magnetoimpedance effect in the nanocrystalline Fe–Zr–Cu–B–Al alloy system. J Appl Phys 87:5269–5291
56. Viegas ADC, de Andrade AMH, Sommer RL, Jiang JS, Chien CL (2001) Magnetoimpedance in Fe73.5Cu1Nb3Si13.5B9 amorphous films at microwave frequencies. J Magn Magn Mater 226–230:707–708
57. de Cos D, Fry N, Orue I, Panina PV, Garcia-Arribas A, Barandiaran JM (2006) Very large magnetoimpedance (MI) in FeNi/Au multilayer film systems. Sens Actuators A 129:256–259
58. de Andrade AMH, da Silva RB, Correa MA, Viegas ADC, Severino AM, Sommer RL (2004) Magnetoimpedance of NiFe/Ag multilayers in the 100 kHz–1.8 GHz range. J Magn Magn Mater 272–276:1846–1847
59. Xiao SQ, Liu YH, Yan SS, Dai YY, Zhang L, Mei LM (2000) Giant magnetoimpedance and domain structure in FeCuNbSiB films and sandwiched films. Phys Rev B 61:5734–5739
60. Xiao SQ, Liu YH, Dai YY, Zhang L, Zhou SX, Liu GD (1999) Giant magnetoimpedance effect in sandwiched films. J Appl Phys 85:4127–4130
61. Morikawa T, Nishibe Y, Yamadera H (1997) Giant magnetoimpedance effect in layered thin films. IEEE Trans Magn 33:4367–4372
62. Morikawa T, Nishibe Y, Yamadera H, Nonomura Y, Takeuchi M, Sakata J, Taga Y (1996) Enhancement of giant magneto-impedance in layered film by insulator separation. IEEE Trans Magn 32:4965–4967
63. Li XD, Yuan WZ, Zhao ZJ, Ruan JZ, Yang XL (2005) The GMI effect in nanocrystalline FeCuNbSib multilayered films with a SiO_2 outer layer. J Phys D Appl Phys 38:1351–1354
64. Nie HB, Pakhomov AB, Yan X, Zhang XX, Knobel M (1999) Giant magnetoimpedance in crystalline Mumetal. Sol Stat Commun 112:285–289
65. Amalou F, Gijs MAM (2004) Giant magnetoimpedance of amorphous ribbon/Cu/amorphous ribbon trilayer microstructures. J Appl Phys 95:1364–1371
66. Phan MH, Peng HX, Wisnom MR, Yu SC, Nghi NH Great enhancement of GMI effect in polymer composites containing Co-based ferromagnetic microwires. J Magn Magn Mater (in press)

67. Fu CM, Hsu CY, Chao YC, Kim DS, Matsushita N, Abe M (2004) Tunnel magnetoimpedance effect of the ZnNi-ferrite encapsulated NiFe micropsheres. J Magn Magn Mater 272–276: e1839–e1841
68. Hu J, Qin H, Qi G, Jiang M (2006) Giant magnetoimpedance in a MnZn ferrite. J Magn Magn Mater 302:375–377
69. Carara M, Sommer RL (1997) Giant magnetoimpedance in highly textured (110)[001] FeSi3 %. J Appl Phys 81:4107–4109
70. Gomez-Polo C, Perez-Landazabal JI, Recarte V, Ciurzynska W (2003) Effect of the ordering on the magnetic and magnetoimpedance properties of Fe-6.5 % Si alloy. J Magn Magn Mater 254–255:88–90
71. Jantaratana P, Sirisathitkul C (2004) Giant magnetoimpedance in silicon steels. J Magn Magn Mater 281:399–404
72. Hu J, Qin H (2002) Magnetoimpedance effect in Fe flakes. J Magn Magn Mater 246:375–378
73. Soares JM, de Araujo JH, Cabral FAO, Dumelow T, Machado FLA, de Araujo AEP (2002) Giant magnetoimpedance in FeAg granular alloys. Appl Phys Lett 80:2532–2534
74. Fraga GLF, Pureur P, Brandao DE (2002) Spontaneous magnetoimpedance in the Heusler compounds Pd_2MnSn and Pd_2MnSb near the Curie temperature. Sol Stat Comm 124:7–10
75. Fu CM, Hsu KS, Lin ML, Wen ZH (2000) Giant magnetoimpedance effects in sintered $La_{1-x}Ca_xMnO_3$ oxides. J Magn Magn Mater 209:151–153
76. Hu J, Qin HW (2003) Magnetoimpedance effect at various temperatures for manganite $La_{0.7}Ca_{0.3}MnO_{3-\sigma}$. Mater Sci Eng B 100:304–306
77. Castro GMB, Rodrigues AR, Machado FLA, de Araujo AEP, Jardim RF, Nigam AK (2004) Magnetoimpedance measurements in bulk samples of La0.7Ca0.3MnO3 and La0.6Y0. 1Ca0.3MnO3. J All Comp 369:108–111
78. Hu J, Qin HW (2001) Magnetoimpedance effect in La0.7Sr0.3MnO3. J Magn Magn Mater 234:419–422
79. Hu J, Qin HW (2001) Giant magnetoimpedance effect in La0.65Sr0.35MnO3 under low dc magnetic fields. Mater Sci Eng B 79:186–189
80. Hu J, Qin HW (2002) Magnetoimpedance effect in semiconducting $La_{0.4}Sr_{0.6}MnO_3$. Mater Sci Eng B 88:18–21
81. Patanjali PV, Theule P, Zhai Z, Hakim N, Sridhar S, Suryanarayanan R, Apostu M, Dhalenne G, Revcolevschi A (1999) High-frequency magnetoimpedance of double perovskite $La_{1.2}Sr_{1.8}Mn_2O_7$: secondary transitions at high temperatures. Phys Rev B 60:9268–9271
82. Hu J, Qin HW, Zhang Y (2000) Giant magnetoimpedance effect in La–Ba–Mn–O oxide. Mater Sci Eng B 77:280–281
83. Hu J, Qin HW (2000) Magnetoimpedance effect in $La_{0.67}Ba_{0.33}MnO_3$ under low dc magnetic fields. Sol Stat Commun 116:159–162
84. Hu J, Qin HW, Niu HD, Zhu L, Chen J, Xiao W, Pei Y (2003) Magnetoimpedance effect in manganite La2/3Ba1/3MnO3 at various temperatures. J Magn Magn Mater 261:105–111

Chapter 8
Giant Magnetoimpedance Sensors and Their Applications

Since GMI changes as a function of external dc magnetic field or applied dc/ac current, it is possible to design and produce GMI-based sensors that can measure either magnetic fields or dc/ac currents. GMI also changes sensitively with applied stress, and this provides a new opportunity to develop stress sensors. A brief description of these typical sensors is given in this chapter. It shows that the high sensitivity of GMI to applied magnetic field, current, and external stress is very useful for a wide range of industrial and engineering applications.

8.1 Types of Giant Magnetoimpedance-Based Sensors

8.1.1 Magnetic Field Sensors

A primary magnetic sensor based on the GMI effect (the so-called GMI sensor) has been proposed and analysed by Atkinson et al. [1]. The circuit of a GMI sensor is displayed in Fig. 8.1. In the circuit, a single-wire sensing element that can be from 0.1 to 10 m long is connected to a bridge circuit via coaxial leads. Herein the source voltage and source resistance play an important role in the bridge balance. In order to use this circuit for a GMI sensor, the impedance changes as a function of external magnetic field at a fixed frequency are needed. This typical sensor operates in an open mode and can be used for measuring or tracking the presence of both homogeneous and inhomogeneous magnetic fields. A detailed investigation of how the processing parameters can be controlled, as well as the influences of these parameters on the performance of a designed GMI sensor, has been reported [2, 3]. Moreover, here the circuit of the GMI sensor is more complicated than the case of [1]. Different classes of novel GMI field sensors using Co-rich amorphous wires have been developed by Mori and his group in collaboration with Aichi Steel Co., Japan [4–7]. In particular, they have developed a reliable amorphous wire CMOS IC multivibrator GMI sensor using the analogue switches instead of the

H.-X. Peng et al., *Ferromagnetic Microwire Composites*,
Engineering Materials and Processes, DOI 10.1007/978-3-319-29276-2_8

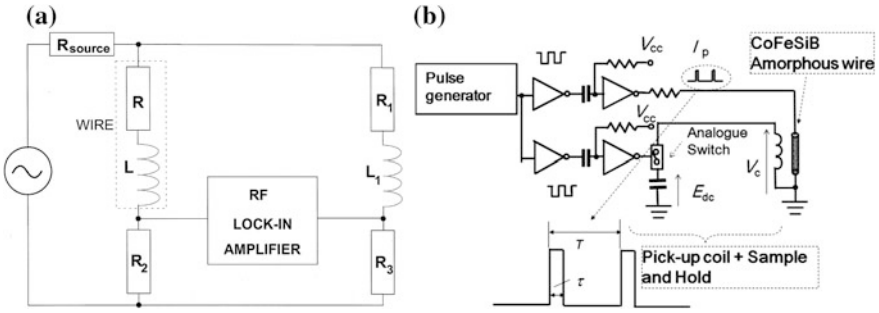

Fig. 8.1 **a** Simple circuit of a primary GMI sensor using a Co-rich amorphous wire (reprinted with permission from Elsevier [1]); **b** complex circuit of a modern GMI sensor using a Co-rich amorphous wire with a field resolution of up to 10^{-8} Oe and high thermal stability (reprinted with permission from Elsevier [2])

Schottky diodes for achieving high temperature stability [3] and many stable and highly sensitive GMI sensors [4–6].

For comparison, Table 8.1 summarises several magnetic induction sensor types, with their range and typical sensitivity. It is worth mentioning that the sensitivity of the GMI sensor is much higher than that of conventional magnetic sensors (e.g. Hall and GMR sensors). A pico-Tesla (10^{-8} Oe) resolution has been achieved for micro-GMI sensors making use of ultralow intrinsic magnetic noise in Co-rich amorphous wires with the pulse GMI effect. This type of sensor is useful especially for biomagnetic measurements without any magnetic shielding at room temperature. Therefore, the GMI sensor is superior to a superconducting quantum interference device (SQUID)-based sensor, which is highly sensitive but requires cryogenic liquids to operate. GMI sensors are also cost-effective, power-efficient, reliable, quick response, and portable [2–7].

8.1.2 Passive, Wireless Magnetic Field Sensors

By combining GMI sensors and the surface acoustic wave (SAW) transponder devices, Hauser et al. [8] designed a new wireless sensor for measuring magnetic fields. Figure 8.2 illustrates the diagram of a passive, wireless magnetic field sensor.

Table 8.1 Magnetic induction sensor types, range, and typical sensitivity

Sensor type	Magnetic induction typical range (Oe)	Typical sensitivity (Oe)
Hall	$1–10^{6}$	10
Magnetoresistance	$1–10^{6}$	1
Magnetoimpedance	$10^{-6}–1$	10^{-8}
Flux gate	$10^{-6}–1$	10^{-6}
SQUID	$10^{-9}–10^{-6}$	10^{-10}

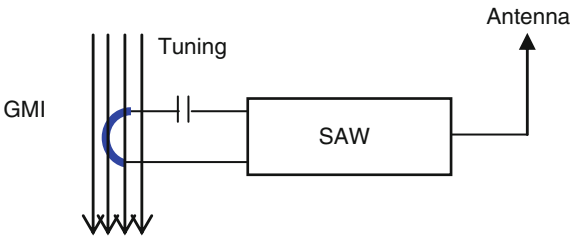

Fig. 8.2 Passive, wireless magnetic field sensor (reprinted with the permission of IEEE [8])

In this diagram, the GMI device is coupled with the second port of the SAW transponder, and the circuit is adjusted to the resonance of the transducer's capacitance. Tuning the resonance for one octave in frequency by applying a magnetic field to the GMI sensor can yield a sufficient effect for radio request readout. The main advantage of this sensor is that it can be used for applications where a magnetic field has to be measured without physical contact and where a wired power supply is not feasible for the sensor.

Recently, Al Rowais et al. [9] developed a wireless magnetic field sensor consisting of a three-layer thin-film GMI sensor and a SAW device on one substrate. However, it is unclear whether a sensor using a thin-film GMI sensor is more advantageous than one using a Co-based amorphous wire.

8.1.3 Current Sensors

Using a nearly zero magnetostrictive Co–Fe–Si–B amorphous wire, Valenzuela et al. [10] have successfully produced a current sensor based on the GMI effect. In this sensor, the dc current to be monitored flows through a solenoid, and the magnetic field produced by this solenoid on the wire leads to a controlled decrease of its impedance response. Consequently, the axial magnetic field dependence of impedance is used to measure the dc current accurately. The advantage of this sensor is its reduced dimensions, since the sensing element is a wire. In another work, Rheem et al. [11] developed a high-sensitivity current sensor based on the asymmetric GMI (AGMI) effect and using a field-annealed Co-based amorphous ribbon. Figure 8.3 shows the AGMI effect of the ribbon and a current sensor set-up utilising the AGMI effect of this ribbon. It has been shown that the sensor output voltage increases with applied current up to 1A with a good linearity. Due to the asymmetric characteristic of the GMI effect, this sensor can only measure dc currents. Obviously, the two GMI current sensors [10, 11] are suitable for dc current measurements but not for ac current measurements. This therefore warranted further development for a GMI current sensor that can be used to measure both dc and ac currents.

A new design of the contactless current GMI sensor has been reported [12]. A double-core structure was used in order to improve the temperature stability. The temperature coefficient of sensitivity and offset drift were reduced to one-half compared to a single-core sensor. It was also suggested that the design of this

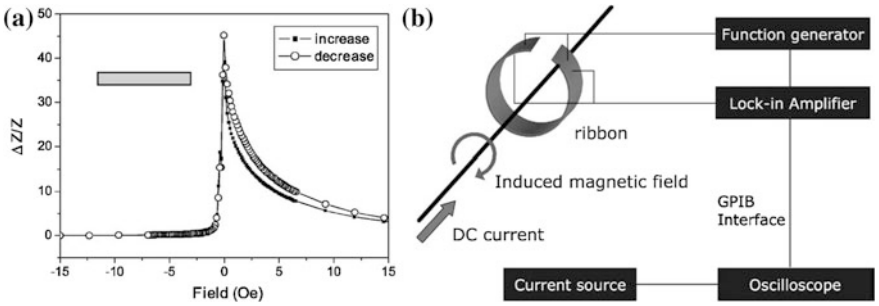

Fig. 8.3 **a** Asymmetric GMI of a field-annealed Co-rich amorphous ribbon and **b** the current sensor set-up based on the GMI effect of the ribbon (reprinted with the permission of Elsevier [11])

current sensor enhanced its stability as compared to that using the AGMI effect [11]. This is because the asymmetry in GMI was achieved by surface crystallisation as well as internal stress, which are often temperature-dependent and unstable in time. Recently, a high dynamic range dc–ac current sensor utilising the GMI effect has been developed [13]. The sensor exhibited good sensitivity (0.24 V/A) and very good linearity, free from hysteresis, in a wide dynamic range of ±40 A.

8.1.4 Stress Sensors

Based on the applied stress dependence of the GMI effect, Tejedor et al. [14] first proposed the development of stress sensors using amorphous ribbons. This showed that for a Co-based amorphous ribbon, the application of a tensile stress changes the effective anisotropy and influences the GMI effect. The maximum stress sensitivity of the effective anisotropy field ($\sim$214 MPa/Oe) is found at a given frequency of 1 MHz for the conventionally annealed ribbon. For the stress-annealed ribbon, the sensitivity is 167 MPa/Oe, and the impedance variation as a function of the applied stress is about 100 MPa/Ω.

Recently, a magnetoelastic sensor based on the stress dependence of the GMI effect in a Co–Mn–Si–B amorphous microwire has been introduced by [15]. This showed that the stress dependence of the GMI effect induced variation on the ac voltage measured between the ends of the sample placed in the magnetic field under applied tensile stress (Fig. 8.4). For instance, when the sample was under a load of 3 g, the change of the voltage across the microwire was found to be about 3.5 V [15]. The high sensitivity of the GMI ratio in responding to quite small values of mechanical load makes this stress-sensitive GMI effect promising for practical applications. More recently, utilising Co–Fe–Si–B amorphous ribbons and a unique magnetic field bias, Bowles et al. [16] developed a low-cost and high proportional change stress sensor. This stress sensor, combined with a battery-free analogue tag, allows the data to be transmitted inductively to a remote transceiver without a

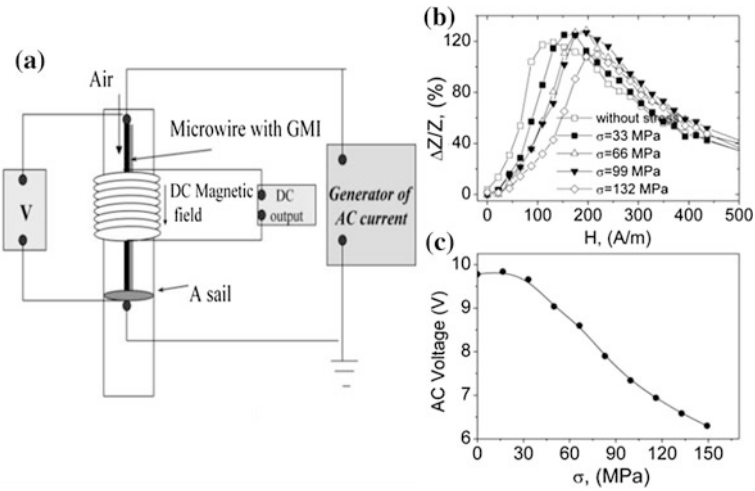

Fig. 8.4 Schematic representation of the magnetoelastic sensor based on stress dependence of GMI effect (**a**), $\Delta Z/Z(H)$ dependencies of Co–Mn–Si–B amorphous microwire measured at different applied stresses (**b**), and calibration curves of sensor (**c**) (reprinted with the permission of Elsevier [15])

hardwire connection. This showed that the stress-induced impedance sensor has several advantages over conventional stress sensors. For instance, a semiconductor strain gauge usually shows a change in resistance of only 15 % when strained to its maximum recommended stress level, while the amorphous alloy sensor has been demonstrated to show a large change in the inductance of 315 % when strained to its maximum working level [16]. Furthermore, a lower cost and power analogue electrical circuit is superior to the amorphous alloy sensor. Indeed, the discovery of the giant stress impedance (SI) effect in several amorphous wires [17] has provided the opportunity for developing these materials for novel stress-sensor applications.

8.1.5 RF and Energy Sensors

It has been shown that Co-rich amorphous microwires with vanishing magnetostriction exhibit both the GMI and the ferromagnetic resonance (FMR) effects [17]. While GMI is a large change in the ac impedance of a ferromagnetic conductor subject to an external magnetic field, FMR arises due to the precession of the magnetic moments of a ferromagnetic material when subjected to an external magnetic field, making the microwires attractive for electromagnetic energy absorption applications. Vazquez et al. [18–20] have attributed these two effects to the same origin in the microwires and established a correlation between them. As the microwires show excellent microwave absorption properties [19], they have recently been exploited for applications in metamaterials and structural health

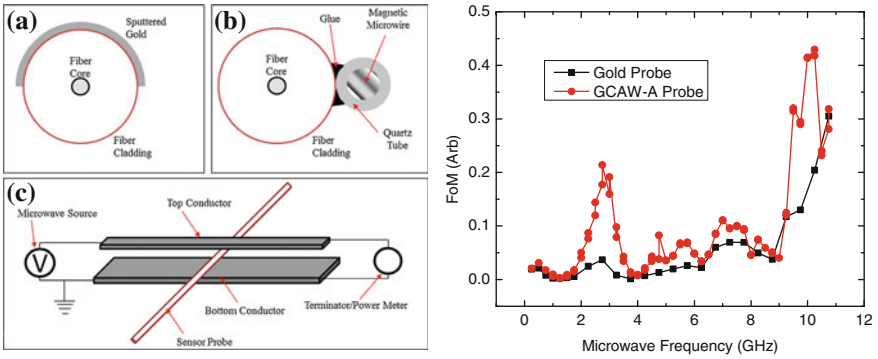

Fig. 8.5 *Left panel* Schematic of an FBG probe. Cross-sectional view of **a** the gold-based probe; **b** the microwire-based probe; **c** a sensor probe in the microstrip transmission line (TEM cell). The sensor was perpendicular to the length of the TEM cell conductors; *Right panel* FoM of the microwire-A microwire-based probe and the gold-based probe

monitoring [21, 22]. Very recently, Phan and co-workers have developed a new method of using a Co-rich glass-coated amorphous microwire as a microwave absorber for the fabrication of a fibre Bragg grating-based microwave energy sensor with improved sensitivity and less perturbation of the microwave field [23]. As compared to a similar approach that uses gold to absorb electromagnetic radiation, the microwire yields a device with greater sensitivity ($\sim$10 times at f = 3.25 GHz) relative to the perturbation of the microwave field. The set-ups of the energy sensors using two different probes and their sensitivities achieved over a wide frequency range are displayed in Fig. 8.5.

To optimise the overall performance of the sensor, the relationship between the magnetic properties, GMI, and microwave absorption effects in the microwires has been thoroughly investigated by the same group [24]. The authors have demonstrated that the larger GMI and microwave absorption effects achieved in the microwires originate mainly from higher saturation magnetisation, given that the coercivity, the effective anisotropy field, and the thickness of the glass-coating layer are the same. This knowledge is essential in tailoring the magnetic and microwave properties of microwires for RF and energy sensing applications. Since this type of sensor is physically small and minimally perturbs the field being measured, it can be deployed as a distributed sensor.

8.1.6 Temperature Sensors

Based on the temperature dependences of GMI and inductance of amorphous microwires exhibiting low Curie temperatures, Zhukov and co-workers have proposed different types of temperature sensors [25, 26]. The basic set-up and working principle of a GMI-based temperature sensor are displayed in Fig. 8.6.

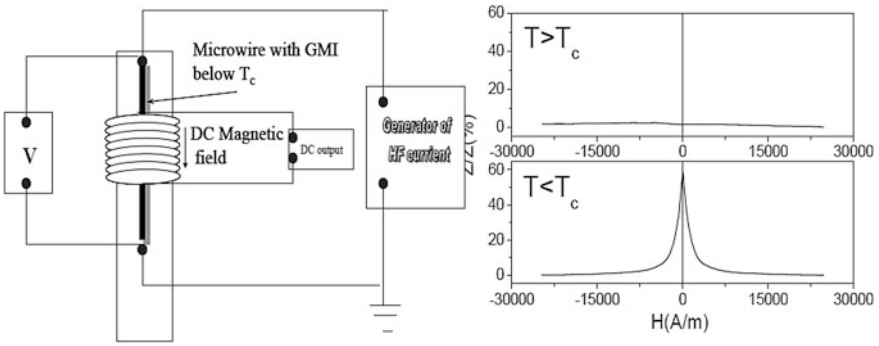

Fig. 8.6 *Left panel* Basic set-up of a GMI-based temperature sensor. *Right panel* using the drastic variation in GMI in the vicinity of the Curie temperature (reprinted with the permission of Elsevier [25])

It can be seen in Fig. 8.6 (left panel) that the GMI-based temperature sensor operates by utilising the drastic variation in GMI signal in the ferromagnetic ($T < T_C$) and paramagnetic ($T > T_C$) regimes in the vicinity of the Curie temperature of the microwire. A similar mechanism is applied to the case of inductance-based temperature sensors. In both cases, it should be noted that the sensitivities and working ranges of the sensors depend strongly on variations in the magnetisation at the Curie temperature. These sensors may find useful applications in automatically switching temperature-on/off systems. On the other hand, since the temperature of the microwire varies sensitively with microwave field intensity [23, 24], it is possible to design a new class of microwave field sensor for temperature sensing. Further research is needed to fully exploit this possibility.

8.2 Applications of Giant Magnetoimpedance-Based Sensors

Many industrial and engineering applications of GMI have been proposed to date, including computer disk heads, rotary encoders, pin-hole detectors, displacement and detection sensors, direction sensors for navigation (electronic compass), current sensors, field sensors, stress sensors, biomedical sensors, environmental sensors, car traffic monitoring, anti-theft systems, and so forth. Here, we briefly describe some GMI-based sensing devices of practical importance.

8.2.1 Target Detection and Control of Industrial Processes

A magnetic field sensor based on the GMI effect (or a GMI sensor) in an amorphous wire can be used to detect the presence or passage of moving objects, simply by fixing a small permanent magnet on the vehicles/pieces [27], as displayed in Fig. 8.7.

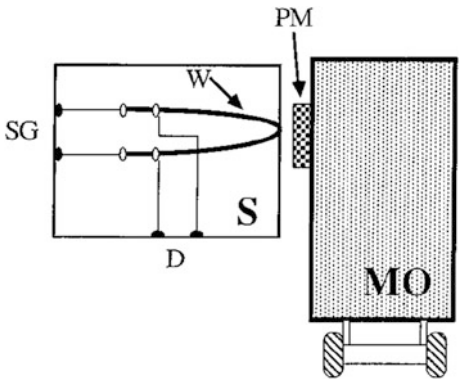

Fig. 8.7 Layout of the sensor and the moving vehicle, showing the sensor (S), the wire (w), the moving vehicle (MO), the permanent magnet (PM), and the signal generator (SG) and detector circuit (D) contacts, respectively (reprinted with the permission of AIP [27])

The detection is observed as a decrease in the ac voltage on the wire's ends. Such a device has been used to monitor and control many industrial processes, and the advantages of using GMI sensors include simplification and low costs for devices fabrication. Indeed, the monitoring and control systems employing GMI sensors have been found to be much superior to those based on optical devices in the case of industrial processes involving (non-magnetic) dusty atmospheres. From this perspective, the passive and wireless magnetic field sensor is best suited for remote control of industrial processes [2].

Recently, a new type of magnetic sensing device based on the GMI effect, the so-called nano-GMI sensor, has been developed [28]. It has been used in anti-lock brake systems (ABS) and the electric injector speed measuring for automotive and truck industries (see Fig. 8.8).

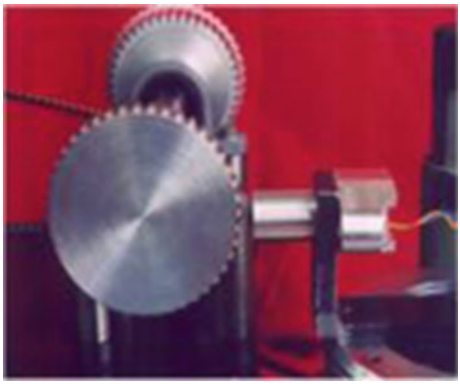

Fig. 8.8 Picture of an anti-lock brake system (ABS) using nano-GMI sensor (reprinted with the permission of [28])

8.2.2 *Space Research and Aerospace Applications*

The role of magnetic sensors is important in the field of space physics research. For instance, accurate measurement of the ambient magnetic field vector and its orientation in space can be achieved with the use of highly sensitive magnetic sensors such as GMI sensors. The space magnetic instruments utilising the GMI sensors can be used on board spacecraft to precisely measure magnetic fields in space. These magnetic sensors can also be used to eliminate the sources of stray magnetic fields generated by complex systems of mechanical, electrical, and electronic components on board the spacecraft.

Magnetic sensors have played an important role in aerospace applications [29]. Figure 8.9 shows a road map for space applications of AMR and GMR technologies. As compared to the AMR and GMR sensors, the higher sensitivity of the GMI sensor makes it more attractive for aerospace applications. For instance, in aerocraft engines the precise determination of the gear-tooth position can be achieved with the use of high-sensitivity magnetic sensors such as GMI sensors [30]. This gear-tooth sensor detects the presence and absence of a gear tooth made of a ferrous material. It detects a fixed level of magnetic field when no magnetic material is present over it. When a tooth moves over the sensor, the ferrous material acts a flux concentrator, thus leading to a change of the magnetic flux that can be detected by the sensor. Consequently, the sensor can be used to control the speed of the gear as

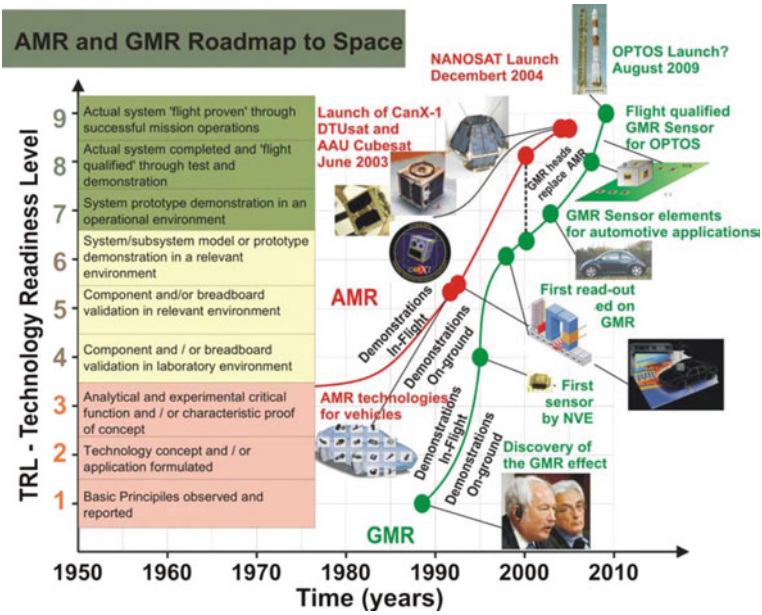

Fig. 8.9 Road map for space applications of AMR and GMR technologies (reprinted with the permission of Elsevier [29])

well as determining the gear-tooth position precisely. Furthermore, the development of non-contact switching systems utilising magnetic sensors has been successful in greatly improving the safety standards of flights. In this case, the GMI sensors can be ideal because of their ultrahigh sensitivity.

8.2.3 Electronic Compasses

Electronic compasses using flux gate (FG) sensors are used for a wide variety of engineering and electronic devices such as in cars, small boats, and for mobile phones. However, the disadvantages of electronic compasses using FG sensors include large size and high power consumption. Recently, the development of electronic compasses using GMI sensors has proved very successful [2–7]; when compared with the FG sensor, the GMI sensor is much reduced in its dimensions and has low power consumption (see Fig. 8.10).

8.2.4 High-Density Information Storage

Today, magnetic sensors play an important role in magnetic storage disks and tape drives [31]. In particular, the reading module comprises a special GMR or GMI sensor that is a multilayer structure consisting of magnetic and non-magnetic layers. The writing module operation induces local magnetic moments in bit areas of the hard disk magnetic layer. Bits with remanent magnetisation cause measurable change in the resistance of the GMR or GMI sensor of the reading module, which enables one to distinguish between two levels of digital signal. It should be emphasised that because the sensitivity of the GMI sensor is much higher than that of the GMR sensor, the GMI sensors will be the future option for magnetic storage disks and tape drives. Indeed,

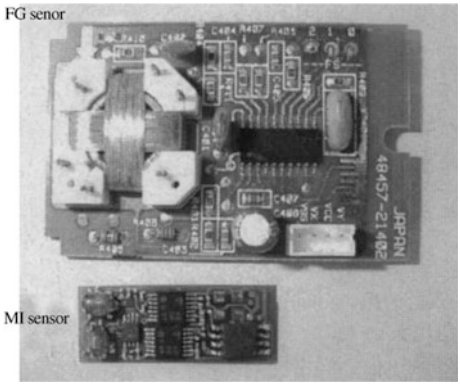

Fig. 8.10 Comparison of flux gate (FG) and magnetoimpedance (MI) electronic compasses. The size of the MI sensor is much smaller (reprinted with the permission of Elsevier [2])

GMI chips with extremely high reproducibility have been successfully manufactured and used in electronic circuits of computer and mobile devices [2–7].

8.2.5 *Traffic Control*

Accidents and jams present serious problems in our transportation; this is partially due to the lack of automatic controlling and monitoring systems. Many systems such as ultrasonic sensors and video cameras have been used for monitoring traffic conditions. Uchiyawa et al. [32] proposed and developed a new car-sensing system using an amorphous wire GMI sensor built into a disk set on the road. A systematic illustration of this device is presented in Fig. 8.11. When a car passes over the disk, the GMI sensor detects stray fields from the car body. The speed and length of a car can be estimated by processing the signals from two GMI sensors. Using a microcomputer, the disk system can record the length, velocity, and time for 2000 cars. The advantages of this sensing technique are that it can be easily installed, it is insensitive to weather conditions, it does not obstruct the stress surface, and it is very reliable. The new sensing system is useful for automatic traffic measurements.

8.2.6 *Magnetic Tracking Systems*

Using GMI sensors and magnet markers, magnetic guidance systems have been designed and developed for use in the automated highway system (AHS). One example is a car that can drive itself automatically using this magnetic guidance system, as shown in Fig. 8.12 [2]. Research on the automatic control of a car has been carried out mainly in Japan. In this research, the magnetic markers are fixed into the road, and the GMI sensors are placed on the car to sense the position of these markers. By travelling from marker to marker, the car can automatically drive without the help of a driver (see Fig. 8.12). In similar principles, these magnetic

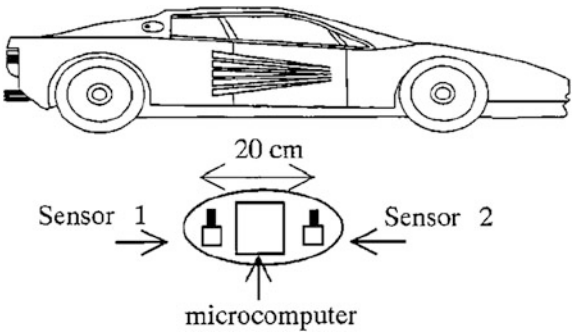

Fig. 8.11 Car-sensing system using two MI sensors and a microcomputer built into the disk set on the road (reprinted with the permission of IEEE [32])

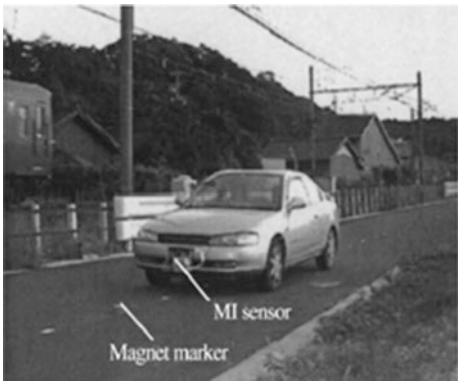

Fig. 8.12 Automated highway system (AHS) experiment with a MI sensor: this car drives automatically without a driver (reprinted with the permission of Elsevier [2])

guidance systems can be used in many industrial processes involving the automatic control of transporting products.

8.2.7 Magnetic Rotary Encoders

Switch-type GMI sensors can be used in magnetic encoders because of their ultrahigh sensitivity. These sensors are superior for producing a simplified and less expensive product with increased management control over conventional magnetic sensors [29]. Recently, He and co-workers have developed a sensitive magnetic sensor using a Fe–Co–Si–B amorphous wire and a coil wrapped around it [33]. To show the sensitivity and the spatial resolution, the magnetic field of a Japanese 1000 yen bill was scanned using this newly developed sensor Fig. 8.13.

Fig. 8.13 Scanning result of Japanese 1000 yen bill using the GMI field sensor (reprinted with the permission of MDPI [33])

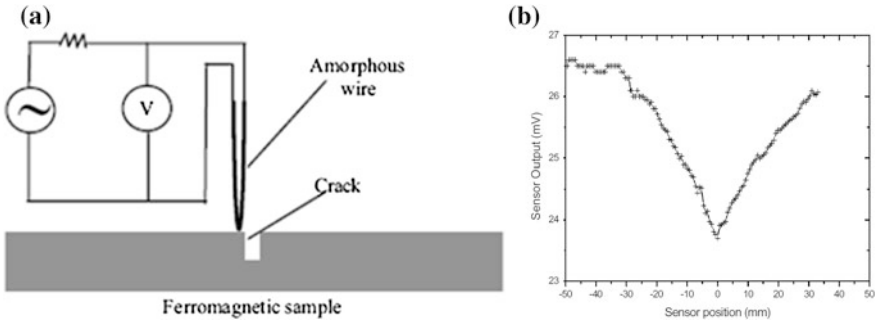

Fig. 8.14 *Left panel* a circuit diagram of the amorphous wire as GMI sensor and a crack. *Right panel* GMI sensor output as a function of the position of the Co–Fe–Si–B amorphous wire sensor at a driving current frequency of 1 MHz (reprinted with the permission of AIP [34])

Figure 8.14 shows a circuit diagram of the amorphous wire GMI sensor used for crack detection (the left panel). It can be seen from the right panel of Fig. 8.14 that there is a large decrease in the output voltage of the GMI sensor circuit when the sensor is moved across the crack [34]. This indicates that the GMI sensor can be used for non-destructive crack detection.

8.2.8 Non-destructive Crack Detection

Magnetic methods of non-destructive evaluation have been widely used either to monitor the material state and properties or to find defects. For instance, the eddy current method and the residual magnetic field technique are often used to prevent catastrophic breakage of mechanical parts in machines. In this context, the GMI sensor can be used either to detect magnetic fields created by current passing through conductors or to detect localised magnetic fields [34, 35]. The lack of continuity resulting from a crack produces disturbance in the magnetic field in the material, and the magnitude of the disturbance is determined by the size and shape of the crack. In particular, the GMI property of the amorphous wire can be used to capture cracked regions in the materials.

8.2.9 Biological Detection

In biomedical applications, magnetic methods have proved useful for disease treatments and improving human health. For instance, magnetic trackers are used to determine the position of medical tools inside the body (e.g. endoscope, colonoscope, and biopsy needle) and to observe biomechanical motions. Magnetopneumography is a magnetic method that can detect ferromagnetic dust deposited in human lungs by

using its magnetic moment after dc magnetisation. In fact, the sources of magnetic induction in biological systems (e.g. body, human brain, and animals) are detected to be very small; the magnetic field range is 10^{-10}–10^{-5} Oe. In order to detect such small magnetic fields, the requirement for a detection device lies in its high sensitivity. A miniature GMI magnetic sensor should be the option, because it can detect magnetic fields as small as 10^{-8} Oe.

A new type of magnetic sensing device utilising the miniature GMI sensor has been designed successfully for biological detection, such as fast identification and diminution of the direction threshold of pathogens or other targeted biomolecules (e.g. DNA, RNA, antibodies, and metabolites). This magnetic method has proved to be superior to the classical methods (electrical, electrochemical, and optical). That is, while the main disadvantages of the classical methods are high cost, time-consuming, and high detection threshold, the magnetic method provides several advantages such as rapid results, multianalyte detection, low cost, and reduced waste handling. The produced new magnetic sensing device (e.g. GMI-based biomagnetic sensor) comprises a magnetic wire or ribbon as a GMI sensing element [36–42]. A typical example is illustrated in Fig. 8.15 [37]. The principle of the GMI-based biosensor is briefly described as follows. The labelled target biomolecules are intercepted on the sensing element surface by fixed specific natural or artificial bioreceptors such as aaDNA, antibodies, proteins, and enzymes. Thereafter, the functionalised magnetic microparticles (e.g. streptavidin magnetic beads) are introduced to mark the structures formed on the sensing element surface. The magnetic microparticles with high affinity for target biomolecules (e.g. biotinylated biomolecules) are designed to be attached to each magnet biomolecule. Subsequently, upon the application of an external magnetic field, the magnetic microparticles bound to the sensing element's active surface will develop a dipole field that will be detected by the GMI sensor. Accordingly, the sensor impedance

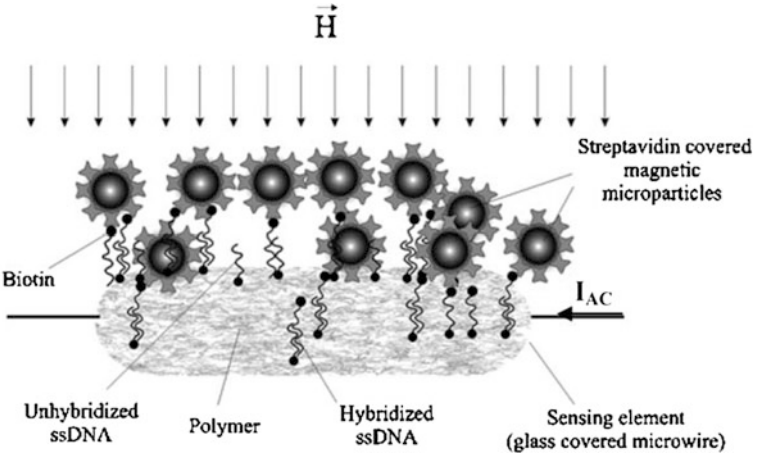

Fig. 8.15 The principle of a GMI-based magnetic biosensor using the ssDNA hybridisation phenomenon (reprinted with the permission of Elsevier [37])

will be modified proportionally to the magnetic microparticle concentration. Consequently, the target biomolecules will be detected and quantitatively evaluated.

Recently, the research group led by Phan has successfully integrated the radio-frequency magnetoimpedance technology with superparamagnetic nanoparticles to develop a novel biosensing platform for quick, reliable, and sensitive detection of cancer cells and biomolecules [38–40]. Instead of developing a biosensor based on the conventional MI effect, which has limited sensitivity, the authors have demonstrated that by exploiting the MR and MX effects it is possible to improve the sensitivity of the biosensor by up to 50 and 100 %, respectively [38]. The MX-based approach shows the most sensitive detection of superparamagnetic nanoparticles at low concentrations, demonstrating a sensitivity level comparable to that of a SQUID-based biosensor. It is cryogen-free and operates at room temperature, providing a promising avenue to the development of low-cost highly sensitive biosensors. The biosensor has been successfully employed to detect and quantify various bioanalytes, such as Curcumin-type anticancer drugs, bovine serum albumen (BSA) proteins, and Lewis lung carcinoma (LLC) cancer cells that have taken up surface-functionalised iron oxide nanoparticles [39, 40]. Since the iron oxide nanoparticles are widely used as magnetic resonance imaging (MRI) contrast agents, the newly developed biosensing technique can also be used as a new, low-cost, fast, and easy predetection method before MRI.

Using the ultrasensitive wire-based GMI field sensors, the research group led by Mori has developed many novel biosensing devices for the detection of magnetic activity that enables non-contact and non-invasive evaluation of electrical activity in humans [41–44]. The biomagnetic field in the living cell tissue has been successfully detected using pT-MI sensor. Figure 8.16a illustrates the experimental set-up for detection of biomagnetic fields in a living tissue. The stomach musculature of a guinea pig was used, which produces pace-making electric activity with a rather regular cycle even after isolation. The results of simultaneously detected time series of the electric and magnetic oscillatory signals are displayed in Fig. 8.16b. These studies have demonstrated the high capacity of using the pT-MI sensors to detect cardiac magnetic activity in several healthy subjects, and suggest future applications of this biosensing technology in biomedicine.

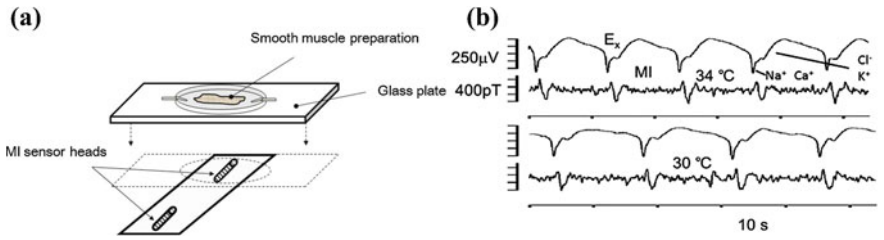

Fig. 8.16 **a** Experimental set-up for measuring the active magnetic field in smooth muscle preparations, which are dipped in a circulating wormed physiological saline solution. **b** Measured results of simultaneously detected time series of the electric and magnetic oscillatory signals for a guinea pig stomach preparation (reprinted with the permission of IEEE [3])

8.2.10 Magnetic Anomaly Detection and Geomagnetic Measurements

Our living system is governed in nature by the Earth's magnetic field, the magnitude of which may vary from 10^{10} Oe to 10^{-4} Oe when going from inside the Earth to the Earth's surface. Nevertheless, the magnitude of the Earth's surface magnetic field varies between 10^{-4} and 1 Oe depending upon its geometry. The detection and orientation of the Earth's magnetic field have found wide applications in petroleum and minerals exploration or shielding used for degaussing of high-performance monitors [29]. However, because the Earth's magnetic field is very small, detecting it is a difficult task, and this requires a highly sensitive magnetic sensor. This requirement can be fulfilled by using a GMI sensor. A GMI-based sensing element (e.g. wire or microwire) as small as 1 mm used in the constructed GMI sensor can be used to detect magnetic anomalies and localised weak magnetic fields. Many devices utilising the GMI sensors have been used in anti-theft systems and in magnetic marking and labelling technology. The GMI sensor can be used to eliminate the error of measurements due to the effect of the Earth's magnetic field. It can also be used for the detection of stray magnetic fields created by engines and machines during their operating processes.

8.2.11 Stress-Sensing Applications

Altering the GMI response with mechanical stress paves the way towards the development of strain sensors. For example, engineers and manufacturers have been faced with the problem of the accurate measurement of torque. The new finding of the giant impedance-stress effect in amorphous wires or ribbons offers a new opportunity to develop strain sensors that can be used for accurate measurements of torque [17].

Stress-induced impedance sensors utilising amorphous alloys have proved useful for wireless, battery-free applications. A demonstration unit has recently been developed for vehicle tyre pressure monitoring (see Fig. 8.17). A quick response acceleration sensor has been constructed using the SI element of amorphous wires combined with a CMOS IC multivibrator [3]. This sensor has a very high sensitivity so its application to the sensing of road bridge seismovibration due to passing cars has been realised.

8.2.12 Other Applications

Many other applications of GMI can be found in [2–7, 26]. In these cases, such magnetic sensing devices utilising GMI-based sensors can be used to measure

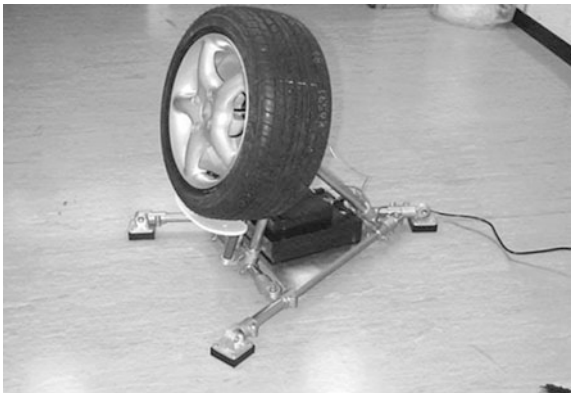

Fig. 8.17 Tyre pressure monitoring system incorporating an amorphous alloy wireless, battery-free sensor (reprinted with the permission of Elsevier [17])

variables, instead of measuring magnetic field or current. However, some of these devices usually use principles similar to those of magnetic field sensors [26]. Aside from this, it is emphasised that GMI has been successfully used as a research tool to investigate intrinsic and extrinsic magnetic properties of novel artificially grown soft magnetic materials [17, 45].

References

1. Atkinson D, Squire PT, Maylin MG, Gore J (2000) An integrating magnetic sensor based on the giant magneto-impedance effect. Sens Actuators A 81:82–85
2. Honkura Y (2002) Development of amorphous wire type MI sensors for automobile use. J Magn Magn Mater 249:375–377
3. Uchiyama T, Mohri K, Life Fellow, IEEE, Honkura Y, Panina LV (2012) Recent advances of pico-tesla resolution magneto-impedance sensor based on amorphous wire CMOS IC MI sensor. IEEE Trans Magn 48:3833
4. Kawajiri N, Nakabayashi M, Cai CM, Mohri K, Uchiyama T (1999) Highly stable MI micro sensor using C-MOS IC multivibrator with synchronous rectification. IEEE Trans Magn 35(5):3667–3669
5. Mohri K, Uchiyama T, Shen LP et al (2002) Amorphous wire and CMOS IC-based sensitive micromagnetic sensors utilizing magnetoimpedance (MI) and stress-impedance (SI) effects. IEEE Trans Magn 38(5):3063–3068
6. Mohri K, Humphrey FB, Panina LV et al (2009) Advances of amorphous wire magnetics over 27 years. Phys Status Solidi A 206(4):601–607
7. Mohri K, Uchiyama T, Panina LV, Yamamoto M, Bushida K (2015) Recent advances of amorphous wire CMOS IC magneto-impedance sensors: innovative high-performance micromagnetic sensor chip. J Sens Article ID 718069:8
8. Hauser H, Steindl R, Hausleitner C, Pohl A, Nicolics J (2000) Wirelessly interrogable magnetic field sensor utilizing giant magnetoimpedance effect and surface acoustic wave devices. IEEE Instrum Measur 49:648–652
9. Al Rowais H, Li B, Liang C, Green S, Gianchandani Y et al. (2011) Development of a passive and remote magnetic microsensor with thin-film giant magnetoimpedance element and surface acoustic wave transponder. J Appl Phys 109:07E524

10. Valensuela R, Freijo JJ, Salcedo A, Vazquez M, Hernando A (1997) A miniature dc current sensor based on magnetoimpedance. J Appl Phys 81:4301–4303
11. Rheem YW, Kim CG, Kim CO, Yoon SS (2003) Current sensor application of asymmetric giant magnetoimpedance in amorphous materials. Sen Act A 106:19–21
12. Malátek M, Ripka P, Kraus L (2005) Double-core GMI current sensor. IEEE Trans Magn 41:3703–3705
13. Asfour A, Yonnet JP, Zidi M (2012) A high dynamic range GMI current sensor. J Sens Technol 2(4):7p. Article ID:25485. doi:10.4236/jst.2012.24023
14. Tejedor M, Hernando B, Sanchez ML, Prida VM, Vazquez M (2001) Magneto-impedance effect in amorphous ribbons for stress sensor application. Sens Actuators A 81:98–101
15. Cobeno AF, Zhukov A, Blanco JM, Larin V, Gonzalez J (2001) Magnetoelastic sensor based on GMI of amorphous microwire. Sen Act A 91:95–98
16. Bowles A, Gore J, Tomka G (2005) A new, low-cost, stress sensor for battery-free wireless sensor applications. Proc SPIE Int Soc Opt Eng 5765:1104–1111
17. Phan MH, Peng HX (2008) Giant magnetoimpedance materials: fundamentals and applications. Prog Mater Sci 53:323
18. Lofland SE, Garcia-Miquel H, Vazquez M, Bhagat SM (2002) J Appl Phys 92:2058
19. García-Miquel H, Esbrí MJ, Andrés JM, García JM, García-Beneytez JM, Vázquez M (2001) IEEE Trans Magn 37:561
20. Dominguez M, Garcia-Beneytez JM, Vazquez M, Lofland SE, Bhagat SM (2002) J Magn Magn Mater 249:117
21. Peng HX, Qin FX, Phan MH, Tang J, Panina LV, Ipatov M et al (2009) J Non-Cryst Solids 355:1380
22. Qin FX, Peng HX (2013) Prog Mater Sci 58:183
23. Colosimo P, Chen A, Devkota J, Srikanth H, Phan MH (2014) Sensing RF and microwave energy with fiber Bragg grating heating via soft ferromagnetic glass-coated microwires. Sens Actuators, A 210:25
24. Devkota J, Colosimo P, Chen A, Larin VS, Srikanth H, Phan MH (2014) Tailoring magnetic and microwave absorption properties of glass-coated soft ferromagnetic amorphous microwires for microwave energy sensing. J Appl Phys 115:17A525
25. Zhukov A, Zhukova V (2009) In magnetic properties and applications of ferromagnetic microwires with amorphous and nanocrystalline structure. Nova Science Publishers, Hauppauge, NY, pp 1–162
26. Zhukova V, Ipatov M, Zhukov A (2009) Thin magnetically soft wires for magnetic microsensors. Sensors 9:9216–9240
27. Valensuela R, Vazquez M, Hernando A (1996) A position sensor based on magnetoimpedance. J Appl Phys 79:6549–6591
28. http://www.snpc.org.cn
29. Díaz-Michelena Marina (2009) Small magnetic sensors for space applications. Sensors 9:2271–2288. doi:10.3390/s90402271
30. Lenz JE (1990) A review of magnetic sensors. Proc IEEE 78:973–989
31. Maekawa S, Shinjo T (eds) (2002) Spin dependent transport in magnetic nanostructures. Gordon and Breach Science Publishers, New York (Advances in Condensed Matter Science. Vol. 3)
32. Uchiyawa T, Mohri K, Itho H, Nakashima K, Ohuchi J, Sudo Y (2000) Car traffic monitoring system using MI sensor built-in disk set on the road. IEEE Trans Magn 36:3670–3672
33. He Dongfeng, Shiwa Mitsuharu (2014) a magnetic sensor with amorphous wire. Sensors 14:10644–10649. doi:10.3390/s140610644
34. Kim DJ, Park DA, Hong JH (2002) Nondestructive evaluation of reactor pressure vessel steels using the giant magnetoimpedance sensor. J Appl Phys 91:7421–7423
35. Goktepe M, Ege Y, Bayri N, Atalay S (2004) Torsional stress impedance effect in $Fe_{71}Cr_7Si_9B_{13}$ amorphous wire. Phys Status Solidi (c) 1:3436–3439

36. Kurlyandskaya GV, Sanchez ML, Hernando B, Prida VM, Gorria P, Tejedor M (2003) Giant-magnetoimpedance-based sensitive element as a model for biosensors. Appl Phys Lett 82:3053–3055
37. Chiriac H, Tibu M, Moga AE, Herea DD (2005) Magnetic GMI sensor for detection of biomolecules. J Magn Magn Mater 293:671–673
38. Devkota J, Ruiz A, Wang C, Mohapatra S, Mukherjee P, Srikanth H, Phan MH (2013) Detection of low-concentration superparamagnetic nanoparticles using an integrated radio frequency magnetic biosensor. J Appl Phys 113:104701
39. Devkota J, Trang MT, Stojak K, Ha PT, Pham HN, Ngo TL, Phuc NX, Mukherjee P, Srikanth H, Phan MH (2014) Synthesis, inductive heating, and magnetoimpedance-based detection of multifunctional Fe_3O_4 nanoconjugates. Sens Actuators B 190:715–722
40. Devkota J, Howell M, Mohapatra S, Mukherjee P, Srikanth H, Phan MH (2015) Magneto-reactance based detection of MnO nanoparticle-embedded Lewis lung carcinoma cancer cells. J Appl Phys 117:17D123
41. Uchiyama T, Nakayama S, Mohri K, Bushida K (2009) Biomagnetic field detection using very high sensitivity magneto-impedance sensors for medical applications. Phys Status Solidi A 206(4):639–643
42. Nakayama S, Atsuta S, Shinmi T, Uchiyama T (2011) Pulse-driven magnetoimpedance sensor detection of biomagnetic fields in musculatures with spontaneous electric activity. Biosens Bioelectron 27:34–39
43. Uchiyama T, Mohri K, Nakayama S (2011) Measurement of spontaneous oscillatory magnetic field of guinea-pig smooth muscle preparation using pico-tesla resolution amorphous wire magneto-impedance sensor. IEEE Trans Magn 47(10):3070–3073
44. Mohri K, Nakamura Y, Uchiyama T, Mohri Y, Mohri Yu, Inden Y (2010) Sensing of human micro-vibration transmitted along solid using pico-tesla magneto-impedance sensor (pT-MI sensor). Piers Online 6(2):161–164
45. Knobel M, Pirota KR (2002) Giant magnetoimpedance: concepts and recent progress. J Magn Magn Mater 242–245:33–40

Chapter 9
Multifunctional Microwire Composites: Concept, Design and Fabrication

With microwires fully discussed in the previous chapters, we now divert our attention to innovative microwire-based materials, i.e. advanced microwire multifunctional composites, which have attracted much attention [1] due to the multitude of their properties and the associated broad range of engineering applications, from structural health monitoring to electromagnetic interference shielding. From this chapter on, we will focus on the design, fabrication, and characterisation of microwire composites. In order to provide the readers with a comprehensive picture of this novel kind of composite, both the art of application-oriented design of versatile microwire composites and the fundamental physics will be fully discussed.

9.1 Concept of Multifunctional Composites

First of all, we need to understand the basic concept of multifunctional composites. A multifunctional composite conventionally refers to a composite material that, beyond the primary structural function, possesses other functionalities as well, achieved by constituent components in an optimised structure [2, 3]. Gibson [4] divided multifunctional composites into three types: (i) multiple structural functions, (ii) non-structural functions plus structural functions, and (iii) both. This is a classification of multifunctionalities in a broad sense. In view of the recent development and the trend of multifunctional composites, our discussion has been limited to type (ii), which we deem to be a judicious and strict definition. Therefore, two points are underscored in this definition: (i) the composite must have multiple functions, and (ii) they are enabled by the constitutive materials. Such logic may lead one to a picture of a complicated composite structure consisting of any specific materials according to the recipe of intended functionalities, without regard to the compatibility of these materials. However, the architecture design of the composite will be a huge issue to tackle. It will also be difficult to predict the properties of the resultant composite from those of the constitutive materials insofar as the physical and chemical interactions

H.-X. Peng et al., *Ferromagnetic Microwire Composites*,
Engineering Materials and Processes, DOI 10.1007/978-3-319-29276-2_9

between them are concerned. The brilliant idea of multifunctionalities is then tarnished by the high cost of manufacturing and maintenance. It appears that the making of this kind of composites remains far from ideal, as demonstrated by a wide spectrum of so-called multifunctional composites in the literature, inasmuch as they merely show a plus functionality at the expense, typically, of the mechanical performance. Strictly speaking, they are closer to multifunctional structures or systems rather than materials. To address these issues, the following should be realised: (i) an omnipotent functional filler is essential, in that it will ensure the achievement of multifunctionalities and a relatively simple composite architecture. This does not necessarily mean that all the functionalities must be exceptional. But the versatility thus obtained warrants no increase of cost, weight, and complexity [5]; (ii) a homogeneous material is a great priority for structural integrity and implementation, which can be approached in two ways: chemical intimacy between the fillers and matrix and extremely low loading of fillers that permits physical perturbations only. It is therefore reasonable to consider these standards as implicit behind the term of multifunctionalities, based on which the concept of truly multifunctional composites is initiated. To approach this concept, a couple of aspects are of major concern: (i) the functional fillers as described above and (ii) the topological arrangements of these fillers. To sum up, in realising the multifunctionalities, the filler answers the question of yes or no and the filler topology answers the question of how good it can be.

In line with this philosophy of multifunctional composites, microwires are certainly an ideal filler to be pursued in realising such composite materials in light of their following merits: (i) they are fine fillers with excellent mechanical properties. A typical glass-coated microwire fabricated by the Taylor-wire technique has a diameter of 1–30 μm, which can well match the size of reinforcing fibres such as carbon fibre and glass fibre. As such, they can retain, if not improve, the mechanical properties of structural matrix. (ii) They have superior GMI and GSI effects, rendering them useful inclusions into polymer matrices to realise microwave field-tunable composites and self-sensing smart composites. (iii) They have outstanding soft magnetic properties and good conductive properties, suggesting that they can be easily excited by the electromagnetic waves to realise many useful microwave behaviours such as absorption and negative refractive index. (iv) They are inexpensive and have strong market potential in the energy and aerospace engineering sectors, which have an increasing demand for multifunctional composites. In this context, multifunctional microwire composites have been developed to meet both the trend and the need.

9.2 Design and Preparation of Microwire Composites

9.2.1 General Design Strategy

As the microwire composites are expected to be applied in many different areas, their design should follow different criteria set by the application specifications.

The design of microwire composites mainly involves the following tasks: (1) **Choice of matrix**. This is relatively easy in the microwire composite case, as it is not required to have any special functional properties. But special polymers such as conjugated polymers can be a plus for some applications such as shielding; (2) **Choice of wires**. It has taken us seven chapters to discuss the close relationship between the wires' properties and numerous influencing factors such as geometry, composition, and post-processing conditions. When it comes to embedding microwires into polymer, these factors should also be considered, as the composite behaviour is very much dependent on the properties of the microwires embedded; and (3) **Mesostructure**, i.e. the topological arrangement of fillers. For this kind of two-phase heterogeneous composites, the mesostructure is believed to be the most crucial factor that dominates the composite behaviour [6]. In the case of microwire composites, the mesostructure is parametrised by the interwire spacing or concentration.

This subject will be treated from two categories of composites: continuous-wire composites and short-wire composites. Short-wire composites can also be subdivided into two categories according to whether the wires are randomly dispersed or periodically arranged. The design of microwire composites appears to be a complicated task, inasmuch as all the aforementioned relevant parameters may need to be varied to meet different application requirements. Without a full knowledge of these multiple functionalities, especially in terms of their relations with the composite structure, it is not possible to fulfil this task. Therefore, we attempt here just to outline the general principles, although more details are given in the later sections when individual cases are examined.

Generally speaking, to meet the basic structural requirement, a proper matrix should be adopted with either large strength or ductility. The wires should have a fine size and good mechanical properties. When it comes to the mesostructure, the long continuous wires should be aligned regularly and short wires are preferably homogeneously dispersed in the matrix, and a good interfacial bonding is always desirable. On the other hand, to realise various functionalities, some particular design of mesostructure is essential. Specifically, to realise a negative refractive index, a periodical arrangement of long continuous wires with proper interwire spacing is required. To obtain large magnetic field tunability, proper wire diameter and interwire spacing are needed to obtain the large relaxation parameters associated with the skin effect in a continuous-wire composite [7], while in the case of short-wire composites, the length and concentration of the microwires have to be fully considered [8]. For absorption purposes at a certain frequency, the relative permittivity and permeability play key roles, so the wire diameter, microstructure, and domain structure need to be carefully devised [9]. It is worth mentioning that, as there are conflicts arising from the requirement for different functionalities, it may be necessary to prioritise the need for target functionality but compromise on other, conflicting, functionalities. For example, at the same frequency, the absorption and metacomposite behaviours demand opposite characteristics of scattering spectra; this will be discussed in later sections.

Loosely defined, a microwire composite can be any form of material consisting of wires and a matrix material, although in engineering parlance, microwire

composites conforming to the above definition may not be able to serve general structural purposes and hence cannot be categorised as composite materials. In this book, the scope will be extended to any form of microwire composite, with a particular note of its application range. The emphasis is placed on the microwire composites that meet the quest for both functional and structural use.

9.2.2 *Microwires–Epoxy*

Epoxy is believed to be the most extensively used matrix material for all kinds of composites and coatings for engineering applications. Zhang et al. [10] prepared a microwire composite coating on the surface of aluminium plate using polyamine dissolved by alcohol. The resultant composite and microwires arrangement are shown in Fig. 9.1. Liu et al. [11] also used epoxy to cast the toroidal samples for microwave characterisation. Starostenko and Rozanov [12] fabricated a composite mat by coprecipitation of glass fibre and wire pieces in a dilute solution of polystyrene. It should be noted that the wire pieces used in these works are in the range of 5–10 mm. If the wires are too long, it will be challenging to realise a good dispersion of wire pieces and receive the 2D plane-isotropic composite. If the wires are too short, the demagnetising effect will be too strong and ruin the overall electromagnetic properties of the microwire composite. The type of composite thus made is suitable for microwave absorption or shielding as a functional coating layer.

9.2.3 *Microwires–Elastomers*

Compared to epoxy, elastomers usually have much smaller Young's modulus (2 MPa) and hence will strain appropriately when subject to even a relatively small

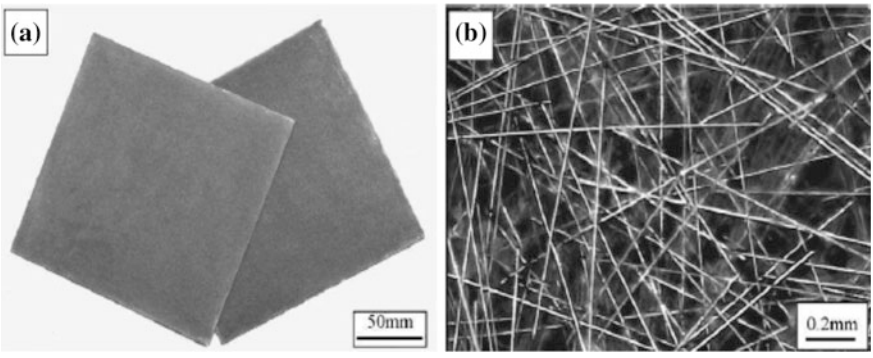

Fig. 9.1 Morphology of polymer composite plate sample (**a**) and arrangement of the short-cut microwires in it (**b**). Reprinted with permission from [10], copyright 2010 Elsevier

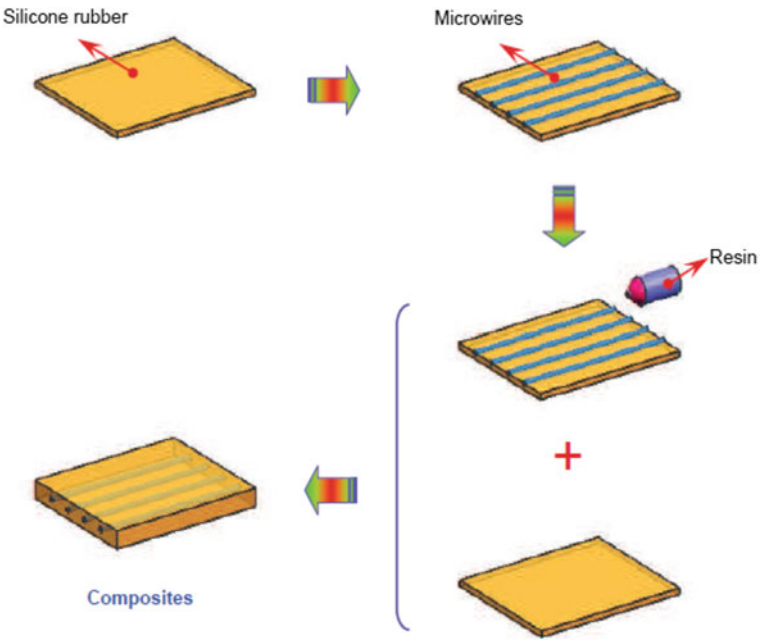

Fig. 9.2 Schematic of the preparation of continuous-wire composites based on silicone rubber for freespace measurements; the final dimensions of the resultant composite are 520 × 500 × 1.5 mm

force. Thus, rubber-based composites can then be exploited as high-performance stress self-sensing composites.

Qin et al. [13, 14] used two pieces of transparent silicone rubber sheets to prepare planar composites with periodically arranged continuous wires. The procedure schematically shown in Fig. 9.2 is as follows:

(1) 500-mm-long microwires were laid out in a periodical manner with a fixed wire spacing on the white sheet.
(2) Around 80 g of thoroughly stirred and vacuumed liquid silicone rubber/hardener mixture was uniformly cast on the surface as the adhesion layer, which was followed by covering the transparent layer right on top. An aluminium plate and heavy weights were then placed on top of the preform to assist the curing process in the ambient air.
(3) After 24 h, when the resin was cured, four surface-roughed glass fibre tabs of 10 mm × 500 mm with two drilled holes of diameter 6.35 mm were attached on both sides normal to the longitudinal direction of the sheet. The holes were designed for load bearing.
(4) The sample was then sent to an oven to cure the resin used for gluing the tabs at 70 °C for 1 h. As a final step, the holes in the tabs were further pierced through the sample, and strings were passed through the holes for fastening the weights for the study of the stress-tunable effect.

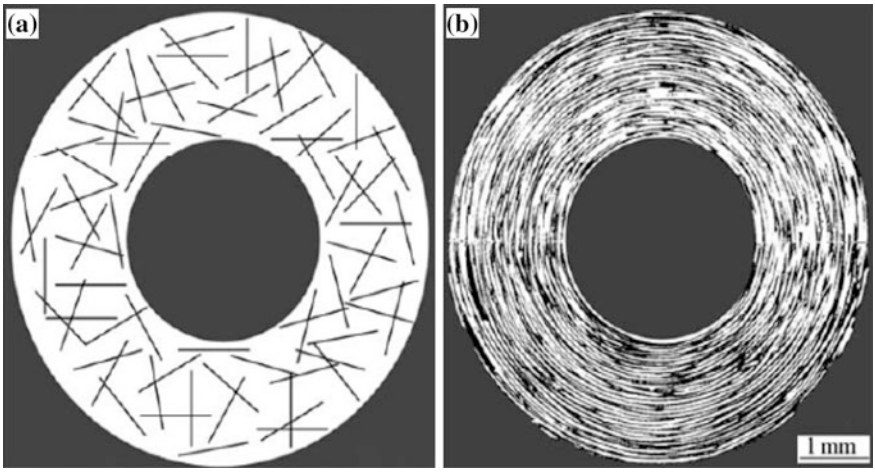

Fig. 9.3 Schematic structure of toroidal composites: **a** isotropic samples; **b** anisotropic sample. Reprinted with permission from [16], copyright 2007 Nonferrous Metals Society of China

For the case of short-wire composites, Marin et al. [15] dispersed 40 g of 1 mm Fe-rich microwires into silicon resin to receive a composite sheet for microwave absorption application. Di et al. [16] and Zhang et al. [10] used rubber dissolved by acetone to prepare composite of a toroidal ring shape, such that it could fit the specific sample holder used for the measurement by a vector network analyser. The wire arrangement can be made either regular or random, as shown in Fig. 9.3, which determines whether the composite is isotropic or anisotropic. Yet this kind of composite (inner diameter of 3 mm, outer diameter of 7 mm, height of 3.5 mm) is very small and has limited application.

9.2.4 Microwire E-glass Prepregs

E-glass prepregs have been widely used in industry and are themselves excellent structural composites. Naturally, using these as a matrix to make microwire composite secures the structural function even with a very small amount of microwires.

Reference [17] detailed the preparation of short-wire composites and continuous-wire composites with E-glass prepregs as matrices. For example, the preparation work of the short-wire composite was done in the following steps:

(1) 5-cm wire pieces were laid out at the zero degree along the glass fibre direction between the two layers of prepregs with in-plane size of 50 cm × 50 cm (the size may vary to fit different measurements). The wire spacing was controlled at fixed values of the order of centimetres (comparable to the wavelength at gigahertz range) in perpendicular and parallel directions as shown in Fig. 9.4

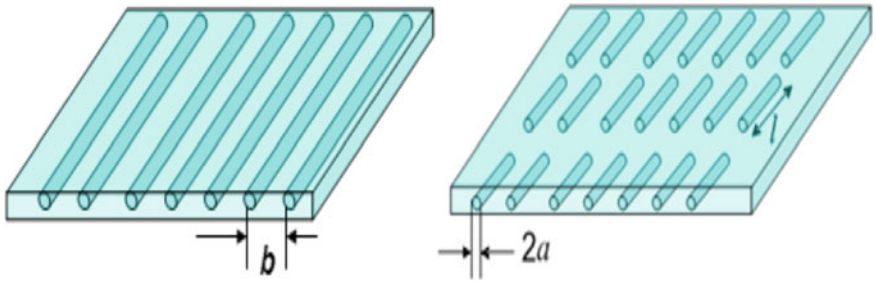

Fig. 9.4 Schematic of the continuous-wire composite, where *b* is the interwire spacing (*left-panel*) and short-wire composites (*right panel*), in which *a* denotes the wire radius and *l* denotes the wire length

(right panel). Note that the wire length and spacing are selected within the resolution range of the microwave measurements at gigahertz.

(2) Another two layers were laid up on the top and bottom of the wire-embedded layers in the same direction, giving a lay-up of four prepreg layers containing short wires.

(3) After bagging the composite on an aluminium plate with air sucked out to the required vacuum of 94.6–104.7 kPa, the material was cured in an autoclave. The curing conditions are as follows: the temperature was raised at a rate of 2 °C/min to 127 °C and kept for 80 min before cooling down naturally to room temperature. At a rate of 69 kPa/min, the pressure was increased to 206.7 kPa (30 psi) and kept at this level for 30 s and then 690 kPa for 600 min before decreasing at a rate of 20.7 kPa/min.

With the same procedure, one can also prepare the continuous-wire composite and fishnet-structured composites. These will be especially useful for realising metacomposites characteristics. In comparison with the short-wire composites, they are much easier to fabricate and hence have a better application perspective.

A typical in-plane view of prepreg-based wire composite is shown in Fig. 9.5a. On the exterior surface, one can see several ridges of different colours from other regions (indicated by arrows), which is attributed to a non-uniform distribution of the resin and glass fibre in the prepregs, as revealed in the scanning electron microscope image of the cross section (Fig. 9.5b). It is the microwire, which is slightly larger than the glass fibres in diameter, that results in the non-uniform distribution of the resin in the region close to it. However, this influence of the microwires is limited to the near-wire region only and is comparable to the inherent defects in the prepregs.

Besides, since the wire composite is intended to contain a very small number of wires that are separated by spacings of a few millimetres to a few centimetres, which is 3–4 orders of magnitude higher than the diameter of the microwires, the disruption of microwires to the composite integrity is minimal.

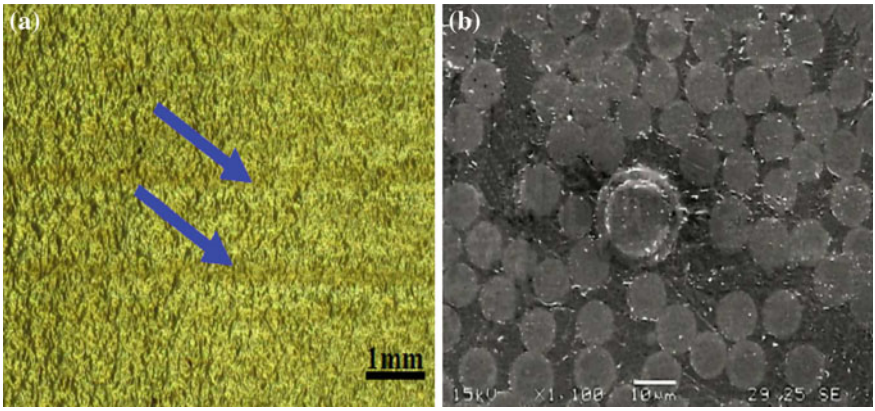

Fig. 9.5 **a** In-plane view optical micrograph of composite surface and **b** a cross-sectional SEM image of the composite where the single metal wire with both glass coating and glass fibres in the composite is shown. Reprinted with permission from [18], copyright 2010 Elsevier

References

1. Qin FX, Peng HX (2013) Ferromagnetic microwires enabled multifunctional composite materials. Prog Mater Sci 58:183–259
2. Torquato S, Hyun S, Donev A (2002) Multifunctional composites: optimizing microstructures for simultaneous transport of heat and electricity. Phys Rev Lett 89:266601
3. Thomas JP, Qidwai MA (2004) Mechanical design and performance of composite multifunctional materials. Acta Mater 52:2155–2164
4. Gibson RF (2010) A review of recent research on mechanics of multifunctional composite materials and structures. Compos Struct 92:2793–2810
5. Asanuma H (2003) Formation of sensitive phases in metal and polymer based structural materials for health monitoring. Struct Health Monit 2:169–178
6. Brosseau C, Queffelec P, Talbot P (2001) Microwave characterization of filled polymers. J Appl Phys 89:4532–4540
7. Panina LV, Ipatov M, Zhukova V, Zhukov A, Gonzalez J (2011) Magnetic field effects in artificial dielectrics with arrays of magnetic wires at microwaves. J Appl Phys 109:053901
8. Ipatov M, Zhukova V, Panina LV, Zhukov A (2009) Ferromagnetic microwires composite metamaterials with tuneable microwave electromagnetic parameters. PIERS Proc 5:586–590
9. Wang H, Qin FX, Xing D, Cao F, Wang XD, Peng H, Sun J (2012) Relating residual stress and microstructure to mechanical and GMI properties in cold-drawn co-based amorphous microwires. Acta Mater 60:5425–5436
10. Zhang Z, Wang C, Zhang Y, Xie J (2010) Microwave absorbing properties of composites filled with glass-coated $Fe_{69}Co_{10}Si_8B_{13}$ amorphous microwire. Mater Sci Eng B 175:233–237
11. Liu L, Kong L, Lin G, Matitsine S, Deng C (2008) Microwave permeability of ferromagnetic microwires composites/metamaterials and potential applications. IEEE Trans Magn 44: 3119–3122
12. Starostenko SN, Rozanov KN (2009) Microwave screen with magnetically controlled attenuation. Prog Electromagnet Res 99:405–426
13. Qin F, Peng HX, Prunier C, Brosseau C (2010) Mechanical–electromagnetic coupling of microwire polymer composites at microwave frequencies. Appl Phys Lett 97:153502–153503

14. Qin FX, Peng HX, Popov VV, Panina LV, Ipatov M, Zhukova V, Zhukov A, Gonzalez J (2011) Stress tunable properties of ferromagnetic microwires and their multifunctional composites. J Appl Phys 108:07A310
15. Marin P, Cortina D, Hernando A (2005) High-frequency behavior of amorphous microwires and its applications. J Magn Magn Mater 290–291:1597–1600
16. Di YJ, Jiang JJ, Gang DU, Tian B, Bie SW, He HH (2007) Magnetic and microwave properties of glass-coated amorphous ferromagnetic microwires. Trans Nonferrous Met Soc China 17:1352–1357
17. Peng H, Qin F, Phan MH, Tang J, Panina L, Ipatov M, Zhukov A, Zhukova V, Gonzalez J (2009) Co-based magnetic microwire and field-tunable multifunctional macro-composites. J Non-Cryst Solids 355:1380–1386
18. Qin F, Peng HX, Tang J, Qin LC (2010) Ferromagnetic microwires enabled polymer composites for sensing applications. Compos A Appl Sci Manuf 41:1823–1828

Chapter 10
Basic Magnetic and Mechanical Properties of Microwire Composites

10.1 Magnetic Properties of Composites

Due to the inclusion of magnetic fillers, the polymer composite becomes magnetic, i.e. responsive to the external static or dynamic magnetic field. Although most studies are devoted to the dynamic response of these kinds of heterogeneous composite media [1], i.e. complex permeability, it is worth exploring the static magnetic properties of microwire composites for two reasons: (i) the composite with wire arrays could be of some application interest in the magnetic sensing field, as quite a few studies are devoted to the microwire arrays [2–7]. (ii) ac permeability is associated with the static magnetic properties such as saturation magnetisation and the anisotropy field, according to the modified model based on Snoek's law proposed by Acher et al. [8, 9].

$$\int_0^F \mu''(f) f \mathrm{d}f \leq \frac{\pi}{6} \tau (\bar{\gamma} 4\pi M_s)^2, \tag{10.1}$$

where μ is the imaginary part of complex permeability, f is the frequency, τ denotes the volume fraction of magnetic fillers, $\bar{\gamma}$ is the gyromagnetic factor with a value of 2.8 MHz/Oe, and M_s is the saturation magnetisation. In this connection, this section addresses some of the static magnetic properties of microwire composites.

Phan et al. [10] prepared E-glass prepreg-based composites with bundles of microwires and measured their magnetic properties in comparison with those of the single wires. Figure 10.1 shows the M–H curves of the single microwire and composite. It is interesting to note that, for both longitudinal and transverse measurements, the coercivity of the as-prepared composite is much smaller than that of the single microwire. This indicates better soft magnetic properties for the microwire composite than single wires. It is also shown that the effective anisotropy field for the bundles of microwire is strongly increased as compared to the single wire

H.-X. Peng et al., *Ferromagnetic Microwire Composites*,
Engineering Materials and Processes, DOI 10.1007/978-3-319-29276-2_10

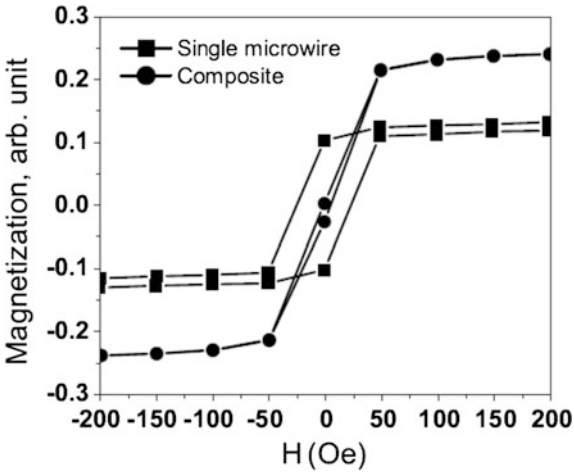

Fig. 10.1 Comparison of magnetic hysteresis loops of a single magnetic microwire and its as-prepared composite. Reproduced with permission from [10], copyright 2007 AIAA

[11]. Such changes of magnetostatic and magnetoelastic characteristics are due to the long-range dipolar interactions [7, 12] between neighbouring wires, as well as the interfacial stress between microwires and the matrix. The dipolar interactions have a strong impact on the magnetic properties in a similar way to classical spins interacting throughout the long-range interactions, resulting in the changes in the hysteresis loop. Equally, interfacial stress of the order of hundreds of MPa [13, 14], resulting from the different coefficients of thermal expansion between the microwire and polymer matrix, will have a significant effect on the magnetoelastic features of the wires according to $K_{\mathrm{me}} = 3/2\lambda(\sigma_i + \sigma_{\mathrm{app}})$, where K_{me} is the magnetoelastic energy component, λ is the magnetostriction constant, and σ_{i} and σ_{app} are the internal stress and applied stress on the wire, respectively [15, 16]. In the case of Fe-based wire of a length greater than the critical length, due to the dipolar interactions, the coercivity and anisotropy field should increase with the number of wires. On the other hand, the coercivity is decreased with increasing stress, and anisotropy presents an opposite trend [13, 15, 17]. The combination of these two mechanisms results in the observed contrast between the microwire composites and monolithic wire. The presented magnetic properties indicate that the microwire composites are promising for magnetic sensing applications [18].

Due to the involvement of the polymer, magnetic filler, and multi-interfaces, temperature plays an important role in regulating the magnetic behaviour of composites. The glass transition temperature (tg) of the composite samples is evaluated to gain a better understanding of their magnetic properties (see Fig. 10.2). Phan et al. found that, by annealing in the vicinity of the glass transition temperature, there exists a critical temperature of 177 °C. Before the temperature reaches this, the coercivity decreases, while afterwards the opposite trend is shown. This is contrary to the conventional case that the coercivity should decrease with the stress relaxation due to the thermal annealing below the crystallisation temperature [19]. Clearly, such a complex annealing temperature dependence of coercivity involves

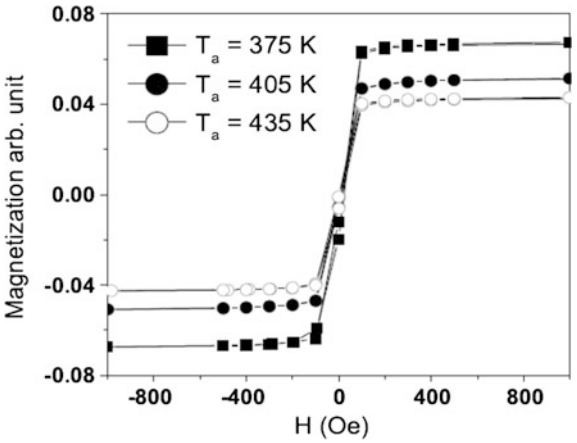

Fig. 10.2 Magnetic hysteresis loops of the as-prepared composite annealed at Ta = 375, 405, and 435 K. The glass transition temperature is 449.5 K. Reproduced with permission from [10], copyright 2007 AIAA

multiple mechanisms at different interfaces, viz. the structural relaxation in the wire and the stress relief in the polymer–wire interface. The competitive and interdependent relationship between these two mechanisms varies sensitively with the temperature. At low temperatures relative to the glass transition temperature, the second mechanism prevails and can result in a rearrangement of microwires, i.e. regulation of the composite mesostructure. Thus, the coercivity could be increased due to the enhanced interaction between the wires [20]. Subsequently, a decrease of coercivity should result from the stress relief contributed by both glass transition and wire structural relaxation. The gradual decrease of remanent magnetisation can be accounted for by the reduction in the volume of the axially magnetised area as an effect of stress relief due to the positive magnetostriction constant [15, 17].

10.2 Giant Magnetoimpedance Effect

As with wires, their composite also presents a significant GMI effect. It has been shown by Phan et al. [10] that, at a given frequency of 10 MHz, the GMI ratio and its field sensitivity reached the highest values of 450 and 45 %/Oe for those composites containing four wires, while the composite containing only one wire gave 14 and 1 %/Oe, respectively (see Fig. 10.3). The wire addition effect on the GMI is believed to be attributed to the reduction in resistivity as one of the causes. Another cause is the combination of the high circumferential permeability of the microwire, and a multiwire parallel configuration is likely to cause a magnetic flux closure and hence resulted in an extremely high effective permeability [20, 21]. It is worth noting both GMI and anisotropy field are enhanced, which is highly desirable for realising high-performance sensing entailing large sensitivity and broad working range. In addition, compared to single wire, the existence of polymer matrix could accommodate a versatile and judiciously designed multiwire system, which

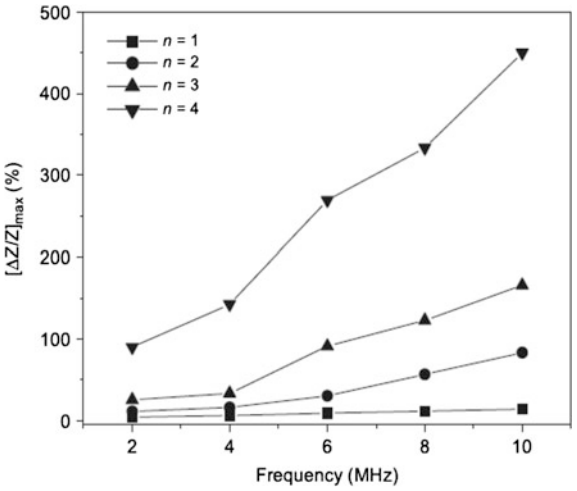

Fig. 10.3 Frequency dependence of GMI profiles with varying wire number $n = 1, 2, 3, 4$ mm. Reproduced with permission from [24], copyright 2007 Elsevier

provides more possibility to extend its applications. However, the GMI presented in Ref. [10] is very weak, with the suitable optimisation of single wires via advanced annealing techniques such as stress–Joule annealing [22] and recently reported multiangle annealing techniques [23], and the GMI of wire composite could be further improved.

Qin et al. [25] also demonstrated the pronounced improvement of the maximum MI ratio with the increasing number of wire inclusions, attributed to the effective response of all the wires. The microwire composite is shown to yield a larger GMI at higher frequencies but with a minor increase of energy loss, which is desirable for sensing applications. The multiwires in the parallel manner constitute an increase of the total cross-sectional area of the wires, resulting in a stronger skin effect when considering the ratio of radius and penetration depth. Consequently, the GMI effect is improved. In addition, if the wire is simply dealt with as a single-domain substance, the interactions between wires in the multiwire composites induce a magnetic closure to make the whole structure more stable, although the total internal energy is increased [12]. These results differ significantly from those reported by Garcia [26], who demonstrated a multiwire system exhibiting a reduced GMI effect with the number of wires, which is explained by the authors as an effect of shielding between wires. This difference should be ascribed to the functions of the matrix and the curing process for our composite media. The wire sample underwent annealing in the curing stage, and the domain structure was significantly modified. It is suggested that the confinement of the matrix also helps maintain the modified configuration, giving rise to the peculiarity of the GMI behaviour. Of note is that the involvement of a polymer matrix opens up new routes to modulate the GMI performance, although limited study has been hitherto reported. A particularly important aspect is interface. The homogeneities of the interface would be critical to the GMI characteristics, so it is necessary to study the detailed interfacial

conditions. Surface treatment using chemical agents such as silane or nanotubes [27] could also be considered to enhance both the interfacial bonding and GMI properties. Another aspect of practical interest [28, 29] is to develop superior bonding technology to accommodate multiple wires so that a highly stable GMI signal output can be ensured.

It is well established that the GMI effect of microwires associated with the magnetic properties is strongly influenced by the length of the wires [3, 30–33]. The argument holds true for the microwire composite system. It has been revealed that the GMI ratio increased from 15.5 to 268 % as the microwire length decreased from 4 to 1 mm [10]. This is attributed to the decrease of the electric resistivity in the multiwire system compared to the single wire, in spite of the increase of the demagnetising effect [3] for single wire. Based on the outstanding magnetic properties of microwire composites, they show a promising application perspective. Indeed, the polymer matrix provides a "platform" to assemble the microwires and exhibit the properties that are significantly different from the single wire, which is the motivation for developing these composites [34].

10.3 Giant Stress Impedance Effect

As mentioned above, stresses can play an important role in investigating the GMI materials, and these can be treated in two respects. One concerns the stress influence on the GMI behaviour, and a number of works have been published on this topic for various materials including ribbons [35–37] and microwires [38–40]. Second is the so-called giant stress impedance (GSI) effect, which refers to a stress-induced variation of impedance in magnetic materials. This effect in the intermediate frequencies has been evaluated on amorphous wires and ribbons. Shen [41] reported that the GSI effect of a CoSiB microwire reached about −35 % for stress σ = 140 MPa, which is 5–6 times more sensitive than a conventional semiconductor stress sensor. One kind of Fe-based ribbon was also found to possess an SI ratio of 20 % for σ = 84.8 MPa with the stress perpendicular to the geomagnetic field [42]. In this regard, the wire-based composite is expected to be a good candidate for studying the GSI effect over a wider stress range, since it can be treated as a multilayer medium consisting of a metallic core, a glass coat, and a composite matrix. Such a hierarchical structure would enable a sensitive response to the applied stress for the composite media, where the coupling of internal and external stresses is likely to be able to manipulate the GMI and GSI behaviour. Both aspects of the GSI effect of microwire composites were investigated by Qin et al. [13].

Figure 10.4 illustrates the magnetic field dependence of the GMI ratio taken at f = 1 MHz under various applied tensile stresses for the single-wire composite of four layers obtained by the method described in Sect. 9.2.2. Here, the tensile stress was applied along the microwire axis. It can be seen from the figure that the maximum GMI ratio decreased as the applied stress was increased. While the GMI ratio decreased gradually with the applied magnetic field (H_{dc}) for the unstressed

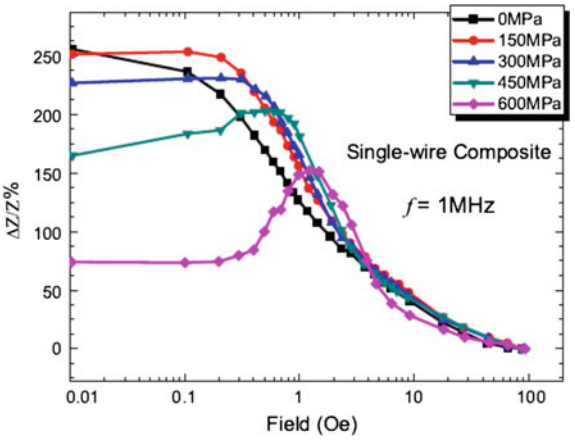

Fig. 10.4 GMI profiles of composites containing single wire as a function of applied stress. Reproduced with permission from [13], copyright 2011 Elsevier

composite, the case is different for the stressed composites. With increasing H_{dc}, the GMI ratio first increased, then reached a maximum, and finally decreased for the stressed composites. The magnetic field at which the GMI ratio reached its maximum can be considered as the circular anisotropy field (H_k) induced by the applied tensile stress.

Figure 10.5a illustrates the tensile stress dependence of the maximum GMI ratio and the anisotropy field. Clearly, the GMI ratio decreased slightly from 255 % for $\sigma = 0$ to 253 % for $\sigma = 150$ MPa and drastically reduced to 151 % for $\sigma = 600$ MPa by more than 100 %. An opposite trend was observed for the σ dependence of H_k.

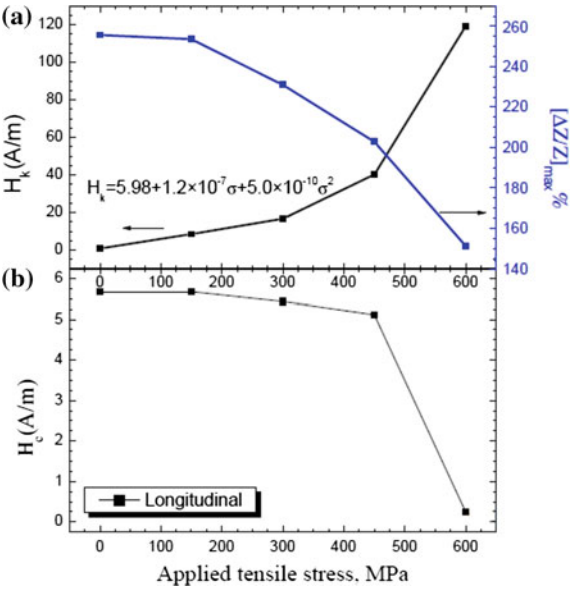

Fig. 10.5 **a** Tensile stress dependences of anisotropy field (H_k) determined from GMI profiles and maximum GMI ratio. **b** Longitudinal coercivity versus applied tensile stress. Reproduced with permission from [13], copyright 2011 Elsevier

A subtle increase of H_k by 8A/m for σ = 150 MPa was followed by a further increase of 112 A/m for σ = 600 MPa. The σ dependence of longitudinal coercivity (H_c) was also measured, and the result is shown in Fig. 10.5b. The drop of H_c was observed at σ = 600 MPa. For the case of the unstressed composite, the gradual decrease of the GMI ratio with H_{dc} is likely to be caused by decreasing circular permeability due to the rotation of magnetic moments. However, an opposite effect observed for the stressed composites arises from the fact that the application of tensile stress to the microwire with a negative magnetostriction strengthened the circular magnetoelastic anisotropy field, giving rise to the occurrence of a maximum in GMI that shifted towards higher H_{dc} as σ was increased. The occurrence of such a maximum in GMI for the stressed composites can be attributed to the competition in the rotational magnetisation processes between H_{dc} and H_k. The decrease of the GMI ratio with σ at H_{dc} = 0 is attributed to a reduction in the circular permeability due to the domain wall displacement.

Furthermore, it should be noted that, since the microwires were embedded in a polymer matrix, any heat treatment or variation coming from the polymer matrix is expected to have a significant influence on the GMI properties of the microwire and hence the composite. To gain insight into this, the influences of annealing treatment and the number of layers on the GMI properties are studied. The results are shown in Fig. 10.6. For the case of the as-prepared samples, the four-layer composite exhibited a higher maximum GMI ratio (255 %) when compared with the eight-layer composite (216 %). Meanwhile, the annealed composite samples (treated at 100 °C for 3 h) exhibited higher maximum GMI ratios (282 and 248 % for the four-layer and eight-layer composites, respectively) than the as-prepared ones. These findings are explained as follows. In this kind of composite, a higher stress will be induced as the number of composite layers increases. In the present study, the eight-layer composite may impose more stress in the through-thickness direction than the four-layer composite. As a result, the GMI ratio decreased and H_k increased for the as-prepared composite of eight layers when compared with the as-prepared composite of four

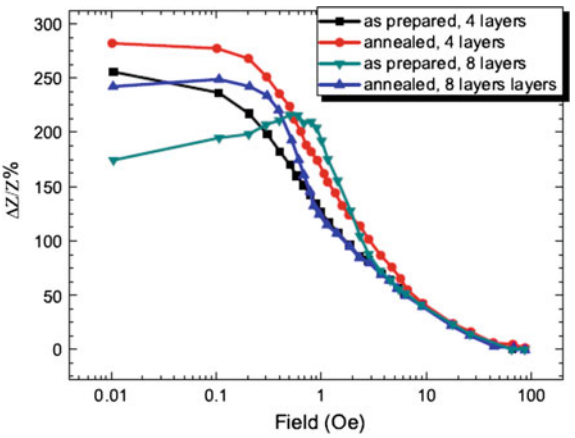

Fig. 10.6 GMI profiles for the wire composites of four prepreg layers and eight prepreg layers in the as-prepared and annealed states taken at f = 1 MHz. Reproduced with permission from [13], copyright 2011 Elsevier

layers. On the other hand, the annealing treatment is believed to have relieved the stress between the microwire and matrix produced during the curing process. This explains consistently the larger GMI ratio and smaller H_k obtained for the annealed composite samples relative to the as-prepared ones.

It is also interesting to see that the GMI behaviour observed for the as-prepared eight-layer composite is similar to that of the four-layer composite subject to a tensile stress of 450 MPa. This clearly suggests that the applied tensile stress and residual stress imposed by the composite matrix on the microwire could affect its GMI behaviour in a similar fashion. To understand this quantitatively, the contribution of the applied stress and the matrix-induced residual stress to the anisotropy field was calculated, respectively.

In a cylindrical coordinate system (z, r, ϕ), there exist three components for the residual stress in z (along the wire axis), r (radial direction), and ϕ (azimuthal direction): zz, rr, and $\phi\phi$, respectively. The magnetoelastic energy density is given by Antonov et al. [43]:

$$U_{\mathrm{me}} = -\frac{3}{2}\lambda_{\mathrm{s}}(\sigma_{zz}\alpha_z^2 + \sigma_{rr}\alpha_r^2 + \sigma_{\phi\phi}\alpha_\phi^2), \tag{10.2}$$

where λ_{s} is the saturation magnetostriction constant. α_i denotes the component of the unit magnetisation vector. The residual stresses are assumed to be a function of $x(r/a)$ only, a being the wire radius.

The anisotropy field can then be deduced by the following equation [43]:

$$H_k = \frac{3|\lambda_{\mathrm{s}}|}{M_{\mathrm{s}}}\left(\sigma_{zz} - \sigma_{\phi\phi} + \frac{1}{(1-k)p^2 + k}\overline{\sigma_{zz}}\right), \tag{10.3}$$

where all symbols have the same meaning as in Eq. (10.2).

Taking into account the residual stress imposed by the composite matrix, which is primarily along the negative radial direction (σ_{rr}), Eq. (10.3) can be modified to the following:

$$H_k = \frac{3|\lambda_{\mathrm{s}}|}{M_{\mathrm{s}}}\left(\sigma_{zz} - \sigma_{\phi\phi} + \overline{\sigma_{rr}} + \overline{\overline{\sigma_{zz}}}\right); \tag{10.4a}$$

$$\overline{\overline{\sigma_{zz}}} = \frac{1}{(1-k)p^2 + k}\overline{\sigma_{zz}}. \tag{10.4b}$$

For the four-layer composite, when $\overline{\sigma_{zz}}$ = 450 MPa, given k = 0.5 and p = 0.67, one obtains the effective contribution to H_k, $\overline{\overline{\sigma_{zz}}}$ = 619 MPa. For the eight-layer composite, according to the difference of its anisotropy field relative to that of the unstressed four-layer composite (ΔH_k = 0.5 Oe), the concerned stress $\overline{\sigma_{rr}}$ is given by the following:

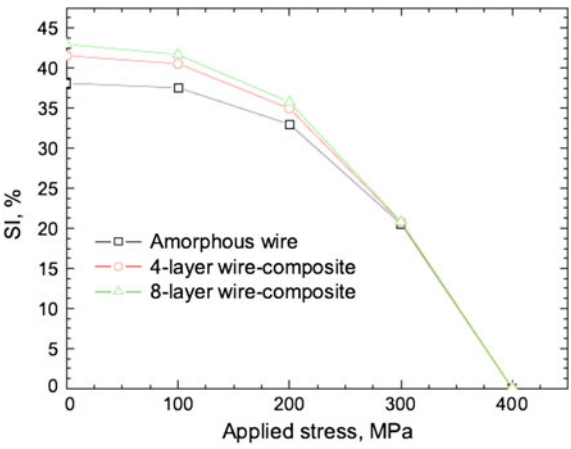

Fig. 10.7 GSI profiles for amorphous wire, four-layer wire composite, and eight-layer wire composite in the as-prepared states taken at $f = 1$ MHz. Reproduced with permission from [13], copyright 2011 Elsevier

$$\overline{\sigma_{rr}} = \frac{\Delta H_k M_s}{3|\lambda_s|}. \tag{10.5}$$

Given the typical numerical values: $M_s = 400$ G, $\lambda_s = -10^{-7}$, $\overline{\sigma_{rr}} = 667$ MPa is received. The similar numerical values of $\overline{\sigma_{rr}}$ and $\overline{\overline{\sigma_{zz}}}$ explain the roles of applied stress and residual stress in influencing the magnetoelastic properties and GMI properties. This result affords significant technical applications in the composite industry in terms of probing the residual stress and tailoring the related manufacturing conditions.

The GSI effect in the microwire and the microwire-based composites with four and eight layers was investigated. The results are shown in Fig. 10.7. It can be readily seen that the stress impedance ratio $[\Delta Z/Z]_{max}$ decreased monotonously with stress for all the samples. Interestingly, while the maximum stress impedance ratio ($[\Delta Z/Z]_{max}$) is 38.1 % for the single microwire, it is reinforced for the composite samples (41.5 and 43.0 % for the four-layer and eight-layer composites, respectively). These results indicate that the prepared composites are very appealing candidates for the stress-sensing applications. In the composite, in addition to the residual stress frozen in between the glass and metallic core, there exists residual stress at the interface between the microwire and polymer matrix. The enhancement of the GSI effect in the composites clearly points to the important coupling between the internal and external stresses that coexist in these materials.

10.4 Mechanical Properties

Since the fabricated composite is intended for structural applications, its mechanical properties are one of the major concerns. Also, the influence of microwires on the mechanical integrity of the composite is a key issue for the success of such

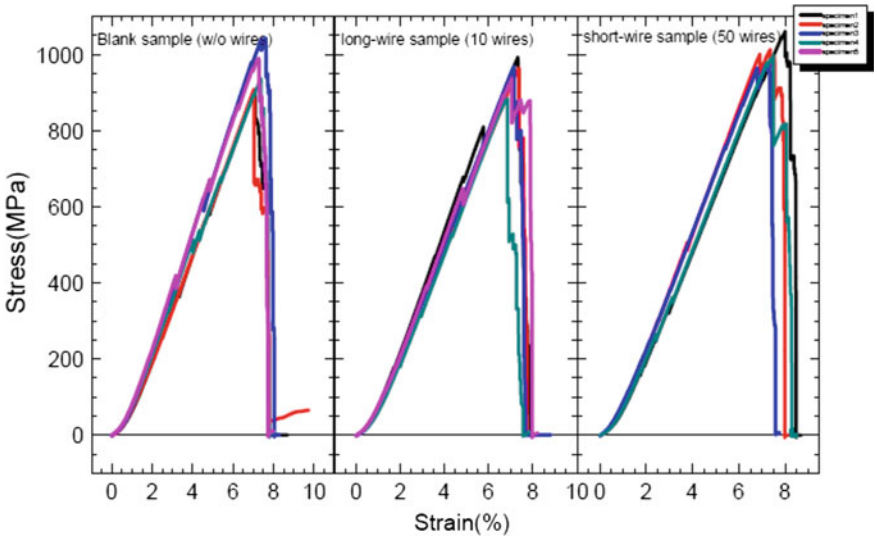

Fig. 10.8 Stress–strain curves of blank composites (free of wires), composites containing 10 wires and 50 wires measured by a 30 kN load cell. Reproduced with permission from [25], copyright 2010 Elsevier

sensor-embedded technology. Therefore, it is necessary to discuss the mechanical properties of the composite matrix influenced by the embedded wires [25, 44–46].

Qin et al. [25, 46] found that, in a dilute composite with glass fibre-reinforced epoxy as a matrix, the fibre shows little effect, as shown in Fig. 10.8, which displays the stress–strain curves obtained for blank composite samples and 10-wire and 50-wire samples under a maximum force of 30 kN [25]. The tensile strengths are summarised in Table 10.1. It is observed that all the mechanical parameters are very close to each other for the different types of samples. In terms of the tensile strength, the coefficients of variation (CV) for each type of sample are 6.3, 5.6, and 3.8. Upon performing cross-comparison of their average properties, the CV is 3.7. The negligible wire effect can be understood from the basic law of mixture that postulates a considerable volume fraction of fillers needed to realise reinforcement.

Qin et al. [47] also studied the impact resistance of this kind of microwire composite. With reference to the obtained time dependences of the impact force for all tested samples (Fig. 10.10), one can see that the additional wires yield negligible changes in the impact resistance of the composites parametrised by the impact

Table 10.1 Mean values and coefficients of variation (CV*) of tensile strength for each set of samples

	Blank sample	10-wire sample	50-wire sample
Young's modulus (GPa)	14.22 (3.1*)	14.48 (1.1)	14.97 (3.0)
Tensile strength (MPa)	951.48 (6.3)	935.18(5.6)	1003.80(3.8)

The asterisk (*) is used to indicate that the number in the parenthesis is coefficient of variation, i.e. CV

energy, in that the major energy dissipation mechanism is delamination rather than fibre failure, as shown in a typical damage pattern at the surface (inset of Fig. 10.10; the bright region indicates the delamination). This suggests that the embedded wires do not degrade the interfacial bonding. This is of particular importance for aeronautical structures that are subject to low-velocity impact caused by, e.g., dropped tooling or runway debris, throughout their service life [48]. Another notable feature concerns the first load peak, which exhibits a significant increase for the sample containing three layers of wires as compared to other samples. This clearly indicates that the fibre failure occurred near the surface as the initial impact damage [49]. The metallic wires with the strong tensile strength of 3–4 kMPa effectively improve the fracture load. It can be expected that, for high-velocity impact, the addition of wires can also improve the toughness of the composites. In considering the wide application of glass fibre composites in wind turbines, the addition of microwires can simultaneously improve the impact resistance performance and electromagnetic interference shielding (this will be discussed in Chap. 12) of the composites, rendering such microwire composites particularly useful for improving on the current green energy technology.

Back in the 1980s, Goto et al. [44, 45] had done excellent work in connection with the mechanical performance of metallic filament-reinforced composites. Goto et al. [44] studied the reinforcing effect of metallic wires with and without glass coats on the epoxy matrix and reported that the mechanical properties of epoxy are strongly enhanced in wires without a glass coating, with the tensile strength reaching 600 MPa at 30 vol.% wire volume. Meanwhile, the glass-coated wires do not show such a good reinforcing effect due to the poor bonding between the metallic core and glass coating. These effects are readily demonstrated in the fracture morphology images (Fig. 10.9). Apparently, the quality of the interfaces plays a critical role in determining the ultimate mechanical performance of the wire composites. These fine wires, after removing the glass coating, are also found to be capable of improving the thermal properties of the composite by increasing the

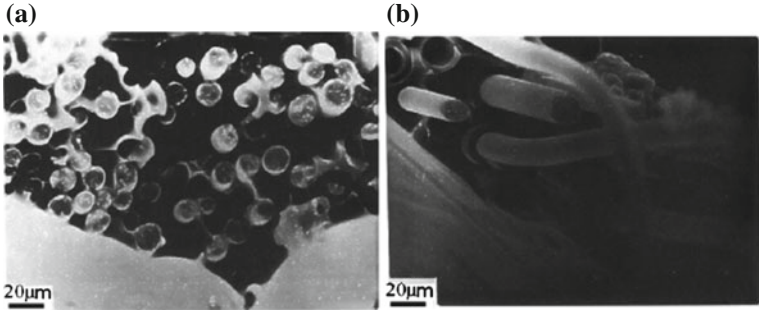

Fig. 10.9 Fracture morphology of microwire (glass coat removed)/epoxy composite (**a**) and glass-coated microwire/epoxy composite (**b**). Reproduced with permission from [44], copyright 1987 Springer

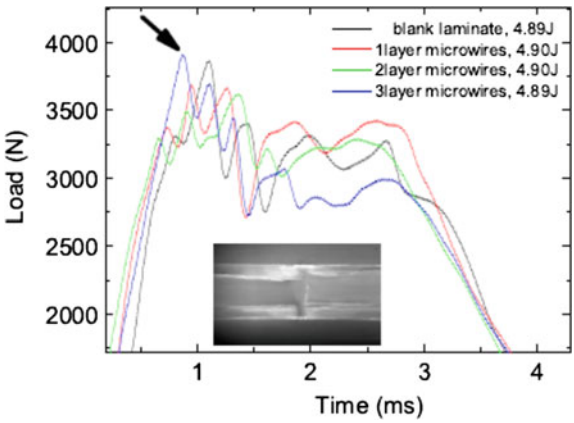

Fig. 10.10 Time dependence of impact force for blank sample and heavily wire-loaded composites containing one layer of microwires (embedded depth h = 1 mm), two layers (h_1 = 0.75 mm h_2 = 1.25 mm), and three layers (h_1 = 0.5 mm, h_2 = 1 mm, h_3 = 1.5 mm). Each layer contains 200 microwires. The inset shows in-plane view of the damaged spot in the 950 E-glass laminates after the impact test

glass transition temperature, as the wires can hinder the molecular motion (Fig. 10.10).

Although the microwires can reinforce the polymer materials with adequate concentration and proper orientation, a trade-off is often inevitable if one tends to integrate the structural function and other functionalities which do not necessarily favour a large concentration or unidirectional fillers. For the designers of such multifunctional composites, it is necessary to maximise the most desirable function for the targeted application, while keeping the cost of other functionalities as low as possible.

References

1. Sihvola A, Lindell I (1992) Effective permeability of mixtures Prog Electromagn Res 1–36
2. Laroze D, Escrig J, Landeros P, Altbir D, Vázquez M, Vargas P (2007) A detailed analysis of dipolar interactions in arrays of bi-stable magnetic nanowires. Nanotechnology 18:415708
3. Di Y, Jiang J, Bie S, Yuan L, Davies HA, He H (2008) Collective length effect on the magnetostatic properties of arrays of glass-coated amorphous alloy microwires. J Magn Magn Mater 320:534–539
4. Vázquez M (2001) Soft magnetic wires. Phys B 299:302–313
5. Sampaio LC, Sinnecker EHCP, Cernicchiaro GRC, Knobel M, Vázquez M, Velázquez J (2000) Magnetic microwires as macrospins in a long-range dipole-dipole interaction. Phys Rev B 61:8976–8983
6. Velazquez J, Vazquez M, Zhukov A (1996) Magnetoelastic anisotropy distribution in glass-coated microwires. J Mater Res 11:2499–2505

7. Velazquez J, Garcia C, Vazquez M, Hernando A (1999) Interacting amorphous ferromagnetic wires: a complex system. J Appl Phys 85:2768–2774
8. Acher O, Dubourg S (2008) Generalization of snoek's law to ferromagnetic films and composites. Phys Rev B 77:104440
9. Acher O, Adenot AL (2000) Bounds on the dynamic properties of magnetic materials. Phys Rev B 62:11324–11327
10. Phan M, Peng H, Wisnom M, Mellor P (2007) Optimizing the nano-structure of magnetic micro-wires for multifunctional macro-composites. AIAA-2007-2032 48th Qin, Phan and Peng, submitted to Springer AIAA/ASME/ASCE/AHS/ASC Structures, Structural Dynamics, and Materials Conference, Honolulu, Hawaii
11. Di Y, Jiang J, Du G, Tian B, Bie S, He H (2007) Magnetic and microwave properties of glass-coated amorphous ferromagnetic microwires. Trans Nonferrous Met Soc China 17:1352–1357
12. Velázquez J (1996) Dynamic magnetostatic interaction between amorphous ferromagnetic wires. Phys Rev B 54:9903–9911
13. Qin F, Peng H, Popov V, Phan M (2011) Giant magneto-impedance and stress-impedance effects of microwire composites for sensing applications. Solid State Commun 151:293–296
14. Qin FX, Peng HX, Popov VV, Panina LV, Ipatov M, Zhukova V, Zhukov A, Gonzalez J (2011) Stress tunable properties of ferromagnetic microwires and their multifunctional composites. J Appl Phys 108:07A310
15. Zhukova V, Zhukov A, Blanco JM, Gonzalez J, Gomez-Polo C, Vazquez M (2003) Effect of stress applied on the magnetization profile of Fe–Si–B amorphous wire. J Appl Phys 93:7208–7210
16. Zhukov A, Ipatov M, Gonzalez J, Blanco JM, Zhukova V (2009) Recent advances in studies of magnetically soft amorphous microwires. J Magn Magn Mater 321:822–825
17. Zhukova V, Larin VS, Zhukov A (2003) Stress induced magnetic anisotropy and giant magnetoimpedance in Fe-rich glass-coated magnetic microwires. J Appl Phys 94:1115–1118
18. Vazquez M, Hernando A (1996) A soft magnetic wire for sensor applications. J Phys D: Appl Phys 29:939–949
19. Zhukova V, Cobeno AF, Zhukov A, Blanco JM, Larin V, Gonzalez J (1999) Coercivity of glass-coated Fe73.4-xCu1Nb3.1Si13.4 + xB9.1 (0 <=x <=1.6) microwires. Nanostruct Mater 11:1319–1327
20. Chizhik A, Zhukov A, Blanco JM, Szymczak R, Gonzalez J (2002) Interaction between Fe-rich ferromagnetic glass-coated microwires. J Magn Magn Mater 249:99–103 (Qin, Phan and Peng, submitted to Springer)
21. Amalou F, Gijs MAM (2002) Giant magnetoimpedance in trilayer structures of patterned magnetic amorphous ribbons. Appl Phys Lett 81:1654–1656
22. Kraus L, Chiriac H, Ovari TA (2000) Magnetic properties of stress-joule-heated amorphous fecrbsimicrowire. J Magn Magn Mater 215–216:343–345
23. Liu J, Cao F, Chen D, Xue X, Sun J (2012) Multiangle combined magnetic-field annealing of Cobased amorphous microwires for sensor applications. Phys Status Solidi A 209:984–989
24. Phan M, Peng H, Yu S, Wisnom M (2007) Large enhancement of GMI effect in polymer composites containing Co-based ferromagnetic microwires. J Magn Magn Mater 316:e253–e256
25. Qin F, Peng HX, Tang J, Qin LC (2010) Ferromagnetic microwires enabled polymer composites for sensing applications. Compos A Appl Sci Manuf 41:1823–1828
26. Garcia C, Zhukova V, Zhukov A, Usov N, IpatovM, Gonzalez J, Blanco J (2007) Effect of interaction on giant magnetoimpedance effect in a system of few thin wires. Sens Lett 5:10–12
27. Chaturvedi A, Stojak K, Laurita N, Mukherjee P, Srikanth H, Phan MH (2012) Enhanced magnetoimpedance effect in co-based amorphous ribbons coated with carbon nanotubes. J Appl Phys 111:07E507
28. Liu J, Wang X, Qin F, Xing D, Cao F, Peng H, Xiang X, Sun J (2011) Gmi output stability of glasscoated co-based microwires for sensor application. PIERS Online 7:661–665

29. Liu JS, Sun JF, Xing DW, Xue X, Zhang SL, Wang H, Wang XD (2011) Experimental study on the effect of wire bonding by cu electroplating on gmi stability of co-based amorphous wires. Physica status solidi (a) 208:530–534
30. Qin F, Peng H, Phan M (2010) Wire-length effect on gmi in co70.3fe3.7b10si13cr3 amorphous glasscoated microwires. Mater Sci Eng B 167:129 – 132
31. Severino AM, Gomez-Polo C, Marin P, Vazquez M (1992) Influence of the sample length on the switching process of magnetostrictive amorphous wire. J Magn Magn Mater 103:117–125
32. Vazquez M, Li YF, Chen DX (2002) Influence of the sample length and profile of the magnetoimpedance effect in fecrsibcunb ultrasoft magnetic wires. J Appl Phys 91:6539–6544
33. Zhukova V, Usov NA, Zhukov A, Gonzalez J (2002) Length effect in a co-rich amorphous wire. Phys Rev B 65:134407
34. Ajayan PM, Tour JM (2007) Materials science: nanotube composites. Nature 447:1066–1068
35. Coisson M, Tiberto P, Vinai F, Kane S (2003) Influence of stress-annealing on magneto-transport properties in co-based amorphous ribbons. Sens Actuators A 106:199–202
36. Ohnuma M, Hono K, Yanai T, Nakano M, Fukunaga H, Yoshizawa Y (2005) Origin of the magnetic anisotropy induced by stress annealing in Fe-based nanocrystalline alloy. Appl Phys Lett 86:152513
37. Fels A, Friedrich K, Hornbogen E (1984) Reinforcement of a brittle epoxy resin by metallic glass ribbons. J Mater Sci Lett 3:569–574
38. Mandal K, Mandal SP, Vázquez M, Puerta S, Hernando A (2002) Giant magnetoimpedance effect in a positive magnetostrictive glass-coated amorphous microwire. Phys Rev B 65:064402
39. Blanco JM, Barbon PG, Gonzalez J, Gomez-Polo C, Vazquez M (1992) Stress induced magnetic anisotropy in non-magnetostrictive amorphous wires. J Magn Magn Mater 104–107:137–138
40. Cobeno AF, Zhukov A, Blanco JM, Larin V, Gonzalez J (2001) Magnetoelastic sensor based on GMI of amorphous microwire. Sens Actuators A 91:95–98
41. Shen L, Uchiyama T, Mohri K, Kita E, Bushida K (1997) Sensitive stress-impedance micro sensor using amorphous magneostrictive wire. IEEE Trans Magn 33:3355–3357
42. Hu J, Qin H, Chen J, Zhang Y (2003) Giant stress-impedance effect in Fe73.5CuNb3-xVxSi13.5B9 amorphous ribbons. J Magn Magn Mater 266:290–295
43. Antonov AS, Borisov VT, Borisov OV, Prokoshin AF, Usov NA (2000) Residual quenching stresses in glass-coated amorphous ferromagnetic microwires. J Phys D Appl Phys 33:1161
44. Goto T, Nishio K (1987) Mechanical properties of high strength and high toughness metallic filament composites with epoxy and poly(ether ether ketone) matrices. J Mater Sci 22:2357–2362
45. Goto T, Tsubouchi H (1988) High temperature mechanical properties of high toughness metallic filament composites with polyimide and epoxy matrices. J Mater Sci 23:3630–3635
46. Qin F, Peng H (2010) Macro-composites containing ferromagnetic microwires for structural health monitoring. Nano Commun Netw 1:126–130
47. Qin F, Peng H, ZChen, Wang H, Zhang J, Hilton G (2013) Optimization of microwire/glass-fiber reinforced polymer composites for wind turbine application. Appl Phys A Mater Sci Process. 10.1007/s00339-013-7820-2
48. Guinard S, Allix O, Guedra-Degeorges D, Vinet A (2002) A 3d damage analysis of low-velocity impacts on laminated composites. Compos Sci Technol 62:585–589
49. Breen C, Guild F, Pavier M (2005) Impact of thick cfrp laminates: the effect of impact velocity. Compos A Appl Sci Manuf 36:205–211

Chapter 11
Microwave Tunable Properties of Microwire Composites

With a knowledge of the static properties of magnetic wires and their composites, we now usher this chapter into the dynamic properties of microwave composites at the gigahertz frequency range of application interest, i.e. microwave tunable properties. The main tunable events displayed here are all driven by external stimuli including dc magnetic field, tensile stress, and temperature. Although the mechanism varies for different types (or order of magnitude for magnetic field) of stimuli, the underlying physics is the same; that is, the microwires are excited by the incident EM wave and the variation of external field induces the change of skin effect or even ferromagnetic resonance in wires, resulting in the external field dependence of the frequency dispersion of EM parameters for the whole composite. But if we examine each composite with its varying structure, such as the local properties of wires (e.g. geometry and composition) and the topological arrangement of wires, some peculiar phenomena are observed. In the following, we treat categorically each type of tunable composite and give particular attention to the cases where unique field effects are exhibited.

11.1 Basic Theory of Field and Stress Tunable Properties

The microwave tunable properties of a microwire composite, by nature, are the response of effective permittivity to the electromagnetic wave through the surface impedance. Therefore, to explain this phenomenon, one needs to understand the basics of wave interactions with the materials and the effective medium approaches to characterise heterogeneous composites.

11.1.1 Effective Permittivity

The effective permittivity should be treated differently in two types of composites that will be discussed in this chapter: those with short wires and those with long

H.-X. Peng et al., *Ferromagnetic Microwire Composites*,
Engineering Materials and Processes, DOI 10.1007/978-3-319-29276-2_11

wires. In composites containing short wires, the Lorentz model proves to be effective, whereas the Drude model is applicable to composites containing long wires. The Lorentz model is first considered to be applicable to all insulator materials. Along the inclusion length, the current with a linear density $j(x)e^{-i\omega t}$ is induced by the local electrical field $e_{\mathrm{loc}}\exp(-i\omega t)$. Using the continuity equation and integration by parts with boundary conditions, the electric dipole moment D can be calculated as:

$$D = \frac{i}{\omega}\int_{1/2}^{1/2} j(x)\mathrm{d}x \Rightarrow \alpha = \frac{D}{Ve_{\mathrm{loc}}}, \tag{11.1}$$

where l is the length of the wire and V is the inclusion volume. Within the frame of this approach, the dielectric polarisability α of the inclusion can also be calculated [1]:

$$\alpha(\omega) = \sum_n \frac{A_n}{(\omega_{\mathrm{res},n}^2 - \omega^2) - i\Gamma_n\omega}, \tag{11.2}$$

where $\omega_{\mathrm{res},n}$ is the angular resonance frequency, A_n are amplitude constants, and Γ_n are the damping parameters. A_1 contributes most to the polarisability corresponding to the lowest frequency. Γ_n is considerably influenced by the resistive magnetic losses [2], and it presents a strong dependence on the external magnetic field or stress in the vicinity of an antenna resonance in certain conditions. An experimental proof of this equation has been provided in Refs. [3] and [4].

The bulk polarisation of the composites can be expressed as:

$$P = \langle e_{\mathrm{loc}}\rangle p_v\alpha = e_0\chi_{\mathrm{eff}}, \tag{11.3}$$

where e_{loc} is the averaged local field, p_v is the volume concentration of the inclusions, e_0 is the external electric field, and χ_{eff} is the effective bulk susceptibility. When $p_v \ll p_c$, it follows that $e_{\mathrm{loc}}c \approx e_0$ [5]. Thus, the effective permittivity can be obtained by:

$$\varepsilon_{\mathrm{eff}} \approx \varepsilon + 4\pi p_v\langle\alpha\rangle \tag{11.4}$$

where ε is the permittivity of the matrix and $\langle\alpha\rangle$ is the averaged polarisability of an individual inclusion. Further calculations involve the GMI effect and surface impedance of wires, which are presented in the following section.

For continuous-wire composites, charge distribution along the wire axis is absent, and hence, no current or dipole response exists. It can then be treated as a medium with diluted plasma according to Pendry et al. [6]. Thus, the dispersion of

effective permittivity for this kind of composite is characterised by the plasma frequency expressed as:

$$\omega^2 = \frac{2\pi c^2}{b^2 \ln(b/a)}, \tag{11.5}$$

where b is the wire period. In this context, the deduction of effective permittivity can be approached by solving the Maxwell equations in a homogenisation procedure as the wire parameters have no influence on the permittivity. For a non-magnetic wire composite, the effective permittivity can be given by [7]:

$$\begin{aligned} \varepsilon_{\text{eff}} &= \varepsilon - p_v \frac{2\varepsilon_c F_1(k_c a)}{(ak_c)^2 F_1(k_c a)\ln(L/a) - 1}, \\ F_1 &= J_1(x)/xJ_0(x), \left| p_v = \pi a^2/L^2, \right. \\ \varepsilon_c &= 4\pi i\sigma/\omega\, k_c = 4\pi i\omega\sigma/c^2, \end{aligned} \tag{11.6}$$

where p_v is the wire volume concentration, ε_c is the dielectric permittivity of the conductor, σ is the wire conductivity, k_c is the wave number, and $J_{0,1}$ are Bessel functions. At microwave frequency, there is a very strong skin effect, i.e. $ak_c \sim a/\delta \gg 1$. Thus, Eq. 11.6 can be reduced to Eq. 11.5, justifying the application of the model for continuous-wire composites. As with short-wire composites, impedance should be calculated first.

11.1.2 Impedance Tensor

The surface impedance is a parameter to characterise the voltage response in the wire system, as described in the GMI phenomenon. To calculate the impedance tensor in the wire, the electromagnetic conditions about the wire should be fully understood. Figure 11.1 shows the current e_x along the wire axis direction inducing the circular field h_ϕ, of which the tangential component $h_{x,0}$ plus the external field induce the electric field e_ϕ. In this case, the response to the electromagnetic field from the wire via the impedance tensor with the boundary conditions can be written as follows [8]:

$$\overline{E_t} = \zeta(\overline{H_t} \times n), \tag{11.7}$$

where **n** is the unit normal vector directed inside the wire, $\overline{E_t}$ and $\overline{H_t}$ are the tangential vectors of the total electric and magnetic fields at the wire surface, including both scattered and external fields. Adopting the typical simplified

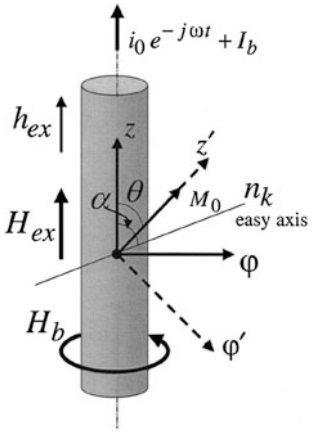

Fig. 11.1 Schematic diagram of the magnetic configuration in a wire. Reprinted with permission from [9], copyright 2005 Nova Science

approach for antenna problems, Eq. 11.7 can be written in polar coordinates (x, ϕ) [9]:

$$\begin{aligned} \overline{E_x} &= \varsigma_{xx}\overline{H_\phi} - \varsigma x\phi\overline{H_x}, \\ \overline{E_\phi} &= \varsigma_{\phi x}\overline{H_\phi} - \varsigma_{\phi\phi}\overline{H_x}. \end{aligned} \tag{11.8}$$

11.1.3 Stress and Field Dependence of Impedance and Permittivity

For short-wire composites, it follows from Eq. 11.4 that the averaged polarisability needs to be worked out. When the interactions between the wires are reasonably neglected, it can be derived as [10]:

$$\begin{aligned} \langle\alpha\rangle &= \frac{1}{2\pi\ln(1/a)(ka)^2}\left(\frac{2}{kl}\tan(kl/2) - 1\right), \\ k &= \omega\frac{\sqrt{\varepsilon}}{c}\left(1 + \frac{ic\varsigma_{xx}}{\omega\alpha\ln(1/a)}\right)^{1/2}. \end{aligned} \tag{11.9}$$

It should be noted that the equations right above are established in the frame of the composites in question with a moderate skin effect, under which the radiation loss is overshadowed by the magnetic and resistive losses.

It can be seen from Eqs. 11.4 and 11.9 that the permittivity depends on the surface impedance in this case. Due to the GMI effect as previously analysed, the dependence of permittivity through impedance on the external field is well established according to Eq. 11.12.

In the case of long-wire composites, Eq. 11.6 was extended to approach the case of magnetic wires. By substituting the impedance formula, Eq. 11.6 is transformed to [11]:

$$\varepsilon_{\text{eff}} = \varepsilon - p_v \frac{w_p^2}{w^2\left(1 + i\frac{c\varsigma_{xx}}{wa\ln(b/a)}\right)}. \tag{11.10}$$

Thus, the effective permittivity for continuous-wire composites is dependent on the wire surface impedance via the plasma frequency.

Due to the amorphous structure of the microwires, their anisotropy is dominated by the magnetoanisotropy coupled with the internal and/or external stress and magnetostriction, but the shape anisotropy makes no contribution. The influence of internal stress and applied stress on GMI has been reported theoretically in [12] and [13]. Regarding the glass-coated microwires, the following equations are held:

$$K = K_0 - 1.5\lambda(\sigma_{zz} - \sigma_{\phi\phi} + \sigma_{\text{applied}}), \tag{11.11a}$$

and

$$H_k = 2K/\mu_0 M_s, \tag{11.11b}$$

where K and H_k are the anisotropy constant and field, respectively; σ_{zz}, $\sigma_{\phi\phi}$, and σ_{applied} are the axial, azimuthal stress, and applied stress, respectively; M_s is the saturation magnetisation; and μ_0 the permeability in vacuum. Also the effective permeability depends on the ratio of H_k to M_s, which is determined by K, expressed as [14]:

$$\mu_{\text{eff}} = \frac{M_s \sin^2(\theta + \theta_e)}{H_k\left[h\sin^2(\theta + \theta_e) + \cos(2\theta)\right]}, \tag{11.12}$$

where the anisotropy field $H_k = 2\,K/M_s$ and $h = H_{ex}/H_k$. θ is between the anisotropy angle θ_e and $\pi/2$. Besides, the static magnetisation angle also changes with the anisotropy angle, as indicated in the equation for the magnetostatic energy U_m based on the equivalent uniaxial anisotropy [15]:

$$U_m = -|K|\cos^2(\alpha - \theta) - M_0 H_{ex}\cos\theta, \tag{11.13a}$$

$$\left|\widetilde{K}\right| = \frac{K + (3/2)\lambda\sigma_a}{\cos(2\widetilde{\alpha})}, \tag{11.13b}$$

$$\widetilde{\alpha} = \frac{1}{2}\tan^{-1}\frac{3|\lambda\sigma_t|}{|K + (3/2)\lambda\sigma_a|}, \tag{11.13c}$$

where α is the anisotropy angle, which takes different values according to the relationship between the anisotropy constant K and the product of magnetostriction constant λ multiplying the axial stress σ_a [10].

The tunable properties can be characterised by the free-space measurement. From what has been discussed above, the dependencies of effective permittivity through magnetoimpedance on the field and stress are well established. A note is in order here. Such metal–dielectric composites incorporating wire-shaped inclusions have been treated theoretically and experimentally for decades [16]. Most recently, researchers have found that it is possible to obtain a negative permittivity and/or permeability at certain frequencies for this kind of composite and recognised its importance [17]. This brings about the next important functionality of the wire composite, i.e. metamaterial properties, which will be discussed in the following section. Further to the understanding of the GMI/GSI behaviours of microwires and their composites, this section targets the microwave tunable properties of the microwire composites, i.e. tunable electromagnetic properties by magnetic field [2, 9, 11, 18–26], stress [9–11, 15, 27], and temperature [18, 19]. The tunable property is actually the so-called cross-variable response unique to multifunctional composites, i.e. a given field can control two or more variables, or a variable can be switched by two or more external fields. To achieve such tenability or adjustability is essential for microwave applications such as tunable microwave devices [9] and remote-interrogated sensors [28]. It will also be called for to realise reconfigurable local network environments, beam-steering antennas, and microwave remote sensing and control. Most of the proposed methods have been based on biased ferroelectric, ferrite, or magnetic composite substrates and reconfigurable resonant elements implementing active devices or a system of microactuators [29–31]. These technologies each have their advantages and limitations, such as high power consumption, low operational speed, limited frequency band, and high cost. Dilute composites with ferromagnetic microwires were proposed in this context by Panina et al. [9, 11]. Together with the following studies [21, 22, 24–27, 32], the possibility of tailoring the collective dielectric response of the wire media by changing the local magnetic properties with external stimuli without changing the structural parameters has been demonstrated.

In what follows, after a brief introduction of the measurement techniques, the tunable properties will be discussed in three categories: magnetic field tunable properties, stress tunable properties, and temperature tunable properties. In each section, both the wires and their composites will be discussed. Note that all the composites under discussion here are non-percolating due to either the periodical arrangement of the wires with fixed spacing or the existence of glass coating for random-wire composites. Thus, there is no concern that the formation of a conductive network will hinder their interactions with the microwave.

11.2 Measurement Techniques

11.2.1 Free-Space Measurement System

Investigation of the microwave tunable properties of composites was carried out in free space using the standard calibration technique named through-reflection-line (TRL), as a well-received testing method for dielectric materials and any non-coaxial measurements of *S*-parameters [33–37]. The schematic graph of the measuring system employed for our experiments is shown in Fig. 11.2 [38]. To neutralise the influences of the noises on the scattering, the walls of the compact anechoic chamber are made of plywood and covered on the inside by a microwave absorber and a network analyser with which the time-domain option is employed [34, 39, 40]. Antennas are connected to the ports of a HP8720ES spectrum network analyser through RG402 cables with Subminiature version A (SMA) connectors (see Fig. 11.3) [18]. The detailed features of the antennas are as follows: (1) length: 887 mm; (2) aperture: 351 × 265 mm; (3) frequency range: 0.85–17.44 GHz; (4) standing-wave ratio (SWR) < 1.7; (5) effective area > 150 mm^2 in the range of 0.85–15 GHz.

The distance between antennas is controllable with the mobile front walls of the chamber where the antennas are fastened to meet the requirement of preliminary TRL calibration. The frame's function is to guarantee the uniform heating or magnetic field along the sample surface when the microwave response depends on

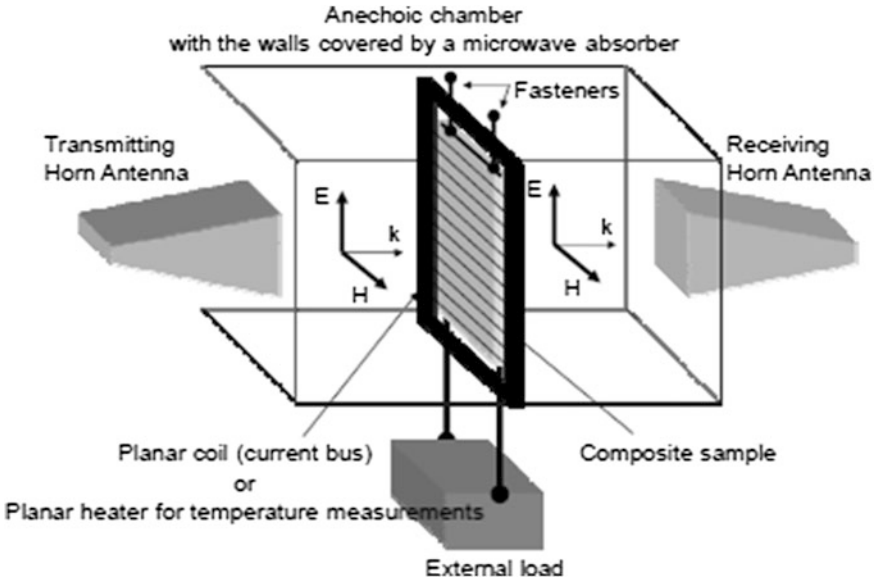

Fig. 11.2 Free-space measuring system. Two types of external action were applied to the sample: tensile stress and dc magnetic field. Reprinted with permission from [41]

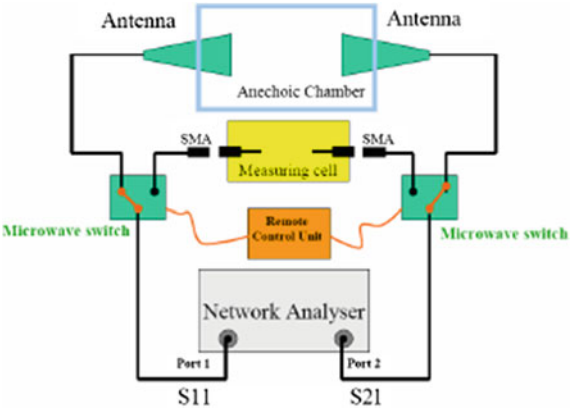

Fig. 11.3 The scheme of measuring track showing the option of switching between chamber and cell. Reprinted with permission from [41]

the external stimuli including field, stress, and temperature. A current bus or a planar coil was used for the same reason and also makes the composites easily tunable by a weak magnetic field. It is highlighted that the parallel current wires must be oriented perpendicularly to the vector of the electrical field in the plane-polarised accidental electromagnetic wave in order to allow for nothing but the interaction between the composites and electromagnetic wave. Note that the design of the switch makes the most of the analyser, between the non-contact microwave test in the anechoic chamber and the contact test on magnetic wires in the measuring cell (Fig. 11.3) [18, 38].

If a very high magnetic field is required, the planar coil is preferred to the current bus because all turns in a coil are connected in series, thus passing the total current. The construction of the frame out of planar coil is shown in Fig. 11.4. The sample is placed between the two coil layers. The complex permittivity can be computed from the *S*-parameters collected from the measurement. *S*-parameters S_{11} and S_{21} can be expressed via reflection coefficient Γ and transmission coefficient T as [33]:

$$S_{11} = \frac{\Gamma(1 - T^2)}{1 - \Gamma^2 T^2}, \tag{11.14a}$$

and

$$S_{21} = \frac{T(1 - T^2)}{1 - \Gamma^2 T^2}. \tag{11.14b}$$

Γ and T can then be calculated by:

$$\Gamma = \frac{(Z_{sn} - 1)}{(Z_{sn} + 1)}, \tag{11.15a}$$

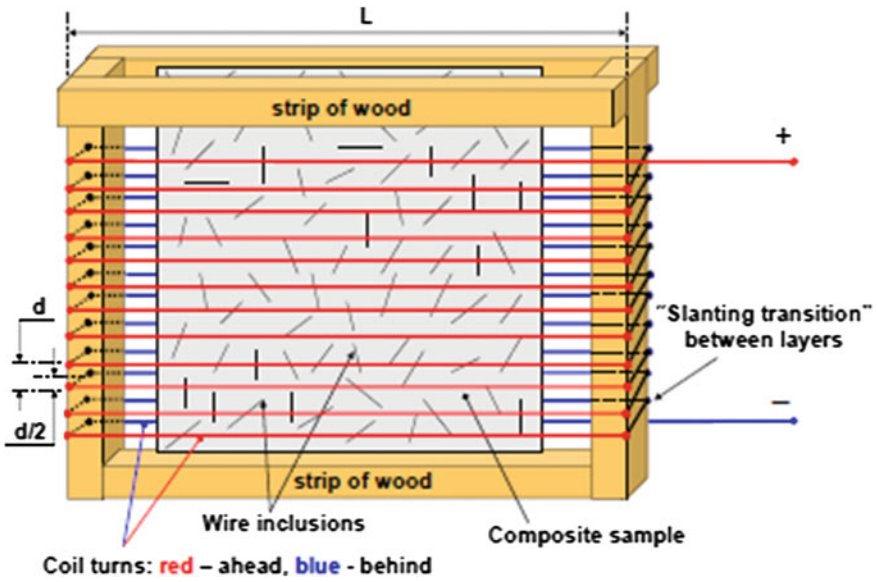

Fig. 11.4 The construction of a planar coil for laboratory investigations. The composite sample is placed in between two coil layers. The coil becomes "invisible" for a plane-polarised wave with the electrical vector directed transversely to the coil turns, as shown in Fig. 11.2. To provide the uniform magnetic field inside the coil, the distance between the coil layers must be equal to the interturn distance d, and these layers must be shifted transversely across one another over steps of $d/2$. Reprinted with permission from [41]

and

$$Z_{sn} = (1/\sqrt{\varepsilon^*})T = e^{-\gamma d}, \gamma = (2\pi/\lambda_0)(\varepsilon^*)^{1/2}, \tag{11.15b}$$

where λ_0 is the wavelength in the free space and d is the thickness of the sample. The complex permittivity is given by:

$$\varepsilon^* = \frac{\gamma}{\gamma_0}\left(\frac{1-\Gamma}{1+\Gamma}\right). \tag{11.16}$$

11.2.2 Microwave Frequency-Domain Spectroscopy

A modified microwave frequency-domain spectrometer is shown in Fig. 11.5. Figure 11.5a shows the instrument specifically designed to study the effects of stresses or magnetic field on the samples. A strain as large as 100 % is obtainable if within the flexibility of the sample. The extension was measured with a hand gauge. The samples were mounted strictly along the direction of stress applied. A solenoid

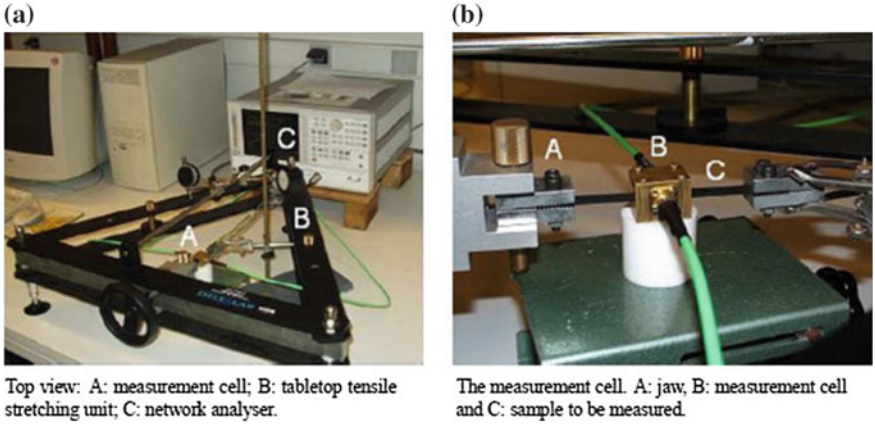

Fig. 11.5 Photographs of instrumentation for microwave measurements. Reprinted with permission from [42], copyright 2005 IOP

can be easily set up to allow a measurement in the presence of magnetic field along the wave propagation direction.

Figure 11.5b illustrates the perspective view of the measurement cell. With *S*-parameters measured by the network analyser, the permittivity and permeability can be extracted by a utility program. Note that this instrument is capable of simultaneous measurement of electric permittivity and magnetic permeability in the presence of magnetic field and/or stress at a very wide spectra coverage up to gigahertz.

Full details of the design and specification of this spectroscopy can be found in Ref. [43]; herein only a brief summary will be provided. In outline, the microwave characterisation using this equipment consists of measuring the transmission and reflection coefficients of an asymmetric microstrip transmission line containing the tested sample in the presence of a magnetic bias or tensile stress.

The measurement of the scattering parameters (*S*-parameters) was achieved using an Agilent H8753ES network analyser with short-open-load-thru (SOLT) calibration. A utility program extracts the data and generates complex permittivity ε and magnetic permeability spectra as individual files in .txt format. As outlined in [42], the quasi-transverse electric and magnetic mode, which is the only mode that propagates in the structure, makes analysis of the complex transmission and reflection coefficients created by the discontinuity between the line and the sample relatively uncomplicated. Using the Nicolson–Ross procedure for the transformation of the load impedance by a transmission line, e is determined by the transmission S_{21} and reflection S_{11} parameters. An error analysis indicates modest uncertainties in ε', μ' (<5 %) and μ'', μ'' (<1 %) for the data. One further feature of the measurement system is worth commenting on. To obtain accurate measurements of ε and μ, it is particularly important to account for the residual air-gap between the sample and the line walls; that is, the gap is determined by the roughness of the surfaces of the measured samples.

11.3 Low-Field Tunable Properties

11.3.1 Field Effect on the Impedance of Single Wire

The static magnetic field is essential to generate the GMI effect. With our focus on the gigahertz frequency range, the numerous studies on the megahertz frequency range (see [44] and references therein) will be skipped. At high frequency, the GMI effect is believed to be caused by the natural ferromagnetic resonance in the outer layer of wires occurring at a relatively small ac field [45–48]. The resonance frequency is dependent on the anisotropy field, anisotropy angle, and external field (if it exists) [10, 15, 21, 49, 50]. At around resonance frequency, the field sensitivity can reach a maximum [51]. The typical field effect is shown in Fig. 11.6. Note that the real (imaginary) part of Z corresponds to the imaginary (real) part of circumferential permeability [48]. Similar effects are also shown elsewhere [52–55].

11.3.2 Continuous-Wire Composites

For continuous-wire composites, the dependence of effective permittivity on the external field is established via the field dependence of plasma frequency according to Eq. 11.10. As the plasma frequency is dependent on the interwire spacing and wire diameter following Eq. 11.5, these two geometrical parameters are critical in governing the effective response of the composite to the external field. Actually, this is quite reasonable since these two parameters constitute the basic mesostructure and are decisive in the dielectric heterogeneous composites [56–58]. Also, the tunable properties are largely determined by the local magnetic properties

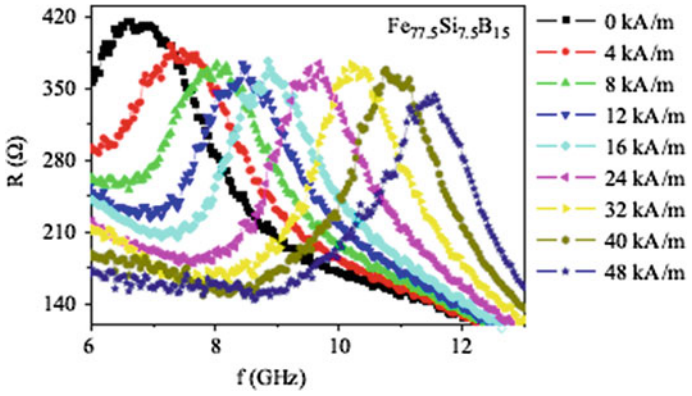

Fig. 11.6 Real component of impedance for a FeSiB glass-coated microwire as a function of frequency for selected values of applied field. Reprinted with permission from [50], copyright 2009 Elsevier

of the wires. Therefore, the following discussion of tunable properties of continuous-wire composites is carried out from these three critical influencing factors, i.e. interwire spacing (also known as cell parameter, periodicity), wire diameter, and local magnetic property of wires.

11.3.2.1 Influence of Wire Periodicity

Figure 11.7 displays the dependence of complex effective permittivity on the frequency, with magnetic field as a parameter for composites with wire $Co_{68.7}Fe_4Ni_1B_{13}Si_{11}Mo_{2.3}$ with different periodicity. The dependence of the effective permittivity is well displayed in both graphs below the corresponding plasma frequency.

It can also be seen that, with increasing wire periodicity from 7 to 15 mm, the frequency dispersion of effective permittivity on the magnetic field is remarkably depreciated as the tunability (defined as the ratio of variation of the electromagnetic parameter to that of the corresponding field [29]) is reduced from 0.16 m/A to 7.7×10^{-3} m/A. This means that a small wire periodicity is preferable for a field tunable property. However, a decrease of wire periodicity will increase the plasma frequency and hence the skin effect. If the skin effect is too strong, the field effect will be rather weak. Therefore, the wire diameter may also need to be decreased to

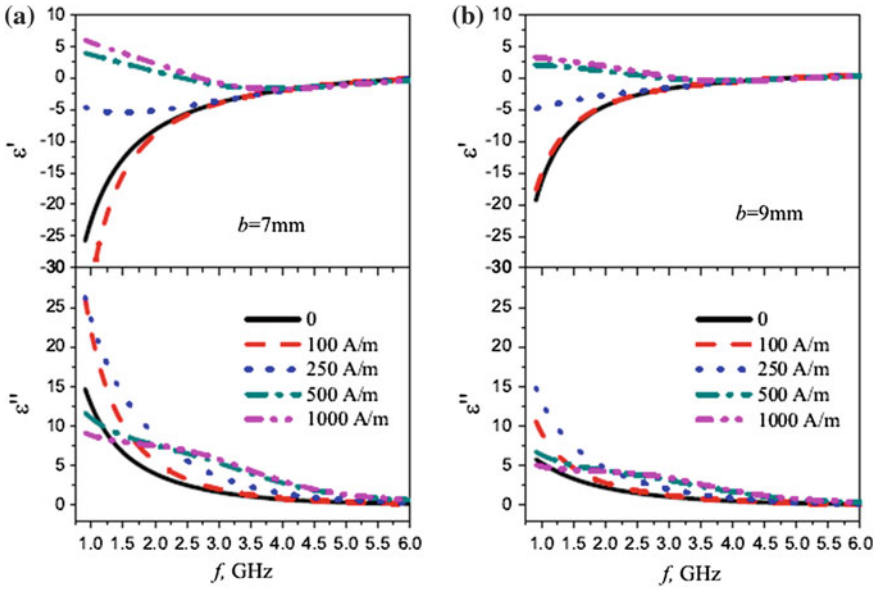

Fig. 11.7 Frequency plots of the real and imaginary part of effective permittivity for composites containing long continuous wires with the external field as a parameter. **a** Wire spacing $b = 7$ mm; **b** $b = 9$ mm. Reprinted with permission from [59], copyright 2012 Elsevier

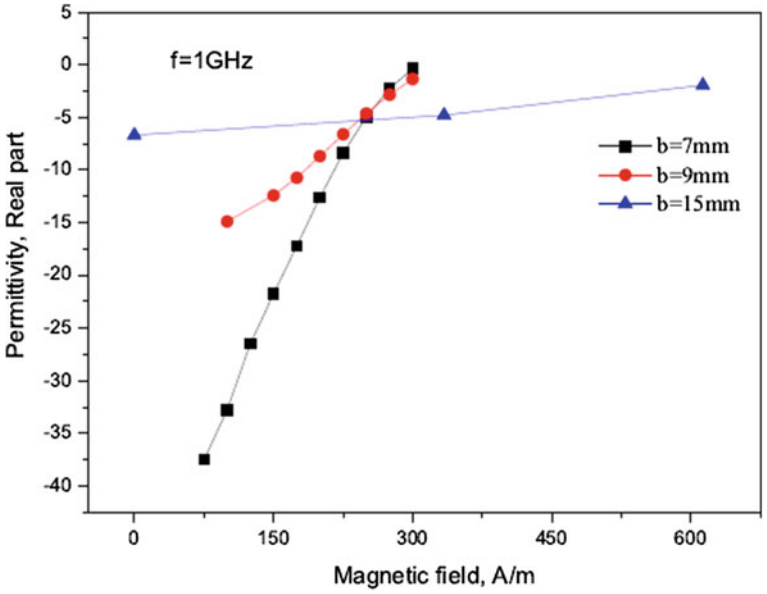

Fig. 11.8 Effective permittivity, real part, as a function of external field for composites containing continuous wires with different wire periodicity b = 7, 9, and 15 mm. Reproduced with permission from [59], copyright 2012 Elsevier

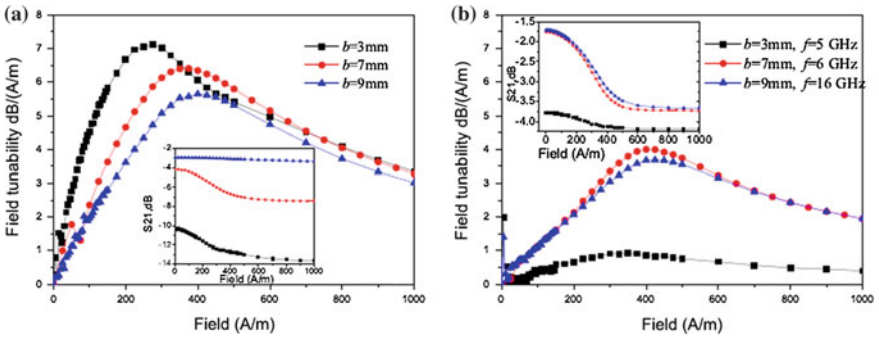

Fig. 11.9 Field tunability of transmission parameter S_{21} as a function of external field for composites containing continuous wires with different wire periodicity b = 3, 7, and 9 mm at (**a**) 4 GHz and (**b**) plasma frequencies for each wire periodicity. The ordinate profiles are divided by the factor 0.001. *Inset graphs* are the corresponding field dependence of S_{21}. Reprinted with permission from [22], copyright 2010 AIP

compensate the decrease of skin depth. Thereby, there exists an optimum value of wire periodicity matching the diameter for the microwave tunable properties. This is consistent with the theoretical prediction that for b = 0.5 mm, the best tunability will be achieved for a wire radius of 5–10 μm [60] (see Figs. 11.8 and 11.9).

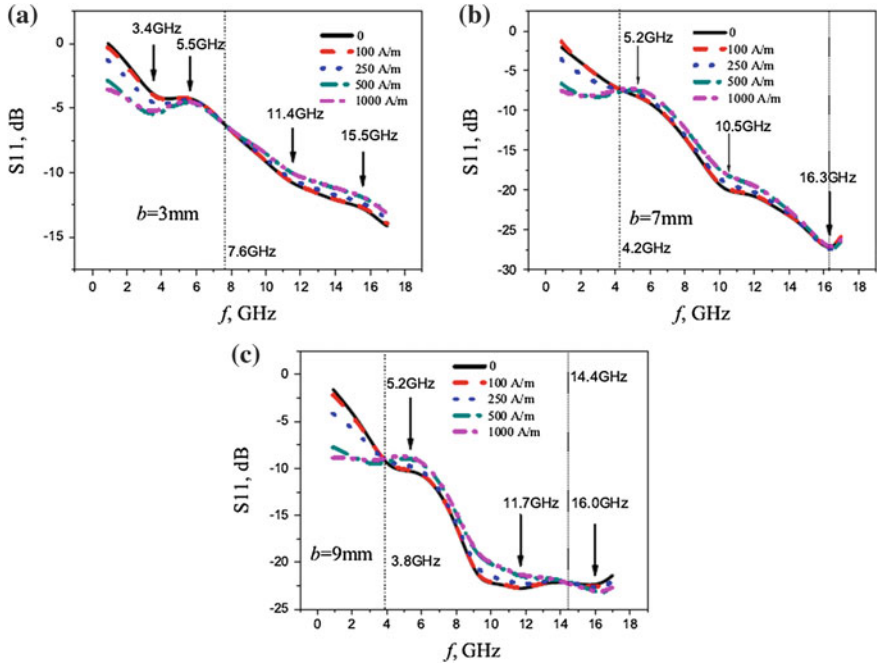

Fig. 11.10 Experimental reflection spectra (S_{11}) for composite sample of 640 μm thick and 50 cm × 50 cm in-plane size with continuous amorphous wires spaced at 3 mm (**a**), 7 mm (**b**), and 9 mm (**c**). Reprinted with permission from [59], copyright 2012 Elsevier

Figure 11.10 shows the frequency dependence of the reflection parameter (S_{11}) taken at different magnetic fields for the composites with b = 3, 7, and 9 mm. It can be seen that the shape of the curves varies remarkably as the wire periodicity increases from 3 to 9 mm. For the b = 3-mm sample, the spectra can be divided into two frequency zones at 7.6 GHz. Below 7.6 GHz, the reflectivity decreases as the magnetic field is applied. This is due to the absorption effect. However, the opposite trend is observed for $f > 7.6$ GHz. For the b = 7- and 9-mm samples, one more zone is found for $f > 16.3$ GHz and $f > 14.4$ GHz. The frequency at which the signal of S_{11} changes with magnetic field is considered the characteristic frequency. It is worth noting here that as b increases from 3 to 9 mm, the characteristic frequency decreases from 7.6 to 3.8 GHz (between zones 1 and 2). One can also see that the characteristic frequency (between zones 2 and 3) decreases from 16.3 GHz for the b = 7-mm sample to 14.4 GHz for the b = 9-mm sample. For the b = 3-mm sample, the characteristic frequency cannot be determined due to the limited measurement frequency range, but it appears to be higher than those for the b = 7- and 9-mm composites. This finding points to an important consequence that the characteristic frequency shifts to a lower value for composites with larger wire periodicity in the reflection spectra.

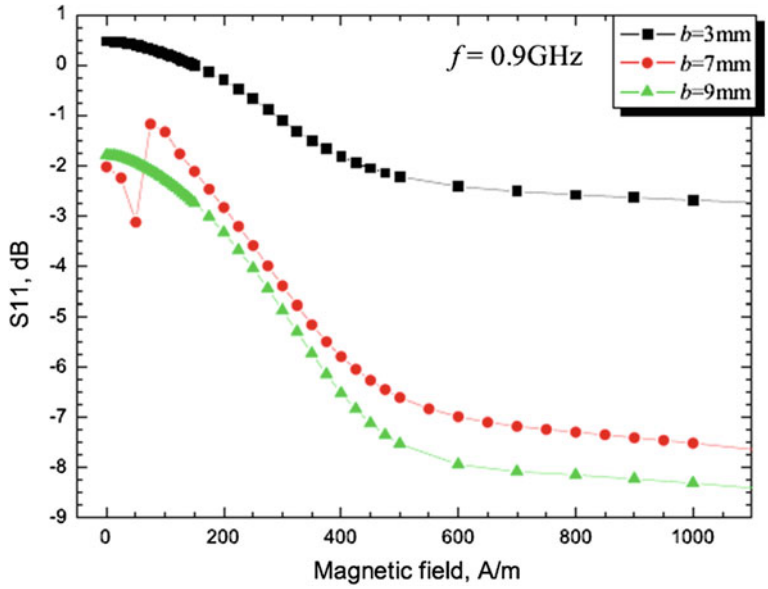

Fig. 11.11 Reflection parameter as a function of external field for composites containing continuous wires with different wire periodicity b = 3, 7, and 9 mm at the initial frequency of 0.9 GHz

Figure 11.11 shows the magnetic field dependence of the reflection parameter (S_{11}) taken at 900 MHz. The sensitivity of S_{11} to the magnetic field is positively correlated to b. For the composites with b = 9 mm, S_{11} falls from −1.8 dB at Hex = 0 to −7.5 dB at Hex = 500 A/m.

11.3.2.2 Influence of Wire Diameter

It is well known that the wire diameter has a strong impact on the GMI properties of microwires [61–64]. Figure 11.12 shows that composites containing wires with a larger diameter present a higher-field tunability than those with a smaller diameter, which can be explained by the wire geometry dependence of the GMI effect and associated skin effect. It has already been demonstrated that the GMI effect is positively correlated to the wire diameter [65]. Accordingly, the dielectric response of the composite containing wires of larger diameter is stronger than otherwise [2].

A comparison between the transmission spectra (cf. Fig. 11.13) reveals that the diameter of the wire has a profound impact on the intensity of S_{21} but much less effect on the tunability. The variation of diameter of several microns has a negligible influence on the plasma frequency of 5 GHz, and the frequencies at which S_{21} reaches the minimum are about 3 GHz for both of them. It follows that the plasma frequency probably decides the patterns of transmission spectra. The phase shift of

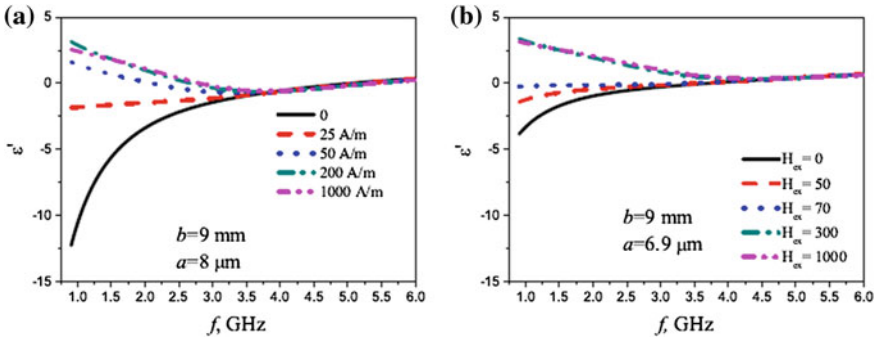

Fig. 11.12 Frequency dependence of real part of effective permittivity with external field as a parameter for composites containing wires of different radius a. Reproduced with permission from [59], copyright 2012 Elsevier

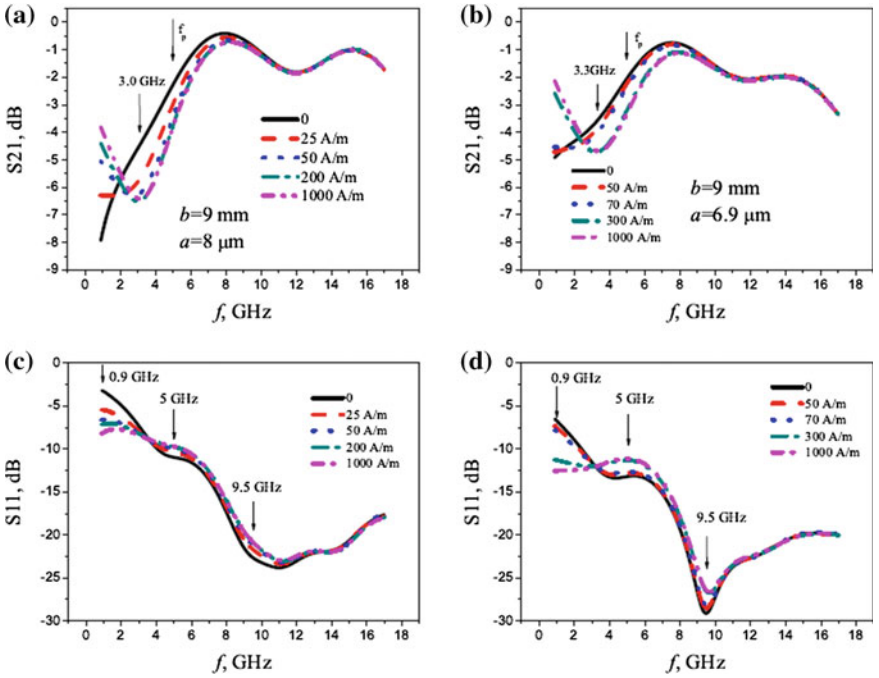

Fig. 11.13 Frequency dependence of S-parameters with external field as a parameter for composites containing wires of different radius: (**a**, **c**) a = 8 μm; (**b**, **d**) a = 6.8 μm. Reproduced with permission from [59], copyright 2012 Elsevier

S_{11} in the presence of an external field (*cf.* Fig. 11.14) suggests a promising sensing application of the composite. For the composite with 8-μm-thick wire, the phase going through $\pm\pi$ is completely suppressed when it is under a small field of 25 A/m.

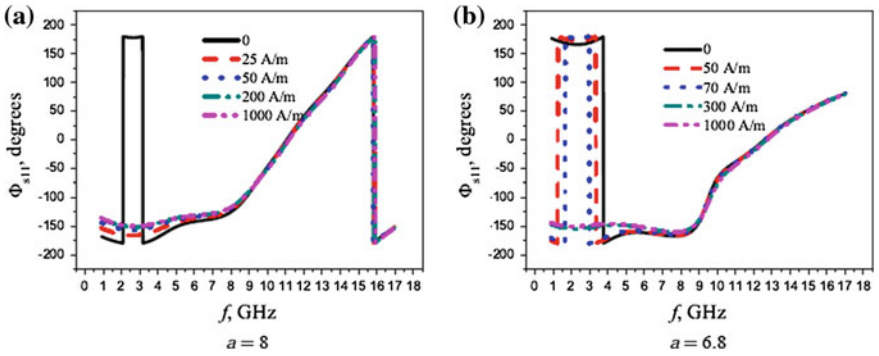

Fig. 11.14 Frequency dependence of phase of S_{11} with external field as a parameter for composites containing wires of different radius. Reproduced with permission from [59], copyright 2012 Elsevier

For the composite with 6.8-μm-thick wire, the concerned phase shifts to a lower value, from 3.7 in the absence of a field to 3.0 in the presence of a field of 70 A/m. These considerable changes suggest that the ferromagnetic microwires enable their composite with a self-monitoring capacity: any stress change that occurs to the wire through the composite can be detected via the microwave tunable spectra.

11.3.2.3 Influence of Wire Composition

Following from the very strong dependence of the GMI property on the composition of microwires [44, 63, 64, 66], the change of local magnetic properties with the composition is expected to vary the field effect. Figure 11.15 shows a comparison between the composites containing wires of the same geometry but different composition. The two wire composites present rather good dispersion properties but differing field effects. The scattering spectra for the two composites with a periodicity of 7 mm are presented in Fig. 11.16. In the spectra of S_{11}, the two composites possess almost the same characteristic frequencies but differing field tunability. All these observed effects are attributed to the difference in soft magnetic properties. Specifically, $Co_{68.7}Fe_4Ni_1B_{13}Si_{11}Mo_{2.3}$, with a better soft magnetic property than the other composition, has a larger dynamic magnetic permeability μ at the concerned frequency range, giving rise to a larger relaxation parameter γ according to $\gamma \propto \sqrt{\mu}\cos^2\theta$ [60] where θ is the static magnetisation angle. As it has been proved that field tunable effects are positively dependent on the relaxation parameter, the excellent magnetic softness would be preferable to realise strong field tunable effects. In considering that the soft magnetic features of microwires are sensitive to the composition [67, 68], one should try to achieve a precise control of composition in the fabrication process and appropriate tailoring in the post-fabrication treatments before proceeding to the manufacture of microwire composites for field tunable functionality.

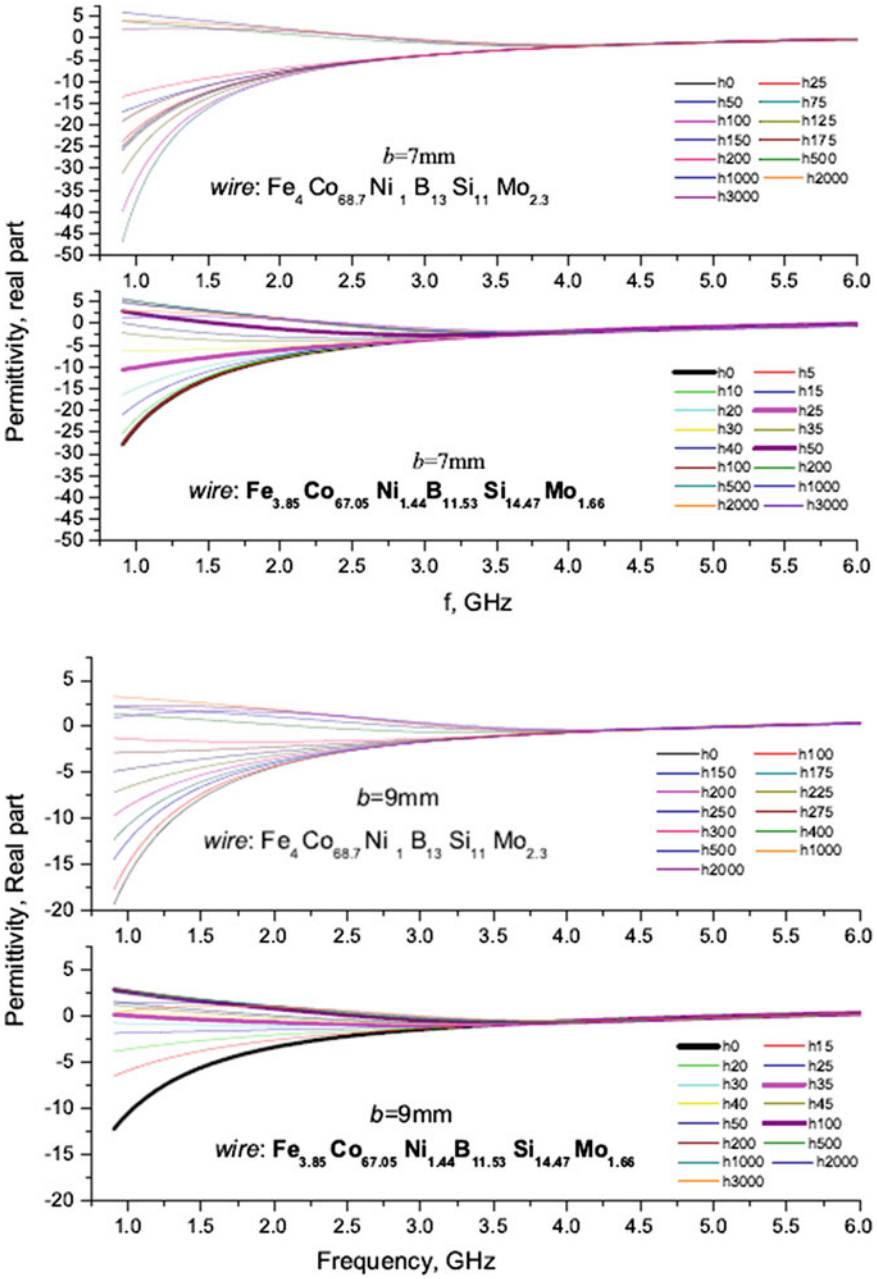

Fig. 11.15 Frequency plots of the effective permittivity, real part, for composites containing long continuous wires ($Co_{68.7}Fe_4Ni_1B_{13}Si_{11}Mo_{2.3}$ and $Co_{67.05}Fe_{3.85}Ni_{1.44}B_{11.53}Si_{14.47}Mo_{1.66}$) with the external field H_{ex} as a parameter. Wire radius a = 10 μm; wire periodicity b = 7 mm (*upper plot*) and b = 9 mm (*lower plot*). Reprinted with permission from [69], copyright 2013 Elsevier

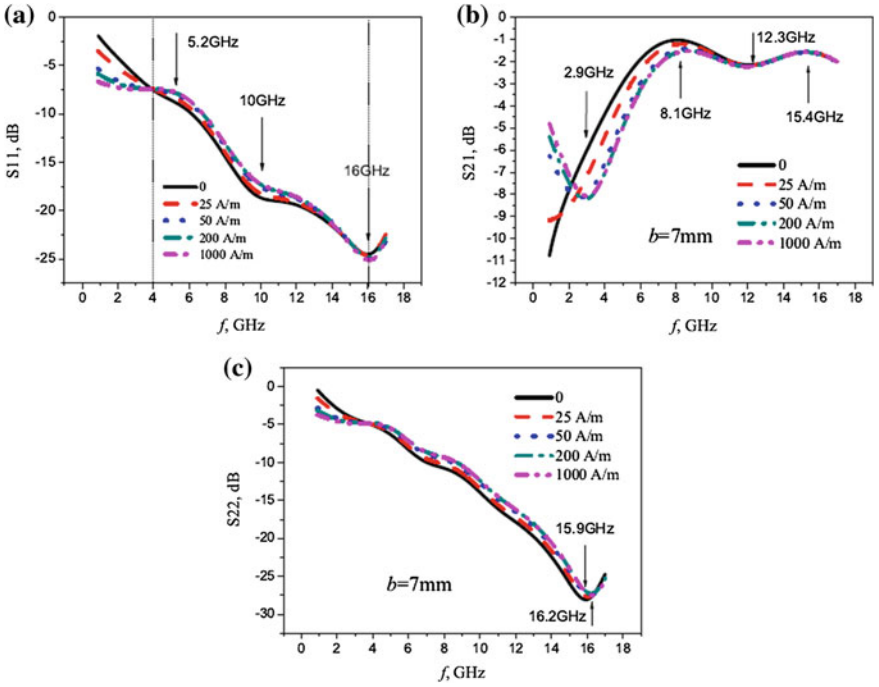

Fig. 11.16 Frequency dependencies of magnitude of *S*-parameters for composite containing amorphous wires $Co_{67.05}Fe_{3.85}Ni_{1.44}B_{11.53}Si_{14.47}Mo_{1.66}$ spaced at 7 mm. (**a**) S_{11}, (**b**) S_{21}, and (**c**) S_{22}. Reprinted with permission from [69], copyright 2013 Elsevier

11.3.3 Short-Wire Composites

In a short-wire composite, short wire pieces may be uniformly dispersed in a random manner [24–26] or in a periodical manner [21, 22, 27, 32, 70–72]. In this section, the magnetic bias (field) effects of short-wire composites are presented and discussed within the theoretical framework detailed in Sect. 11.1.

Figure 11.17 shows the dispersion of effective permittivity for a short-wire composite with the parameters (l, a, n_c) detailed in the graph. The value of ε' is rather small due to the low concentration of the microwires (Fig. 11.17a). Nevertheless, a dependence of ε' on the applied magnetic field is demonstrated. The transformation of resonance to relaxation can be inferred from the frequency evolution of these curves. The anisotropy field can be used as a critical value to distinguish the frequency dependence of ε' at the studied frequency range (1–5 GHz). The same trend is also observed in the frequency plots of ε'' (Fig. 11.17b). This is explained as follows. When $H_{ex} < H_k$, the impedance is increased with H_{ex}. Therefore, the internal loss increases and the relaxation dispersion occurs. The relaxation behaviour is fully achieved when $H_{ex} = H_k$, whereby the impedance reaches a maximum. Further increase of Hex results in a reverse trend. Note that the dielectric response to the

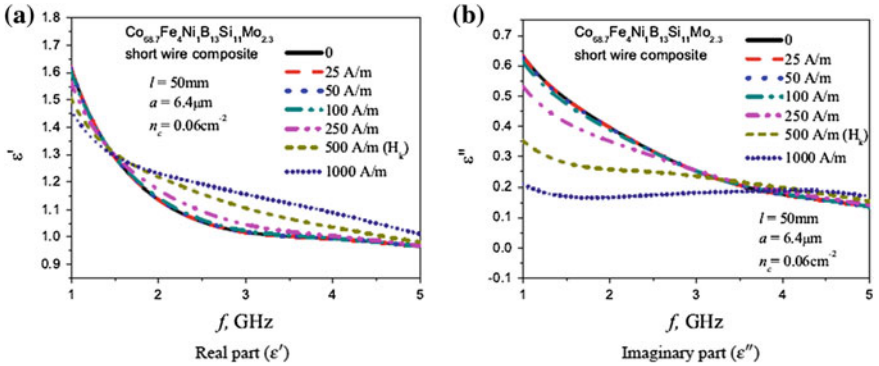

Fig. 11.17 Effective permittivity spectra of a short-wire composite with varying magnetic field relative to anisotropy field (500 A/m). The material parameters are given in the graph: l is the wire length, a is the wire radius, n_c is the ratio of wire number to the area containing them. Reprinted with permission from [69], copyright 2013 Elsevier

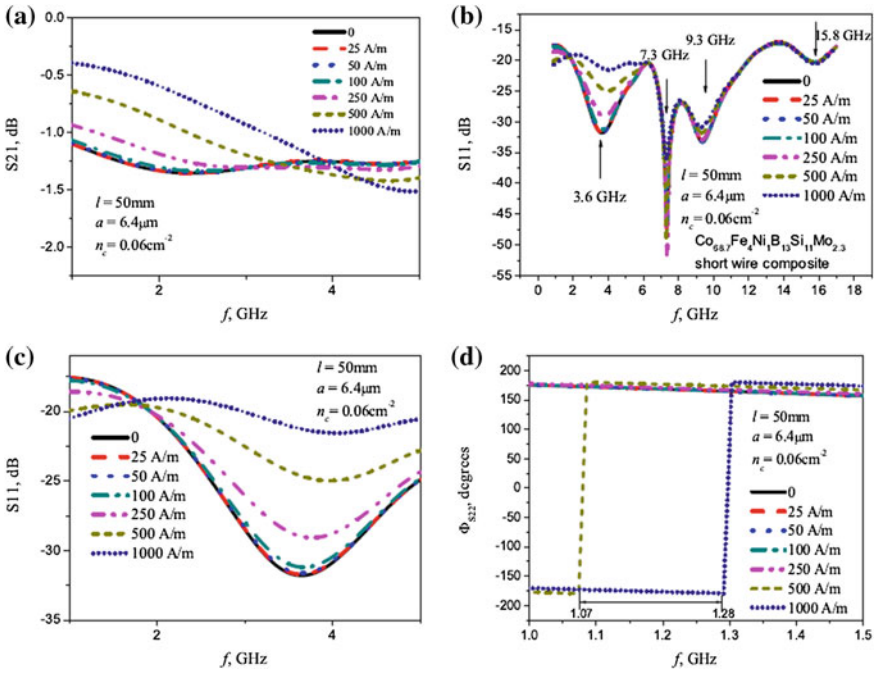

Fig. 11.18 **a** Transmission and **b** reflection spectra of a short-wire composite with the magnetic field as a parameter; **c** part of (**b**) at 1–5 GHz; **d** the phase of reflection coefficient. The phase reversal shift is indicated in the graph with coordinate values given. The material parameters are given in the graph by the same symbols as in Fig. 11.17. Reprinted with permission from [69], copyright 2013 Elsevier

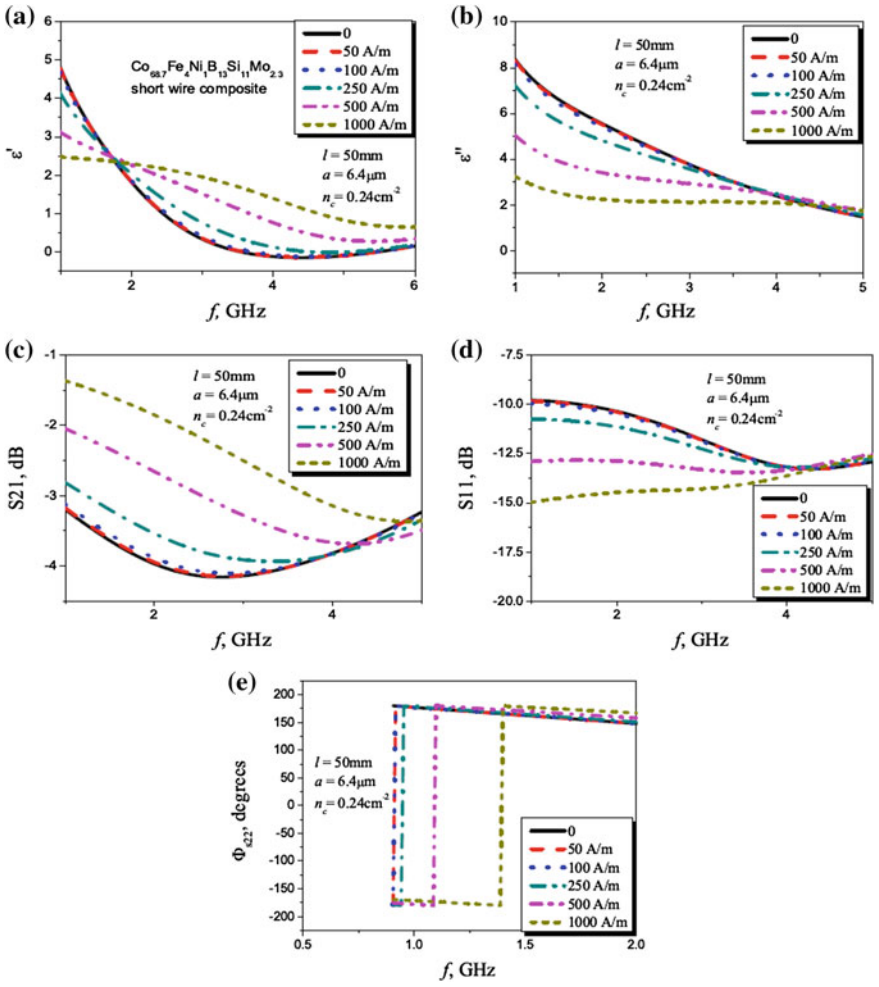

Fig. 11.19 Experimental dispersion of **a** real and **b** imaginary part of effective permittivity; **c** measured transmission and **d** reflection spectra of the short-wire composite with the magnetic field as a parameter; **e** presents the phase of reflection coefficient. The material parameters are given in the graph by the same symbols as in Fig. 11.17. Reprinted with permission from [69], copyright 2013 Elsevier

magnetic field is not seen until the field reaches 250 A/m; this is likely due to the relative insensitivity of magnetoimpedance for this range of magnetic field.

As with the complex permittivity spectra, the transmission is increased as the field increases, with a concomitant resonance/relaxation change, as seen in Fig. 11.18a. Strikingly, the transmission spectra present a large transmission of *ca.* 90 %, which corresponds to a very large return loss (see Fig. 11.18b). With the same spectra zoomed at 1–5 GHz (Fig. 11.18c), the resonance/relaxation

transformation is clearly observed with increasing magnetic field. The resonance/relaxation frequency shifts to a higher value with increasing magnetic field. The phase shift Φ is also shown in the reflection spectra, as depicted in Fig. 11.18d.

By decreasing the wire periodicity from 20 to 5 mm, the area concentration of wires is greatly increased from 0.06 to 0.24 cm^{-2}. As a result, the values of the measured *S*-parameters are largely increased while their field dependences remain unchanged (Fig. 11.19a–d). Inasmuch as the wire geometry (length, diameter and aspect ratio) remains unchanged, there will not be significant changes in the dispersion behaviour as far as the composite mesostructure is concerned. It should be noted that, although the phase shift remains unchanged when the field increases from 500 to 1000 A/m, a reduction from 500 to 100 A/m is found to cause a phase reversal between $-\pi$ and π in the reflection spectra (Fig. 11.19e).

11.4 High Field Tunable Properties

The high field effect that we aim to study here refers to the magnetic field of the order of 100–1000 Oe, which is in contrast to the low magnetic field of no more than 50 Oe. In this section, we will treat the effective permittivity of different kinds of microwire composites by a modified frequency-domain spectroscopy and reveal intriguing physics behind some unique phenomena such as the crossover field and double peak exhibited in the permittivity spectra.

11.4.1 High Field Dependence of Permittivity

Two kinds of samples containing Co-based melt-extracted microwires are used for microwave characterisation, i.e. continuous-wire samples and random-wire samples. For the random-wire sample, 50 mg of 5-mm-long wires were randomly dispersed in a silicone rubber by mechanical mixing. The mixture was subsequently mould-casted to obtain samples with dimensions 70 × 10 × 1.8 mm^3 and cured at ambient temperature for 24 h (Fig. 11.20a). The resultant sample has a microwire content of 3 wt%. For continuous-wire samples, 70-mm-long microwires were aligned in a periodical manner (Fig. 11.20b) with fixed wire spacing of 0.77 mm into silicon rubber matrix sheets which were bonded together using silicone resin.

Representative spectra of the real, ε', and imaginary, ε'', parts of the complex permittivity at five different magnetic bias values for sample A are shown in Fig. 11.21. At zero magnetic field, the permittivity shows a relaxation behaviour. When a magnetic field of 100 Oe is applied, ε' is found to increase and the relaxation remains visible. With further increase of the magnetic field up to 500 Oe, an absorption peak is seen near 4.1 GHz (Fig. 11.21b). This maximum shifts to higher frequencies of, respectively, 4.6 and 4.7 GHz as the magnetic field is

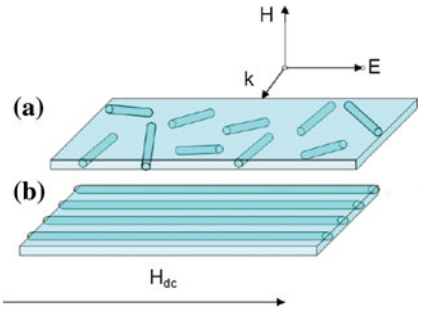

Fig. 11.20 **a** Schematic illustration of random-wire sample. **b** Same as in (**a**) for continuous-wire sample. The electric field vector of the electromagnetic wave is parallel to the wire axis. The applied magnetic field H_{dc} is directed along the wire axis. Reprinted with permission from [23], copyright 2012 AIP

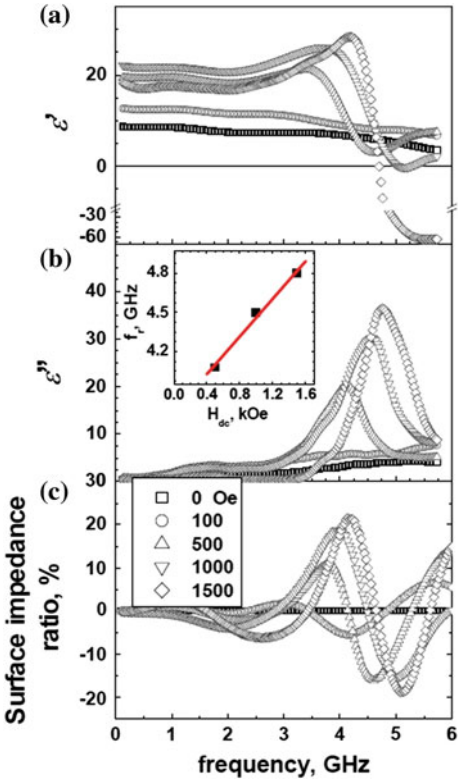

Fig. 11.21 **a** Frequency dependence of the real part of the effective permittivity for random-wire sample at varying magnetic fields. **b** Same as in (**a**) for the imaginary part of the effective permittivity; the inset shows the field dependence of magnetoimpedance resonance extracted from (**b**). **c** Frequency dependence of the surface impedance ratio at varying magnetic fields. Reprinted with permission from [23], copyright 2012 AIP

increased to 1 and 1.5 kOe, with increased height and width. The peak is associated with anomalous dispersion of Fig. 11.21a, leading to negative values of ε' for frequencies higher than 4.7 GHz for magnetic fields over 1 kOe.

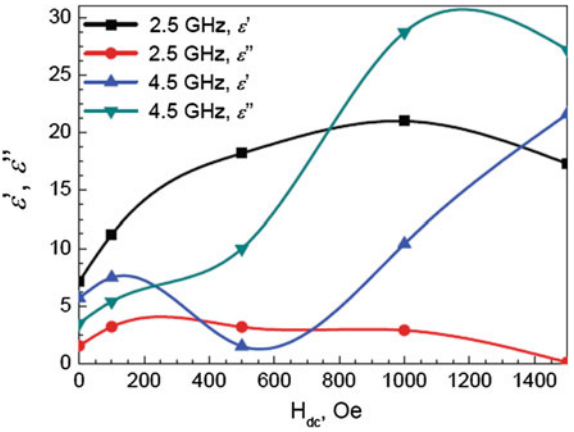

Fig. 11.22 Magnetic field dependence of the real and imaginary parts of the effective complex permittivity for random-wire sample at 2.5 and 4.5 GHz. Reprinted with permission from [23], copyright 2012 AIP

Figure 11.22 presents the magnetic bias dependence of the real and imaginary parts of the effective complex permittivity for the random-wire sample at 2.5 and 4.5 GHz. At 2.5 GHz (off resonance), the variations in and ε'' are small. This contrasts with the rather pronounced changes of ε' and ε'' observed at 4.5 GHz (resonance). It can also be seen that, at 4.5 GHz, the application of a magnetic field excitation gives rise to an ε'' larger than ε', which is not seen at 2.5 GHz.

In order to examine the influence of the magnetic bias on the permittivity of the continuous-wire sample, we turn now to analysing the microwave absorptive behaviour probed by our electromagnetic measurements (Fig. 11.23). Two well-separated absorption lines are found in the ranges 1–2 and 4–5 GHz, respectively. Note that the bias dependence of permittivity can be clearly observed for each

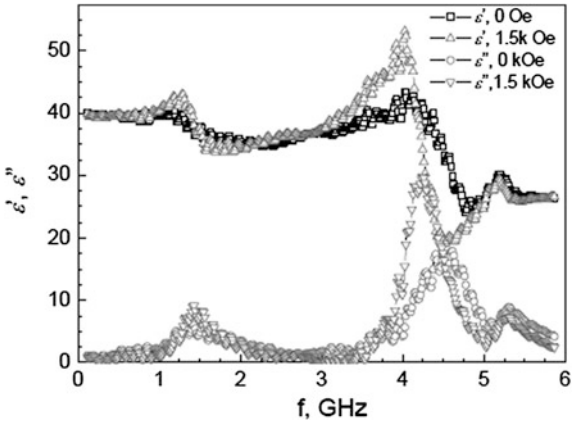

Fig. 11.23 Frequency dependence of the real and imaginary parts of the effective complex permittivity for continuous-wire sample at zero magnetic field and 1.5 kOe. Reprinted with permission from [23], copyright 2012 AIP

resonance region. As the magnetic field is increased, the absorption line at 4–5 GHz grows in magnitude and becomes narrower. The linewidths of the dielectric and magnetoimpedance resonances present opposite variations as the field is increased.

Two aspects of the above results should be noted. The first is that microwires respond to the electromagnetic wave like electric dipoles for sample A. The dipole resonance can be expressed as $f_{\text{res}} = c/2l\sqrt{\varepsilon_m}$ [11], where c is the electromagnetic wave velocity in vacuum, l is the wire length, and ε_m is the permittivity of the host matrix. When l is chosen at 5 mm, the resonance frequency is close to 15 GHz, which is out of the measurement range of the present work. This explains the absence of the absorption line in the spectrum without, or with low applied magnetic field. With the application of high magnetic field, our results demonstrate that the current induces resonance of circumferential permeability; that is, the magnetoimpedance resonance results in a significant change of the effective permittivity of the wire-filled composites [24, 25, 73]. Since the applied magnetic field strongly influences the current distribution in the microwires through the skin effect, this gives rise to a significant change of the dielectric response in the GHz range of frequencies. As the magnetoimpedance resonance frequency is below the dielectric resonance frequency, absorption within the skin effect predominates over dipolar absorption and has the effect of increasing the absorption linewidth [24]. The blueshift of resonance frequency with the field H_{dc} (cf. the inset of Fig. 11.21b) is consistent with the field effect on the surface impedance profiles calculated from S-parameters, as shown in Fig. 11.21c. The interest in the microwave behaviour of these composite samples lies also partly in its anomalous dispersion [74]. Since application of a magnetic bias can lead to large eddy current losses, we suggest that wire-filled composites can be exploited for designing microwave absorbers having a large absorption bandwidth. In addition, the anomalous dispersion is often associated with a negative value of ε'. Thus, a variety of unusual properties can be engineered to meet the requirements of a high-performance frequency selective surface. It should be noted that while the magnetic bias has a strong influence on the permittivity, it has a negligible effect on the magnetic permeability (not shown here). Since the wire concentration is low, the magnetic permeability is close to unity in the GHz range of frequencies. For sample B, the wires which are perpendicular to the microwave magnetic field do not contribute, whereas those which are parallel have no response to the field in the GHz range of frequencies. Hence, we predict that the sensitivity of permittivity to frequency and magnetic field will result in useful applications of this kind of microwire composite samples.

The second point deals specifically with the continuous-wire sample. Compared with the random-wire sample, it is notable that it has a much lower dipole resonance frequency at 1.1 GHz according to $f_{\text{res}} = c/2l\sqrt{\varepsilon_m}$, which is in good agreement with the lower-frequency peak shown in Fig. 11.22. The difference observed with the experimental value of the resonance frequency can be attributed to interfacial defects in the composite, e.g. imperfect bonding.

To summarise, we have evaluated in this section the microwave response of composite samples containing glass-covered amorphous microwires embedded in a

rubber matrix with different wire lengths and topological arrangements. The obtained results show that there is a strong dependence of the permittivity spectra on the external magnetic bias. For wire composites containing randomly dispersed wires of 5 mm length, the real part of the permittivity increases as the magnetic bias is increased until it attains a maximum which corresponds to the maximum absorption induced by the magnetoimpedance resonance. The absorption resonance frequency and linewidth can be conveniently tuned by the magnetic bias. Composites containing periodically arranged longer wires (70 mm) are characterised by a double-resonance permittivity spectrum. The higher-frequency resonance is associated with magnetoimpedance resonance. It has a narrower linewidth than that of the lower-frequency (dipole) resonance as the magnetic field is increased. The assessment of the high field effect points to interesting physics in our understanding of the electromagnetic properties of composite materials with tunable microwave properties at very high magnetic fields.

11.4.2 Crossover Phenomenon

In the present and next section, we will discuss some unusual phenomena observed in the microwave spectra of the microwire composites in the presence of high magnetic fields. Understanding the physics behind these peculiar observations provides insights into the structure–property relationship of the microwire composites. Thus, we can optimise the design of the composite architecture and, in another perspective, exploit the usefulness of microwave characterisation techniques as a research tool to probe the materials' micron or even nanostructure.

The crossover phenomenon we deal with in this section refers to the existence of a critical field dividing a reverse field effect on the electromagnetic parameters below and above. The phenomenon was observed in a set of epoxy-based microwire composites containing 25-mm Co-based glass-coated microwires randomly dispersed as shown in Fig. 11.24 and submitted to an external magnetic field from 0 to 1 kOe.

Figure 11.25 compares the zero-field transmission, reflection, and permittivity spectra for three microwire weight fractions. The observed difference in the frequency dependence of these quantities is not surprising. Two features can be noticed. Firstly, a large increase of ε' and ε'' is observed with increasing contents of microwires; the most prominent feature in Fig. 11.25c is the peak in the ε'' spectra, which is related to a dipolar resonance phenomenon. While the peak positions do

Fig. 11.24 Image of the composite sample containing 0.026 vol% microwires. Reprinted with permission from [75], copyright 2012 AIP

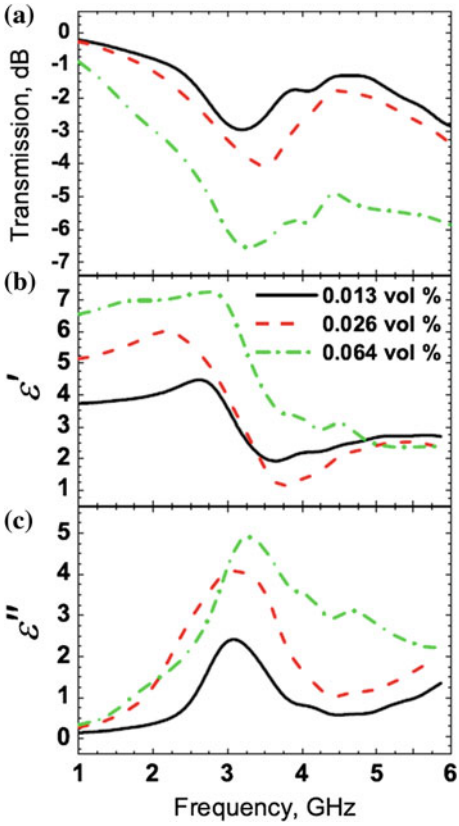

Fig. 11.25 The transmission spectra (**a**), frequency dispersion of the real, ε', (**b**) and imaginary parts, ε'', **c** of the effective complex permittivity for microwire/epoxy composites with varying concentration. Reprinted with permission from [75], copyright 2012 AIP

not significantly shift with wire concentration, the peak size and width increase strongly with wire content. The dipolar resonance frequency is calculated to be 3.2 GHz, which is close to the peak positions observed in Fig. 11.25c. The differences in peak height and width between the three wire weight fractions are probably related to the microwire content. Secondly, a minimum of transmission is observed close to the resonance position.

In Fig. 11.26, the field dependence of the electromagnetic parameters for the sample containing 0.013 vol% of microwires is plotted as a function of frequency at low magnetic field (up to 300 Oe). First, we note the contrasting behaviour of the transmission and reflection coefficients as the magnetic field is increased, as seen in Fig. 11.26a and c, respectively. Further, the reflection maximum or transmission minimum corresponding to the resonance frequency is redshifted with increase of the magnetic field. For a quantitative analysis, we fitted the *H*-dependent resonance position with a linear function and plotted it in Fig. 11.26c. We exhibit in Fig. 11.27 the corresponding spectra at higher fields (between 300 Oe and 1 kOe). In all cases, we observe opposing field-dependent behaviour of the electromagnetic parameters. That is, the reflection spectra increase in magnitude, whereas the corresponding

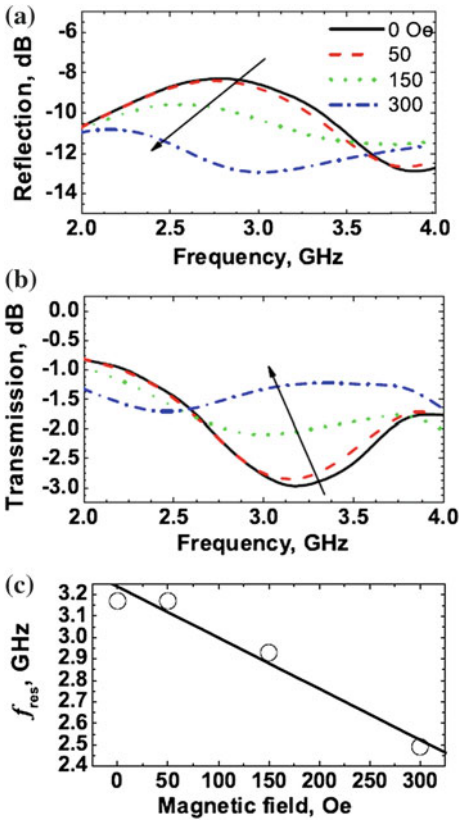

Fig. 11.26 The transmission spectra (**a**), reflection spectra (**b**), and field dependence of resonance frequency (**c**) under a dc field of 0–300 Oe. The sample contains 0.013 vol% microwires. The solid line in (**c**) is a linear fit to the data. Reprinted with permission from [75], copyright 2012 AIP

transmission spectra decrease. We note that this contrasting behaviour has not been predicted previously. For other composite samples containing different microwire concentrations, the field crossover at 300 Oe was also evident (Fig. 11.28). Interestingly, we observe that the magnitude of the transmission and reflection spectra at 300 Oe of the composite samples is quite similar for the different microwire concentrations investigated. Together, these observations support the conclusion that the linear variation of the resonance position shift against the magnetic field is an intrinsic property of the microwires in the samples.

One can think of this crossover at 300 Oe as arising from a competition between the two resonant phenomena characterising this system. As was seen earlier, the first resonance is the dipole resonance (3.2 GHz). The second resonance phenomenon is associated with the ferromagnetic resonance (2.3 GHz), which is in close proximity to the dipole one. Specifically, when the ferromagnetic resonance occurs to the microwire at sufficiently high magnetic fields, the skin depth reaches a minimum and hence gives rise to a maximum dielectric loss. As is now well established, the Co-based amorphous wires possess remarkable GMI properties. In the GHz range of frequencies, the GMI effect 1 dominates the features of dipolar

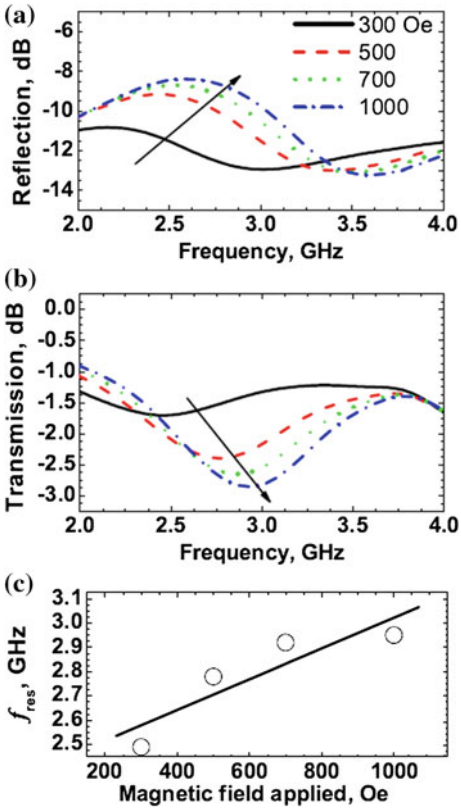

Fig. 11.27 Same as in Fig. 11.26 for the dc magnetic field in the range 300–1000 Oe. Reprinted with permission from [75], copyright 2012 AIP

absorption at low magnetic field bias. As the magnetic field is increased, the impedance increases. Hence, the permittivity together with the reflection and absorption is decreased. Consequently, the transmission is increased, as seen in Figs. 11.26b, 11.28a and c. This is also consistent with what was observed in free-space characterisation of short-cut microwire composites [72]. Now, if the magnitude of the magnetic field is larger than 300 Oe, we hypothesise that the electromagnetic characteristics are dominated by the FMR. As the magnetic field is increased, losses are enhanced. This is reminiscent of the eddy current in the microwires at FMR. Although the penetration depth at 2.4 GHz falls between 1 and 2 μm, microwaves can still penetrate the outer layer of the wire and result in eddy current loss [76]. Several reasons may contribute to the actual value of the crossover field at 300 Oe. For instance, we notice that the GMI effect requires relatively small magnetic field magnitudes, while the FMR is driven by a stronger field. This is consistent with the experimental results and the insensitivity of the crossover field against microwire content.

We now briefly turn to the magnetic field tunability of the effective permittivity of the samples. In Fig. 11.29, the quantities shown are the ratios $[\varepsilon'(H) - \varepsilon'(H = 0)]/\varepsilon'(H = 0)$ and $[\varepsilon''(H) - \varepsilon''(H = 0)]/\varepsilon''(H = 0)$, where different curves denote

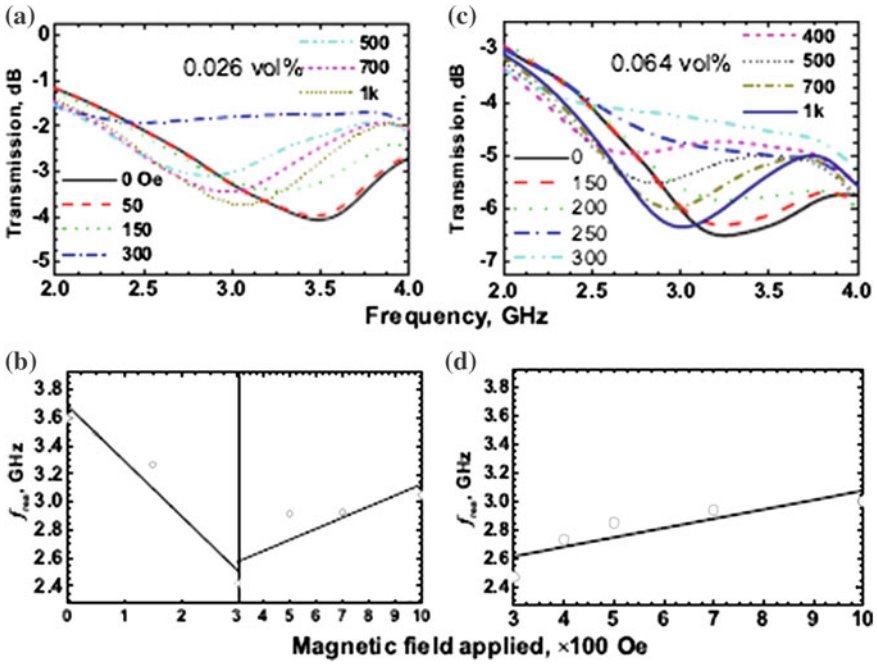

Fig. 11.28 **a** The transmission spectra for the sample containing 0.026 vol% microwires and different dc magnetic field excitations in the range 0–1 kOe. **b** The resonance frequency plotted as a function of the applied magnetic field. The *solid lines* are linear fits to the data. Notice the change in the slope of these lines at ≈300 Oe. **c** Same as in (**a**) for the sample containing 0.064 vol% microwires. **d** Same as in (**b**) for the sample containing 0.064 vol% microwires. Reprinted with permission from [75], copyright 2012 AIP

the different frequencies. Figure 11.28 shows a detailed comparison of these quantities for the three microwire contents. Overall, one can clearly see a peak feature at 300 Oe and the magnitude of this peak observed in these data can be as high as 150 % for 2.4 GHz, i.e. close to the FMR. Surprisingly, however, both Fig. 11.29c–d show that the larger effect is observed for the sample containing 0.2 wt% of microwires. We present a simple explanation for this behaviour. One expects that a large amount of microwire will improve the field-induced polarisation properties of the sample. Hence, the reflection and transmission coefficients and the value of the effective permittivity increase when the wire concentration increases from 0.013 to 0.026 vol%. Both magnetic and dielectric losses are enhanced, and consequently the overall absorption is also increased in agreement with previous measurements [77, 78]. However, the reflection losses also increase with microwire content. If these losses are too high, they will prevent efficient tuning of the microwire composites. This observation supports that low-loaded composites are required for efficient tunability. One might expect the maximum at 0.026 vol%

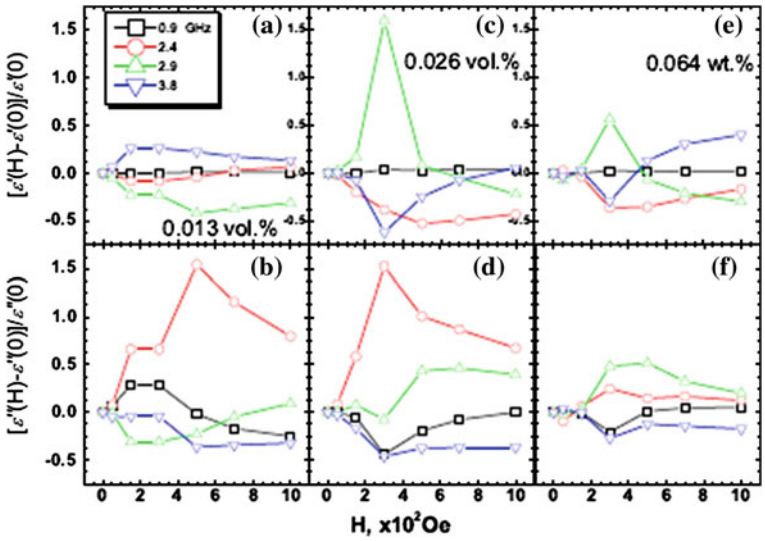

Fig. 11.29 **a** The magnetic field dependence of $[\varepsilon'(H) - \varepsilon'(H = 0)]/\varepsilon'(H = 0)$ at different frequencies for the sample containing 0.013 vol% microwires. **b** Same as in (**a**) for $[\varepsilon''(H) - \varepsilon''(H = 0)]/\varepsilon''(H = 0)$. **c** Same as in (**a**) for the sample containing 0.026 vol% microwires. **d** Same as in (**b**) for the sample containing 0.026 vol% microwires. **e** Same as in (**a**) for the sample containing 0.064 vol% microwires. **f** Same as in (**b**) for the sample containing 0.064 vol% microwires. Reprinted with permission from [75], copyright 2012AIP

to vary according to the microwires aspect ratio and intrinsic properties, and also fabrication protocol.

As a summary of this section, the crossover phenomenon has been identified via the investigation of the electromagnetic parameters of glass-covered amorphous microwires/epoxy composites with various concentrations of microwires over a broad magnetic field range up to 1 kOe. The results presented here show that the effective permittivity presents a strong tunability with respect to a dc magnetic field excitation. An inherent crossover field due to the microwires is further observed at 300 Oe. This observation can be understood intuitively by considering that the GMI effect dominates the features of dipolar absorption at low magnetic field bias (<300 Oe), while the opposite behaviour is expected at larger dc magnetic field excitations. We also point out that this crossover field is insensitive to changes in the microwire content. The largest magnetic field tunability of the effective permittivity of the samples is found at the microwire content of 0.026 vol%. These conclusions add strong impetus for designing glass-covered amorphous microwires/epoxy composites as adaptive materials for reconfigurable electronic devices and sensing applications, for which manipulation of the dielectric properties via a magnetic field excitation can be accomplished. It is also worth mentioning that the latest results obtained from our laboratory show that this crossover effect can also be found in the Fe-based microwire composites.

11.4.3 Double-Peak Phenomenon

The double-peak phenomenon has been found in the composites containing melt-extracted microwires. We present this unique case to demonstrate the versatility of the microwave behaviour of the microwire composites. Also, since microwire composites are primarily advantageous in their electromagnetic functionalities at microwave frequency, which are partially attributed to the soft magnetic properties of wires, characterisation of these with the aid of high field will give us a better understanding of the structure and the properties of wires. This suggests that the microwire composites can serve as a valuable medium to study the microwires.

The primary results of this section are shown in Figs. 11.30 and 11.31, which plot the effective complex permittivity spectra for the continuous-wire composite sample with, respectively, 6 and 8 wires and for field magnitudes from 0 to 1 kOe. Prominent in the data are the two pronounced and broad absorption peaks at 2.6 and 4.2 GHz. The peak at 2.6 GHz is much broader than the one at 4.2 GHz. Interestingly, there are some substantial differences between the behaviour of the two peaks when a magnetic field is applied. The magnitude of the ε'' peak at 2.6 GHz increases by a factor of 2 and its full-width half-maximum (FWHM) is significantly reduced when the magnetic field is increased from 0 to 1 kOe. The line shape and intensity of the peak at 4.2 GHz exhibit little change as a function of magnetic field; however, increasing magnetic field produces a visible redshift.

The comparison of Figs. 11.30 and 11.31 is instructive. We find that the value of ε'' for the peak at 2.6 GHz for the sample with 8 wires is significantly smaller than the corresponding peak for the sample with 6 wires, while the opposite trend is shown at the second peak of 4.2 GHz. The relative importance of the field effect

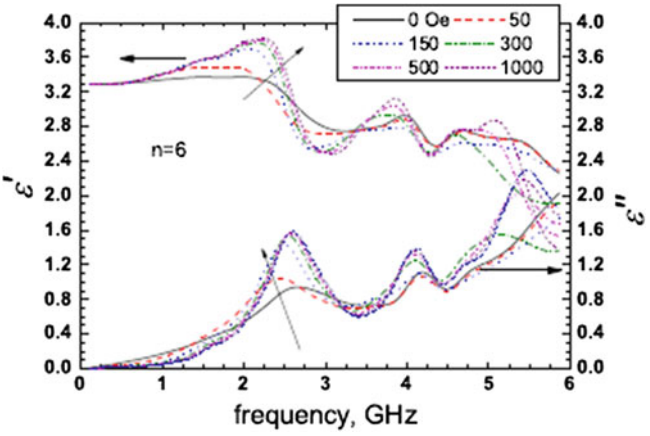

Fig. 11.30 The ε' and ε'' spectra for the sample containing 6 wires and for magnetic field magnitudes from 0 to 1 kOe. Reprinted with permission from [79], copyright 2013 AIP

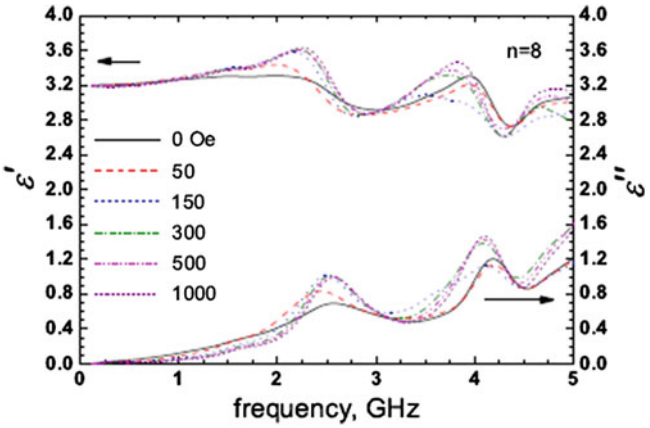

Fig. 11.31 Same as in Fig. 11.30 for the sample containing 8 wires. Reprinted with permission from [79], copyright 2013 AIP

from 150 Oe onwards in varying the permittivity is much larger at the first resonance for the $n = 6$ sample than the $n = 8$ one, while little change appears at the second resonance. The two-peak feature of the dielectric losses evidenced in Figs. 11.30 and 11.31 warrants further discussion. As noted in the previous sections, the ferromagnetic resonance (FMR) mode is intrinsic to the ferromagnetic microwires. When no external static magnetic field is applied, the FMR depends on the saturation magnetisation M_s and anisotropy field H_k of the microwires, expressed as $f_{\mathrm{FMR}} = \gamma = (M_s + H_k/2\pi)$, where γ is the gyromagnetic ratio [80]. For amorphous microwires with a small anisotropy field $(H_k \ll 2\pi M_s)$, one can write $f_{\mathrm{FMR}} \approx \gamma 2\pi M_s$. Taking M_s = 850 G, f_{FMR} = 2.4 GHz, which is in close correspondence to the value of 2.6 GHz observed experimentally. This small discrepancy can be attributed to the complex internal stress distribution appearing in the microwires during the rapid cooling rate, leading to a non-uniform distribution of local magnetoelastic anisotropy. When a magnetic field is applied, the relative importance of stress is weakened and the FMR mode is blueshifted as the field is increased, according to Kittel's law. The electromagnetic response of homogenised grids of parallel amorphous ferromagnetic microwires has been studied recently by Liberal et al. [81] by using the local field method and the transmission-line analogy. Following these authors, the reduction of the skin depth as the magnetic field is increased could provide an explanation for the increase of permittivity at the first peak observed in Figs. 11.30 and 11.31.

The resonance peak at 4.2 GHz can be distinguished from the FMR mode by examining the dependence of the dielectric losses versus the magnetic field. To put this into perspective, we assume that the microwires have a core-shell (CS) structure, i.e. a core amorphous phase surrounded by a nanocrystalline shell, and we consider that the nanocrystalline phase is responsible for the resonance peak at 4.2 GHz. HRTEM is a unique analytical tool for such study because it

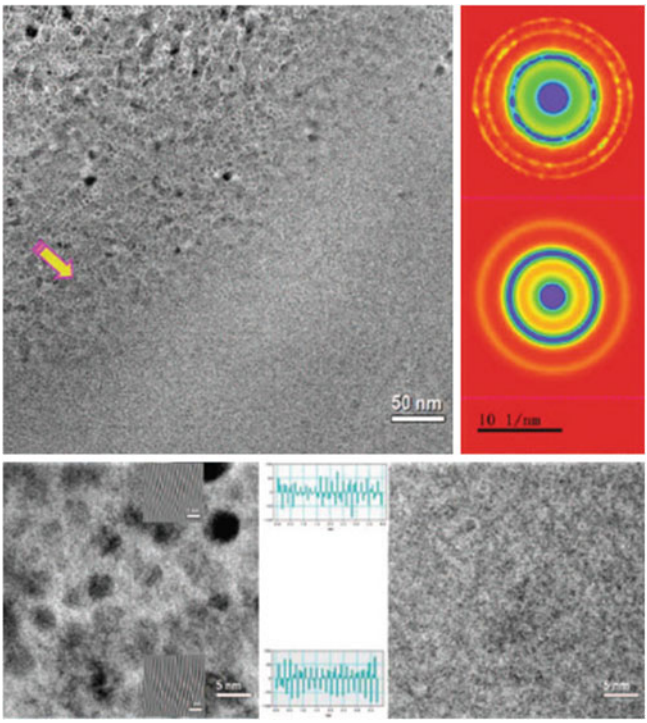

Fig. 11.32 HRTEM images and SAED of the studied microwire, and the corresponding local magnifications. **a** HRTEM images of biphasic structure of microwires, including nanocrystalline region I, amorphous region II and transition region III; The unidirectional arrow indicates the radial direction of the microwire. **b** SAEDs of biphasic structure, marked by *blue rectangles* (as shown in 1 and 2, respectively) in (**a**); the upper I is polycrystalline rings (consisting of CoFe, CoSi, and Co2B) SAED of rectangle 1 and the lower II is halo ring SAED of rectangle 2. **c** Local magnifications (rectangles 3 and 4) and their corresponding IFFT patterns and the estimative interplanar distances (D3 and D4) of nanocrystalline structure; **d** Local magnification of amorphous structure of rectangle 2 in (**a**). Reprinted with permission from [79], copyright 2013 AIP

can provide high-resolution microstructural and well as electron diffraction data. As shown in Fig. 11.32a, the nanocrystalline phase, amorphous phase split by a transition region, is clearly identified along the radial direction from the surface to the inner core. The polycrystalline rings representing the nanocrystalline phase and the halo ring representing the amorphous phase are also readily present in the selective area electronic diffraction (SAED) images (Fig. 11.32b). Further observations of the magnified nanocrystalline region and amorphous region were displayed in Fig. 11.32c and d, respectively. The nanocrystallites average 2 nm. The formation of nanocrystallites is attributed to the melt extraction process [82]. As schematically shown in Fig. 11.33, in the first stage, heat transferred rapidly and unidirectionally from the thin layer to the copper wheel, and the resulting

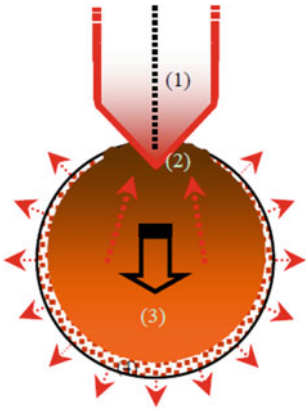

Fig. 11.33 Proposed schematic model illustrating the formation of nanocrystalline phase in the melt extraction process. The numbers in the graphs have the following denotations: (*1*) indicates the copper wheel; (*2*) indicates the connection area between the copper wheel and melt drop; (*3*) and (*4*) label the amorphous and nanocrystalline phase, respectively. The *red up arrows* and *circular array of arrows* indicate the heat conduction and radiation, respectively. The *black down arrow* refers to the uniaxial solidification. Reprinted with permission from [79], copyright 2013 AIP

inhomogeneities from the non-uniform chemistry and stress distribution can thus act as nucleation sites for nanocrystallites in the subsequent solidification process. In the second stage, the heat energy dissipation changes from heat exchange to much-slower thermal radiation, which facilitates the precipitation of nanocrystallites on the top layer of the free surface. A similar phase separation in melt-extracted FeCuSiB microwires has been reported by Nagase and Umakoshi [83]. We would like to stress that the thin glass-coated wires fabricated by the Taylor–Ulitovskiy method do not show a two-peak structure of the absorption losses. This is due to the absence of such crystalline phase because glass-coated wires are generally too thin to give the slow cooling rate which is of paramount importance for nanocrystallite formation. Note that this could explain why the thin wires fabricated by the Taylor–Ulitovskiy method have much better magnetic softness and associated GMI properties than melt extraction microwires [84].

The existence of nanocrystallites is also evidenced in the microwave characterisation. The first peak is broader than the second one, in that the above-mentioned strong non-uniform distribution of magnetoelastic anisotropy contributes multiple resonance frequencies which merge into a broad one. In this sense, the minor fraction of nanocrystalline phase shows a much narrower resonance. In addition, the Co nanocrystalline phase is much magnetically harder than the amorphous phase, which results in the negligible field effect (<150 Oe) in the low magnetic field, and even the high magnetic field (>150 Oe) is only adequate to improve the resistance but not sufficient to tune the resonance frequency. With increasing wire concentration, the magnetic shielding effect predominates over the

increasing polarisation with more wires [85], which results in the reduction of the first peak and the diminished field effect accordingly. While the nanocrystalline phase does not respond very well to the external field, the increasing concentration predominates over the shielding effect and results in an increase of permittivity.

In the following, we are going to check whether our experimental data are consistent with a two-phase CS modelling. First, we consider that the intrinsic permittivity of the microwires can be written as $\varepsilon_i = \beta\varepsilon_m^{\text{amor}} + (1-\beta)\varepsilon_m^{\text{nano}}$, where β is a relative weight of the amorphous phase with respect to the nanocrystalline phase. Here, $\varepsilon_m^{\text{nano}}$ and $\varepsilon_m^{\text{amor}}$, respectively, represent the shell and core contributions to the intrinsic permittivity of the microwires. The Drude–Lorentz model is applied here to model the effective permittivity; that is, $\varepsilon'' m$ can be written in the form $\varepsilon'' m = A_k(f/f_k)[\left(1-\left(f/f_{0,k}\right)^2\right)^2 + \left(f/f_{r,k}\right)^2]$, where the A_ks are resonance peak amplitudes, f denotes the frequency of the wave, $f_{r,k}$ is the resonance frequency of the kth peak, and $f_{0,k}$ is related to the width of the kth resonance line. A simple model of the effective permittivity of our samples in the long-wavelength limit is to use an arithmetic mean of the intrinsic permittivity of the phases weighted by their respective volume fractions. Inspection of Fig. 11.34 shows a good agreement between the fit and data. Residual discrepancy observed may be due to imperfect bonding between the rubber and the microwires and uncertainty in our ε_i value.

Finally, we examine the influence of frequency in the three zones of Fig. 11.32 within the context of the CS structure of the microwires. In Fig. 11.35, we plot the Cole-Cole representation of the permittivity data for the sample containing 6 wires. The observed behaviour is complicated and could be described by three zones. On the one hand, it is apparent from Fig. 11.34 that several relaxation mechanisms contribute to the permittivity spectra shown in Figs. 11.30 and 11.31. On the other hand, ferromagnetic/rubber composites enable the optimisation of the field-induced tunability of the effective permittivity, as we can simultaneously vary ε'' and ε' in a controlled manner. One intuitive explanation for the three zones would be to consider that they are associated with, respectively, the amorphous and crystalline phases, and the amorphous to crystalline phase interface. We find that the change in the effective permittivity due to the magnetic perturbation is a sensitive indicator of dielectric relaxation and resonance mechanisms. As to the purely amorphous region, GMI is predominant at low magnetic bias, while FMR is important at high bias, as discussed in the preceding section. Another relaxation process can be related to the amorphous to crystalline phase interface. While at low magnetic field excitation the amorphous phase contributes significantly to the dielectric response, an increasing magnetic bias tends to increase the importance of the crystalline phase of this microwave response. The relaxation associated with the crystalline phase requires the involvement of a high magnetic field.

In summary, in this section, we have evaluated the features associated with the two-peak behaviour of the permittivity spectra for ferromagnetic microwire/rubber composites in the 0.3–6 GHz range of frequencies. We have investigated how these spectra vary with magnetic field and the number of microwires inside the sample. We argue that this spectral feature may be attributed to the amorphous

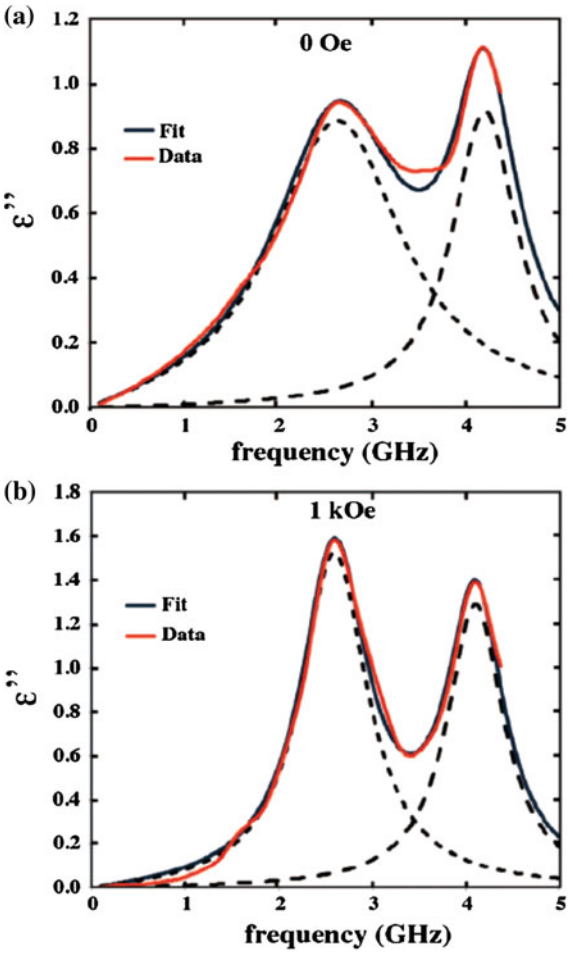

Fig. 11.34 Simulated ε'' spectra for the structure containing 6 wires and two values of the magnetic field amplitudes (0 and 1 kOe). The *solid line* is a fit to the data for an amorphous core-crystalline shell model with 0.15 vol%. Reprinted with permission from [79], copyright 2013 AIP

core-crystalline nanoshell structure of the microwires. Electromagnetic simulations show that the Drude–Lorentz model of dispersion can describe satisfactorily the effective permittivity in the range of frequencies explored. Based on the analyses of HRTEM images and the microwave spectra, the microwave characterisation using frequency-domain spectroscopy can be exploited for express detection of the minor fraction of nanocrystallites formed in the surface of materials.

Before closing the whole section dealing with the high field effect, we would like to comment that although a strong field may not be desirable in practice, since most applications desire to be free from cumbersome magnets, they are useful to reveal some special functionalities and associated physics that would otherwise be obscured in natural conditions. From a practical point of view, they can be exploited as facile but effective research tools to study the materials structure. Above all, the physics underlying the high field effect may also extend the possibilities of

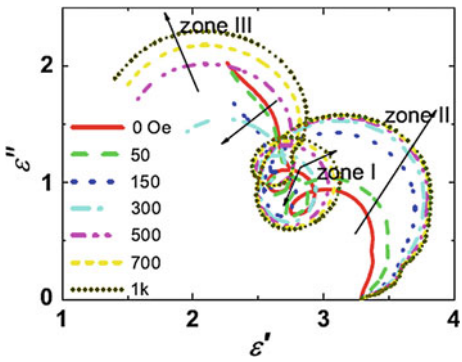

Fig. 11.35 The Cole–Cole representation of the data in Fig. 11.30 for the sample containing 6 wires. Three zones are identified as the magnetic field magnitude is varied from 0 to 1 kOe. The evolution of each zone as the magnetic field is increased is indicated by the *arrows*. Reprinted with permission from [79], copyright 2013 AIP

optimising the microwire composite structure and broaden its functionalities and applications.

11.5 Stress Tunable Properties

Due to the stress effect on the impedance of amorphous wires, the stress will have a significant impact on the prorogation of microwaves when they pass through the microwire(s). This is characterised by the variation of electromagnetic parameters (reflection, transmission, permittivity, and permeability) with stress. This is the basic working principle for microwave NDT methods [86–92]. Compared to other NDT methods, employing ultrasound [93, 94], infrared thermography [94–96], radiography [97, 98], radioactive computed tomography, and ground-penetrating radar (GPR) [99, 100], microwave proves to be advantageous due to the fact that microwaves can penetrate deep inside the composite, scatter little compared to acoustic waves, offer excellent contrast between matrix and reinforcing fibres, have good resolution, are not hazardous, are cost-effective compared to radioactive methods, and are robust to environmental conditions unlike infrared methods [86–92]. Both near-field [101, 102] and far-field free-space [86] characterisations of composite structure have proved to be useful in detecting the debonds and delaminations of composite structure, demonstrating the usefulness of microwave NDT technology in structural health monitoring applications. However, without embedding sensors, it is hard to detect the local damage. Most recently, the potential of using carbon fibres themselves as antennae and sensors to precisely detect the damage in CFRP has also been demonstrated [103]. However, the interactions of CFRP and microwaves are limited by the high conduction loss of CF due to the high volume fraction. The use of microwires as sensor elements is

advantageous for their strong interactions with microwaves and high sensitivity to external fields. In what follows, we will discuss the stress effect on the wire impedance and the stress tunable effects of microwire composites at gigahertz frequencies.

11.5.1 Stress Sensing Based on Microwires

The stress influence of GMI or stress-impedance effect has been mostly discussed in the megahertz frequencies due to the application interest [104–110]. Interested readers are kindly referred to [44, 66, 67] and the references therein. The focus here is on the stress effect of GMI behaviour in the gigahertz frequency.

At gigahertz frequencies, the skin effect is very strong with a small skin depth (e.g. around 1.2 μm at 1–10 GHz) [11]. The permeability is contributed by the outer layer of the microwire. For Co-based microwire with the circumferential domain structure in the outer layer, the permeability is determined by the natural ferromagnetic resonance [47]. According to the Landau–Lifshitz–Gilbert (LLG) equation, the permeability is strongly dependent on the anisotropy field of the wires. Considering the significant stress impact on the anisotropy field of wires [12, 62, 111–113] and anisotropy angle [10, 15, 49], the permeability (or impedance) spectra can be regulated by the variation of internal stress due to that of geometry [113–116] or glass removal [117], and external stress [21] as shown in Fig. 11.36a. The resonance frequency can be regulated by the parameter of the microwires and the number of wires. Therefore, this effect could be utilised, beyond stress sensing, for detecting and locating damage in the microwire-based composites [103], which is of much interest in engineering applications. In Fig. 11.36b and c, the sensing resolution is obtained from the shift of resonance with stress/strain with values of 1.06 MHz/MPa and 134.5 kHz/microstrain, respectively. These results lead to an important revelation that the microwires can be used as stress sensors in a wide frequency range, provided the permeability can be obtained. Compared with the newly proposed SRR-based sensor with a sensitivity of 5.148 kHz/microstrain [118], the microwires are much more cost-effective and possess a higher Q factor and sensitivity. The susceptibility of permeability to stress can be tailored either by tuning the composition, geometry, and microstructure of the microwires [113], or through developing composites containing magnetic fillers [119] and non-magnetic fillers [120].

It is worth mentioning that the stress sensitivity of impedance for single wires can be modulated by the dc bias field. When the external magnetic field is equal to the value of the anisotropy field, the stress sensitivity reaches a maximum. This is demonstrated in Fig. 11.37 [121], where the maximum sensitivity is shown at 15 Oe. The reason for this is well explained by the dependence of permeability on the anisotropy angle, formulated as [49]:

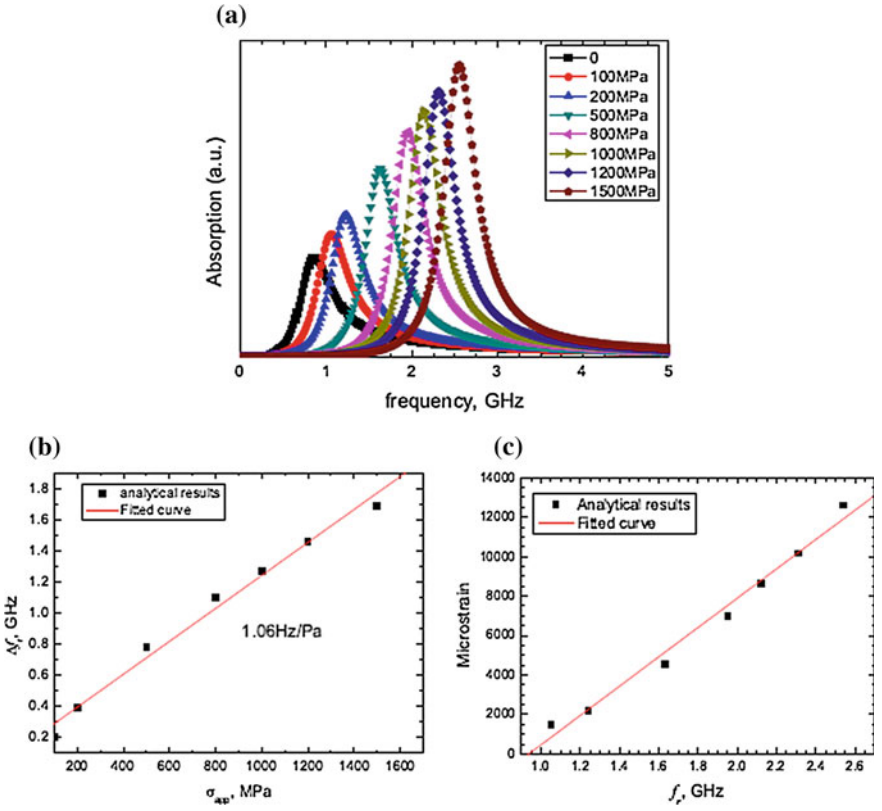

Fig. 11.36 **a** Calculated absorption spectra under varying σ_{app} according to LLG formula $\mu = 1 + \frac{\mu_0\gamma M_s[\mu_0\gamma(H_{dc}+H_k)-j\omega\alpha]}{-\omega^2+\omega_{\text{FMR}}^2-j\omega\alpha\mu_0\gamma[2(H_{dc}+H_k)+M_s]}$, and $H_k = \frac{3|\lambda_s|}{M_s}(\sigma_{zz} - \sigma_{\phi\phi} + \sigma_{\text{app}})$ with the material parameters obtained from magnetisation test: $M_s = 10^6 \sim \text{A/m}$, $\gamma = 2.21 \times 10^5\ \text{mA}^{-1}\text{s}^{-1}$, $\alpha = 0.02$, $H_s = 880 \sim \text{A/m}$ and $\mu_0 = 1$. **b** Applied stress dependence of resonance frequency shift. The slope of fitted line represents the stress-sensing resolution. **c** Resonance frequency dependence of microstrain. The slope of *fitted line* represents the strain-sensing resolution. Reprinted with permission from [21], copyright 2010 Elsevier

$$\mu = 1 + 4\pi\cos^2(\theta). \tag{11.17}$$

The application of magnetic field along the wire axis increases the circumferential magnetic permeability by rotating the magnetisation vector towards the wire axis. On the other hand, when a stress is applied along the microwires with a negative magnetostriction, the magnetisation vector rotates away from the axis direction. As a result, the circumferential magnetic permeability is decreased [10]. It is expected, therefore, that the application of longitudinal stress will compensate the effect of the magnetic field. The influence of stress is more obvious with a high magnetic field. Indeed, with reference to Fig. 11.37, the maximum applied stress of

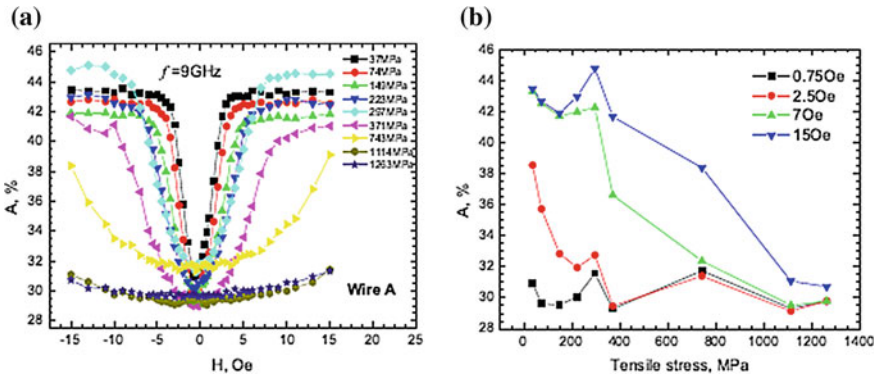

Fig. 11.37 **a** Axial field dependence of absorption in the presence of varying stress at 9 GHz for a $Co_{67}Fe_{3.9}Ni_{1.4}B_{11.5}Si_{14.5}Mo_{1.7}$ wire of total diameter 30.6 μm and glass coat 5.2 μm. **b** Tensile stress dependence of absorption (impedance) at varying magnetic fields for the same wire. Reprinted with permission from [121], copyright 2011 Elsevier

1263 MPa encourages the absorption back to the original value by offsetting the effects of the magnetic field. The magnetic field along the wire axis is desirable for the absorption of microwires and can also be utilised to increase the stress sensitivity of absorption. Similar results were also reported in [10, 15]. Upon analysing the data in Fig. 11.37, it can be obtained that the sensitivity of absorption to stress increases by ca. 39 times when the field increases from 0.75 to 15 Oe. This has profound implication in designing wire-based stress sensors.

11.5.2 Stress Tunable Properties of Composites

11.5.2.1 Stress Tunable Properties of Composites in Free Space

Figure 11.38 [27] shows the complex permittivity spectra for as-prepared intact rubber-based composite prepared by the method described in Sect. 9.2.3 and after being damaged with the occurrence of wire breakage. There are pronounced changes for both the real part ε' and the imaginary part ε'' of effective permittivity. In particular, a drastic change of ε' is seen with a reversal of sign from negative to positive when the wire breakage happened to the composite in question.

For the composites containing $Fe_{4.84}Co_{56.51}B_{14.16}Si_{11.41}Cr_{13.08}$, there is no response at all for the composite subjected to a load range from 0 to 4 kg (not shown here). However, a stress tunable behaviour parallel to the field tunable behaviour is observed in the transmission spectra (Fig. 11.39). Interestingly, the composite shows a similar response to stress and magnetic field, although the evolution of transmission with magnetic field is steadier than that with stress. To gain a deeper insight into such stress tunable characteristics, Fig. 11.40 is plotted to

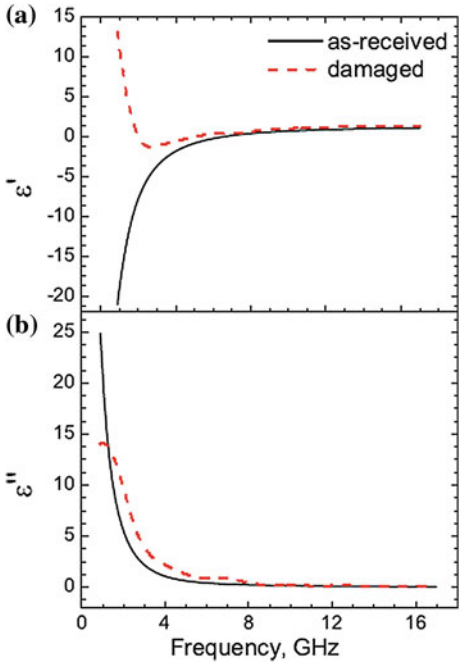

Fig. 11.38 Complex permittivity spectra of as-received composite and after damage by tensile stress. Reprinted with permission from [27], copyright 2011 AIP

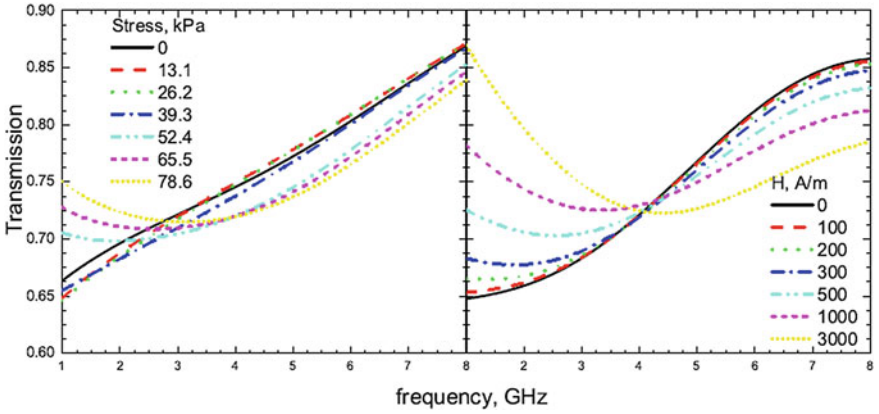

Fig. 11.39 Effect of stress (*left*) and magnetic filed (*right*) on transmission spectra of microwire composite containing $Fe_4Co_{68.7}Ni_1B_{13}Si_{11}Mo_{2.3}$ microwires. Reprinted with permission from [27], copyright 2011 AIP

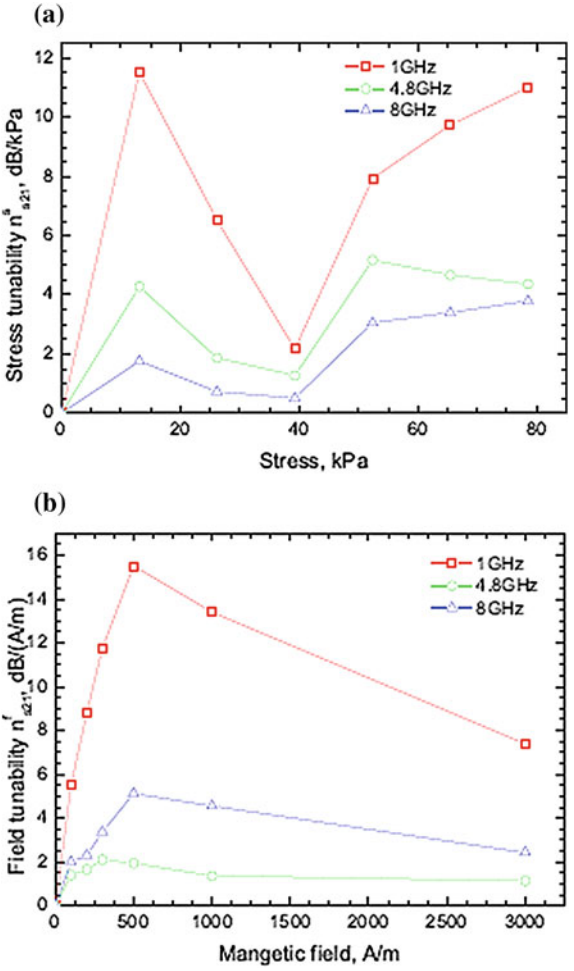

Fig. 11.40 **a** Stress and **b** field dependence of tunability at 1, 4.8, and 8 GHz, plasma frequency f_p = 4.8 GHz, the ordinate profiles are normalised by 10^{-4} and 10^{-5}, respectively. Reprinted with permission from [27], copyright 2011 AIP

show the calculated stress (resp. magnetic field) tunability versus stress (resp. magnetic field) at 1, 4.8, and 8 GHz, which are lower, equal, and higher in relative to the plasma frequency (f_p), respectively. The overall evolution of tunability remains the same trend at all three frequencies. In comparison with the single peak feature displayed in the magnetic field dependence of tenability (Fig. 11.40b), both a maximum and a minimum appeared in the stress dependence of tunability.

The primary principle pertinent to the stress tunable phenomenon is as follows. For composite containing ferromagnetic wires exhibiting a giant magnetoimpedance effect at microwave frequencies, the effective permittivity may depend on a dc magnetic field via the corresponding dependence of the surface impedance. The surface impedance can also be changed by applying a stress which modifies the magnetic anisotropy and domain structure in the wires. Thus, the effective

permittivity may also depend on the external stress or strain. It follows that the stress-impedance (SI) property of microwires is critical to the susceptibility of the whole composite to the stress. SI depends strongly on the magnetoelastic characteristics of the microwire, which are conditioned by a number of factors: composition, domain structure, geometry, etc. This accounts for the observed insensitivity and sensitivity of the microwire composites in terms of their permittivity to the external stress when dealing with different wires. Although all these amorphous wires can be expected to show a drastic change when breakage occurs in the composite, the choicest wires have to be evaluated when it comes to a more delicate stress-sensing application.

The single peak presented in the stress tunability of S_{21} ($n^f_{s_{21}}(H)$) is associated with the anisotropy field. By contrast, a more complex relationship of $n^f_{s_{21}}(\sigma)$ merits more discussion. It is well established that the Co-based microwires with a negative magnetostriction have a bamboo-like domain structure, consisting of an inner core and an outer shell [44]. The surface impedance depends on the circumferential anisotropy at the outer shell. When a stress is applied along the axis of a microwire with negative magnetostriction, a magnetoelastic field is induced in the circumferential direction and this drives the spins rotating towards that direction. As a result, the circumferential magnetic permeability is decreased, and hence, the surface impedance is also reduced. It is expected, therefore, that the application of a longitudinal stress will compensate the effect of the magnetic field. This explains the maximum that occurred at around 13 kPa (Fig. 11.40a). Afterwards, with increasing stress, the well-defined circumferential anisotropy may remain unchanged and hence the surface impedance shows very little variation to the incremental stress, giving rise to a minimum of tenability at 40 kPa. Larger stress than 40 kPa may depreciate the circumferential anisotropy and increase the surface magnetoimpedance, which accounts for the recovery of the increased tunability with stress. It should be noted that tens of kPa imposed on the composite yields hundreds of MPa on each wire, according to a simple calculation as follows. As the present case meets the isostrain condition, the following equation holds:

$$\varepsilon = \frac{\sigma_c}{E_c} = \varepsilon_w = \frac{\sigma_w}{E_w}, \tag{11.18}$$

where ε_c and ε_w denote the strain for composite and microwires, respectively; σ_c and σ_w the stress exerted on the composite and microwires, respectively; E_c and E_w the Young's modulus of the composite and microwires, respectively. Using the law of mixture, the stress each microwire experiences is given by

$$\sigma_w = \frac{\sigma_c}{\left(\frac{E_m}{E_w}\right) f_m + f_w}, \tag{11.19}$$

where f_m and f_w are the volume fraction of the matrix and microwires, respectively. Due to the significant difference between the Young's modulus of rubber matrix

(2 MPa) and of microwires (100 GPa), 10 kPa on the composite can result in 500 MPa on the microwires. This is within the reasonable stress range as commonly discussed in literature, in terms of the stress effect on GMI properties of microwires (see, e.g. [13, 62]).

11.5.2.2 Stress Influence of Electromagnetic Properties Measured by Spectroscopy

For composite containing ferromagnetic wires exhibiting a giant magnetoimpedance effect at microwave frequencies, the effective permittivity may depend on a dc magnetic field via the corresponding dependence of the surface impedance. The surface impedance can be changed by applying a stress which modifies the magnetic anisotropy and domain structure in wires. Thus, the effective permittivity may also depend on the external stress or strain. Following the stress tunable theory proposed by Panina et al. [9], Qin et al. [32, 122] approached the strain effect on the electromagnetic responses from the technological aspects of the multifunctional composites: $Co_{56.51}Fe_{4.84}B_{14.16}Si_{11.41}Cr_{13.08}$ glass-covered magnetic microwires having a total diameter of 29.4 mm and silicone rubber were used for the preparation of composite materials. Continuous microwires with the same length of 70 mm were embedded in a parallel manner into the silicone rubber matrices, which were bonded by silicone resin (see Sect. 9.2.3 for further details). The number (n) of the microwires in composites varied with n = 6, 12, and 17 corresponding to the wire spacing d = 2, 1, and 0.8 mm. For comparison, copper wires with a diameter of 60 mm were also used as fillers. The resultant composites are of uniform dimension of 70 mm × 13 mm × 1.8 mm.

The electromagnetic measurement was carried out with a wave vector of the electromagnetic field perpendicular to the wires using a modified microwave frequency-domain spectroscopy within the frequency range between 300 MHz and 5 GHz. Details of the instruments were discussed in Sect. 11.2.2. All measurements were done at ambient temperature.

Figure 11.41 shows the permittivity spectra for composites containing different amounts of microwires and 12 copper wires. For the unstressed sample, the real component of permittivity ε' increases with the wire amount. For the same amount of wires, composite containing copper wires displays a larger ε' than that with ferromagnetic microwires. The same trend remains when the strain reaches 2.4 % as the tensile stress is applied along the longitudinal direction of the composite. Noticeably, there appears a broad relaxation peak at about 4 GHz for the n = 12 sample when λ = 2.4 % and, with the same strain, a sharper peak occurs at around the same frequency for the n = 17 sample. A similar evolution of permittivity spectra with strain is also shown in the imaginary component (ε''). But such a phenomenon is not observed for the n = 6 sample and the sample with copper wires. It is also interesting to note that ε'' of the sample with copper wires is smaller than those with magnetic microwires.

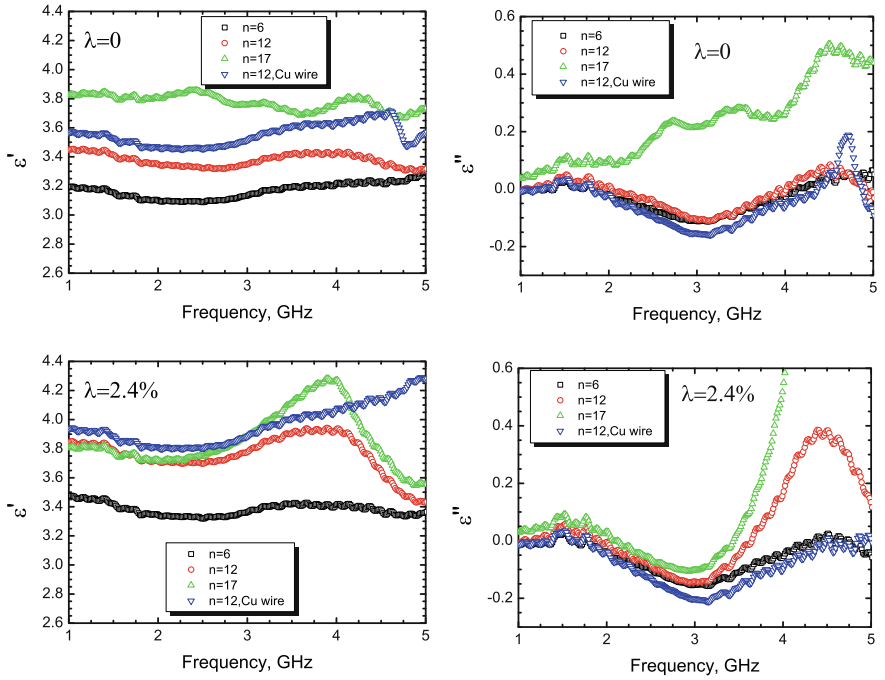

Fig. 11.41 Effective complex permittivity spectra for unstressed composites ($\lambda = 0$) and stressed composites with 2.4 % strain containing varying amounts of microwires. Reprinted with permission from [69], copyright 2013 Elsevier

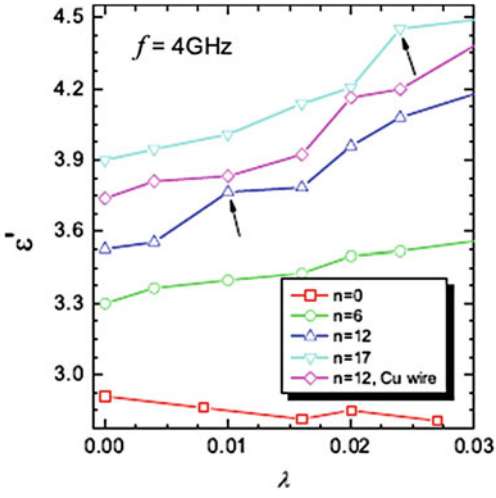

Fig. 11.42 Strain dependence of ε' for composites with n as a variable. Reprinted with permission from [69], copyright 2013 Elsevier

Figure 11.42 summarises the strain dependence of ε'. The sample without wires shows the expected response of ε' to stress. After adding fillers into the composite, its ε' starts to show relatively stronger stress sensitivity, which increases with the

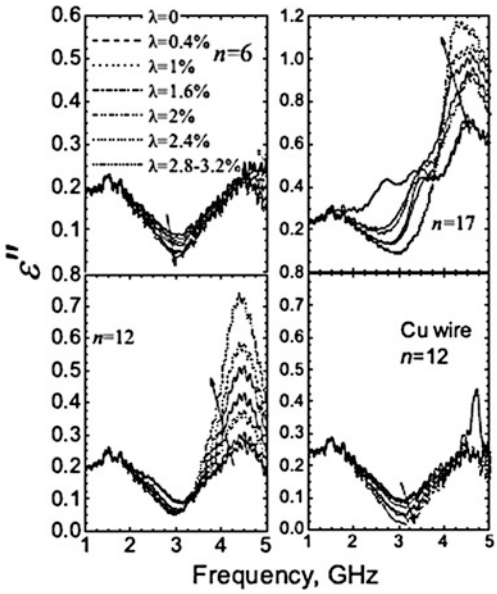

Fig. 11.43 Spectra of ε'' for composites containing ferromagnetic microwires n = 6, 12, 17, and 12 copper wires with strain λ as a parameter. Reprinted with permission from [69], copyright 2013 Elsevier

amount of wire. The sample with copper wires presents a similar stress sensitivity of ε' to that containing the same amount of magnetic microwires. Figure 11.43 summarises the ε'' spectra for all samples, with strain ranging from zero to 2.8–3.2 %. Note that the strain values discussed herein are nominal. Overall, there is a significant influence of the microwire amount on ε''. The strain effects also vary with the wire amount. For the n = 6 sample, ε'' is almost independent of the strain. For the n = 12 sample, there is a remarkable dependence of ε'' on strain, featured as the evolution of a symmetric resonance peak at 4.5 GHz. As n increases to 17, the peak position and the evolution trend with the strain remain unchanged, but the shape becomes asymmetric. In contrast, the sample with the copper wires exhibits a complex evolution of the resonance peak with the strain, such that the resonance peak occurring at the unstressed state increases with a small strain of 2 % but disappears at larger strains. To exclude the influence of geometrical factors of the composites 0 and the microwires, Fig. 11.44 was plotted to show the frequency dependence of tan δ (ratio of ε'' to ε'), and the evolution of peak features with strain remains the same trend as in Fig. 11.43.

The strain dependence of effective permittivity is quantitatively analysed by the Gaussian molecular network model (GMNM) [42]. Figure 11.45 shows the λ dependence of Δ with varying amounts of wires, where $\Delta = (\varepsilon'(\lambda) - \varepsilon'(\lambda = 0)/\varepsilon'(\lambda = 0)$. This relationship is well fitted by a functional form $k(1 + \lambda - 1/(1 + \lambda)^2)$, where k is a constant, the value of which varies with the wire amount as shown in Fig. 11.45.

The effective permittivity (ε) is dependent on the wire concentration (p_v) and the averaged polarisability ($\langle a \rangle$): $\varepsilon = \varepsilon_m + 4\pi p_v \langle a \rangle$, where ε_m denotes the permittivity of

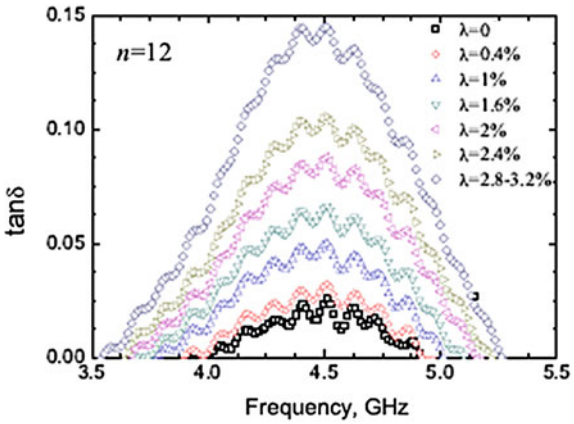

Fig. 11.44 Frequency dependence of loss tangent with strain as a parameter. Reprinted with permission from [32], copyright 2010 AIP

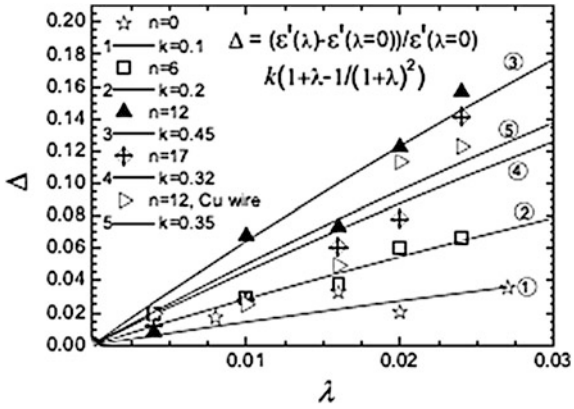

Fig. 11.45 Variations of Δ with strain for composites with differing amount of wires as shown in the *open symbols* at 4 GHz. The best *fitted lines* to the function of $k(1 + \lambda - 1/(1 + \lambda)^2)$ and values of k corresponding to different n are also shown. Reprinted with permission from [32], copyright 2010 AIP

matrix [9]. Thus, increasing the wire amount improves the effective polarisation and hence the permittivity. The polarisability is primarily dependent on electric excitation. For the present composite configuration with microwires perpendicular to the electric field vector, although the sample is aligned with the tensile axis of the deformation apparatus, an axial component of electrical field still exists due to the inevitable misalignment of the wires within the sample and/or the possible inhomogeneity of the electrical field in the cell, which may affect the electric excitation of the wires. This accounts for the observed dielectric response of the composite

samples due to the polarisation and the induced circumferential magnetisation of the wires. For the magnetic microwires, the strain modifies the magnetisation process and hence the circumferential permeability, resulting in the changes of ε'. However, since the experimental data were obtained using the same protocol and measurement cell, the changes of permittivity can be solely attributed to strain.

It is also shown that more microwires induce a sharper peak at ca. 4 GHz, indicating an increased stress sensitivity. However, this argument does not hold true for the composites with $n = 6$ and copper wires which can be understood as follows: for $n = 6$, the wires concentration is not high enough to satisfy the response of a noticeable peak to the external stress; for copper wires, they have no response to the induced circumferential magnetic field, and therefore, the composite does not show any stress-induced peaks. Overall, the effective permittivity of wire composites increases with the strain, which is further discussed later based on the GMNM approach. It is worth pointing out that, owing to the higher concentration of copper wires as a result of larger diameter than that of ferromagnetic microwires, the composite sample with copper wires shows a larger permittivity than that with the same amount of ferromagnetic microwires.

From the application point of view, it is important to find ways to improve the stress sensitivity. Obviously, this can be approached by increasing the amount of microwires in the composite. However, it should be noted that this does not necessarily mean that more is better. In this work, the sensitivity of permittivity to stress showed little change between the $n = 12$ and $n = 17$ samples. Somewhat surprisingly, it is found that the samples containing magnetic microwires and containing non-magnetic microwires appear to yield a similar stress sensitivity of ε''. This observation suggests an independence of the stress sensitivity in wire composites to the conductivity and magnetic permeability of the wires for a sufficiently high concentration of wires, although the reason for this result is not obvious.

The most striking feature shown in Fig. 11.43 is the evolution of the peak with the stress for the n = 12 and $n = 17$ samples. It is proposed that the gradual spectral change from relaxation to resonance at 4.5 GHz can also be attributed to the influence of stress on wire magnetisation, as discussed above, which modifies the eddy current loss and contributes to the steady evolution of the ε'' resonance due to the circumferential ferromagnetic resonance.

The loss tangent (tan δ) retains the same changing trend with the strain as ε'' (λ), indicating that such a strain effect is independent of any geometrical factors [123]. It should be noted that such a transformation of relaxation to resonance is absent for the $n = 6$ sample and composite with copper wires in the spectra of complex permittivity. This suggests the exclusivity of ferromagnetic microwires and the requirement of the wire concentration to realise a steady evolution of the peak feature defined by the stress [24].

Now we discuss the strain–permittivity relationship. Basically, the GMNM approach is related to the elasticity network of the composite material. Excellent agreement between the experimental results and the GMNM model is observed for

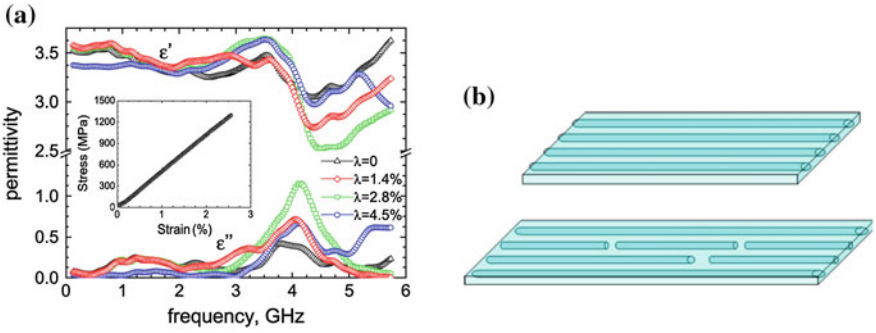

Fig. 11.46 Spectra of complex permittivity for microwire composites with strain λ

all samples (Fig. 11.45), which suggests the applicability of the model at the measured strain range. By introducing more microwires ($n \leq 12$) into the rubber matrix, a higher stress sensitivity (characterised by the k value in this case) and a closer experimental–model match is obtained. But when n increases to 17, k is decreased and a relatively larger mismatch is observed. This can be attributed to the enhanced complexity of the composite mesostructure, arising from the larger amount of embedded microwires [42]. Nevertheless, due to the periodical topology of the microwires within the composite, GMNM gives fairly good predictions for all samples.

The significance of wire patterns is manifested in Fig. 11.46a, in which a non-linear dependence of ε'' on the strain is shown. In this case, the wire starts to snap when the strain exceeds 2.8 %. Due to the uneven interfacial properties, each single wire may experience a different stress, which results in partial but not total fracture of all wires. We then receive a similar resonance response for two patterns (Fig. 11.46b). This indicates that the increase of dielectric loss with the stress is compensated with the opposite effect resulting from the reduction of strained wires. There are two possible mechanisms involved in this phenomenon. First is the stress effect: the stress changes the current distribution in the wires and induces higher dielectric loss, and release of stress results in the opposite effect. Second is the shape effect: the wires are fractured to relatively shorter pieces and the anisotropy field of the wire becomes non-uniform and results in the reduction and broadening of the resonance linewidth. This leads us to a striking revelation in a larger context, that the functional fillers enabled heterogeneous composites, the macroscopic behaviour is dependent on the collective response of the fillers on the one hand, and each single filler on the other hand. This then poses the challenge of how to manipulate some, if not each, of the fillers. In so doing, we will have greater control of the properties of the composite presented to meet specific applications.

11.6 Temperature Tunable Properties

By analogy with stress, the temperature tunable properties are derived from the temperature dependence of GMI properties. Because the magnetic permeability is sensitive to temperature, the GMI changes rapidly as a function of temperature, especially in the vicinity of the Curie temperature T_c. In general, for Co-based microwires, the GMI effect first increases with increase of the measuring temperature due to the internal stress relief, reaches a maximum value near the Curie temperature of the material, and then finally decreases at higher temperatures [124, 125]. The dramatic change of GMI at temperatures above the Curie point was attributed to the collapse of the magnetic coupling in the material [126], which has been exploited for the development of temperature sensors [127]. In terms of composites, the magnetic phase transition at T_c will lead to a large transformation of the dispersion of effective permittivity, as well as the reflection and transmission coefficients [18]. Figure 11.47 shows the theoretical permittivity spectra and transmission/reflection spectra for $T < T_c$ and $T > T_c$. By analogy with the influence

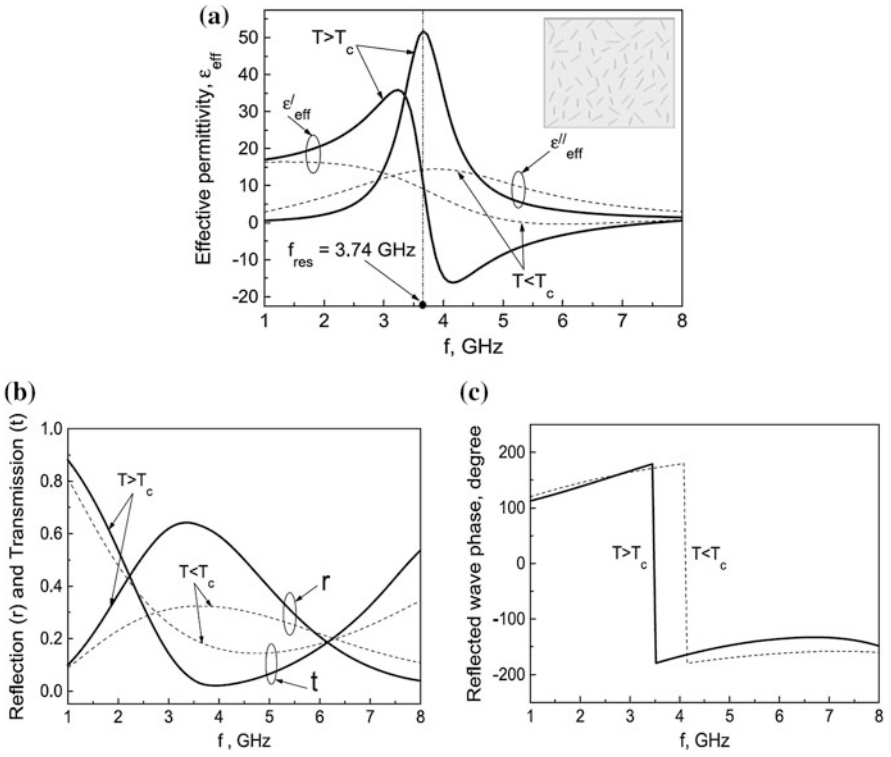

Fig. 11.47 **a** Calculated dispersion spectra of resonance complex effective permittivity in the vicinity of antenna resonance under the influence of temperature: the *inset* shows the schematic configuration of the composite. **b** Typical transmission and reflection spectra under the influence of temperature. **c** Typical reflection phase spectra under the influence of temperature. [18]

of the stress or magnetic field, there is an anomalous dispersion of $\varepsilon'(f)$ and relaxation/resonance transformation when T exceeds T_c. All these features demonstrate strong temperature effects, which can be exploited for temperature sensing. A very promising application is to embed these microwires into the pre-form of polymer laminates. The microwires can then serve as self-regulating heating elements in the microwave curing process, which is believed to be much more efficient than conventional curing methods [128]. Meanwhile, with proper choice of composition and tailoring, the wires can be made highly sensitive [129] to the temperature to be applied for process monitoring, which remains a challenging issue in composite manufacture [130]. In addition, the wires remain as stress-sensing elements in the cured composites for various kinds of structural application. With increasing use of advanced fibre-reinforced composites in industry [131], the addition of microwires may well renovate the composite industry to some extent.

Through most of this text, we have emphasised the basic physical principles underlying the tunable behaviour of the microwire composites. By examining individual cases of a generic or specific nature, we hoped to suggest the practical importance and versatility of the microwire composites for tunable devices at the microwave frequency range of considerable technical interest. We believe these examples are only the tip of an iceberg of possibilities that are yet to be discovered. In this sense, the chapter may also serve to stimulate the imaginations of researchers in diverse fields who will, in the end, turn the application potential afforded by this kind of microwave tunable composites into realities.

References

1. Born M, Wolf E (1968) Principles of optics, 4th edn. Pergamon, New York
2. Makhnovskiy DP, Panina LV (2003) Field dependent permittivity of composite materials containing ferromagnetic wires. J Appl Phys 93:4120–4129
3. Lagarkov AN, Matytsin SM, Rozanov KN, Sarychev AK (1998) Dielectric properties of fiber-filled composites. J Appl Phys 84:3806–3814
4. Liu L, Matitsine SM, Gan YB, Rozanov KN (2005) Effective permittivity of planar composites with randomly or periodically distributed conducting fibers. J Appl Phys 98:063512–063517
5. Lagarkov AN, Sarychev AK (1996) Electromagnetic properties of composites containing elongated conducting inclusions. Phys Rev B 53:6318–6336
6. Pendry JB, Holden AJ, Stewart WJ, Youngs I (1996) Extremely low frequency plasmons in metallic mesostructures. Phys Rev Lett 76:4773–4776
7. Sarychev AK, Shalaev VM (2000) Electromagnetic field fluctuations and optical nonlinearities in metal-dielectric composites. Phys Rep 335:275–371
8. Makhnovskiy DP, Panina LV, Mapps DJ (2001) Field-dependent surface impedance tensor in amorphous wires with two types of magnetic anisotropy: helical and circumferential. Phys Rev B 63:144424
9. Makhnovskiy DP, Panina LV (2005) Field and stress tunable microwave composite materials based on ferromagnetic wires. In: MurrayNova VN (ed) Progress in ferromagnetism research. Science Publishers Inc, Hauppauge

10. Panina LV, Sandacci SI, Makhnovskiy DP (2005) Stress effect on magnetoimpedance in amorphous wires at gigahertz frequencies and application to stress-tunable microwave composite materials. J Appl Phys 97:013701–013706
11. Makhnovskiy DP, Panina LV, Garcia C, Zhukov AP, Gonzalez J (2006) Experimental demonstration of tunable scattering spectra at microwave frequencies in composite media containing Cofepris glass-coated amorphous ferromagnetic wires and comparison with theory. Phys Rev B 74:064205
12. Torcunov AV, Baranov SA, Larin VS (1999) The internal stresses dependence of the magnetic properties of cast amorphous microwires covered with glass insulation. J Magn Magn Mater 196–197:835–836
13. Adenot AL, Deprot S, Bertin F, Bois D, Acher O (2004) Magneto-elastic anisotropy of ferromagnetic glass-coated microwires. J Magn Magn Mater 272–276:E1115–E1116
14. Panina L, Mohri K, Uchiyama T, Noda N, Bushida K (1995) Giant magneto-impedance in Co-rich amorphous wires and films. IEEE Trans Magn 31:1249–1260
15. Sandacci S, Makhnovskiy D, Panina L, Larin V (2005) Stress-dependent magnetoimpedance in Co-based amorphous wires with induced axial anisotropy for tunable microwave composites. IEEE Trans Magn 41:3553–3555
16. Sarychev A, Shalaev V (2007) Electrodynamics of metamaterials. World Scientific Publishing Co. Pte. Ltd., Singapore
17. Shalaev VM, Cai W, Chettiar UK, Yuan HK, Sarychev AK, Drachev VP, Kildishev AV (2005) Negativeindex of refraction in optical metamaterials. Opt Lett 30:3356–3358
18. Makhnovskiy D, Panina L (2007) Free-space microwave testing of stress and temperature distributions in composite materials incorporating ferromagnetic wires. In: The XII electromagnetic nondestructive evaluation conference (ENDE-2007), Cardiff, UK
19. Makhnovskiy D, Panina L (2005) Tuneable microwave composites based on ferromagnetic wires. http://www.microwirescom/Surveyphp November 2005
20. Qin F, Peng H (2010) Macro-composites containing ferromagnetic microwires for structural health monitoring. Nano Commun Netw 1:126–130
21. Qin F, Peng HX, Tang J, Qin LC (2010) Ferromagnetic microwires enabled polymer composites forsensing applications. Compos A Appl Sci Manuf 41:1823–1828
22. Qin FX, Pankratov N, Peng HX, Phan MH, Panina LV, Ipatov M, Zhukova V, Zhukov A, Gonzalez J (2010) Novel magnetic microwires-embedded composites for structural health monitoring applications. J Appl Phys 107:09A314–09A314-3
23. Qin FX, Brosseau C, Peng HX, Wang H, Sun J (2012) In situ microwave characterization of microwire composites with external magnetic field. Appl Phys Lett 100:192903
24. Starostenko S, Rozanov K, Osipov A (2006) Microwave properties of composites with glass coated amorphous magnetic microwires. J Magn Magn Mater 298:56–64
25. Starostenko SN, Rozanov KN (2009) Microwave screen with magnetically controlled attenuation. Prog In Electromagnet Res 99:405–426
26. Starostenko SN, Rozanov KN, Osipov AV (2004) Microwave spectra of composites with an ordered amorphous microwire. J Commun Technol Electron 49:1399–1404
27. Qin FX, Peng HX, Popov VV, Panina LV, Ipatov M, Zhukova V, Zhukov A, Gonzalez J (2011) Stress tunable properties of ferromagnetic microwires and their multifunctional composites. J Appl Phys 108:07A310
28. Shin KH, Inoue M, Arai KI (1999) Strain sensitivity of highly magnetostrictive amorphous films for use in microstrain sensors. J Appl Phys 85:5465–5467
29. Tagantsev AK, Sherman VO, Astafiev KF, Venkatesh J, Setter N (2003) Ferroelectric materials for microwave tunable applications. J Electroceram 11:5–66
30. Giere A, Zheng Y, Maune H, Sazegar M, Paul F, Zhou X, Binder JR, Muller S, Jakoby R (2008) Tunable dielectrics for microwave applications. In: 2008 17th IEEE international symposium on the applications of ferroelectrics, vol 2, pp 1–2
31. Laur V, Rousseau A (2006) At microwave frequencies for tunable applications. Circ Des 53:2280–2286

32. Qin F, Peng HX, Prunier C, Brosseau C (2010) Mechanical–electromagnetic coupling of microwire polymer composites at microwave frequencies. Appl Phys Lett 97:153502–153503
33. Ghodgaonkar D, Varadan V, Varadan V (1989) A free-space method for measurement of dielectric constants and loss tangents at microwave frequencies. IEEE Trans Instrum Meas 38:789–793
34. Bryant G (1993) Principles of microwave measurements. IEE Electrical Measurement Series 5. ISBN 0-86341-296-3
35. Varadan VV, Jose KA, Varadan VK (2000) In sutimicrowave characterization of nonplanar dielectric objects. IEEE T Microw Theor 48:388–394
36. Hollinger RD, Jose KA, Tellakula A, Varadan VV, Varadan VK (2000) Microwave characterization of dielectric materials from 8 to 110 GHz using a free-space setup. Microwave Opt Technol Lett 26:100–105
37. Trabelsi S, Nelson S (2003) Free-space measurement of dielectric properties of cereal grain and oilseed at microwave frequencies. Meas Sci Technol 14:589–600
38. ELIRI Institute, Chisinau, Republic of Moldova. http://eliri.md/eng/about.htm
39. Search "application note 1304-07" at http://www.home.agilent.com
40. Agilent85071E Materials Measurement Software at www.agilent.com/find/mate-rials
41. Makhnovskiy D, Zhukov A, Zhukova V, Gonzalez J (2008) Tunable and self-sensing microwave composite materials incorporating ferromagnetic microwires. Adv Sci Tech 54:201–210
42. Christian B, Philippe T (2005) Instrumentation for microwave frequency-domain spectroscopy of filled polymers under uniaxial tension. Meas Sci Technol 16:1823
43. Salahun E, Queffelec P, Le Floch M, Gelin P (2001) A broadband permeameter for "in situ" measurements of rectangular samples. IEEE Trans Magn 37:2743–2745
44. Phan MH, Peng HX (2008) Giant magnetoimpedance materials: fundamentals and applications. Prog Mater Sci 53:323–420
45. Yelon A, Melo LGC, Ciureanu P, Ménard D (2002) High-frequency behavior of magnetically soft wires. J Magn Magn Mater 249:257–263
46. Yelon A, Menard D, Britel M, Ciureanu P (1996) Calculations of giant magnetoimpedance and of ferromagnetic resonance response are rigorously equivalent. Appl Phys Lett 69:3084–3085
47. Acher O, Jacquart PM, Boscher C (1994) Investigation of high frequency permeability of thin amorphous wires. IEEE Trans Magn 30:4542–4544
48. Britel MR, Menard D, Melo LG, Ciureanu P, Yelon A, Cochrane RW, Rouabhi M, Cornut B (2000) Magnetoimpedance measurements of ferromagnetic resonance and antiresonance. Appl Phys Lett 77:2737–2739
49. Sandacci S, Makhnovskiy D, Panina L (2004) Valve-like behavior of the magnetoimpedance in the GHz range. J Magn Magn Mater 272–276:1855–1857
50. Vazquez M, Adenot-Engelvin AL (2009) Glass-coated amorphous ferromagnetic microwires at microwave frequencies. J Magn Magn Mater 321:2066–2073
51. de Cos D, Lepalovskij V, Kurlyandskaya G, García-Arribas A, Barandiarán J (2008) High-frequencymagnetoimpedance in multilayer thin films with longitudinal and transverse anisotropy. J Magn Magn Mater 320:e954–e957
52. Labrador A, Gómez-Polo C, Pérez-Landazábal JI, Zablotskii V, Ederra I, Gonzalo R, Badini-Confalonieri G, Vázquez M (2010) Magnetotunable left-handed FeSiB ferromagnetic microwires. Opt Lett 35:2161–2163
53. Vázquez M (2001) Giant magneto-impedance in soft magnetic "Wires". J Magn Magn Mater 226–230:693–699
54. Garcia-Miquel H, Carbonell J, Boria V, Sánchez-Dehesa J (2009) Experimental evidence of lefthanded transmission through arrays of ferromagnetic microwires. Appl Phys Lett 94:054103
55. Garcia-Miquel H, Carbonell J, Sanchez-Dehesa J (2010) Left handed material based on amorphous ferromagnetic microwires tunable by dc current. Appl Phys Lett 97:094102

56. Brosseau C (2003) Computational electromagnetics and the rational design of new dielectric heterostructures. Prog Mater Sci 48:373–456
57. Tinga W (1992) Mixture laws and microwave-material interactions. Elsevier, Amsterdam, pp 1–36
58. Brosseau C (2008) Prospects in filled polymers engineering: mesostructure, elasticity network, and macroscopic properties. Research Signpost, Trivandrum
59. Qin FX, Peng HX, Phan MH, Panina LV, Ipatov M, Zhukov A (2012) Effects of wire properties on the field-tunable behaviour of continuous-microwire composites. Sens Actuators, A 178:118–125
60. Panina LV, Ipatov M, Zhukova V, Zhukov A, Gonzalez J (2011) Magnetic field effects in artificial dielectrics with arrays of magnetic wires at microwaves. J Appl Phys 109:053901
61. Zhukova V, Ipatov M, Zhukov A, Gonzalez J, Blanco J (2007) GMI effect in ultra-thin glass-coated Co-rich amorphous wires. Sens Actuators, B 126:232–234
62. Zhukov A, Zhukova V, Blanco JM, Cobeno AF, Vazquez M, Gonzalez J (2003) Magnetostriction in glass-coated magnetic microwires. J Magn Magn Mater 258–259: 151–157
63. Larin VS, Torcunov AV, Zhukov A, Gonzalez J, Vazquez M, Panina L (2002) Preparation and properties of glass-coated microwires. J Magn Magn Mater 249:39–45
64. Chiriac H (2001) Preparation and characterization of glass covered magnetic wires. Mater Sci Eng, A 304–306:166–171
65. Qin F, Peng H, Phan M (2010) Influence of varying metal-to-glass ratio on GMI effect in amorphous glass-coated microwires. Solid State Commun 150:114–117
66. Zhukova V, Ipatov M, Zhukov A (2009) Thin magnetically soft wires for magnetic microsensors. Sensors 9:9216–9240
67. Zhukov A, Zhukova V (2009) Magnetic properties and applications of ferromagnetic mircowires with amorphous and nanocrystalline structure. Nova Science Publishers, Inc., New York. (Qin, Phan and Peng, submitted to Springer)
68. Vazquez M (2007) Handbook of magnetism and advanced magnetic materials, vol 4. Novel Materials. Wiley. Advanced Magnetic Microwires, 1–29
69. Qin FX, Peng HX (2013) Ferromagnetic microwires enabled multifunctional composite materials. Prog Mater Sci 58:183–259
70. Panina L, Ipatov M, Zhukova V, Zhukov A, Gonzalez J (2010) Microwave metamaterials with ferromagnetic microwires. Appl Phys A Mater Sci Process 103:653–657
71. Ipatov M, Zhukova V, Panina LV, Zhukov A (2009) Ferromagnetic microwires composite metamaterials with tuneable microwave electromagnetic parameters. PIERS Proc 5:586–590
72. Peng H, Qin F, Phan MH, Tang J, Panina L, Ipatov M, Zhukov A, Zhukova V, Gonzalez J (2009) Co-based magnetic microwire and field-tunable multifunctional macro-composites. J Non-Cryst Solids 355:1380–1386
73. Acher O, Ledieu M, Adenot AL, Reynet O (2003) Microwave properties of diluted composites made of magnetic wires with giant magneto-impedance effect. IEEE Trans Magn 39:3085–3090
74. Zou TC, Zhao NQ, Shi C (2007) Design of activated carbon fibres/epoxy resin composites. J Funct Mater Dev 13:54–58
75. Qin FX, Peng HX, Fuller J, Brosseau C (2012) Magnetic field-dependent effective microwave properties of microwire-epoxy composites. Appl Phys Lett 101:152905
76. Qin FX, Peng HX, Phan MH, Panina LV, Ipatov M, Zhukova V, Zhukov A, Gonzalez J (2011) Smartcomposites with short ferromagnetic microwires for microwave applications. IEEE Trans Magn 47:4481–4484
77. Liu L, Kong L, Lin G, Matitsine S, Deng C (2008) Microwave permeability of ferromagnetic microwires composites/metamaterials and potential applications. IEEE Trans Magn 44: 3119–3122
78. Zhang Z, Wang C, Zhang Y, Xie J (2010) Microwave absorbing properties of composites filled with glass-coated $Fe_{69}Co_{10}Si_8B_{13}$ amorphous microwire. Mater Sci Eng B 175: 233–237

79. Qin FX, Quere Y, Brosseau C, Wang H, Liu JS, Sun JF, Peng HX (2013) Two-peak feature of the permittivity spectra of ferromagnetic microwire/rubber composites. Appl Phys Lett 102:122903
80. Baranov S (2009) Radioabsorption properties of amorphous microwires. Moldavian J Phys Sci 8:332–336
81. Liberal I, Nefedov I, Ederra I, Gonzalo R, Tretyakov S (2011) Electromagnetic response and homogenization of grids of ferromagnetic microwires. J Appl Phys 110:064909
82. Wang H, Xing D, Wang X, Sun J (2011) Fabrication and characterization of melt-extracted co-based amorphous wires. Metall Mater Trans A 42:1103–1108
83. Nagase T, Umakoshi Y (2010) Formation of melt-extracted wire of fëccücsicb alloy with corewire/surface-cover-layer structure by arc-melt-type melt-extraction method. J Alloys Compd 495:L1–L4
84. Wang H, Qin FX, Xing D, Cao F, Wang XD, Peng H, Sun J (2012) Relating residual stress and microstructure to mechanical and GMI properties in cold-drawn co-based amorphous microwires. Acta Mater 60:5425–5436
85. Garcia C, Zhukova V, Zhukov A, Usov N, Ipatov M, Gonzalez J, Blanco J (2007) Effect of interaction on giant magnetoimpedance effect in a system of few thin wires. Sens Lett 5(3):10–12
86. Arunachalam K, Melapudi V, Udpa L, Udpa S (2006) Microwave NDT of cement-based material susing far-field reflection coefficients. NDT & E Int 39:585–593
87. Reynolds W (1985) Nondestructive testing (NDT) of fibre-reinforced composite materials. Mater Des 5:256–270
88. Scott I, Scala C (1982) A review of non-destructive testing of composite materials. NDT Int 15:75–86
89. Prakash R (1980) Non-destructive testing of composites. Composites 11:217–224
90. Henneke E (1990) Ultrasonic nondestructive evaluation of advanced composites. Nondestr Test Fiber-Reinf Plast Compos 2:55–159
91. Adams R, Cawley P (1988) A review of defect types and nondestructive testing techniques for composites and bonded joints. NDT Int 21:208–222
92. Burke S, McKcousland S, Scala C (1994) Nondestructive characterization of advanced composite materials. Mater Forum 18:85–109
93. Prassianakis I, Prassianakis N (2004) Ultrasonic testing of non-metallic materials: concrete and marble. Theoret Appl Fract Mech 42:191–198
94. Garnier C, Pastor ML, Eyma F, Lorrain B (2011) The detection of aeronautical defects in situ on composite structures using non destructive testing. Compos Struct 93:1328–1336
95. Maser K, Roddis W (1980) Principles of thermography and radar for bridge deck assessment. J Transp Eng ASCE 116:583–600
96. Pastor M, Balandraud X, Grédiac M, Robert J (2008) Applying infrared thermography to study the heating of 2024-t3 aluminium specimens under fatigue loading. Inf Phys Technol 51:505–515
97. Liao TW, Li Y (1998) An automated radiographic NDT system for weld inspection: part II–flaw detection. NDT and E Int 31:183–192
98. Graeme W, Jr, Eizember A, Douglass J (1990) Digital image analysis of nondestructive test in gradiographs. Mater Eval 117–120
99. Mast JE, Lee H, Murtha JP (1992) Application of microwave pulse-echo radar imaging to then on destructive evaluation of buildings. Int J Imaging Syst Technol 4:164–169
100. Pieraccini M, Luzi G, Mecatti D, Noferini L, Atzeni C (2003) A microwave radar technique for dynamic testing of large structures. IEEE Trans Microwave Theor Tech 51:1603–1609
101. Hughes D, Kazemi M, Marler K, Zoughi R, Myers J, Nanni A (2002) Microwave detection of delaminations between fiber reinforced polymer (FRP) composite and hardened cement paste. AIP Conf Proc 615:512–519
102. Bois K, Benally A, Zoughi R (2000) Microwave near-field reflection property analysis of concrete for material content determination. IEEE Trans Instrum Measur 49:49–55

103. Matsuzaki R, Melnykowycz M, Todoroki A (2009) Antenna/sensor multifunctional composites for the wireless detection of damage. Compos Sci Tech 69:2507–2513
104. Aragoneses P, Blanco JM, Cobeno AF, Dominguez L, Gonzalez J, Zhukov A, Larin V (1999) Stress dependence of the switching field in co-rich amorphous microwires. J Magn Magn Mater 196–197:248–250
105. Bayri N, Atalay S (2004) Giant stress-impedance effect in $Fe_{71}Cr_7Si_9B_{13}$ amorphous wires. J Alloy Compd 381:245–249
106. Cobeno AF, Zhukov A, Blanco JM, Larin V, Gonzalez J (2001) Magnetoelastic sensor based on GMI of amorphous microwire. Sens Actuators, A 91:95–98
107. Garcia C, Chizhik A, Zhukov A, Zhukova V, Gonzalez J, Blanco J, Panina L (2007) Influence of torsion and tensile stress on magnetoimpedance effect in fe-rich amorphous microwires at high frequencies. J Magn Magn Mater 316:e896–e899
108. Gonzalez J, Chen A, Blanco J, Zhukov A (2002) Effect of applied mechanical stresses on the impedance response in amorphous microwires with vanishing magnetostriction. Phys Status Solidi A 189:599–608
109. Knobel M, Vasquez M, Sanchez ML, Hernando A (1997) Effect of tensile stress on the field response of impedance in low magnetostriction amorphous wires. J Magn Magn Mater 169:89–97
110. Knobel M, Sanchez ML, Vazquez M (1995) Stress dependence of the giant magneto-impedance effect in amorphous wires. J Phys: Condens Matter 7:L115–L120
111. Antonov AS, Borisov VT, Borisov OV, Prokoshin AF, Usov NA (2000) Residual quenching stresses in glass-coated amorphous ferromagnetic microwires. J Phys D Appl Phys 33:1161
112. Aranda GR, Usov NA, Zhukova V, Zhukov A, Gonzalez J (2008) Magnetostatic properties of co-rich amorphous microwires: theory and experiment. Phys Status Solidi A 205:1800–1804
113. Zuberek R, Szymczak H, Gutowski M, Zhukov A, Zhukova V, Usov NA, Garcia K, Vazquez M (2007) Internal stress influence on FMR in amorphous glass-coated microwires. J Magn Magn Mater 316:e890–e892
114. Zhukov A, Cobeno AF, Gonzalez J, Torcunov A, Pina E, Prieto MJ, Blanco JM, Larin V, Baranov S (1999) Ferromagnetic resonance, magnetic behaviour and structure of fe-based glasscoated microwires. J Magn Magn Mater 203:238–240
115. Valenzuela R, Zamorano R, Alvarez G, Gutierrez M, Montiel H (2007) Magnetoimpedance, ferromagnetic resonance, and low field microwave absorption in amorphous ferromagnets. J Non-Cryst Solids 353:768–772
116. Montiel H, Alvarez G, Gutierrez M, Zamorano R, Valenzuela R (2006) The effect of metal-to-glass ratio on the low-field microwave absorption at 9.4 GHz of glass-coated CoFeBSi microwires. IEEE Trans Magn 42:3380–3382
117. Chiriac H, Colesniuc CN, Ovari TA, Ticussan M (1999) In situ investigation of the magnetization processes in amorphous glass-covered wires by ferromagnetic resonance measurements. J Appl Phys 85:5453–5455
118. Melik R, Unal E, Perkgoz NK, Puttlitz C, Demir HV (2009) Metamaterial-based wireless strain sensors. Appl Phys Lett 95:011106
119. Sakai K, Asano N, Wada Y, Yoshikado S (2010) Composite electromagnetic wave absorber made of soft magnetic material and polystyrene resin and control of permeability and permittivity. J Eur Ceram Soc 30:347–353
120. Xu X, Qing A, Gan YB, Feng YP (2007) An experimental study on electromagnetic properties of random fiber composite materials. Microwave Opt Technol Lett 49:185–190
121. Qin F, Popov V, Peng HX (2011) Stress tunable microwave absorption of ferromagnetic microwires for sensing applications. J Alloy Compd 509:9508–9512
122. Qin F, Brosseau C, Peng HX (2011) In situ microwave characterization of microwire composites under mechanical stress. Appl Phys Lett 99:252902
123. Kim B, Lee J, Yu I (2003) Electrical properties of single-wall carbon nanotube and epoxy composites. J Appl Phys 94:6724–6728

124. Chiriac H, Marinescu CS, Ovari TA (1999) Temperature dependence of the magneto-impedance effect. J Magn Magn Mater 196–197:162–163
125. Kim Y, Cho W, Kim T, Kim C, Lee H (1998) Temperature dependence of magnetoimpedance effect in amorphous $Co_{66}Fe_4Nib_{14}Si_{15}$ ribbon. J Appl Phys 83:6575–6577
126. Chen G, Yang XL, Zeng L, Yang JX, Gong FF, Yang DP, Wang ZC (2000) High-temperature giant magnetoimpedance in fe-based nanocrystalline alloy. J Appl Phys 87:5263–5265
127. Zhukova V, Ipatov M, Zhukov A, Varga R, Torcunov A, Gonzalez J, Blanco J (2006) Studies of magnetic properties of thin microwires with low curie temperature. J Magn Magn Mater 300:16–23
128. Papargyris D, Day R, Nesbitt A, Bakavos D (2008) Comparison of the mechanical and physical properties of a carbon fibre epoxy composite manufactured by resin transfer moulding using conventional and microwave heating. Compos Sci Technol 68:1854–1861
129. Zhukova V, Blanco JM, Ipatov M, Zhukov A, Garcia C, Gonzalez J, Varga R, Torcunov A (2007) Development of thin microwires with low curie temperature for temperature sensors applications. Sens Actuators, B 126:318–323
130. Fernando G, Degamber B (2006) Process monitoring of fibre reinforced composites using optical fibre sensors. Int Mater Rev 51(42):65–106
131. Serkov A, Radishevskii M (2008) Status and prospects for production of carbon fibres based on polyacrylonitrile. Fibre Chem 40:24–31

Chapter 12
Microwave Absorption Behaviour

The high-frequency absorption behaviour of amorphous ferromagnetic materials, among others, is of considerable interest for microwave absorber applications [1]. Since amorphous glass-coated microwires have small dimensions (1–30 μm in diameter), high electrical conductivity ($\sim 6\times10^5$ S/m), high magnetic permeability ($\sim 10^4$), and high mechanical strength ($\sim 10^3$ MPa), they can be incorporated into polymer-based composites for creating high-performance microwave absorption [2–4] or EMI shielding [5] composite materials. Compared with dielectric absorbents, magnetic absorbents provide additional magnetic losses and achieve a better impedance match. Compared to other types of magnetic absorbent, e.g. the widely used ferrites, the soft magnetic materials are not as limited by Snoek's law thanks to their large saturation magnetisation and permeability. But their issue lies in the large conductivity, which could make them useless for high-frequency applications owing to the strong eddy current loss, which is formulated as [6]:

$$P_e = \frac{CB^2f^2d^2}{\rho}, \tag{12.1}$$

where C is the proportional constant, B is the flux density, f is the frequency, d is the sample thickness and ρ is the resistivity. In a composite material, the concentration p has to be considered, and Eq. (12.1) can then be revised to [7] the following:

$$P_e = p\frac{CB^2f^2d^2}{\rho}. \tag{12.2}$$

For the low-resistivity material to be used in high frequency, the immediate approach to curb the eddy current loss as indicated by Eq. (12.2) is to limit the thickness of the absorbent (wire diameter in the case of microwire-based absorber) or its concentration in the composite absorber. This is de facto one of the basic rationales for our adopting thin ferromagnetic microwires of limited concentration for microwave absorption at gigahertz, and more relevant details will be discussed later. Another distinct advantage is that microwire composites possess remarkable tunable properties, as presented in the last chapter, rendering likely a broader absorption band compared to their non-tunable counter parts [8].

H.-X. Peng et al., *Ferromagnetic Microwire Composites*,
Engineering Materials and Processes, DOI 10.1007/978-3-319-29276-2_12

In view of the appealing application potential of microwire absorbents, the former Soviet Union had expended enormous efforts investigating the microwave absorption properties of amorphous microwires, but few results are available to the public for confidentiality reasons. Not until 2009 did the Micromag company of Spain successfully commercialise amorphous microwires as absorbents in warships.

A number of groups worldwide have been actively engaged in the development of microwire-based absorbers and shielders, and their seminal works will be surveyed below. It is also worth mentioning that, although microwire composites also exhibit excellent shielding properties in both a regular [5] and a random manner [9], the EMI shielding is absorption-dominated [5, 10]. We will therefore focus on the discussion of the microwave absorption of microwire composites, which is determined by their electromagnetic constitutive parameters, namely permittivity and permeability, through the intrinsic properties of microwires and their mesostructure. The rest of this chapter is organised as follows. A brief introduction to microwave absorption theory will first be given. Two types of microwire absorber will be treated separately, according to the absorption mechanism, i.e. dielectric loss dominated and magnetic loss dominated absorbers. Finally, the design strategies of some specific absorbers containing microwire-based fillers are described.

12.1 Microwave Absorption Theory

While the phenomenon of microwave absorption (MA) has been known for many decades and the cause of the absorption is well formulated, the design of absorbers has occupied the minds of many materials scientists and engineers for centuries. Recently, the problem has garnered even more attention and become more important than ever. In addition to academic reasons, its practical impact on society has been recognised. The growing public concern about possible human health effects in relation to weak RF fields, i.e. health hazards from environmental fields [11], motivates the related research.

In this section, fundamental knowledge of microwave absorption will be presented as well as an overview of mixture law theory. These two together provide a theoretical route to an optimised design of absorbers. Microwave energy, when incident on a lossy dispersive material, creates heating within the material through the interactions of the electromagnetic field with the materials' molecular and electronic structure. Homogeneous and heterogeneous media analysed with in an effective medium approach are described by two material parameters: the complex (relative) permittivity $\varepsilon = \varepsilon' - j\varepsilon''$ and the magnetic permeability (relative) $\mu = \mu' - j\mu''$. The terms ε' and μ' are associated with energy storage, and terms ε'' and μ'' are associated with dielectric loss or energy dissipation within a material, resulting from conduction, resonance, and relaxation mechanisms. The loss tangent of the dielectric material is $\tan\delta = \varepsilon''/\varepsilon'$, where δ is the dielectric loss angle of the material. Energy loss in a material illuminated by electromagnetic waves comes about through damping forces acting on polarised atoms and molecules and through

the finite conductivity of a material. It is common knowledge in electromagnetism that the Poynting theorem governs our understanding of the conservation of power in linear, dispersive media [12]. This states that the total power (for a harmonic electromagnetic field of angular frequency ω entering a volume V through the surface S) goes partially into increasing the field energy stored inside V and is partially lost into heat, i.e.

$$\frac{\partial u}{\partial t} + \nabla \cdot S = -j \cdot E - 2\omega Im\left(\varepsilon\left\langle |E|^2 \right\rangle + \mu\left\langle |H|^2 \right\rangle\right), \tag{12.3}$$

where

$$u = \mathrm{Re}\left[\varepsilon_0 \frac{\mathrm{d}(\omega\varepsilon)}{\mathrm{d}\omega}\left\langle |E|^2 \right\rangle + \mu_0 \frac{\mathrm{d}(\omega\mu)}{\mathrm{d}\omega}\left\langle |H|^2 \right\rangle\right], \tag{12.4}$$

where $\langle \ldots \rangle$ denotes the time average over the period of the carrier frequency, and $S = E \times H$ is the Poynting vector. The quantities ε_0 and μ_0 are the permittivity and the magnetic permeability of vacuum, respectively. The quantities E and H are the electric and magnetic field intensities, respectively. The quantity j accounts for both conductive and dielectric losses. We observe that the conductive and dielectric losses are indistinguishable with respect to the heat generated. Applying external electromagnetic fields to a composite material implies that the electromagnetic waves come across a variety of microscopic boundary conditions due to the inclusions making the heterostructure. The resulting local field variations can have a very strong effect on energy absorption at such boundaries, since absorption depends quadratically on the electric field intensity.

Figure 12.1 shows a multilayer microwave absorber which consists of n layers of different materials backed by a perfect electric conductor (PEC). For simplicity, we consider that the electromagnetic wave is normally incident. Here, d_i, μ_i and ε_i denote the thickness, the complex intrinsic impedance, and the propagation constant of the ith layer, respectively. The conductivity for each individual layer of the

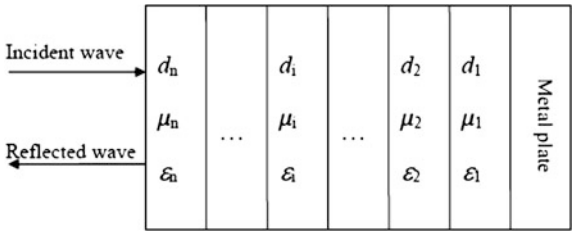

Fig. 12.1 Schematic of a multilayer microwave absorber with a normally incident wave. d_i, μ_i, and ε_i denote the thickness, relative permeability, and permittivity of the ith layer, respectively

absorber is assumed to be zero. According to the transmission-line theory [13–15], the wave impedance (Z_i) of the ith layer is given by

$$Z_i = \eta_i \frac{Z_{i-1} + \eta_i \tan h(\gamma_i d_i)}{\eta_i + Z_{i-1} \tan h(\gamma_i d_i)}, \tag{12.5}$$

where $\eta_i = \eta_0 \sqrt{\mu_i / \varepsilon_i}$, $\gamma_i = j2\pi f \sqrt{\mu\varepsilon}/c$, η_0 are the characteristic impedance of the free space; μ_i and ε_i are the relative complex permeability and permittivity of the ith layer, respectively. Considering that the metal plate is a PEC, $\eta_0 = 0$, the impedance of first layer reads as follows:

$$Z_1 = \eta_1 \tan h(\gamma_1 d_1). \tag{12.6}$$

The reflection loss (RL) of the normal incident electromagnetic wave at the absorber surface is given by

$$\mathrm{RL} = 20 \log|\Gamma| = 20 \log \left| \frac{Z_n - \eta_0}{Z_n + \eta_0} \right|, \tag{12.7}$$

where Γ is the reflection coefficient. Through Eqs. (12.5)–(12.7), we can see that the combination of the magnetic permeability and the permittivity (of both the absorbing and the substrate layers) satisfying the impedance matching condition is the key to producing a high-performance microwave absorber. Specifically, for a single layer of absorber backed by a PEC, which is a common situation in many studies discussed above, the reflection loss is given as follows:

$$\mathrm{RL} = 20 \log \left| \frac{\sqrt{\frac{\mu}{\varepsilon}} \tan h\left(j \frac{2\pi f d}{c} \sqrt{\mu\varepsilon}\right) - 1}{\sqrt{\frac{\mu}{\varepsilon}} \tan h\left(j \frac{2\pi f d}{c} \sqrt{\mu\varepsilon}\right) + 1} \right|. \tag{12.8}$$

The attenuation constant α (real part of the propagation factor γ), in nepers/m, is defined by [13]:

$$\begin{aligned} \alpha &= \mathrm{Re}(\gamma) \\ &= \mathrm{Re}\left(\frac{j\omega\sqrt{\mu\varepsilon}}{c} \right) \\ &= \frac{\omega}{\sqrt{2}c} \sqrt{\mu''\varepsilon'' - \mu'\varepsilon' + \sqrt{(\mu'^2 + \mu''^2)(\varepsilon'^2 + \varepsilon''^2)}}. \end{aligned} \tag{12.9}$$

where c is the light speed in free space. Here we can see that the attenuation constant is dependent on complex magnetic permeability, permittivity, and frequency. If we consider diamagnetic carbonaceous materials, MA is due to dielectric losses. Before we proceed to consider the case of pure dielectrics with $\mu = 1 - j0$, we first consider for the purpose of comparison the case of ferrites with strong magnetic losses, their absorption being mainly due to the ferromagnetic resonance.

To satisfy the minimum reflection loss, according to Eq. (12.8) the perfect matching condition is given as follows:

$$\sqrt{\frac{\mu}{\varepsilon}}\tan h\left(j\frac{2\pi fd}{c}\sqrt{\mu\varepsilon}\right)=1. \tag{12.10}$$

Usually, $\frac{2\pi fd}{c}\sqrt{\mu\varepsilon}\ll 1$, as the thickness d is much smaller than wavelength and ε is also small. It follows from Eq. (12.10) that

$$j\frac{2\pi fd}{c}(\mu'-j\mu'')=1, \tag{12.11}$$

which can be reduced to

$$\mu'=0 \quad \text{and} \quad \mu''=\frac{c}{2\pi fd}. \tag{12.12}$$

We find that the matching frequency f_{m} is given as:

$$f_{\mathrm{m}}=\frac{c}{2\pi fd\mu''}. \tag{12.13}$$

The matching frequency should generally be the same as the natural resonance frequency, which can be given by [16–18]

$$f=\frac{r}{2\pi}H_a, \tag{12.14}$$

where $\gamma/2\pi=2.8$ MHz/Oe is the gyromagnetic ratio. The anisotropy field H_{a} is given by

$$H_{\mathrm{a}}=\frac{2|K_1|}{\mu_0 M_{\mathrm{s}}}, \tag{12.15}$$

where K_1 is the anisotropy constant and M_s is the saturation magnetisation. A larger saturation magnetisation or smaller anisotropy field will redshift the resonance frequency, which also means an improved absorption bandwidth, since there is a trade-off between the resonance frequency and the absorption bandwidth [19]. We now turn to the case of a dielectric absorbent. Assuming that $\mu=1-j0$, Eq. (12.8) can be written as follows:

$$\mathrm{RL}=20\log\left|\frac{\sqrt{\frac{1}{\varepsilon}}\tan h\left(j\frac{2\pi fd}{c}\sqrt{\varepsilon}\right)-1}{\sqrt{\frac{1}{\varepsilon}}\tan h\left(j\frac{2\pi fd}{c}\sqrt{\varepsilon}\right)+1}\right|. \tag{12.16}$$

As $\sqrt{\frac{1}{\varepsilon}}\tan h\left(j\frac{2\pi fd}{c}\sqrt{\varepsilon}\right)<1$, the best possible matching, i.e. $\sqrt{\frac{1}{\varepsilon}}\tan h\left(j\frac{2\pi fd}{c}\sqrt{\varepsilon}\right)$, achieves maximum. As $\frac{2\pi fd}{c}\sqrt{\mu\varepsilon}\ll 1$, the best possible matching condition is given as follows:

$$\sqrt{\frac{1}{\varepsilon}}=j\frac{2\pi fd}{c}\sqrt{\varepsilon}, \tag{12.17}$$

This can be reduced to

$$\varepsilon'=0,\quad \varepsilon''=\frac{c}{2\pi fd}. \tag{12.18}$$

This is quite similar to Eq. (12.12). At the best matching condition, we can calculate the maximum reflection loss as follows:

$$[RL]_{\max}=20\log\left|\frac{\frac{1}{\varepsilon}-1}{\frac{1}{\varepsilon}+1}\right|. \tag{12.19}$$

After some transformation, we obtain the following:

$$[\mathrm{RL}]_{\max}=20\log\left(1-\frac{4}{2+\varepsilon''(\tan\delta+\frac{1}{\tan\delta})}\right). \tag{12.20}$$

Note that $\tan\delta+\frac{1}{\tan\delta}$ is monotonically decreasing, $\forall\tan\delta<1$. Thus, the maximum reflection loss should be evaluated by considering both ε'' and the loss tangent. The usual case is that larger ε'' gives rise to larger loss tangents, so an optimised ε'' and associated loss tangent can be expected to achieve the maximum absorption condition, (too small or too large ε'' will not favour absorption), as shown in Fig. 12.2. This is further confirmed by the attenuation constant

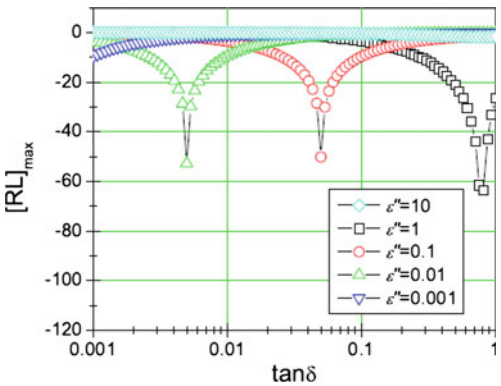

Fig. 12.2 Dielectric loss dependence of the maximum reflection loss for different values of ε''

$$\alpha = \frac{\omega}{\sqrt{2}c}\sqrt{-\varepsilon' + \sqrt{(\varepsilon'^2 + \varepsilon''^2)}}. \tag{12.21}$$

After some transformation, we obtain

$$\alpha = \frac{\omega}{\sqrt{2}c}\sqrt{\varepsilon''\left(\sqrt{1 + \frac{1}{\tan^2\delta}} - \frac{1}{\tan\delta}\right)}. \tag{12.22}$$

At the matching frequency, the attenuation constant reads as follows:

$$\alpha = \frac{\omega}{\sqrt{2}d}\sqrt{\frac{1}{\varepsilon''}\left(\sqrt{1 + \frac{1}{\tan^2\delta}} - \frac{1}{\tan\delta}\right)}. \tag{12.23}$$

12.2 Dielectric Loss Dominated Absorption

In the case of dilute composites, the microwire composites exhibit high complex permittivity but a close-to-unity permeability, with negligible magnetic loss at gigahertz frequency [2, 20, 21]. It follows that the absorption feature is mainly determined by the relaxation polarisation.

The concentration of the wire amount plays an important role in this case. It has been shown that an increasing amount of wires will improve the absorption [5]. However, it is reported that, rather than a simple linear dependence of absorption on the filler content, there is a threshold value at which the percolation network is formed if the glass coatings at the end of wires are spalled, which is often the case [2] (see Fig. 12.3a). This is common in the percolating composite systems (see, e.g. [22–24]). In detail, when the wire content is smaller than the percolation threshold, the loss tangent increases but without a significant increase of dielectric loss as the wire content is increased, whereas further increase of the wire concentration gives a sharp increase of dielectric loss due to the wave reflection rather than absorption. This effect overshadows the contribution of increasing loss tangent to the microwave absorption and results in the decrease of microwave absorption. Note that the tunnelling effect is responsible for the conductivity of the composite before the percolating threshold, which is highly desirable for microwave absorption. It should be mentioned that, at this point, microwires are not as good as ferrite due to its much higher conductivity, which would otherwise free our concerns on the concentration limitation to preserve the dipole nature [25]. To address the conflict between the increasing wire concentration and the percolating network, superior glass quality is the key. Therefore, it is now clear to us that, in addition to the quality of the metallic core, good glass quality is necessary for further improving

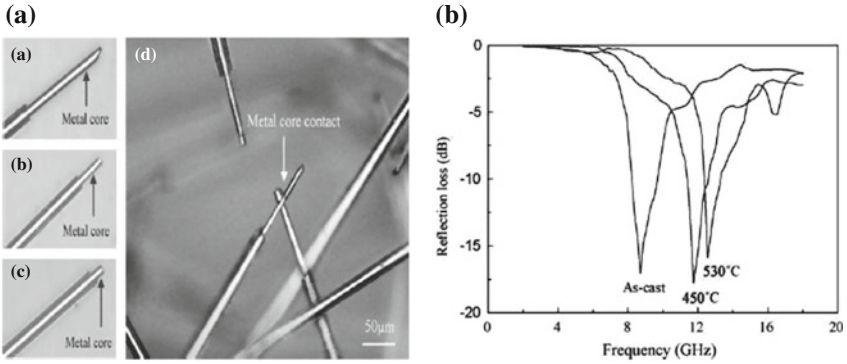

Fig. 12.3 **a** Morphology and metal core contact of the short-cut microwires: (*a*) as-cast; (*b*) annealed at 450 °C; (*c*) annealed at 530 °C; (*d*) metal core contact (as-cast). **b** Calculated reflection losses of planar composites filled with as-cast and annealed microwires (with filling ratio of 15 % and thickness of 1.5 mm). Reprinted with the permission from [2], copyright 2010 Elsevier

the microwave absorption. Indeed, it is shown that the percolation threshold decreases due to the decrease of the length of the naked metallic core via annealing, but the level of maximum absorption is retained. It can then be expected that with a further increase of the annealed wire concentration, the absorption can be increased.

Among the dilute absorbers, the one proposed by Liu et al. [26] is unique as it was made transparent by dispersing short-cut microwires of lengths from 5 to 12 mm into a transparent siliconeelastomer. Such a transparent microwire composite shows more than 10 dB of shielding efficiency with just 0.5 wt% microwires and a thickness of less than 750 μm. The study reveals that a wire length of around 10 mm (with a tolerance of less than 0.4 mm) is the optimum parameter for shielding purposes. The shielding profiles are determined by the wire resonance, depending on the wire length and cluster effect [27].

Qin et al. [7, 28] conducted a detailed study on the influence of the wire diameter, interwire spacing, and the embedded depth on the absorption performance in a set of E-glass fibre-reinforced polymer (GFRP)/microwire composites. They used an equivalent circuit model as shown in Fig. 12.4 to illustrate the influence of these geometrical parameters. Figure 12.5a shows that in the continuous-wire composite with fixed interwire spacing b, reducing b will effectively increase absorption, which can be explained by an equivalent circuit. When an array of microwires is excited by a microwave with electric field e polarised along the microwire, the displacement current flows along both the microwires and the air gaps between neighbouring wires. Hence, the system can be regarded as a parallel combination of lumped impedances; the impedances of the wire and air gap are formulated as follows:

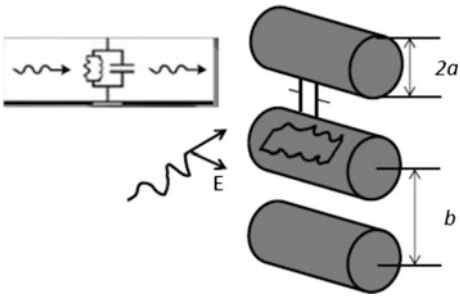

Fig. 12.4 Schematic of equivalent circuit for array of wires excited by an incident microwave with the electrical field component along the wire axes *a* and *b* denote the wire radius and interwire spacing, respectively

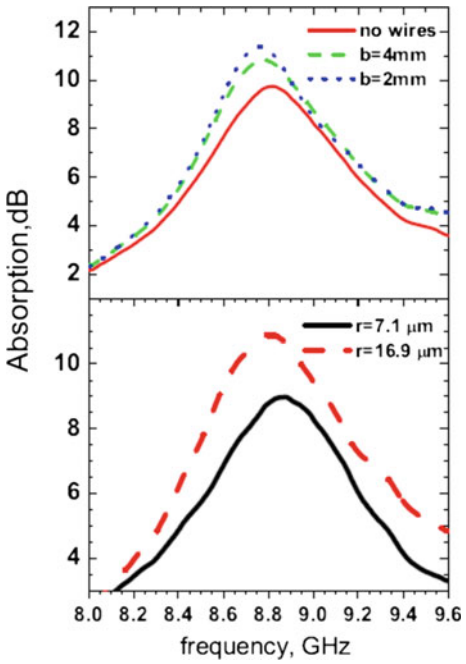

Fig. 12.5 **a** Absorption spectra for continuous microwire/GFRP composites with different wire spacing *b*. **b** Absorption spectra for continuous microwire/GFRP composites with wires of different radius *a*. Reprinted with the permission from [28], copyright 2013 Springer

$$Z_{\text{wire}} = i/\omega\pi a^2\varepsilon_{\text{wire}}; \tag{12.24a}$$

$$Z_{\text{air}} = \frac{i}{\omega(2rb - \pi a^2)\varepsilon_{\text{air}}}, \tag{12.24b}$$

where $\varepsilon_{\text{wire}}$ and ε_{air} are the permittivities of the studied microwire and air gaps; ω is the angle frequency; *a* denotes the radius of the wire. The equivalent impedance $Z_{\text{eq-wire}}$ of the wire/gap system can then be given by

$$Z_{\mathrm{eq-wire}} = \frac{Z_{\mathrm{wire}} Z_{\mathrm{air}}}{Z_{\mathrm{wire}} + Z_{\mathrm{air}}}. \tag{12.25}$$

With reference to the above equations, $Z_{\mathrm{eq-wire}}$ is improved with decreasing b, and consequently reduces transmission and increases absorption. Some comments are in order here. (i) By varying the equivalent impedance of the circuit, the absorption (or transmission) spectra can be modulated; this is very useful for developing effective filters. (ii) By selecting different b and r, one can formulate and control the change of the absorption maximum and the shift of absorption, which can be exploited for metamaterial applications. This effect is exemplified in Fig. 12.5a: as b is reduced, the absorption maximum redshifts and the absorption bandwidth are broadened. This is consistent with the theoretical calculations in [29], which reports that a metal-backed quarter-wavelength radio-absorber containing an array of ultrathin microwires of 4 μm radius exhibits improved absorption and redshift of the absorption peak as the wire spacing is reduced from 10 mm to 1 mm. It should be noted that maximising the function of one parameter that constitutes the mesostructure of composites for modulating the microwave properties also relies on the optimisation of other pertinent parameters [30].

This may explain why the shift presented for the current case is not significant. Indeed, the best absorption performance should meet impedance matching conditions that can only be achieved with appropriate wire impedance, diameter, and spacing [29]. It is expected that further reduction of the airgap (wire spacing) will raise absorption; but when the wires spacing is reduced to be small enough to induce indirect dipolar interactions or even direct exchange interactions, the absorption mechanism will change from the domination of dielectric loss to that of magnetic loss [31] and the composite may become very lossy, while the maximum absorption will shift to a much higher frequency. It should be noted that the influence of interwire spacing on the microwave properties varies for different compositions of microwires. For composites containing continuous Co-based microwires, the dielectric response is sensitive to the external magnetic field via the strong magnetoimpedance effect [32]; but there is a lack of strong microwire interactions between the neighbouring wires and it is generally not possible to observe multiple resonances in the absorption spectra, even with very small spacing. In contrast, for the composites containing continuous Fe-based wires, the field effect is weak as the MI properties of Fe-based wires are inferior [33]; but with decreasing interwire spacing, the closing domain structure can be formed and the strong exchange resonance effect may be expected to benefit the absorption performance [34]. In either case, the wire spacing plays an important role in manipulating the electromagnetic behaviours.

In addition to the wire spacing, another equally important parameter is the wire diameter. As shown in Fig. 12.5b, although composites containing the same loading of thin wires have smaller wire spacing, larger absorption is observed in composites with a larger diameter than in those with smaller diameters. This can be understood

by a theoretical model for the effective permittivity ε_{eff} of wire arrays consisting of thin wires with diameters less than 40 μm [35]:

$$\varepsilon_{\text{eff}} = \varepsilon_0 - \frac{1}{\omega t b} \cdot \left(\frac{\omega L + X_{\text{W}}}{R_{\text{W}}^2} + j \frac{1}{R_{\text{W}}} \right), \tag{12.26}$$

where R_{W}, L, and X_{W} represent the dc resistance, inductance, and reactance of the wire, respectively. In this instance, the effective permittivity is determined by the wire resistance. Thicker wire has smaller resistance and hence larger permittivity; its composite therefore shows better absorption. In addition, although the ratio of the radius square to the wire spacing remains the same for the two composites with the same loading of wires, the composite with thicker wire experiences a stronger skin effect and reduces the value of matching spacing, thereby achieving better impedance matching than with thinner wires in this case [29]. It should be noted that as the wire gets thicker than 40 μm, the inverse relation between ε_{eff} and R_{W} switches to proportional; this was demonstrated in the preceding chapter. This is reasonable as, although the good conductivity of absorbents is essential for absorption, too high conductivity will make the material excessively reflective. On this basis, the above argument is valid that larger permittivity results in larger absorption, as the permittivity here is circumstanced by polarisation only, excluding conduction. In another perspective, embedding a too thick wire into the polymer matrix will lead to a significant diameter mismatch compared with typical reinforcing fibres of 8–12 μm [36], thereby degrading the mechanical properties of the resulting composites. As such, limitation of the wire diameter can retain the advantages of the lightweight structure intrinsic to polymer composites and is thus preferable for the overall composite performance. This consideration should be adopted as a strategy to design multifunctional composites enabled by these Fe-based microwires.

Further study has been conducted upon the effect of embedded depth (the distance of the ferromagnetic microwire layer to the microwave incident surface) on the resultant absorption performance by the same group. They examined whether wires put in the front or back have different responses; indeed, the back-wire sample shows better absorption due to the contribution of the front GFR player and the back wire layer. The even-poorer absorption than the pure GFRP with the wires in the front layer as observed is attributed to the reflection induced by the wires. This clearly suggests that the wires should not be embedded in the front layer so as to prevent a significant impedance mismatch in the surface layer that reflects the wave away. They also tested the configuration with wires embedded in the medium layer, as shown in Fig. 12.6a. The results show that they did not present as good absorption. The second layer of GFRP serves as a substrate layer to slightly increase the impedance mismatch [37], so the absorption is slightly decreased and also the matching frequency is shifted as compared to the single layer, but it is similar to the first configuration, which further substantiates the function of the GFRP as the substrate layer. The fourth configuration shows greatly decreased absorption, which is due to the reflection of the GFRP; this is further confirmed by the case of

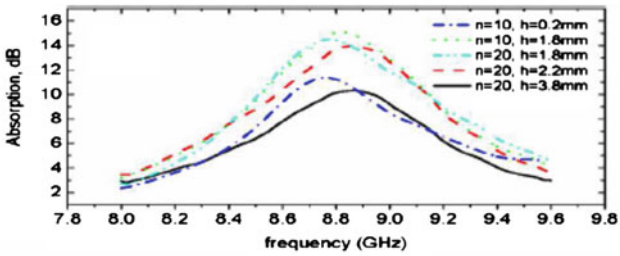

Depth	0.2 mm	1.8 mm	1.8 mm	2.2mm	3.8mm
Configuration					
Absorption (dB)	11.5268	15.6268	14.6284	14.3997	10.5430
Frequency(GHz)	8.7680	8.8260	8.7860	8.8260	8.8260

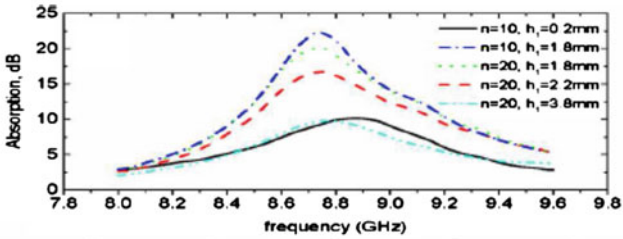

h_1	0.2 mm	1.8 mm	1.8 mm	2.2 mm	3.8 mm
h_2	0.4 mm	1.6 mm	1.6 mm	2.4 mm	3.6 mm
Configuration					
Absorption (dB)	9.9599	22.7887	20.6091	17.0009	10.2595
Frequency(GHz)	8.7860	8.7300	8.7120	8.7200	8.9140

Fig. 12.6 **a** Influence of embedded depth h_i of the ith microwire layer on the absorption spectra for continuous microwire/GFRP composites with 0° wire orientation. The values of h_1 and n (number of laminates) are indicated in the figure legend; the maximum absorption for each composite configuration is summarised in the table below. **b** Same as **a** but with the addition of another layer (h_2) of microwires. Reprinted with the permission from [28], copyright 2013 Springer

3.8 mm embedded depth. The composites containing two layers of microwires of the same configuration are also examined. With reference to Fig. 12.6b, the addition of a second layer of wires retains the same sequence of configuration ranked in terms of absorption, except for the first configuration, i.e. wires at the top with respect to the incident wave, whereby the absorption is the least of all due to very strong reflection. Similar results have been reported for the case of the absorber containing 1-mm microwire absorbents [38], whereby the best absorption has been achieved when the wires are positioned close to the metallic substrate.

The importance of the above result lies in the simultaneous achievement of the optimal absorption and the impact resistance performance offered by the same configuration of such microwire/GFRP composites. GFRPs are widely used in wind turbines, which are essential structural components for wind energy harvesting. As wind turbines can cause interference to normal radar communications due to the unwanted Doppler returns [39], the introduction of wires into GFRP will mitigate the issue and address this conflict of interest between the desire to encourage wide use of renewable and green energy and the desire to maintain the effective operation of the important human safety-associated radars used for air traffic control, weather monitoring, and marine navigation aids.

12.3 Magnetic Loss Dominated Absorbing

In the case of microwire composites with heavy loading, the ferromagnetic resonance may shift to gigahertz frequency due to the enhanced effective anisotropy field via the long-range dipolar interactions between wires [3, 40]. In this case, the ferromagnetic resonance for the planar microwire composites is given by [40]

$$f_{\mathrm{r}} = r\sqrt{4\pi M_{\mathrm{s}}(H_{\mathrm{k}} + H_{\mathrm{n}})}; \tag{12.27a}$$

$$H_{\mathrm{n}} \propto iM_{\mathrm{s}}(a/l)^2, \tag{12.27b}$$

where H_{n} is the field created by neighbouring wires of total number i, or it can be simply understood as an additional anisotropy field induced by wire interactions [41]. Thus, any factors that can influence the anisotropy field should be considered tuning parameters. Directly from Eqs. 12.27a and 12.27b, it is obtained that a larger aspect ratio ($l/2a$) will reduce the resonance frequency and increase the absorption according to Snoek's law; and that the increasing number of wires will enhance the permeability and neighbouring field and hence the resonance frequency. For Co-based wires, the decrease of metal-to-total diameter ratio p will elevate the internal stress and consequently the anisotropy field [42, 43], thus the absorption should be shifted to a higher frequency. This has been analytically explained very well by Baranov et al. [44]. The dependence of resonance frequency can be expressed as follows:

$$f \approx f_0\sqrt{\left(\frac{1-p^2}{1+1.5p^2}\right)}\ (\mathrm{GHz}), \tag{12.28}$$

where

$$f_0 = 1.5\sqrt{\lambda \times 10^6}\ (\mathrm{GHz}). \tag{12.29}$$

Also, note that the reduction of the wire core diameter can reduce the thickness of the outer shell of the domain so that the electromagnetic wave can penetrate into the inner core with an axial anisotropy and easily induce natural ferromagnetic resonance. As the reduced wire diameter can also guarantee a lightweight structure, it is therefore desirable to use very fine wires of less than 20 μm diameter to make absorbers.

Three kinds of microwires of typical positive, negative, and vanishing magnetostriction constant with correspondingly different composition [45] are chosen here to shed light on the usefulness of this theory. By using Eq. (12.28), the metal-to-total diameter (p) dependence of the resonance frequency is calculated for these three wires. The result confirms the role of the wire's cross-sectional geometry on the natural ferromagnetic resonance frequency and also reveals that the Fe-based wires are more suitable for absorption purposes at relatively higher gigahertz frequencies. This is consistent with three ported magnetoabsorption properties of wires with positive, negative, and vanishing magnetostriction constant [46]. For microwave absorption purposes, the best configuration, with respect to the wire axis, is when the static magnetic field and the microwave electrical field are parallel; the microwave magnetic field is perpendicular, as in such configuration, and circumferential FMR will be induced with marked intensity by the microwave electrical field [47]. In contrast, the ferromagnetic resonance induced by the magnetic component of the microwave is much weaker in microwires and can only be well observed in the submicron wires and nanowires [48]. Such a remarkable dependence of FMR on the wire orientation with respect to the microwave and external magnetic field has been well studied in [46]. As shown in Fig. 12.7, we can deduce that, under a constant magnetic field, tilted wires with respect to the axis will give much smaller absorption intensity, and that when the angle increases to a certain value (approaching 90°), the FMR will disappear unless a much higher magnetic field is applied. Also, one can see that the Fe-based wires are the best option for

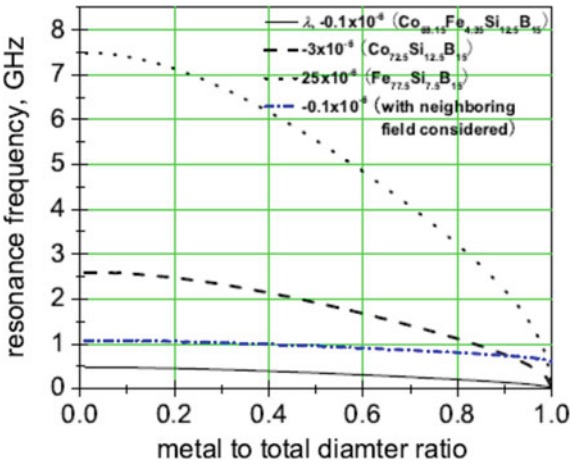

Fig. 12.7 Dependence of resonance field (H_{res}) of absorption spectra on the microwire orientation (α) with respect to the static magnetic field as shown in the inset at 9.5 GHz. Reprinted with the permission from [46], copyright 2002 Elsevier

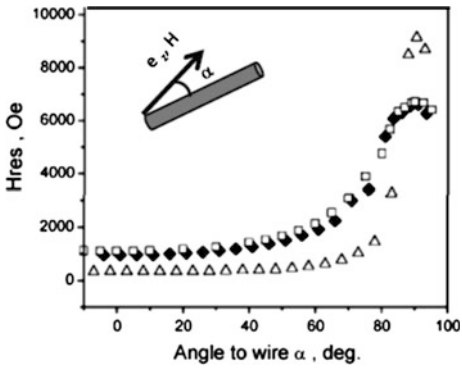

Fig. 12.8 Theoretical curve (*continuous line*) of FMR frequency as a function of x according to Eq. 12.28 for three wires with positive, negative, and vanishing magnetostriction, respectively

magnetic microwires, since they have the largest tolerance to the tilted angle range up to 80° without significant increase of the resonance magnetic field. Clearly this suggests that, for a quasi-isotropic magnetic absorber with wires homogeneously dispersed, Fe-based microwires are more efficient than other types of wires since the effective amount of Fe-based wires, regardless of the orientation of the EM wave, will be larger than other kinds of wires.

Another feature of great interest is that the resonance frequency can be shifted to higher frequency if a large enough neighbouring field is yielded with a good number of wires added into the absorbing medium or tailored wire geometry (Fig. 12.8). A proven method is to make a multilayer-structured microwire film that will enhance the anisotropy field [49] and give an improved initial permeability, as high as 6000 at 1 MHz. With the reduction of the wire length, the demagnetising field increases, and the anisotropy field is reduced accordingly [3, 5, 41, 50], resulting in the reduction of absorption via the collaborative effect with the influence on the neighbouring field H_n. In general, the optimal dimensions for excellent absorption performance require a metallic core of diameter 1–3 μm and length 1–3 mm, comparable to the half wavelength [51] for microwires.

Several important aspects of the implementation of microwires on absorbers should be highlighted here. First, as the anisotropy constant of microwires can be conveniently modulated by the magnetostriction constant, which is subject to the wire composition and stress conditions (either internal stress from different geometry or external stress applied), the tuning of natural FMR resonance and associated absorption features such as the absorption maximum and bandwidth is therefore readily accessible. Second, the dispersion of microwires (i.e. mesostructure control) is critical to meet the requirement for suitable dimensions [51] and arrangements for maximum absorption. As discussed above, the dispersion can have an impact on the orientation of wires and hence the electromagnetic absorption behaviour. This partially explains why the theoretical calculation from complex permittivity and permeability that is obtained typically in a wax-based toroidal

sample usually does not match the reflection loss experimentally measured with planar samples of much larger size (e.g. [2]). Tunable absorption can be realised in the absence of magnetic field and prefers an ultrathin metallic core, making the wires attractive for miniaturisation of microwave devices based on these fine elements. The last important aspect meriting our attention is the use of wires without glass coatings. Although they are inferior in terms of as-cast wire quality due to the fabrication limitation as compared to glass-coated wires, it is the metallic core rather than the glass coating that interacts effectively with the microwave. As such, applying the metallic core only into the absorbing matrix will improve the packing density of the wires [49] and hence the absorbing rate and efficiency. However, an obvious drawback requiring caution is that they can form a percolation network at certain concentrations and will thus induce large reflection. Such a percolating effect explains why weak permittivity is observed for 80 wt% melt-extracted FeSiB wires in a toroidal sample as reported in [52]. The absorption thus calculated is of little practical interest, with over 10 dB loss only occurred at 1–2.7 GHz for thicknesses over 4 mm. This performance is much inferior to what Marin et al. [4] have presented with wires of similar static magnetic behaviour, i.e. more than 15 dB at 8.5 GHz with a wire fraction of *c.a.* 3.1wt%.

12.4 Other Absorbers Based on Microwires

In this section, we will discuss some strategies for designing specific absorbers with microwires or microwire-based absorbents based on the limited data reported in the literature. One approach is to use hybrid microwires with dielectric absorbents or to design a (gradient) multilayer structure to improve the impedance mismatch and hence improve the absorption. The other is to fabricate multilayer microwires by coating with additional layer(s) of magnetic and/or non-magnetic phases so as to yield additional absorption peaks.

Qin et al. [53] propose hybridising microwires with carbon nanotubes (CNT) with good electrical conductivity to make a multiscale hybrid composite absorber. As shown in a group of spectra of lossy parameters (Fig. 12.9), the loss tangent increases significantly with increasing wire concentration, suggesting the possibility of improved absorption; while the intrinsic impedance calculated from $\eta = \sqrt{\mu/\epsilon}$ shows an opposite trend, which is due to the increased conduction loss, although the polarisation loss is also improved. Indeed, the reflection is increased. One can also see that the absorption has been enhanced with the co-work of the wires and CNTs.

Torrejon et al. [54] developed a biphase magnetic microwire consisting of a soft amorphous nucleus and harder outer crystalline shell. The presence of additional hard phase as compared to the conventional single-phase microwire induces a second absorption peak at a lower frequency than that excited in the soft nucleus. Although the second peak is weaker, it helps generate an additional absorption peak and hence enlarge the absorption band. However, a serious issue with this kind of

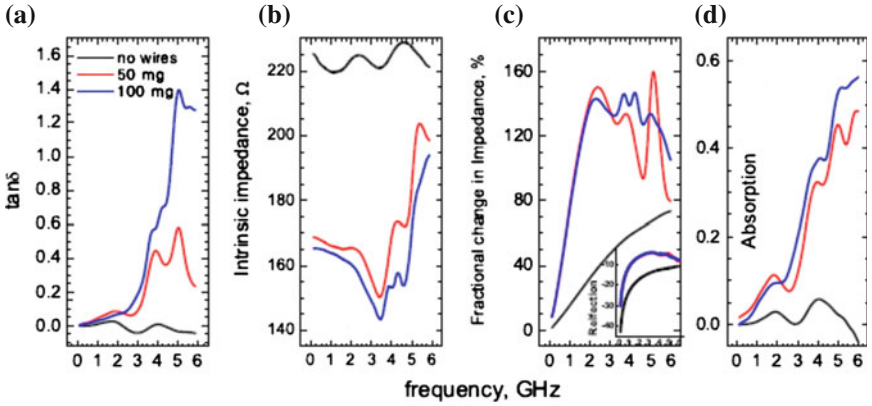

Fig. 12.9 Frequency dependences of loss tangent (**a**), intrinsic impedance (**b**), fractional change in surface impedance (**c**), and absorption (**d**). Reprinted with the permission from [53], copyright 2013 Elsevier

multilayer wire is the tremendous reduction of the magnetoabsorption level compared with conventional glass-coated wires, which is suggested to be attributable to the reduced volume fraction of the inner axial domain in the amorphous nucleus caused by the electroplating-induced stresses. A proper post-annealing is apparently necessary to resolve this problem.

In closing, with all the advantages discussed above at VHF frequency, the microwires can be effectively designed in terms of composition, static magnetic properties, geometry (core diameter, metal-to-total diameter ratio, length, and aspect ratio), concentration, topological arrangement (unidirectional and omni-directional) with the guide of transmission-line theory and when fabricated by a facile mould-casting technique, yielding exceptional absorption or shielding performance. The absorption is readily tunable to meet frequency selective applications. Undoubtedly, the microwire composites can find a market niche as high-performance absorbers for anechoic chambers, modern concealment, biological protection shelters, and so forth.

References

1. Vazquez M, Adenot-Engelvin AL (2009) Glass-coated amorphous ferromagnetic microwires atmicrowavefrequencies. J Magn Magn Mater 321:2066–2073
2. Zhang Z, Wang C, Zhang Y, Xie J (2010) Microwave absorbing properties of composites filled withglass-coated $Fe_{69}Co_{10}Si_8B_{13}$ amorphous microwire. Mater Sci Eng 175:233–237
3. Di Y, Jiang J, Du G, Tian B, Bie S, He H (2007) Magnetic and microwave properties of glass-coated amorphous ferromagnetic microwires. Trans Nonferrous Met Soc China 17:1352–1357

4. Marin P, Cortina D, Hernando A (2005) High-frequency behavior of amorphous microwires and its applications. J Magn Magn Mater 290–291:1597–1600
5. Qin F, Peng H, Pankratov N, Phan M, Panina L, Ipatov M, Zhukova V, Zhukov A, Gonzalez J (2010) Exceptional EMI shielding properties of ferromagnetic microwires enabled polymer composites. J Appl Phys 108:044510
6. Skarman B, Ye Z, Jansson P (2011) Soft magnetic composite materials. US Patent 8,075,710
7. Qin F, Peng H, Chen Z, Hilton G (2013) Microwave absorption of structural polymer composites containing glass-coated amorphous microwires. IEEE Trans Magn 49:4245–4248
8. Liu L, Rozanov K, Abshinova M (2013) Tunable properties of microwire composites at microwavefrequency. Appl Phys A 110:275–279
9. Ababei G, Chiriac H, David V, Dafinescu V, Nica I (2013) Omni-directional selective shielding material based on amorphous glass coated microwires. Rev Sci Instrum 83:014701–014706
10. Liberal I, Ederra I, Gomez-Polo C, Labrador A, Perez-Landazabal JI, Gonzalo R (2011) Theoretical modeling and experimental verification of the scattering from a ferromagnetic microwire. IEEE Trans Microwave Theor Tech 59:517–526
11. Dawson TW, Caputa K, Stuchly MA, Shepard RB, Kavet R, Sastre A (2002) Pacemaker interferenceby magnetic fields at power line frequencies. IEEE Trans Biomed Eng 49:254–262
12. Colin R (1966) Foundations of mIcrowave engineering. McGraw Hill, New York
13. Vinoy KJ, Jha RM (1996) Radar absorbing materials - From theory to design and characterization. Kluwer Academic Publishers, Boston
14. Oh JH, Oh KS, Kim CG, Hong CS (2004) Design of radar absorbing structures using glass/epoxy composite containing carbon black in x-band frequency ranges. Compos B Eng 35:49–56
15. Shen G, Xu Z, Li Y (2006) Absorbing properties and structural design of microwave absorbers based on w-type la-doped ferrite and carbon fiber composites. J Magn Magn Mater 301:325–330
16. Gerber R, Wright C (eds) (1992) GA. Applied magnetism. Kluwer Academic Publishers, Doldrecht
17. Kittel C (1948) On the theory of ferromagnetic resonance absorption. Phys Rev 73:155
18. Maeda T, Sugimoto S, Kagotani T, Tezuka N, Inomata K (2004) Effect of the soft/hard exchangeinteraction on natural resonance frequency and electromagnetic wave absorption of the rareearth-iron-boron compounds. J Magn Magn Mater 281:195–205
19. Acher O, Dubourg S (2008) Generalization of snoek's law to ferromagnetic films and composites. Phys Rev B 77:104440
20. Makhnovskiy DP, Panina LV (2005) Field and stress tunable microwave composite materials based on ferromagnetic wires. In: Murray VN (2005) Progress in ferromagnetism research. Nova Science Publishers Inc., Hauppauge
21. Starostenko S, Rozanov K, Osipov A (2006) Microwave properties of composites with glass coated amorphous magnetic microwires. J Magn Magn Mater 298:5–64
22. Fan ZJ, Luo GH, Zhang ZF, Zhou L, Wei F (2006) Electromagnetic and microwave absorbing properties of multi-walled carbon nanotubes/polymer composites. Mater Sci Eng B-Solid State Mater Adv Technol 132:85–89
23. Liu ZF, Bai G, Huang Y, Li FF, Ma YF, Guo TY, He XB, Lin X, Gao HJ, Chen YS (2007) Microwave absorption of single-walled carbon nanotubes/soluble cross-linked polyurethane composites. J Phys Chem C 111:13696–13700
24. Wu KH, Ting TH, Wang GP, Ho WD, Shih CC (2008) Effect of carbon black content on electrical and microwave absorbing properties of polyaniline/carbon black nanocomposites. PolymerDegrad Stability 93:483–488
25. Baranov SA (1998) Use of a microconductor with natural ferromagnetic resonance for radio absorbing materials. Tech Phys Lett 24:21–23
26. Liu L, Yang Z, Kong L, Li P, Poo C (2012) High permittivity and shielding effectiveness of microwire composites with optical transparency. In: 2012 Asia-Pacific symposium on electromagnetic compatibility (APEMC). IEEE, pp 633–636

27. Liu L, Matitsine S, Gan YB, Rozanov KN (2007) Cluster effect in frequency selective composites with randomly distributed long conductive fibres. J Phys D Appl Phys 40:7534
28. Qin F, Peng H, Chen Z, Wang H, Zhang J, Hilton G (2013) Optimization of microwire/glass-fiber reinforced polymer composites for wind turbine application. Appl Phys A Mater Sci Process. 10.1007/s00339-013-7820-2
29. Ponomarenko V, Popov V, Qin F (2013) Microwire-based analog of a quarter-wavelength radio absorber. Radio Electron Commun Syst 56:285–289
30. Brosseau C, Queffelec P, Talbot P (2001) Microwave characterization of filled polymers. J Appl Phys 89:4532–4540
31. Qin FX, Peng HX (2013) Ferromagnetic microwires enabled multifunctional composite materials. Prog Mater Sci 58:183–259
32. Qin FX, Peng HX, Phan MH, Panina LV, Ipatov M, Zhukov A (2012) Effects of wire properties on the field-tunable behaviour of continuous-microwire composites. Sens Actuators A 178:118–125
33. Phan MH, Peng HX (2008) Giant magneto impedance materials: fundamentals and applications. Prog Mater Sci 53:323–420
34. Chizhik A, Zhukov A, Blanco JM, Szymczak R, Gonzalez J (2002) Interaction between Fe-richferromagnetic glass-coated microwires. J Magn Magn Mater 249:99–103
35. Liberal I, Nefedov I, Ederra I, Gonzalo R, Tretyakov S (2011) Electromagnetic response and homogenization of grids of ferromagnetic microwires. J Appl Phys 110:064909
36. Qin F, Peng HX, Tang J, Qin LC (2010) Ferromagnetic microwires enabled polymer composites for sensing applications. Compos A Appl Sci Manuf 41:1823–1828
37. Qin F, Brosseau C (2012) A review and analysis of microwave absorption in polymer composites filled with carbonaceous particles. J Appl Phys 111:061301–061324
38. Marin P, Cortina D, Hernando A (2008) Electromagnetic wave absorbing material based on magnetic microwires. IEEE Trans Magn 44:3934–3937
39. Krug F, Lewke B (2009) Electromagnetic interference on large wind turbines. Energies 2:1118–1129
40. Ivanov AV, Shalygin AN, Galkin VY, Vedyayev AV (2009) Rozanov3 KN. Meta materials with tunable negative refractive index fabricated from amorphous ferromagnetic microwires: magneto static interaction between microwires. PIERS ONLINE 5:649–652
41. Di Y, Jiang J, Bie S, Yuan L, Davies HA, He H (2008) Collective length effect on the magneto static properties of arrays of glass-coated amorphous alloy microwires. J Magn Magn Mater 320:534–539
42. Zhukov A, Zhukova V (2009) Magnetic properties and applications of ferromagnetic mircowires with amorphous and nano crystalline structure. Nova Science Publishers, Inc., New York
43. Usov N, Antonov A, Dykhne A, Lagar'kov A (1998) Stress dependence of the hysteresis loops ofco-rich amorphous wire. J Phys: Condens Matter 10:2453
44. Baranov S (2009) Radio absorption properties of amorphous microwires. Moldavian J Phys Sci 8:332–336
45. Garcia D, Raposo V, Montero O, Iniguez JI (2006) Influence of magnetostriction constant on magneto impedance-frequency dependence. Sens Actuators A 129:227–230
46. Yildiz F, Rameev BZ, Tarapov SI, Tagirov LR, Aktas B (2002) High-frequency magneto resonance absorption in amorphous magnetic microwires. J Magn Magn Mater 247:222–229
47. Tulin V, Astahov M, Rodin A (2003) Amorphous ferromagnetic microwire in the microwave cavity. Ferromagnetic resonance and absorption. J Magn Magn Mater 258(C259):201 – 203 (Second Moscow international symposium on magnetism)
48. Kraus L, Infante G, Frait Z, Vazquez M (2011) Ferromagnetic resonance in microwires and nanowires. Phys Rev B 83:174438
49. Baranov S, Yamaguchi M, Garcia K, Vazquez M (2010) Application of amorphous microwires for electromagnetic shieldi. Moldavian J Phys Sci 9:76–82
50. Zhukova V, Usov NA, Zhukov A, Gonzalez J (2002) Length effect in a co-rich amorphous wire. Phys Rev B 65:134407

51. Baranov SA, Yamaguchi M, Garcia KL, Vazquez M (2008) Dimensional absorption high-frequency properties of the cast glass coated microwires. Surf Eng Appl Electrochem 44:425–427
52. Han M, Liang D, Deng L (2011) Fabrication and electromagnetic wave absorption properties of amorphousfe[sub 79]si[sub 16]b[sub 5]microwires. Appl Phys Lett 99:082503
53. Qin FX, Brosseau C, Peng HX (2013) Microwave properties of carbon nanotube/microwire/rubbermultiscale hybrid composites. Chem Phys Lett 579:40–44
54. Torrejon J, Badini-Confalonieri GA, Vazquez M (2009) Double-absorption ferromagnetic resonance in biphase magnetic microwires. J Appl Phys 106:023913

Chapter 13
Microwire-Based Metacomposites

13.1 Brief Introduction to Metamaterial

13.1.1 Fundamentals of Metamaterials

Metamaterials are one of the most appealing forefront subjects in materials and physics nowadays (see, e.g. [1–6]) in view of the prospect that their successful application may renovate a number of industrial domains such as aeronautics, optoelectronics, and transportation. It has been theoretically and experimentally demonstrated recently that a single microwire or microwire array is capable of metamaterial behaviour; the recent experimental work in our group demonstrates that the polymer composites containing a single array or a crossing array of Fe-based microwires have metamaterial characteristics; we therefore in this chapter focus on this very exciting aspect of microwire composites. Before proceeding, it will be worthwhile to review essential concepts and background information on metamaterials.

A metamaterial is by definition an artificially engineered material that gains its properties from its structure rather than its constituents. The resultant properties, such as negative refractive index and negative stiffness, are not encountered in naturally occurring materials [7]. First of all, a metamaterial must be non-existent in nature, which accounts for the origin of its name, as meta means "beyond" or "of a higher kind" in Greek [8]. It is an extension to the conventional materials in terms of material behaviours. Second, the unique properties of metamaterials are not derived from their constituent materials but from their structure, which distinguishes them from conventional composite materials. Typically, yet not essentially, a metamaterial possesses an ordered structure, realised by a periodic arrangement of the functional units, as schematically depicted in Fig. 13.1. Another implicit rule is that the physical dimensions of unit (scale) and neighbouring distance (periodicity) must be smaller than the incident wavelength so that homogeneity, without which a material cannot be recognised as a "material", can be ensured [7]. The collective responses (effective responses) of all units to the external field (stimuli) give the

H.-X. Peng et al., *Ferromagnetic Microwire Composites*,
Engineering Materials and Processes, DOI 10.1007/978-3-319-29276-2_13

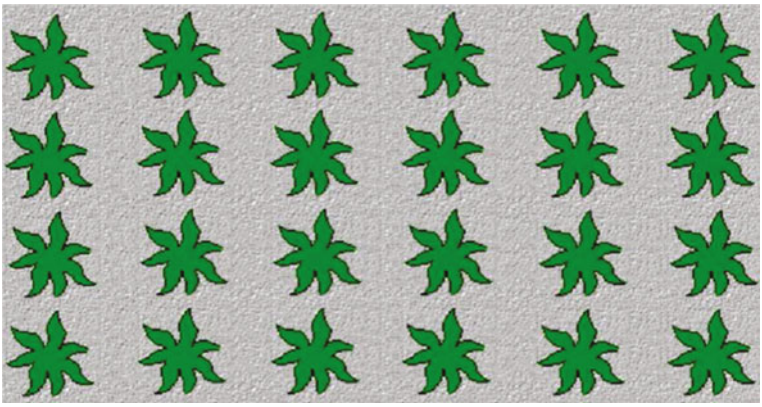

Fig. 13.1 Generic sketch of a volumetric metamaterial synthesised by embedding various inclusions in a host medium

macroscopic properties of a metamaterial. By manipulating the scale and periodicity of these units, one can tailor the properties of a metamaterial. The effective medium theory finds great use herein to study the behaviour of metamaterials, as reviewed in [9], which in turn can be instrumental to metamaterial design and engineering for specific applications. In this sense, metamaterials can also be categorised into smart materials and multifunctional composites.

In this book, the metamaterials are restricted to the electromagnetic metamaterials that are our main interest. An analogy can be drawn between metamaterial engineered by functional units as basic building blocks and the conventional materials composed of atoms. Likewise, Maxwell's equations can be transformed from microscopic to macroscopic form, making it possible to describe the electromagnetic response of a metamaterial via both an effective permittivity ($\varepsilon(\omega)$) and permeability ($\mu(\omega)$). At the subwavelength scale, these two parameters can be manipulated independently and arbitrarily as we desire. Thus, the flow of an electromagnetic wave can be controlled much like a fluid. It follows that some intriguing properties can be achieved for some appropriate materials. For instance, magnetic responses can be realised in metamaterials consisting of mere non-magnetic constituents [10]. At certain frequencies, a negative refractive index material (NIM) can be obtained with both $\varepsilon(\omega)$ and $\mu(\omega)$ being negative ($n = -\sqrt{\mu\varepsilon}$), as depicted in Fig. 13.2. The exploitation of NIMs opens up new prospects of manipulating light and produces revolutionary impacts on present-day optical technologies.

13.1.2 Classification of and Approaches to Metamaterials

Since $\varepsilon(\omega)$ and $\mu(\omega)$ can be controlled independently, it is possible to obtain unusual media with either only negative $\varepsilon(\omega)$ (ENG) or only negative $\mu(\omega)$ (MNG), and both

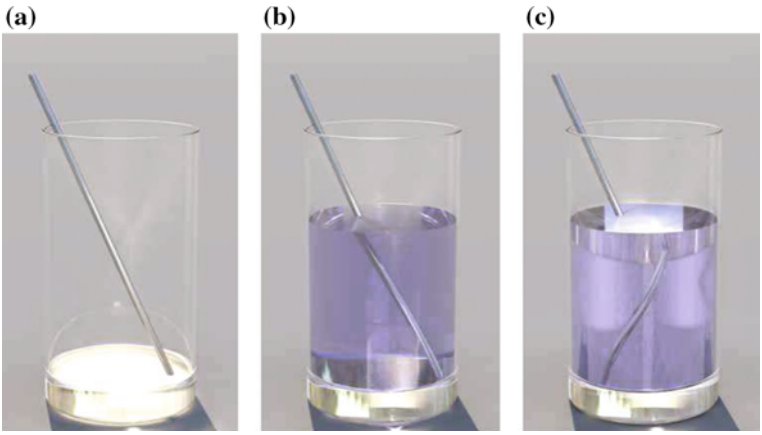

Fig. 13.2 Negative refraction. **a** An empty glass. **b** A glass filled with an ordinary medium with positive refractive index, such as water; the straw inside the glass is refracted. **c** The water is replaced by a negatively refracting medium. Reprinted with the permission from [11], copyright 2006 OSA

of them negative (DNG), as against conventional media with both parameters positive. Such a classification according to the sign of $\varepsilon(\omega)$ and $\mu(\omega)$ is shown in Fig. 13.3, and each class is detailed below.

- **ENG** Many plasmas exhibit this characteristic below plasma frequencies according to the Drude model. Veselago [12] initially proposed gaseous and solid plasmas. Decades later, it was found that noble metallic wires (e.g. silver, gold) behave in this manner in the infrared (IR) and visible frequency domains [2]. This was theoretically proposed first by Rotman and Pendry et al. [13, 14]; Smith et al. [5] and Shelby et al. [4] realised the idea using thin wires as the scattering

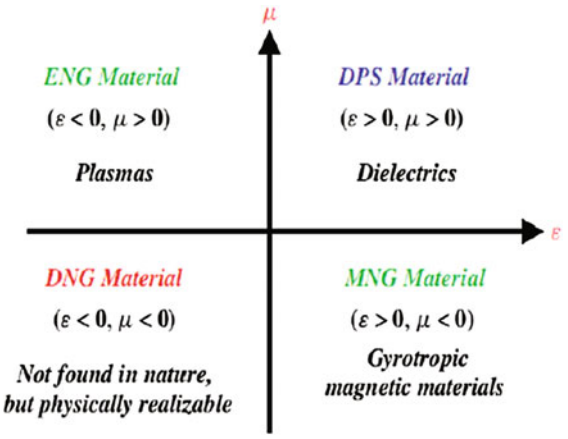

Fig. 13.3 Classification of materials in the $\varepsilon\mu$ plane in terms of their signs. Reprinted with the permission from [3], copyright John Wiley & Sons

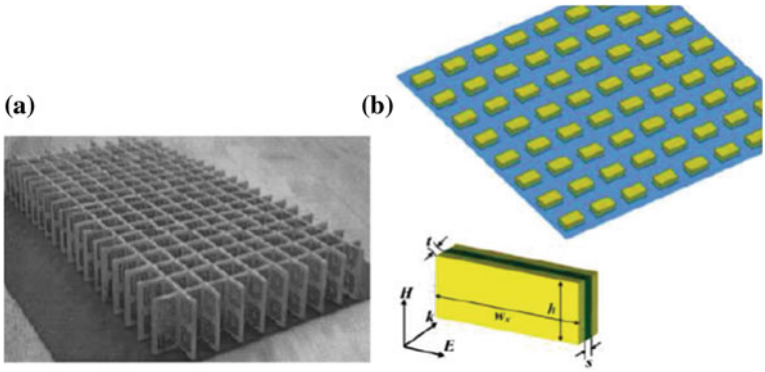

Fig. 13.4 Arrays of SRR structure (**a**) and nanorods (**b**). Reprinted with the permission from [2], copyright 2005 OSA

elements. Composites containing conductive sticks have also been intensively investigated to realise negative permittivity by Lagarkov et al. [15, 16] and Panina et al. [17].

- **MNG** Typical materials of this kind are gyrotropic materials. The composite media with thin wires enabling a resonance feature are also capable of giving negative values of effective permeability near the resonance frequency.
- **DNG** This is also known as a Veselago medium named after its discoverer [12], left-hand material, and NIM. It was realised by Smith and Shelby et al. [5] via split-ring resonators (SRRs), as shown in Fig. 13.4a. It consists of two planar concentric conductive rings, each with a gap. Shalaev et al. [2] also successfully fabricated the NIMs using arrays of gold nanorods or thin wires, as illustrated in Fig. 13.4a.

13.1.3 Applications of Metamaterials

The reason why metamaterials have become a focus of intense study is primarily that they afford a range of novel applications. Perfect lenses proposed by Pendry [1] are one of the most exciting applications. A lossless slab (Fig. 13.5) with a refractive index $n = -1$ projects an image of the object placed into the near field with subwavelength precision. This has profound impacts on biomedical imaging and subwavelength photolithography [18].

Metamaterials are a basis for building a practical cloaking device. The possibility of a working invisibility cloak was demonstrated in [20]. The cloak deflects microwave beams so that they flow around a "hidden" object inside with little distortion, making it appear almost as if nothing were there at all. Such a device typically involves surrounding the object to be cloaked with a shell which affects

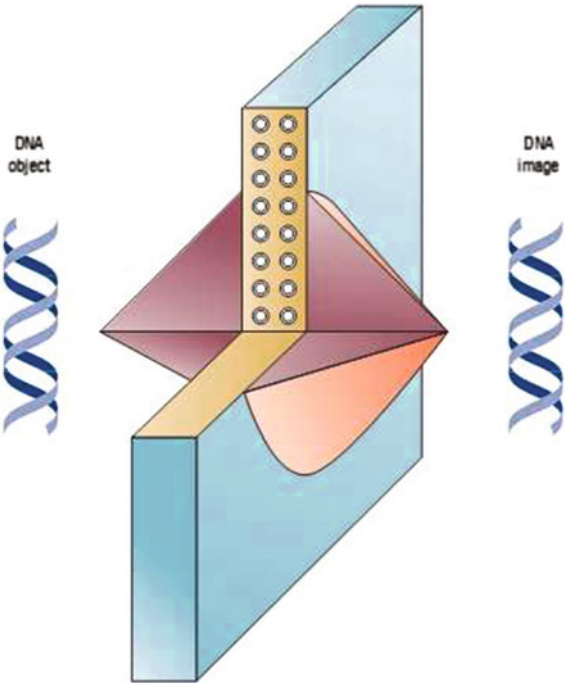

Fig. 13.5 A superlens capable of high-resolution imaging. Reprinted with the permission from [19], copyright 2007 Nature Publishing Group

the passage of light near it. Liu et al. [21] also experimentally demonstrate that a metamaterial cloak is able to revise the reflected waves to make them appear as if reflected from a mirror, thus cloaking the subject behind. Using FE simulations, Cai et al. [22] designed an optical cloaking device which deploys an array of metallic wires projecting from a central spoke that would render an object within the cloak invisible to red light.

Most recently, with an exponential growth of research interest in metamaterials, more potentials are being explored for industrial applications. Sato [23] reviewed the applications of metamaterials in automobiles, as summarised in Fig. 13.6. Melik et al. [24] proposed a metamaterial-based stress sensor with exceptional resolution. Metamaterials are also applied to improve the performance of antennas, as reported, e.g., by Alici and co-workers [25]. The microwave-absorbing capacity of a conventional shielding material can be enhanced by the metamaterial coating, as recently reported by Zou et al. [26]; the metamaterials themselves can also be designed to be perfect absorbers [27], as first demonstrated by Landy et al. [28], who simulated a 99 % absorptivity for a multilayer structure consisting of two metallic layers and a dielectric. Overall, there are still many unknown applications yet to be tapped into for metamaterials. In the present work, arrays of magnetic microwires are employed to obtain negative effective permittivity. Plus, the antiferromagnetic resonance features of ferromagnetic microwires suggest that a

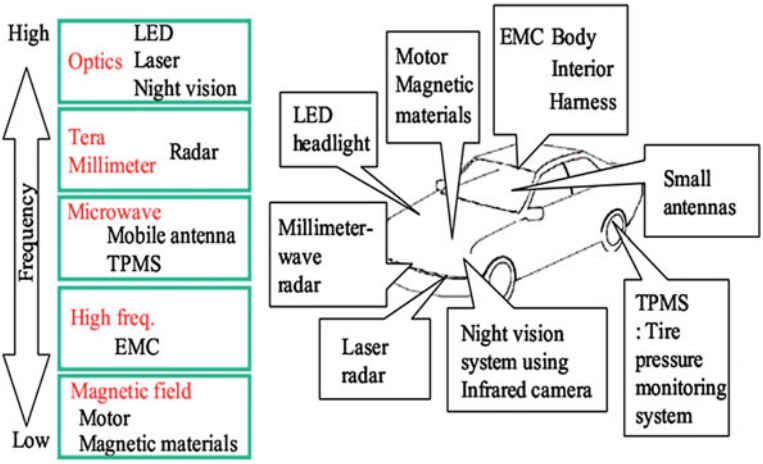

Fig. 13.6 Applications of metamaterials in automobiles [23], reproduced courtesy of the Electromagnetics Academy

negative permeability is also obtainable. In this sense, the microwire composite could demonstrate the metamaterial functionalities, for which corresponding applications are anticipated.

13.2 Metacomposite Characteristics

Thin conducting wire structures are common building blocks for preparing metamaterials with negative permittivity of a range of unusual properties. This has generated a considerable interest in wire media, and a vast amount of literature is devoted to the subject (see, e.g., [29–36]). The negative electrical response also suggests that the wire medium is characterised by a low-frequency stop band from zero frequency to the cut-off frequency, which is often referred to as plasma frequency [37, 38]. For the wire radius on the micron scale, and the lattice constant on millimetre scale, the plasma frequency is in the gigahertz range. In the frequency band above the plasma frequency, the effective permittivity of the wire media enters the negative value region and presents a strong dispersion therein. This may be used to engineer a specific electrical response. However, a single array of non-magnetic wires cannot provide negative magnetic permeability. In order to obtain simultaneously the negative permittivity and permeability, non-magnetic wires are often combined with another array of SRRs [5].

Such design suffers from the drawback of having relatively large dimensions and is not suitable for making into a complex shape when required, e.g., to be made into a coating on a curved surface. Another disadvantage is that such a design is anisotropic and the negative refraction is limited to only a couple of polarisations of

the incident plane electromagnetic wave [39–42], impeding interesting applications such as the perfect lens [1], where an isotropic metamaterial is needed. Most recently, alternative approaches have been proposed capitalising on the magnetic properties of magnetic materials such as ferrites [43, 44], yet during the manufacturing procedure, additional steps are necessary for the combination of non-conducting wires and magnetic materials. This is clearly cumbersome and unappealing for large-scale engineering purposes.

Here comes a question: What is the ideal design for a piece of engineering metamaterial? First of all, the definition of metamaterials is now becoming diverse in that they have covered a range of interdisciplinary subjects and research topics, such as transformation optics [1, 45, 46], electromagnetics [2], and structural mechanics [47]. Yet one key feature remains and is regarded as the centre guideline for conventional metamaterial designs: metamaterials derive their special properties from particular structural effects rather than intrinsic material properties of their constituents [4, 5, 20, 48]. For instance, metamaterials constructed by an array of rods and SRR rings are the most typical prototype. Nevertheless, these existing "metastructures" are not attractive for multifunctional purposes because they lack flexible responses towards external stimuli such as magnetic fields and mechanical stresses. Hence, complicated structures are necessary, albeit unfavourable, to promise the wanted metamaterial properties. Further, it entails a sophisticated fabrication process to guarantee precise dimension control at micro/nanoscales comparable to the concerned wavelength which is a sine qua non for metamaterial design [6, 49]. The downsides confine metastructures for mass production. A remedy is urgently needed.

Enlightened by the beauty of composite materials, we propose a concept of metacomposites where multifunctionalties can be attained from properties of each component. Although the concept has been used by some researchers [50–54], the meaning here is rather different. The metacomposites should meet three essential criteria: (i) a metacomposite is realised by incorporating functional fillers into matrix materials, therefore being a true piece of material with metamaterial features. (ii) Their ultimate properties are dependent on the fillers' material properties apart from structure-associated factors. (iii) They are manufactured via an engineering route.

Ferromagnetic microwires have been recently considered promising for microwave absorption [55, 56] and magnetic sensor applications [57] owing to their distinguished giant magnetoimpedance effect, giant stress impedance effect, and soft magnetic properties [58–60]. Specifically, strong responses from the microwires to the interactive microwave suggest that they can be built into suitable components for applications such as sensing and non-destructive structural health monitoring [61]. In this context, to pursue the most simplified design, a single ferromagnetic wire or array is proposed to provide simultaneous negative permittivity and permeability, in that negative permeability can be obtained at frequencies between the natural ferromagnetic resonance and antiferromagnetic resonance [62–66], while negative permittivity can be obtained below the normalised plasma

frequency $\tilde{f} = f_p/\sqrt{\varepsilon_m}$ [17, 67]. Thus, as long as the ferromagnetic resonance frequency is not higher than the plasma frequency in the continuous-wire case, or the antiantenna resonance in the short-wire case, simultaneous negative permittivity and permeability can be obtained. With a square net configuration, the microwire composite will present isotropic performance. Theoretically, a calculation is given here to illustrate the possibility of obtaining negative permeability and permittivity. For a parallel configuration comprised by conductive wires, the permeability can be expressed as [68]

$$\mu_{\text{eff}} = \frac{1}{2}\frac{(\omega_0+\omega_m)^2-\omega^2}{\omega_0(\omega_0+\omega_m)-\omega^2}\left(1+\sqrt{\left[\frac{\sigma}{\omega\varepsilon}(2\pi\frac{a}{b})^2\right]^2+1}\right) \tag{13.1}$$

where $\omega_0 = \gamma H_{\text{dc}}$ with γ the gyromagnetic constant and H_{dc} the external field. $\omega_m = 2\pi(2\pi\, a/b)2\gamma\, M$ with M the saturation magnetisation of wires of radius a and interwire spacing b and a bulk conductivity σ. For typical values of CoFe–Cr–B–Si wire, $\sigma = 10^{16}$ c^{-1}, $M = 500$ Gs, when $a = 10$ μm, $b = 1$ mm, $H_{\text{dc}} = 10$ Oe, the ferromagnetic resonance is 704 MHz according to $f_r = \mu_0 r\sqrt{H_{\text{dc}}M_{\text{s}}}/2\pi$ [69]. The normalised plasma frequency is 38.9 GHz, when the matrix permeability is 2. In this case, both negative permittivity and permeability are obtained at 1.9–21.7 GHz [68]. It should be noted that by regulating a, b (within the limit) and magnetic bias, the negative index range can be tuned. This could be of great use from the application point of view.

The capability of microwires to realise metamaterial features is demonstrated amazingly in a single wire. Labrador et al. [66] tested a single wire of nominal composition $Fe_{77.5}Si_{12.5}B_{10}$ in a waveguide by paralleling it with the electric field vector on slices of Rohacell foam under a dc magnetic field. Both negative permeability due to the natural FMR and negative permittivity as an effect of interactions with the waveguide are realised in the X-band. Note that, unlike the case of short-circuited microwires with a waveguide, the electrically isolated microwire behaves as if capacitive-loaded, responsible for negative values of the effective permittivity. As the natural FMR occurs at zero magnetic field, a magnetic field is then not an essential element in this metamaterial system, which greatly simplifies its structure. On the other hand, application of a magnetic field could also add the tunable functionality. Such a self-contained and versatile fine element is hence established as a promising metamaterial building block to configure a series of metamaterials, which are discussed below.

Different approaches were developed to realise the metamaterials based on ferromagnetic microwires. Adenot-Engelvin et al. [70, 71] fabricated a wire composite as schematically shown in Fig. 13.7a using CoFeSiB wire with a small negative magnetostriction coefficient of total diameter 9 μm and core diameter 4 μm. The volume fraction of the wires is within the range of 6–11 %. The microwave permeability for this composite is shown in Fig. 13.7b, fitted by a model based on the solenoid approach with a unique set of values for resistance (R), inductance (L), and capacitance (C).

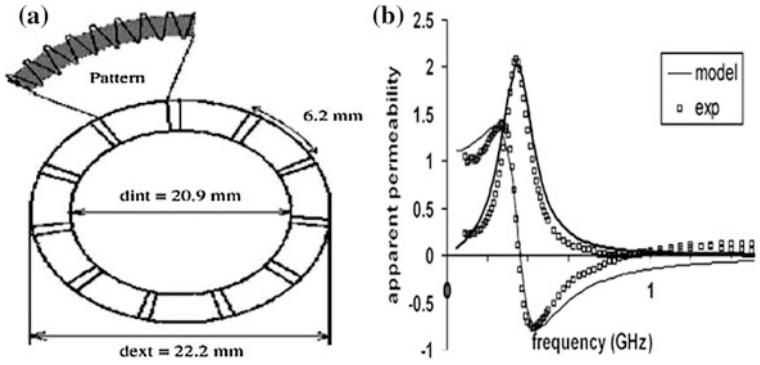

Fig. 13.7 **a** Schematic view of a sample with eleven metamaterial blocks. **b** Measured permeability and model with $R = 0.1$ OΩ, $L = 0.09$ nH, and $C = 9.5$ pF for the eight-loop wire composite. Reprinted with the permission from [70], copyright 2006 Elsevier

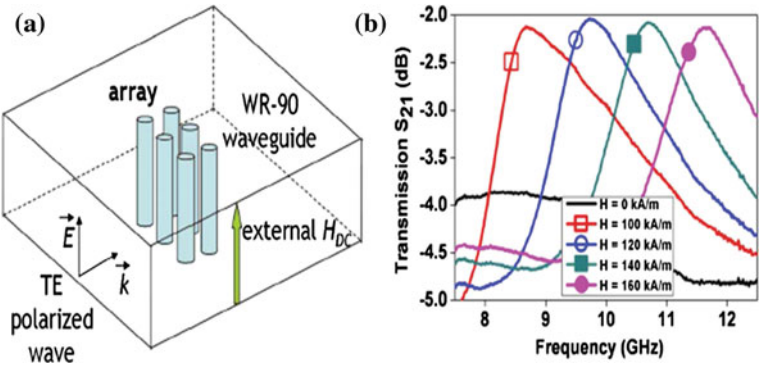

Fig. 13.8 **a** Schematic view of the configuration of wire arrays and measurement set-up. **b** Measured transmission characteristics on an array of two layers of three wires each, as a function of the applied magnetic field H_{dc}. Reprinted with the permission from [62], copyright 2009 AIP

The permeability is also found, in this configuration, to be dependent on the loops, in terms of the resonance frequency by analogy with the magnetic field effect [55, 62] or stress [72]. These field effects can be readily explained by the LLG model for computing the magnetic dynamic susceptibility.

In another configuration (see Fig. 13.8a) [62] constituted by wire arrays of CoSiB with a diameter of 2–3 μm, the transmission spectra were obtained as shown in Fig. 13.8b, exhibiting the rise of transmission with the dc field due to a double-negative condition obtained. Although there is no matrix involved, such wire arrays demonstrate the potential to make metamaterials from these wires. Liu et al. [73] proposed a metamaterial configuration by combining the long conductive fibres along the electric field and microwires along the magnetic field, as shown in Fig. 13.9a. As expected, the negative refraction index is seen at a certain frequency

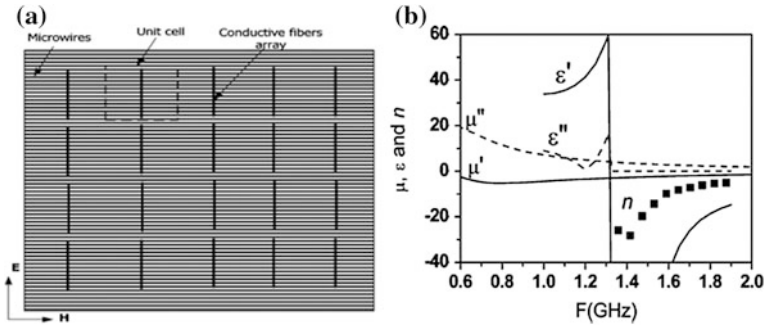

Fig. 13.9 **a** Schematic view of the configuration of composites containing microwires and conductive fibres. **b** Negative refractive index of the microwire composite obtained by HFSS™ [73]

range, as shown in the numerical results (Fig. 13.9b), although the significant resonance loss remains a problem for its application.

A very important sine qua non for realising the metamaterial feature at microwave frequency is that the diameter of the microwire is comparable to the skin depth, as too large a diameter will cause huge reflection [14, 61, 74]. This argument generally holds true for any functions based on microwave/material interactions other than EMI shielding dominated by reflection. For a typical ferromagnetic microwire, $\sigma = 10^{16}$ s^{-1}(10^5 S/m) and $\mu = 20$, the calculated skin depth δ at 10 GHz is about 1 μm [75]. Since the permeability decreases with the frequency, δ changes little. This is larger than even very thin microwires with a typical radius of few microns. Although it is still possible to penetrate into most of the inner core in the Fe-based wire [76] or the outer shell in the Co-based wire [77], the submicron wires [78–83] or nanowires [84–95] would be preferred in this case. On the other hand, reducing the wire diameter will reduce the volume fraction of wires and hence the permittivity and permeability. One may have to accept that such an unavoidable loss is typical for metal metamaterials [96]. Another restriction is set on the "dilute" condition, i.e. $b \gg a$, which is necessary to have a relatively smaller carrier density and large effective carrier mass, such that the plasma frequency can be regulated in the 1–10 GHz range of application interest. The band-stop or band-pass filter, for example, can be designed based on the criticality of plasma frequency on transmission [14, 68]. Also, it is argued that a large number of wires are deleterious since they will absorb most of the electromagnetic wave [64, 72]. This issue must be addressed before the microwire composites can find metamaterial applications such as cloaking. On the other hand, it is desirable for microwave absorption application and field-tunable devices arising from decent dielectric permittivity variation with the presence of external magnetic bias (Fig. 13.10). As such, these two functionalities cannot be pursued simultaneously, but this would greatly extend the freedom of tailoring the electromagnetic properties of the microwire composites.

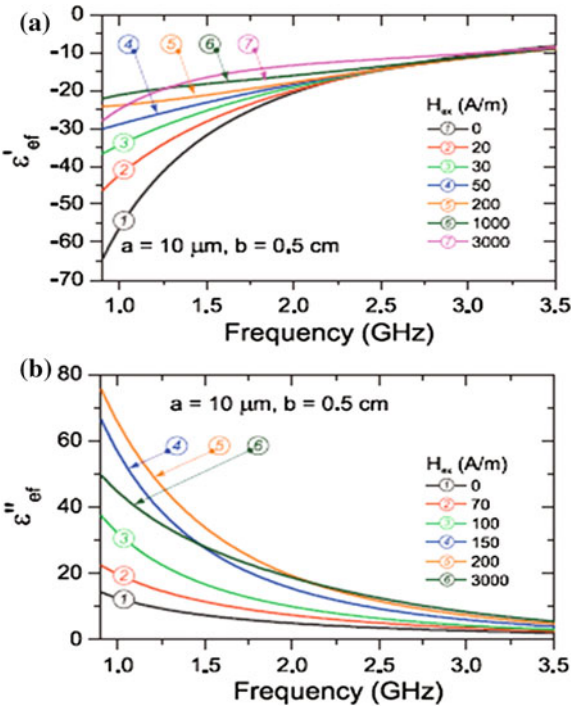

Fig. 13.10 Effective permittivity spectra of $Co_{66}Fe_{3.5}B_{16}Si_{11}Cr_{3.5}$ continuous-wire arrays deduced from the scattering spectra with the external magnetic field as a parameter (wire radius a = 10 μm, spacing between wires b = 5 mm). Reprinted with the permission from [78], copyright 2011 John Wiley & Sons

It should be addressed that above microwire-enabled metamaterial features are still obtained from a pure structure. Although their fascinating properties are derived from their magnetic properties, they are not a composite material in a strict sense. On the other hand, so far all the reports on the ferromagnetic microwire metamaterials are yet limited to the Co-based wires. As is known, Fe-based wires have significantly different domain structure from Co-based wires arising from the positive magnetostriction, and as a consequence, its static and dynamic electromagnetic responses are also distinct from those of Co-based wires [55, 76]. Besides, the natural ferromagnetic resonance (NFMR) of Fe-based wires enables negative permeability dispersion above the FMR frequency, which creates additional degrees of freedom in designing double-negative metamaterial band. In addition, as compared to Co-based wires, Fe-based wires are cost-effective and therefore more desirable for practical applications [58], especially in sensors and transformers. Hence, it is believed that by employing Fe-based microwires alone in a periodical fashion and by incorporating into a high-performance base material, these metamaterial properties can be maintained and new dimensions of functionalities can be realised. Most importantly, this design makes our metacomposites a true piece of material and it is of engineering interest.

Recently, Luo and Qin et al. [97] successfully realised prepreg-based metacomposites containing parallel Fe-based microwire arrays. Experimentally, glass-coated FeSiBC wires were embedded into aerospace graded 950 prepregs

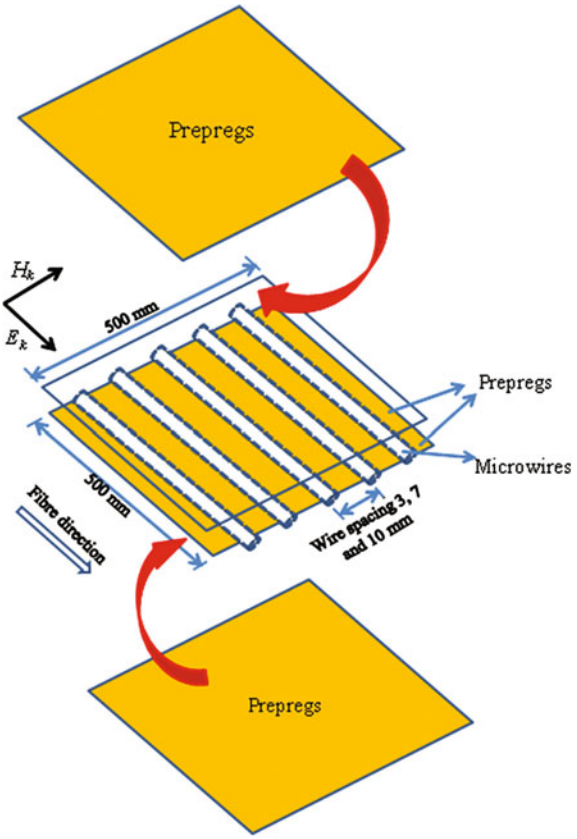

Fig. 13.11 Schematic illustration of the process for manufacturing composites containing Fe-based microwires in parallel manner with wire spacing of *b*. Reprinted with the permission from [99], copyright 2014 AIP

with spacing of 3, 7, and 10 mm, respectively (Fig. 13.11), followed by a hand laying-up and a standard autoclave curing procedure. All the resultant composite samples have an in-plane size of 500 × 500 mm^2 and a thickness of 1 mm. Microwave characterisation was carried in a free-space set-up in 0.9–17 GHz with the presence of a dc magnetic field up to 3 k Oe wherein S-parameters were extracted [61, 98]. Dielectric permittivity was later on calculated from S-parameters via a built-in programme Reflection/Transmission Epsilon Fast Model.

Remarkably, some transmission windows are identified in the 1–7 GHz from the composites containing 3-mm-spaced microwire array (Fig. 13.12a), together with reflection dips and absorption peaks (now shown here). From the permittivity spectra of the same wire composites, one observes that permittivity has negative values below a featured frequency of 16 GHz (Fig. 13.12b), i.e. f_p. From electromagnetic theory, one notes that transmission windows are a typical result of abnormal dispersion and this could be induced by either double-positive or double-negative indices (permittivity and permeability). The observation of negative permittivity denies the former situation, and herein, we can conclude that a negative ε and a negative μ are simultaneously obtained as a metacomposite feature.

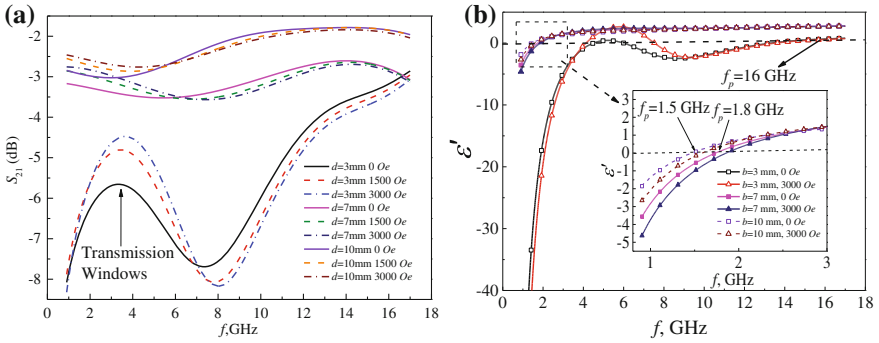

Fig. 13.12 Frequency dependencies of **a** transmission (S_{21}) coefficients and **b** dielectric permittivity of parallel microwire composites with the presence of fields up to 3 k Oe of different wire spacing, b = 3, 7, and 10 mm, respectively. Reprinted with the permission from [97], copyright 2013 AIP

The negative ε is observed below the f_p derived from the parallel alignment of wires [14], while a profile of negative μ is originated from the FMR of wires [58]. Notably, this transmission window can be excited without external magnetic fields, which is also defined as natural DNG feature. This remedies the metastructure consisting of Co-based wire arrays where DNG indices can only be observed in the presence of burden magnets [64]. The designed wire metacomposites renovate the area of realising DNG characteristics where only a simply parallel architecture is needed and can be oriented for microwave cloaking and sensing applications.

Moreover, the transmission windows can only be obtained when the wire–wire spacing is below a spacing of 7 mm. This links to the wire–wire magnetic interaction and the modulation of f_p. From Fig. 13.12b, one observes that when the wire spacing is larger than 3 mm, the plasma frequency is significantly lower than the theoretical prediction. In a wire media, f_p can be described as $f_p^2 = \frac{c^2}{2\pi b^2 \ln\left(\frac{b}{a}\right)}$[14], which is determined by the wire radius a and spacing b. We obtain f_p of 4.8, 6.6, and 16.6 GHz for composites with wire spacing of 10, 7, and 3 mm, respectively. However, from the inset of Fig. 13.12b, we notice that there is a large discrepancy between these calculated values and the experimental ones when the wire spacing is larger than 3 mm, i.e. 1.4 GHz for b = 10 mm and 1.6 GHz for b = 7 mm, respectively. This is arising from the fact that in the above equation, a is the effective diameter that contributes to the overall dielectric response and for microwires, the major response comes from the outer shell of the whole domain structure [14]. Nonetheless, for Fe-based wires, the outer shell volume only occupies a trivial portion [58, 100] such that the final f_p is greatly compromised. Decreasing the wire–wire spacing to a critical value of 3 mm, dynamic wire–wire interactions provide essential offsets to the effective diameter, hence plasma frequency considering the modification of wires' domain structure and magnetic tensor due to the long-range dipolar resonance [76, 101, 102]. It should be stressed

that here the interactions are referred to the dynamic magnetic interactions resulted from the coupling with electrical component of incident waves rather than the magnetostatic coupling, since 3-mm spacing is still too wide to induce meaningful magnetoelastic energy [103, 104].

However, due to the loss generated by the wires, the transmission level is not greatly favourable in this parallel metacomposites. The root cause is the relatively high wire concentration in the case of 3-mm spacing. To overcome the drawback, the same group comes up with an orthogonal array design that is capable of realising the transmission window at much larger wire spacing and providing a much higher transmission level. The orthogonal metacomposites are illustrated in Fig. 13.13. Fabrication and characterisation are detailed elsewhere.

Notably, transmission windows are realised in 1–6 GHz in the metacomposite containing 10-mm-spaced orthogonal microwire array (Fig. 13.14). Furthermore, such configuration attains a higher microwave transmission level yet with a much lower wire content compared with parallel metacomposites filled with wires of 3-mm spacing. This is attractive for miniaturised cloaking devices. Interestingly, one notes that the critical spacing for orthogonal configuration (10 mm) is larger than parallel metacomposites (7 mm); that is, metamaterial features are readily available in orthogonal metacomposites as the spacing is over 10 mm. The 90 degree wires can be regarded as an insertion of an array of discontinuous wires between neighbour continuous 0 degree wires due to small excitation from the axial component of electrical field [105]. The "imaginary" short-cut wires enhance the

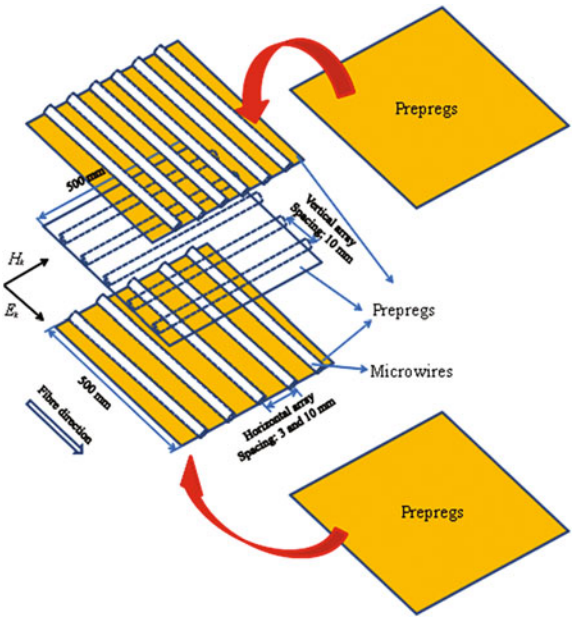

Fig. 13.13 Schematic view of manufacturing process of orthogonal wire array metacomposite with fixed wire spacing 10 mm perpendicular to glass fibres and different horizontal wire spacing of 3 and 10 mm, respectively. Reprinted with the permission from [99], copyright 2014 AIP

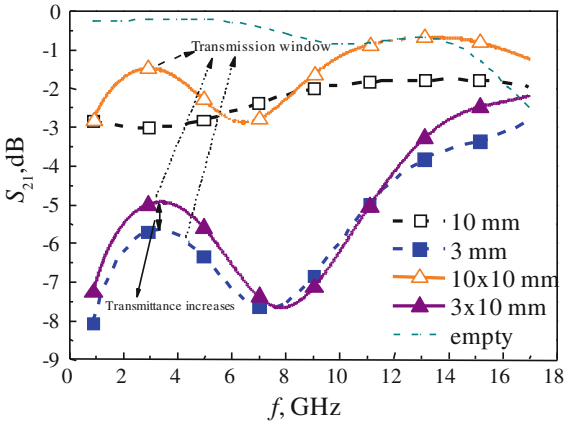

Fig. 13.14 Frequency plots of transmission spectra of polymer composites with parallel and orthogonal wire arrays and blank composite (with no wires) with electrical component along glass fibres in the absence of external fields. Reprinted with the permission from [99], copyright 2014 AIP

wire–wire interaction via the generation of circumferential fields such that the critical spacing is reduced.

Another feature of 3-mm-spaced orthogonal metacomposites is that their transmission is slightly higher than that of the parallel metacomposites with the spacing. This is also attributed to the influence of 90° wire array. In the orthogonal configuration, the small axial component of 90° wires along the electrical field of incident waves enhances both the dielectric permittivity and the magnetic permeability to a similar extent, taking into account the creation of circumferential fields [105]. Furthermore, an extra portion of permeability increase can also be secured via the weak interaction between 90 degree wires and magnetic component in microwaves [55]. Together, the impedance match is improved as per $Z = (\mu/\varepsilon)^{1/2}$, which determines the higher transmission level of orthogonal metacomposites. In this sense, one sees the possibility of a quantitative control of transmission level in the realm of orthogonal metacomposites via the investigation of relation between the transmission increase and amount of 90° wires. This is instrumental to developing cloaking devices out of the microwire composites to reach a required transmittance level from microwave perspective.

So, what is the remaining challenge? If scrutinising the S-parameter spectra of parallel and orthogonal metacomposites, one is able to find that tuning those observed transmission windows is still a tricky issue. Previous studies on meta-metastructures based on Co-based microwires have revealed unique advantages including tunable properties towards fields and stresses [98, 106, 107], thanks to their excellent soft magnetic properties and giant magnetoimpedance (GMI) effect. Absorbing the essence, one naturally comes up with an idea to explore that by incorporating Co-based microwires, how they will interplay with the existing

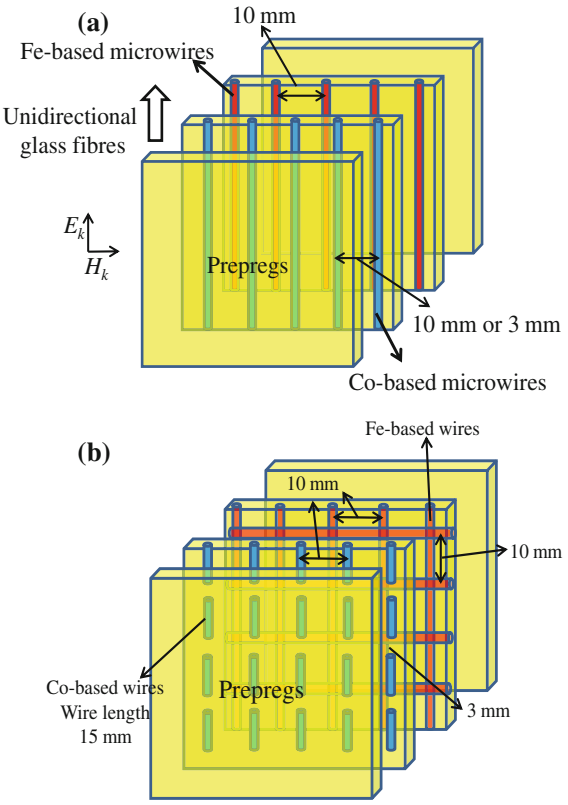

Fig. 13.15 Schematic illustration of the hybridisation of **a** continuous parallel Fe-based microwire array plus continuous Co-based microwire array and **b** orthogonal Fe-based microwire array plus short-cut Co-based microwire array

Fe-based arrays in the composites. Besides, the hybrid metacomposites containing Fe- and Co-based wires would be an interesting topic to investigate how the interactions between Co–Co, Fe–Co, and Fe–Fe wires would influence the transmission windows. Most recently, Luo et al. [108] select two combinations of Fe-based and Co-based microwires, i.e. parallel Co-based and parallel Fe-based wire array (Fig. 13.15a) and short-cut Co-based and continuous orthogonal Fe-based wire array (Fig. 13.15b). We will not harangue the experimental details, yet it should be emphasised that Fe- and Co-based microwires must be embedded into separate prepregs to minimise large reflection losses caused by physical wire contacts otherwise.

From the transmission spectrum of hybrid metacomposite with high wire concentration (10- and 3-mm spacing for Fe- and Co-based wires, respectively) (Fig. 13.16a), one striking feature is that a transmission window emerges with the presence of magnetic field of 300 Oe in the frequency band of 1–3.5 GHz. This suggests that an abnormal transmission dispersion is constructed in the continuous hybridised Fe-/Co-based wire composite system, which is distinct from the previously reported natural transmission windows independent of magnetic field but rather controlled by a critical spacing in the single Fe-based wires containing

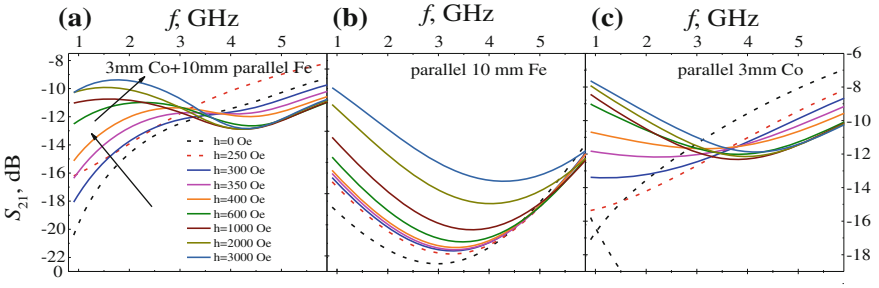

Fig. 13.16 Frequency plots of the transmission coefficients, S_{21}, of composite samples containing **a** hybrid wire arrays with 3-mm-spaced Co-based wires, **b** pure Fe-based wires, and **c** pure Co-based wires

composites [97]. With the evidence of negative permittivity dispersion in the same frequency band and negative phase velocity (not shown here for brevity), it is validated that a magnetic bias-induced double-negative features are obtained. Further, with the external fields increasing, the transmission window peak experiences a redshift–blueshift evolution (Fig. 13.16a). It is implied that such effect is because that the long dipolar resonance dominates at low magnetic fields of 600 Oe, which is induced by the interaction between wire couples [97, 99], and the FMR of Fe-based wires prevails at higher fields than 600 Oe. This magnetic bias-tunable metacomposite behaviour satisfies such working requirements of the microwave invisibility cloaking that can be activated or deactivated by conveniently exerting an additional magnetic field.

However, it should be addressed that at frequencies above 6 GHz, such field-tunable metacomposite behaviour is suppressed due to high reflection loss from the closely packed Co-based wires. Thus, it is natural to realise that, by increasing Co-based wire spacing to 10 mm, a high-frequency transmission window could be attained in the continuous hybrid composite system arising from the possible magnetic resonance between Fe–Co wire couples. A low-frequency transmission window is revealed in the frequency band of 1.5–5.5 GHz without the presence of external fields (Fig. 13.17a), indicating a natural DNG characteristic. This feature resembles the metamaterial feature realised in the parallel metacomposites containing Fe-based wires [97, 99], and readers are reminded of FMR of Fe-based wires and their parallel arrangement in the present case, which are the reasons of the simultaneous achievement of negative permittivity and permeability. Another feature of note is that a transmission enhancement is also achieved at a higher frequency band of 9–17 GHz for such widely spaced wires containing metacomposites, indicating a DNG band (Fig. 13.17b). This is due to the interactive magnetic resonance between Co–Fe wire couples (Co- and Fe-based wires are intentionally mismatched by 1 mm), which is in favour of a negative permeability dispersion in the concerned frequency range. Compared with the metacomposites containing 3-mm-spaced Co-based wires, the hybridisation of a “dilute” microwire array into the composites enables a new way of broadening the metamaterial

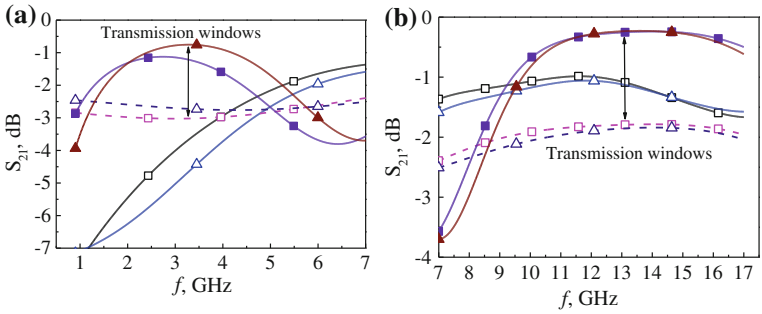

Fig. 13.17 Transmission coefficients of composites containing 10-mm-spaced Fe-based wire array, the 10-mm-spaced Co-based wire array, and their hybridised wire arrays in the frequency band of **a** 0.9–7 GHz and **b** 7–17 GHz

operating frequency band and gives us a paradigm of dual-band metamaterial in the context of composite materials. In a brief conclusion, the spacing of Co-based wires has profound effects on the metamaterial behaviour of wire composites: (i) the magnetic field-tunable properties could only be preserved by significantly decreasing the spacing of Co-based wire array to 3 mm; (ii) increasing Co-based wire spacing can mitigate high reflection loss at high frequencies and induce additional magnetic interaction between Fe–Co wire couples, thus developing a high-frequency transmission enhancement.

Luo and Qin et al. also propose and fabricate an architecture of the combination of orthogonal and short-cut wire arrays [108]. The S-parameters of metacomposites containing, respectively, short-cut Co-based wires, orthogonal Fe-based wires, and their hybridised wire array are shown in Fig. 13.18. Observation of a typical band-stop feature accompanied by a sharp transmission dip and an absorption peak at 6 GHz is identified in the composite containing short-cut Co-based wires. It can be explained by the dipolar behaviour of the short wires. It is established that short wires act as dielectric dipoles when interacting with the electrical component of waves. The dipole resonance can be written as $f_{\mathrm{dr}} = \frac{c}{2l\sqrt{\varepsilon_m}}$ (below the percolation threshold), where ε_m and l denote the permittivity of matrix materials and wire length, respectively [109]. Taking ε_m as 3 [110, 111] and l as 15 mm into above equation, we obtain f_{dr} = 5.8 GHz, which coincides well with the identified resonance peak in Fig. 13.18b. In other sense, the artificial microwave opaqueness in the short Co-based wire composite is induced by the wire configuration therein since no wires' material properties need to be considered. By including such short-cut array into the Fe-based wire–enabled metacomposites, one notes that the observed band-stop feature is maintained along with some enhancement of transmission in the 1–6 GHz frequency (Fig. 13.18a) regime compared with composites containing only orthogonal Fe-based wires. Hence, the introduced short-cut Co-based wires can apply a synergistic influence to enhancing the DNG feature of metacomposites; this is due to the low absorption loss of Co-based wires at DNG

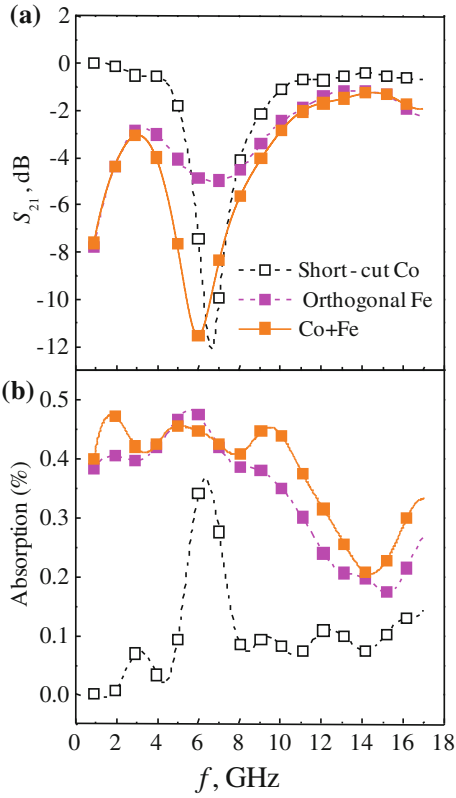

Fig. 13.18 **a** Transmission, S_{21}, and **b** absorption coefficients of composites containing orthogonal Fe-based wire array, short-cut Co-based wire array, and their hybridised wire arrays in the absence of external fields

operating frequencies as also verified in Fig. 13.18b. From this perspective, the observed structure-associated opaqueness arising from the short-cut wires correlated with the transmission enhancement at DNG operating frequencies provide a way out to achieve transmission tunability in the context of engineering metacomposites through manipulation of Co-based wire spacing and its arrangement.

To date, three kinds of hybrid metacomposites are introduced, i.e. dense continuous, dilute continuous, and short-cut metacomposites. It is worth reiterating that, compared with the metacomposite containing single Fe-based wire arrays, hybrid metacomposites demonstrate metamaterial characteristics that are more tunable by external magnetic field. As discussed above, several effects, i.e. FMR in Fe-based wire, Fe–Fe wire, Co–Co wire, and Fe–Co wire interactions, are involved and the predominating mechanism varies at different frequency. A combination of coarse and fine control of metacomposite behaviour is therefore readily available via the selection of different microwires and manipulation of any spacing and arrangement that are involved in this composite system. In view of these merits, the present composite may indicate a significant application of radio frequency identification (RFID), in which structure polymer composites are heavily used. The RFID is a contactless data-capturing technique using RF waves to

automatically identify objects. The ever-increasing applications of RFID for commercial inventory control in warehouses, supermarkets, hospitals as well as military friend-and-foe identification have resulted in considerable research interest on low-cost, long-range sensor design. Conventional RF tags are usually achieved either by the printed spacing-filling curves [112] or by the capacitively tuned dipoles [113]. However, these tags consist of complicated-shaped structure, thus requiring large manufacturing costs. Furthermore, the undesirable parasitic coupling effect of these structures when interacting with EM waves makes the precise analysis of their EM performance rather difficult. Our present study herein proposes a kind of versatile composite containing microwire arrays of a simple structure. By incorporating these wire composites into the objects to be detected, each object will have a unique ID coded in these composites. Moreover, the recent unfortunate "MH370" event calls for application of such multifunctional composites to identify civil airplanes by their distinguished microwave response, considering their DNG features in the radar frequencies. Such application appears to be more practical than cloaking invisibility at this stage, and importantly, for differentiating civil aircrafts from military planes or even identifying every airborne vehicle.

Lastly, the prepreg-based composites possess much better mechanical properties compared to those conventional metamaterials in addition to the metamaterial particularities [114]. Indeed, regardless of the matrix, the wire arrays alone [62] or simply bonding the wire arrays on the paper [74, 115] is able to yield negative permittivity (see Fig. 13.10). But the essential requirement for composites in engineering application is their structural function. In this sense, the proper choice of matrix, fabrication, and the resultant structural performance need to be addressed carefully to obtain a truly applicable multifunctional composite.

References

1. Pendry JB (2000) Negative refraction makes a perfect lens. Phys Rev Lett 85:3966–3969
2. Shalaev VM, Cai W, Chettiar UK, Yuan HK, Sarychev AK, Drachev VP, Kildishev AV (2005) Negative index of refraction in optical metamaterials. Opt Lett 30:3356–3358
3. Alu A, Engheta N (2003) Pairing an epsilon-negative slab with a mu-negative slab: resonance, tunnelling and transparency. IEEE Trans Antennas Propag 51:2558–2571
4. Shelby RA, Smith DR, Schultz S (2001) Experimental verification of a negative index of refraction. Science 292:77–79
5. Smith DR, Padilla WJ, Vier DC, Nemat-Nasser SC, Schultz S (2000) Composite medium with simultaneously negative permeability and permittivity. Phys Rev Lett 84:4184–4187
6. Valentine J, Li J, Zentgraf T, Bartal G, Zhang X (2009) An optical cloak made of dielectrics. Nat Mater 8:568–571
7. Sihvola A (2007) Metamaterials in electromagnetics. Metamaterials 1:2–11
8. http://www.aichi-mi.com/
9. Shamonina E, Solymar L (2007) Metamaterials: how the subject started. Metamaterials 1:12
10. Maier SA (2007) Metamaterials and imaging with surface plasmon polaritons. Springer, New York
11. Dolling G, Wegener M, Linden S, Hormann C (2006) Photorealistic images of objects in effective negative-index materials. Opt Express 14:1842–1849

12. Veselago V (1968) The electrodynamics of substances with simultaneously negative values of ε and μ. Soviet Phys Usp 10:509–514
13. Rotman W (1962) Plasma simulation by artificial dielectrics and parallel-plate media. IRE Trans Anntenas Propag 10:82–95
14. Pendry JB, Holden AJ, Stewart WJ, Youngs I (1996) Extremely low frequency plasmons in metallic mesostructures. Phys Rev Lett 76:4773–4776
15. Lagarkov AN, Matytsin SM, Rozanov KN, Sarychev AK (1998) Dielectric properties of fiber-filled composites. J Appl Phys 84:3806–3814
16. Lagarkov AN, Sarychev AK (1996) Electromagnetic properties of composites containing elongated conducting inclusions. Phys Rev B 53:6318–6336
17. Makhnovskiy DP, Panina LV. (2005) Field and stress tunable microwave composite materials based on ferromagnetic wires. In: Murray VN (ed) Progress in ferromagnetism research. Nova Science Publishers Inc., Hauppauge
18. Fang N, Lee H, Sun C, Zhang X (2005) Sub-diffraction-limited optical imaging with a silver superlens. Science 308:534–537
19. Shalaev VM (2007) Optical negative-index metamaterials. Nat Photon 1:41–48
20. Schurig D, Mock JJ, Justice BJ, Cummer SA, Pendry JB, Starr AF, Smith DR (2006) Metamaterial electromagnetic cloak at microwave frequencies. Science 314:977–980
21. Liu R, Ji C, Mock JJ, Chin JY, Cui TJ, Smith DR (2009) Broadband ground-plane cloak. Science 323:366–369
22. Cai W, Chettiar UK, Kildishev AV, Shalaev VM (2008) Designs for optical cloaking with high-order transformations. Opt Express 16:5444–5452
23. Sato K, Nomura T, Matsuzawa S, Iizuka H (2008) Metamaterial techniques for automotive applications. In: PIERS proceedings, Hangzhou, China, pp 1122–1125, 24–28 Mar 2008
24. Melik R, Unal E, Perkgoz NK, Puttlitz C, Demir HV (2009) Metamaterial-based wireless strain sensors. Appl Phys Lett 95:011106
25. Alici KB, Özbay E (2007) Radiation properties of a split ring resonator and monopole composite. Phys Status Solidi B 244:1192–1196
26. Zou Y, Jiang L, Wen S, Shu W, Qing Y, Tang Z, Luo H, Fan D (2008) Enhancing and tuning absorption properties of microwave absorbing materials using metamaterials. Appl Phys Lett 93:261115
27. Watts CM, Liu X, Padilla WJ (2012) Metamaterial electromagnetic wave absorbers. Adv Mater 24:OP98–OP120
28. Landy NI, Sajuyigbe S, Mock JJ, Smith DR, Padilla WJ (2008) Perfect metamaterial absorber. Phys Rev Lett 100:207402
29. Wakatsuchi H, Christopoulos C (2011) Generalized scattering control using cut-wire-based metamaterials. Appl Phys Lett 98:221105
30. Ourir A, Ouslimani HH (2011) Negative refractive index in symmetric cut-wire pair metamaterial. Appl Phys Lett 98:113505
31. Butt H, Dai Q, Farah P, Butler T, Wilkinson TD, Baumberg JJ, Amaratunga GAJ (2010) Metamaterial high pass filter based on periodic wire arrays of multiwalled carbon nanotubes. Appl Phys Lett 97:163102
32. Wen QY, Zhang HW, Yang QH, Xie YS, Chen K, Liu YL (2010) Terahertz metamaterials with VO_2 cut-wires for thermal tunability. Appl Phys Lett 97:021111
33. Bratkovsky A, Ponizovskaya E, Wang SY, Holmstrom P, Thylen L, Fu Y, Agren H (2008) A metalwire/ quantum-dot composite metamaterial with negative epsilon and compensated optical loss. Appl Phys Lett 93:193106
34. Zhou R, Zhang H, Xin H (2010) Metallic wire array as low-effective index of refraction medium for directive antenna application. IEEE Trans Antennas Propag 58:79–87
35. Gorkunov MV, Osipov MA (2008) Tunability of wire-grid metamaterial immersed into nematic liquid crystal. J Appl Phys 103:036101
36. Cabuz AI, Nicolet A, Zolla F, Felbacq D, Bouchitte G (2011) Homogenization of nonlocal wire metamaterial via a renormalization approach. J Opt Soc Am B Opt Phys 28:1275–1282

37. Dong ZG, Xu MX, Lei SY, Liu H, Li T, Wang FM, Zhu SN (2008) Negative refraction with magnetic resonance in a metallic double-ring metamaterial. Appl Phys Lett 92:064101
38. Falcone F, Martin F, Bonache J, Marques R, Lopetegi T, Sorolla M (2004) Left handed coplanar waveguide band pass filters based on bi-layer split ring resonators. IEEE Microwave Wirel Compon Lett 14:10–12
39. Marqués R, Medina F, Rafii-El-Idrissi R (2002) Role of bianisotropy in negative permeability and left-handed metamaterials. Phys Rev B 65:144440
40. Marques R, Mesa F, Martel J, Medina F (2003) Comparative analysis of edge- and broadside- coupled split ring resonators for metamaterial design - theory and experiments. IEEE Trans Antennas Propag 51:2572–2581
41. Baena JD, Marqués R, Medina F, Martel J (2004) Artificial magnetic metamaterial design by using spiral resonators. Phys Rev B 69:014402
42. Baena J, Bonache J, Martin F, Sillero R, Falcone F, Lopetegi T, Laso M, Garcia-Garcia J, Gil I, Portillo M, Sorolla M (2005) Equivalent-circuit models for split-ring resonators and complementary split-ring resonators coupled to planar transmission lines. IEEE Trans Microwave Theor Techn 53:1451–1461
43. Zhao H, Zhou J, Zhao Q, Li B, Kang L, Bai Y (2007) Magnetotunable left-handed material consisting of yttrium iron garnet slab and metallic wires. Appl Phys Lett 91:131107
44. Zhao H, Zhou J, Kang L, Zhao Q (2009) Tunable two-dimensional left-handed material consisting of ferrite rods and metallic wires. Opt Express 17:13373–13380
45. Pendry JB, Schurig D, Smith DR (2006) Controlling electromagnetic fields. Science 312(5781):1780–1782
46. Vakil A, Engheta N (2011) Transformation optics using graphene. Science 332(6035): 1291–1294
47. Bückmann T, Thiel M, Kadic M, Schittny R, Wegener M (2014) An elasto-mechanical unfeelability cloak made of pentamode metamaterials. Nat Commun 5, doi:10.1038/ncomms5130
48. Pendry JB, Holden AJ, Robbins D, Stewart W (1999) Magnetism from conductors and enhanced nonlinear phenomena. IEEE Trans Microwave Theor Techn 47(11):2075–2084
49. Soukoulis CM, Wegener M (2011) Past achievements and future challenges in the development of three-dimensional photonic metamaterials. Nat Photonics 5(9):523–530
50. Zhu J, Gu H, Luo Z, Haldolaarachige N, Young DP, Wei S et al (2012) Carbon nanostructure-derived polyaniline metacomposites: electrical, dielectric, and giant magnetoresistive properties. Langmuir 28(27):10246–10255
51. Zhu J, Wei S, Zhang L, Mao Y, Ryu J, Mavinakuli P et al (2010) Conductive polypyrrole/tungsten oxide metacomposites with negative permittivity. J Phys Chem C 114(39):16335–16342
52. Guo J, Gu H, Wei H, Zhang Q, Haldolaarachchige N, Li Y et al (2013) Magnetite–polypyrrole metacomposites: dielectric properties and magnetoresistance behavior. J Phys Chem C 117(19):10191–10202
53. Zhu J, Wei S, Zhang L, Mao Y, Ryu J, Karki AB et al (2011) Polyaniline-tungsten oxide metacomposites with tunable electronic properties. J Mater Chem 21(2):342–348
54. Zhu J, Wei S, Ryu J, Guo Z (2011) Strain-sensing elastomer/carbon nanofiber "metacomposites". J Phys Chem C 115(27):13215–13222
55. Vazquez M, Adenot-Engelvin AL (2009) Glass-coated amorphous ferromagnetic microwires at microwave frequencies. J Magn Magn Mater 321:2066–2073
56. Montiel H, Alvarez G, Gutierrez M, Zamorano R, Valenzuela R (2006) The effect of metal-to-glass ratio on the low-field microwave absorption at 9.4 GHz of glass-coated CoFeBSi microwires. IEEE Trans Magn 42(10):3380–3382
57. Phan M, Peng H, Yu S, Wisnom M (2007) Large enhancement of GMI effect in polymer composites containing Co-based ferromagnetic microwires. J Magn Magn Mater 316(2): e253–e256
58. Phan MH, Peng HX (2008) Giant magnetoimpedance materials: fundamentals and applications. Prog Mater Sci 53(2):323–420

59. Qin F, Peng H, Phan M (2010) Wire-length effect on GMI in $Co_{70.3}Fe_{3.7}B_{10}Si_{13}Cr_3$ amorphous glass-coated microwires. Mater Sci Eng B 167(2):129–132
60. Zhukov A, Zhukova V (2009) Magnetic Properties and Applications of Ferromagnetic Microwires with Amorphous and Nanocrystalline Structure. Nova Science Publishers Inc., New York
61. Qin F, Peng H-X (2013) Ferromagnetic microwires enabled multifunctional composite materials. Prog Mater Sci 58(2):183–259
62. Garcia-Miquel H, Carbonell J, Boria V, Sánchez-Dehesa J (2009) Experimental evidence of left handed transmission through arrays of ferromagnetic microwires. Appl Phys Lett 94:054103
63. Chen J, Tang D, Zhang B, Yang Y, Lu M, Lu H, Lu F, Xu W (2007) Left-handed materials made of dilute ferromagnetic wire arrays with gyrotropic tensors. J Appl Phys 102:023106
64. Carbonell J, García-Miquel H, Sánchez-Dehesa J (2010) Double negative metamaterials based on ferromagnetic microwires. Phys Rev B 81:024401
65. Garcia-Miquel H, Carbonell J, Sanchez-Dehesa J (2010) Left handed material based on amorphous ferromagnetic microwires tunable by dc current. Appl Phys Lett 97:094102
66. Labrador A, Gómez-Polo C, Pérez-Landazábal JI, Zablotskii V, nigo Ederra I, Gonzalo R, Badini-Confalonieri G, Vázquez M (2010) Magnetotunable left-handed FeSiB ferromagnetic microwires. Opt Lett 35:2161–2163
67. Sarychev AK, Shalaev VM (2000) Electromagnetic field fluctuations and optical nonlinearities in metal-dielectric composites. Phys Rep 335:275–371
68. Ivanov AV, Shalygin AN, Galkin VY, Vedyayev AV (2009) Rozanov3 KN. Metamaterials with tunable negative refractive index fabricated from amorphous ferromagnetic microwires: magnetostatic interaction between microwires. PIERS. ONLINE 5:649–652
69. Kittel C (1948) On the theory of ferromagnetic resonance absorption. Phys Rev 73:155
70. Adenot-Engelvin AL, Dudek C, Acher O (2005) Microwave permeability of metamaterials based on ferromagnetic composites. J Magn Magn Mater 300:33–37 (The third Moscow international symposium on magnetism 2005)
71. Adenot-Engelvin AL, Dudek C, Toneguzzo P, Acher O (2007) Microwave properties of ferromagnetic composites andmetamaterials. J Eur Ceram Soc 27:1029–1033
72. Qin F, Peng HX, Tang J, Qin LC (2010) Ferromagnetic microwires enabled polymer composites for sensing applications. Compos A Appl Sci Manuf 41:1823–1828
73. Liu L, Kong L, Lin G, Matitsine S, Deng C (2008) Microwave permeability of ferromagnetic microwires composites/metamaterials and potential applications. IEEE Trans Magn 44:3119–3122
74. Panina LV, Ipatov M, Zhukova V, Zhukov A, Gonzalez J (2011) Magnetic field effects in artificial dielectrics with arrays of magnetic wires at microwaves. J Appl Phys 109:053901
75. Makhnovskiy DP, Panina LV, Mapps DJ (2001) Field-dependent surface impedance tensor in amorphous wires with two types of magnetic anisotropy: helical and circumferential. Phys Rev B 63:144424
76. Y DI, Jiang J, Du G, Tian B, Bie S, He H (2007) Magnetic and microwave properties of glass-coated amorphous ferromagnetic microwires. Trans Nonferrous Met Soc China 17:1352–1357
77. Qin FX, Peng HX, Phan MH, Panina LV, Ipatov M, Zhukova V, Zhukov A, Gonzalez J (2011) Smart composites with short ferromagneticmicrowires formicrowave applications. IEEE Trans Magn 47:4481–4484
78. Vazquez M, Chiriac H, Zhukov A, Panina L, Uchiyama T (2011) On the state-of-the-art in magnetic microwires and expected trends for scientific and technological studies. Physica Status Solidi (A) 208:493–501
79. Shinjo T, Shigeto K, Nagahama T, Mibu K, Ono T (2000) Studies on magnetization reversal in submicron wires and domain wall behaviors. J Phys Soc Jpn 69:91–98
80. Otani Y, Kim SG, Fukamichi K, Kitakami O, Shimada Y (1998) Magnetic and transport properties of sub micron ferromagnetic wires. IEEE Trans Magn 34:1096–1098

81. Chiriac H, Corodeanu S, Lostun M, Ababei G, Ovari TA (2010) Magnetic behavior of rapidly quenched submicron amorphous wires. J Appl Phys 107:09A301
82. Ovari TA, Corodeanu S, Chiriac H (2011) Domain wall velocity in submicron amorphous wires. J Appl Phys 109:07D502
83. Chiriac H, Lostun M, Ababei G, Ovari TA (2011) Comparative study of the magnetic properties of positive and nearly zero magnetostrictive submicron amorphous wires. J Appl Phys 109:07B501
84. Saitoh E, Tanaka M, Miyajima H, Yamaoka T (2003) Domain-wall trapping in a ferromagnetic nanowire network. J Appl Phys 93:7444–7446
85. Ono T, Ooka Y, Kasai S, Miyajima H, Nakatani N, Hayashi N, Shigeto K, Mibu K, Shinjo T (2001) Magnetization reversal and electric transport in ferromagnetic nanowires. Mater Sci Eng B-Solid State Mater Adv Technol 84:126–132
86. Chiriac H, Corodeanu S, Lostun M, Stoian G, Ababei G, Ovari TA (2011) Rapidly solidified amorphous nanowires. J Appl Phys 109:063902
87. Kraus L, Infante G, Frait Z, Vazquez M (2011) Ferromagnetic resonance in microwires and nanowires. Phys Rev B 83:174438
88. Vega V, Prida VM, Garcia JA, Vazquez M (2010) Torque magnetometry analysis of magnetic anisotropy distribution in ni nanowire arrays. Physica Status Solidi a-Applications and Materials Science 208:553–558
89. Tartakovskaya EV, Pardavi-Horvath M, Vazquez M (2010) Configurational spin reorientation phase transition in magnetic nanowire arrays. J Magn Magn Mater 322:743–747
90. Gonzalez-Diaz JB, Garcia-Martin JM, Garcia-Martin A, Navas D, Asenjo A, Vazquez M, Hernandez-Velez M, Armelles G (2009) Plasmon-enhanced magneto-optical activity in ferromagnetic membranes. Appl Phys Lett 94:263101
91. Pardavi-Horvath M, Si PE, Vazquez M, Rosa WO, Badini G (2008) Interaction effects in permalloy nanowire systems. J Appl Phys 103:07D517
92. Navas D, Pirota KR, Zelis PM, Velazquez D, Ross CA, Vazquez M (2008) Effects of the magnetoelastic anisotropy in ni nanowire arrays. J Appl Phys 103:07D523
93. Ramos CA, De Biasi E, Zysler RD, Brigneti EV, Vazquez M (2007) "blocking" effects in magnetic resonance? the ferromagnetic nanowires case. J Magn Magn Mater 316:E63–E66
94. Prida VM, Pirota KR, Navas D, Asenjo A, Hernandez-Velez M, Vazquez M (2007) Self-organized magnetic nanowire arrays based on alumina and titania templates. J Nanosci Nanotechnol 7:272–285
95. Gonzalez-Diaz JB, Garcia-Martin A, Armelles G, Navas D, Vazquez M, Nielsch K, Wehrspohn RB, Gosele U (2007) Enhanced magneto-optics and size effects in ferromagnetic nanowire arrays. Adv Mater 19:2643–2647
96. Ivanov A, Galkin VY, Ivanov VA, Petrov DA, Rozanov KN, Shalygin AN, Starostenko SN (2009) Metamaterials fabricated of amorphous ferromagnetic microwires: negative microwave permeability. Solid State Phenom 152–153:333–336
97. Luo Y, Peng HX, Qin FX, Ipatov M, Zhukova V, Zhukov A, Gonzalez J (2013) Fe-based ferromagnetic microwires enabled meta-composites. Appl Phys Lett 103:251902
98. Makhnovskiy D, Zhukov A, Zhukova V, Gonzalez J (2009) Tunable and self-sensing microwave composite materials incorporating ferromagnetic microwires. Adv Sci Technol 54:201–210
99. Luo Y, Peng H, Qin F, Ipatov M, Zhukova V, Zhukov A et al (2014) Metacomposite characteristics and their influential factors of polymer composites containing orthogonal ferromagnetic microwire arrays. J Appl Phys 115(17):173909
100. Vázquez M, Zhukov A (1996) Magnetic properties of glass-coated amorphous and nanocrystalline microwires. J Magn Magn Mater 160:223–228
101. Qin F, Peng H-X, Tang J, Qin L-C (2010) Ferromagnetic microwires enabled polymer composites for sensing applications. Compos A Appl Sci Manuf 41(12):1823–1828

102. Sampaio L, Sinnecker E, Cernicchiaro G, Knobel M, Vázquez M, Velázquez J (2000) Magnetic microwires as macrospins in a long-range dipole-dipole interaction. Phys Rev B 61 (13):8976
103. Velázquez J, García C, Vázquez M, Hernando A (1996) Dynamic magnetostatic interaction between amorphous ferromagnetic wires. Phys Rev B 54(14):9903
104. Velázquez J, Vazquez M, Hernando A (1999) Interacting amorphous ferromagnetic wires: a complex system. J Appl Phys 85(5):2768–2774
105. Kraus L, Frait Z, Ababei G, Chiriac H (2013) Ferromagnetic resonance of transversally magnetized amorphous microwires and nanowires. J Appl Phys 113(18):183907–183908
106. García-Miquel H, Carbonell J, Sánchez-Dehesa J (2010) Left handed material based on amorphous ferromagnetic microwires tunable by dc current. Appl Phys Lett 97(9):094102–094103
107. García-Miquel H, Carbonell J, Boria V, Sánchez-Dehesa J (2009) Experimental evidence of left handed transmission through arrays of ferromagnetic microwires. Appl Phys Lett 94 (5):054103
108. Luo Y, Qin F, Scarpa F, Carbonel J, Ipatov M, Zhukova V et al (2015) Hybridized magnetic microwire metacomposites towards microwave cloaking and barcoding applications. ArXiv Preprint arXiv:150607745
109. Makhnovskiy D, Panina L, Garcia C, Zhukov A, Gonzalez J (2006) Experimental demonstration of tunable scattering spectra at microwave frequencies in composite media containing CoFeCrSiB glass-coated amorphous ferromagnetic wires and comparison with theory. Phys Rev B 74(6):064205
110. Qin F, Peng H, Fuller J, Brosseau C (2012) Magnetic field-dependent effective microwave properties of microwire-epoxy composites. Appl Phys Lett 101(15):152905
111. Luo Y, Peng H, Qin F, Adohi B, Brosseau C (2014) Magnetic field and mechanical stress tunable microwave properties of composites containing Fe-based microwires. Appl Phys Lett 104(12):121912
112. McVay J, Hoorfar A, Engheta N (2006) Space-filling curve RFID tags. In: Radio and wireless symposium. IEEE, pp 199–202
113. Jalaly I, Robertson I (2005) Capacitively-tuned split microstrip resonators for RFID barcodes. In: Microwave conference, European, vol 2. IEEE, 4pp
114. Peng H, Qin F, Phan MH, Tang J, Panina L, Ipatov M, Zhukov A, Zhukova V, Gonzalez J (2009) Cobased magnetic microwire and field-tunable multifunctional macro-composites. J Non-Cryst Solids 355:1380–1386
115. Panina L, Ipatov M, Zhukova V, Zhukov A, Gonzalez J (2010) Microwave metamaterials with ferromagnetic microwires. Appl Phys A Mater Sci Process 103:653–657